Ministry of Education of the Russian Federation
Tomsk Polytechnic University

N.N. Nikitenkov

THE BASICS OF ISOTOPIC, CHEMICAL AND STRUCTURAL ANALYSIS OF THE SURFACE BY MEANS OF ATOMIC PHYSICS

Textbook

Tomsk 2005

УДК 535.33

N.N. Nikitenkov. Basics of isotopic, chemical and structural surface analysis by means of atomic physics methods. Manual. Tomsk: TPU edition, 2005.– 153 p.

The manual consists of 8 parts which are devoted to both theoretical and experimental issues of the analysis of physical properties of solids and films.

The manual was made in the department of general physics of the faculty of natural sciences and mathematics of Tomsk Polytechnic University. It is recommended for undergraduates and masters of the course “The physics of the condensed state of a matter”

The textbook is printed in accordance with decision of edition committee
of Tomsk Polytechnic University

Reviewers: G.V. Kuznetsov, Professor, Department of Physical Mechanics of Tomsk State University

B.P. Romanov, Professor, Department of Applied Mechanics, Tomsk State University of Architecture

Yu. I. Tyurin, Professor, Department of General Physics, Tomsk Polytechnic University

FOREWORD

Importance of fathoming of the processes happening on a surface admitted the beginning of XX century, but only in 1960th years (with development of a ultrahigh vacuum technique) the capability for development of surface research methods has appeared. Interest to a surface on nuclear and an electronic level is dictated both applied, and fundamental problems. In practical aspect propagation of this interest is promoted by the following technological directions: 1) A materials technology in many aspects, and in particular, a heavy growth of the semiconductor industry; 2) Chemical engineerings and first of all a contact catalysis with use ultra- and nano- dimensional powders; 3) Making materials with preset properties; 4) many other things.

At a fundamental level the interest to a surface caused by the following concepts. Presence of a surface erodes ideal three-dimensional periodicity in a structure of a solid and can result in to occurrence of the localized electronic and oscillatory states which are necessary for taking into account at theoretical description of solid's properties.

Study of X-ray, photoelectric and auto-electronic emissions, slow electrons diffractions, secondary ion- and ion-photon- emission, discovery of an Auger effect alongside with perfecting of a ultrahigh vacuum technique and detection of small signals on major noise have given to the creating of basic for new techniques of a surface research.

In last 2-3 decades use of devices and equipments for a surface diagnostic became property not only scientific laboratories, but also the industry that is accompanied by sharp increment of number of yielded and used spectrometers and other devices.

The purposes of the present manual are:

- Acquaintance with the experimental technique and procedures of deriving of the information about the isotopic and chemical composition, about surface structure and other its properties;
- Acquaintance with physical and mathematical patterns of the processes underlying of surface diagnostic methods ;
- Survey of capabilities of these methods;
- Discussion of limitations for these methods;
- обучение студентов методологии диагностики поверхности и приповерхностных слоев материалов, включающей обоснованный выбор методов качественного и количественного анализа, способов отбора и подготовки проб для анализа, проведения измерений и обработки результатов измерений.
- Training of students of surface and near-surface layers diagnostic methodology including the justified choice of qualitative and quantitative analysis methods, expedients of takeoff and preparation of hallmarks for the analysis, conducting of measurings and machining of observed data.
- The manual bases in monographies, surveys and the original articles which have published in Russia and behind its boundaries in last two decades, and also on personal experience of the author in design and practical use of some from methods. Let's underline, that all research techniques besides that they allow to receive the information on the major performances of materials, are object of fundamental scientific researches which continuously improve notions about the processes happening at interaction of particles and radiations with solids. Therefore in some theoretical sections of the manual wider representations about these processes are given than it is required for the routine analysis. The level of an enunciating and discussion corresponds to knowledge of bachelors.

Within the framework of the manual it is impossible to give exhausting description of all methods and orbs of their application, therefore in many events the author had to neglect particulars which knowledge is necessary for successful practical use of the circumscribed methods. The basic attention is given physics of phenomena on which methods of the surface analysis are founded, to survey of methodical capabilities and restrictions, and also the methods which having wide practical application in applied scientific researches and the industry. The manual includes presentation of the basic clusters of analytical equipments as in them the substance of a method is frequently embodied.

The manual is written for students of the high schools training on a direction "Physics", but it, undoubtedly, will be useful for a wide range of persons requiring in diagnostic of a surface.

N. Nikitenkov
June, 2005.

1. Introduction

God created volume and left the surface to Devil.

Wolfgang Pauli.

1.1 From the history of surface science and thin films.

From the ancient times, men have been interested in physical phenomena on the surface of liquids and solids. The earliest record must have appeared in ancient Babylon in cuneiform. The type of witchcraft, today known as lecanomacy, was based on the analysis of oil conduction pored into the bowl with water. With the help of this analysis the foreteller could forecast the end of the military campaign and foresee illness. In XVII-XVIII centuries there was the hypothesis that the sea waves could be made quiet by pouring oil into the sea. In particular, the outstanding naturalist (and fluids lover) Benjamin Franklin (1706-1790) was calming pond's waves down with the help of coreless bamboo stick filled with oil: "Though the amount of oil was not more than one teaspoon it made water calm within the limits of several yards. Then, gradually spreading along the pond oil reached its leeward side. As a result, a quarter of the pond the area of which was approximately half an acre became as glide as a mirror".

In XIXth century the methods of scientific analysis were elaborated. Due to this fact three main results were gained that were of great significance for surface science:

– 1833 - M. Faraday focused his attention on the mysterious phenomenon: hydrogen and oxygen reaction started at noticeably lower temperature than regular combustion with the presence of platinum. M. Faraday, as it was typical of him, elaborated the series of experiments, which led to the creation of qualitative theory of catalysis. This theory has not been changed till nowadays.

– 1874 – K.-F. Brown noticed some deviation from the Ohm's law when he was making the electrical measurements on metal sulfide passing the electricity through the laminated structures consisted of Cu and FeS. Later on he made a correct assumption that the reason for such an unusual dissymmetric resistance today known as rectification was connected with thin film interface.

– 1877 – G. U. Gibbs's work "Balance of heterogeneous substances" was published. In this work he elaborated the mathematical devise of thermodynamics and statistical mechanics. Gibbs described phase surface thermodynamics of heterogeneous systems.

– At the beginning of XXth century, owing to the attempts of I. Lenmurg, surface science became a separate field of analysis. Lenmurg was a pioneer in the elaboration of the experimental methods which were necessary in the field of high-vacuum explorations. He coined such notions as adsorption chemical connection, surface adsorption grid, coefficient of accommodation. He also made basic researches in the work of metal extraction, heterogeneous catalyses and adsorption, and he worked out laws of thermionic emission. In 1932 he was awarded the Nobel Prize for "his remarkable discoveries and elaborations in the field of surface chemistry".

– In 1921 – the Nobel Prize was awarded to A. Einstein for the photoeffect explanation which had a direct relation to the surface.

– In 1937 – the Nobel Prize was given to K. Devisson for his work on electronic diffraction. In 1960s owing to his discoveries, photoemissive spectroscopy and diffraction of slow electrons were widely used for the analysis of electronic and crystal structure of the surface. In 1930s I.E. Tamm and others determined the existence of electronic conditions and their characteristics located on the crystal surface. At the same time the first theory of free metal surface was developed. In 1930s basic research works on the surface of semi-conductors were mainly focused on the "metal-semi-conduction" boundary. In 1940s due to these researches semi-conductors were practically used for the first time. They were selenium rectifiers and dot detectors made out of lead sulphide, the basis of which constituted the division of the semi-conductor and metal properties. Later on, transistors were developed: first bipolar with point contacts (1949) and at the beginning of 1960s FET appeared on the basis of Si with the inversion layer or on the basis of "metal – oxide - semi-conductor” (MOP-structure). Si-SiO_2 boundary played an important role in the work of FET. After that, special attention was paid to the surface explorations and to the phase segregation boundaries, which led to the creation of great variety of semi-conduction devices.

It must be considered that the surface physics really appeared in the second half of 1960. The surface physics appeared due to the following events.

1. The establishment of the fact that the electronic spectroscopy, Auger in particular, allowed to register chemical linkage located on the surface of solids and sensitive even to small parts of monolayer.
2. Due to space programs the industrial technology developments of the ultrahigh vacuum (UHV) chambers appeared which kept the sample clean for a long period of time. So, there appeared the opportunity to carry out controlled experiments on the solid surface and to match them with the theoretical models.
3. The appearance and wide spread of high speed computers gave new opportunities to the theoretical modeling of the most difficult processes on the surface.

The last two centuries had shown that the surface physics became more “complicated”. Nowadays it is likely that physics is at its primary stage. As a result of such development there appeared the adjacent branches (related branches) of surface physics: Thin films physics and boundary physics.

Modern surface physics, thin film physics and boundary physics include the following achievements:

1) The development of preparation and diagnostic methods (elemental and chemical structure test, crystal and electronic test and some other researches) of clear semi-conductor surfaces and boundaries.
2) The elaboration of general notions of clean surface crystal and electronic structure and the determination of definite notions and correlations.
3) The establishment of theoretical calculation methods of crystal and electronic structure of semiconductors and interfaces. The elaboration of erosion theory and surface growth.
4) The decoding of partial certain structures and electronic features in some semi-conductors.
5) The application of experimental and theoretical physics methods of clean surfaces for the investigation of atomic adsorption exploration processes and for the research of certain interfaces.

1.2 The physical phenomena underlying methods of surface diagnostic

The chronology of any research method appeared on the surface (and not only on the surface) can be presented in the following way:

1) Certain physical phenomenon discovery which appears under the influence of any factor on the surface;
2) Physical process exploration chargeable for the certain phenomenon;
3) Connection establishments between phenomenon characteristics and surface characteristics;
4) Purposeful study of the surface characteristics based on the phenomena characteristics.

Electron beams, ion and photon beams, and temperature influential factors of atomic physics are considered to be the most important.

In this section a brief description of physical phenomena based on the methods of surface diagnostics is given. The attention is focused on phenomena, on the basis of which operating and methods proved to be efficient were invented. Some definite physical processes appear on the basis of each phenomenon. Parts 4 and 5 of the given manual are devoted to the most important ones. Parts 6–8 include definite methods of surface investigation through the defined connections of the phenomenon characteristics with surface features.

1.2.1 Ion emission (IE)

The ejection of positive and negative ions by solid surface under the influence of some diving factor is called *ion emission* (IE).

1) Material heating followed by thermal evaporation (sublimation) of its particles from the surface is called *thermionic emission* (TIE). Only single charged ions are emitted.
2) Electrical fields with the strength of $\sim 10^7$ V/cm at the surface cause the so called *field ion emission* (FIE). At the same time single and multi-charged ions are formed.
3) Photon radiation of the material (including laser radiation and X-ray) may be conducted by particles elimination from the surface, some part of which is emitted in the form of ions. This is *photon-ion emission* (PIE), which is also called *radiation-enhanced ion emission* (REIE) when the energy of the photon is high.
4) Electron radiation of the material may cause *electron-ion emission* (EIE).
5) Bombarding of the surface with rapid ions and atoms leads to particles vanishing from the surface: in case of ion bombardment such phenomenon is called *ion-ion* or *secondary ionic emission* (SIE).

All mentioned phenomena can be used for receiving information about the solid body and its surface. However, for surface exploration only those phenomena are widely used that were listed in 2 and 5. The surface structure is studied with the help of FIE (part 8), and SIE forms the basis for power-mass-spectrometer (PMS) method of secondary ions for isotopic and chemical surface mixture investigation (part 6). Let us take a closer look at these two phenomena.

Ion sputtering and secondary ionic emission

As it has been already said, the phenomenon of secondary ionic emission occurs when the surface is bombarded by ions. As ion bombardment is widely used in various aspects of surface diagnostics, let us briefly observe these phenomena and processes it is followed by. The most essential of them are the following:

– volumetric and surface scattering of bombarding ions (including the change of charge state):

– emission of charged and neutral particles and their compositions: spraying, SIE, ion-electronic emission (IEE), ion-stimulated desorption (ISD) from the solid surface:

– emission of electromagnetic radiation with wide frequency spectrum (ion luminescence, ion-photon emission (IFE), X-ray);

– various radiation processes, such as blemish formation both in the solid volume and on its surface.

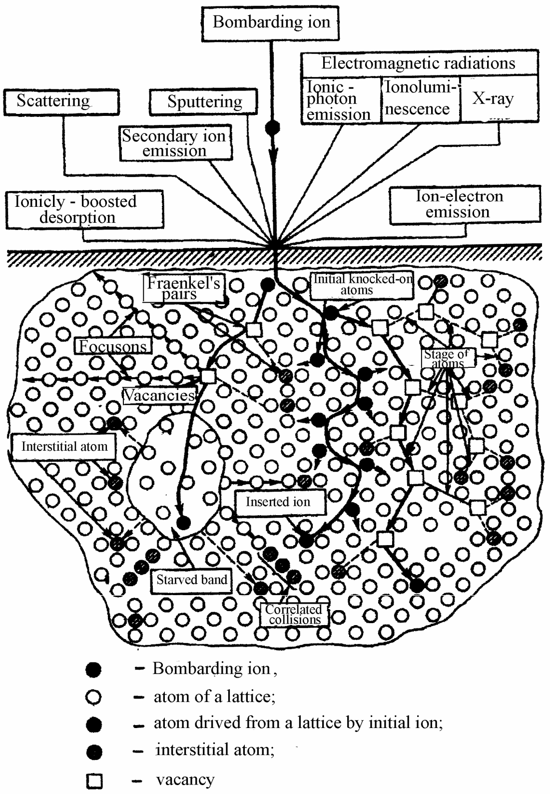

Fig. 1.1. The diagram of essential processes caused by solid ion bombardment. Various emission types of both charged and neutral particles, and different types of radiation faults are shown.

The diagram of mentioned processes and phenomena is shown in Fig. 1.1. The simple fact of collision between an ion and a solid atom can be considered as the first stage. As a result of this process there appears energy rearrangement and bombarding ion momentum between the diffused ion and the target atom. Collision leads to the appearance of extensive clash successions of definite directivity connected with crystallographic features of solids (e.g. focusons, dynamic crowed dions), atomic collision cascade, and some processes of electronic film rearrangements of collided atoms cause repeated processes. Part 4 is devoted to this phenomenon.

Definite features are given for the description of emission processes which define the process itself. So, for the description of secondary ion emission the following defining features are given:

– *output coefficient* of secondary ions or *secondary ion yield* is defined by the ratio

$$K_{\mathrm{i}} = N_{\mathrm{i}}/N_0\ , \tag{1.1}$$

where N_{i} and N_0 – is the number of secondary and bombarding ions

– *ionicity* or *degree of ionization* α is defined as the ratio of the ion number N_i in the course of secondary particles to the number of all atomic particles in this course $N_{\text{в}}$:

$$\alpha = N_{\mathrm{i}}/N_{\text{в}}; \tag{1.2}$$

– *coefficient of the surface sputtering S* is defined as

$$S = N_{\text{в}}/N_0\,. \tag{1.3}$$

All mentioned features are obviously connected with each other by the following ratio:

$$K_{\mathrm{i}} = \alpha \cdot S. \tag{1.4}$$

<u>*Field ionic emission* (FIE)</u>

FIE is necessary to be observed as the combination of two phenomena: *field desorption (and volatilization*) and *field ionization*. Let us briefly observe these two phenomena.

Field desorption – disposition of adsorbed atoms or molecules from the surface of solids by the influence of the electrical field (the strength of which is $E \sim 10^7$-10^8 V\cm). This phenomenon can be observed at the extended temperature range including extremely low ones. Eliminated particles are ionized. High field elimination of atoms from the solid surface is called *field desorption.* This type of surface is better studied on the metal carrying base field. Field desorption and volatilization can be observed as thermal volatilization of atoms, which overcome probable barrier depressed by electrical field. All in all, FIE can be regarded as atom surface ionization when there is a field desorption and volatilization. When particles have rather low ionization energy and not very low temperatures, this theory satisfactorily defines ions extreme charge and explains the connection, which is observed between desorbing field E and temperature T for one and the same desorption speed.

$$E = (ne)^{-3}[\Lambda + I_{\mathrm{n}} - n\Phi - kT\ln(\tau/\tau_0)]. \tag{1.5}$$

n is ionization repetition factor, e – electron charge, Λ - sublimation heat of adsorbed substance, I_{n} – n-multiple ionization strength of emitting particle, Φ - electron work function from the surface, τ – average time of particle overcoming energy barrier with the height $Q = \Lambda + I_{\mathrm{n}} - n\Phi - (n^3e^3E)^{1/2}$, τ_0 - period of particle oscillation in the potential hole.

When thermal excitation does not guarantee barrier overcoming, the representations of tunnel “escaping” of ions through the barrier (tunnel effect) are used for big ionization energy and low temperature. Field penetration into conductor and polarizability of surficial atoms is taken into consideration. Field desorption makes it possible to define bounding energies of adsorbed particles with matrix; it is particularly used in field-emission microscopy for sample cold cleaning (part 8). It can also be used as one of the methods to obtain intensive ion beams in the ion source.

Field ionization close to the metal surface

FI is the ionization process of atoms and gas moleculs in high electric field. Bound in the free atom, the electron can be presented as the one situated in the symmetrical potential hole (Fig. 1.2, a). When the electrical field with E strength is included to the initial potential energy of the electron $V_0(x)$ situated in point x, the potential energy eEx is added, where e is the electron charge. Hence, the potential hole becomes asymmetric: on its one side the potential barrier is formed with the final width x_1-x_2. The electron can "infiltrate" through this barrier, so the tunnel effect appears and ionization can be obtained from the first (basic) level of the atom.

$W(V,E')$ possibility of electron tunneling through the potential barrier is defined by the following formula:

$$W(V,E') = \exp\left\{-\frac{4\pi}{\hbar}\int_{x_1}^{x_2}\sqrt{2m[V(x)-E']}\,dx\right\}, \qquad (1.6)$$

where $V(x)=V_0(x)+eEx$ and E' is the potential and complete electron energy, m is its mass. The possibility of $W(V,E')$ tunneling suddenly increases when the area of the barrier under the right line is reduced. It happens when we increase the field strength E or increase the electron energy in the atom due to some other excitation. So, the probability of hydrogen atom FI from its general state obtains noticeable size only at E~10^8 V/cm and from the excited state at E~10^6 V/cm.

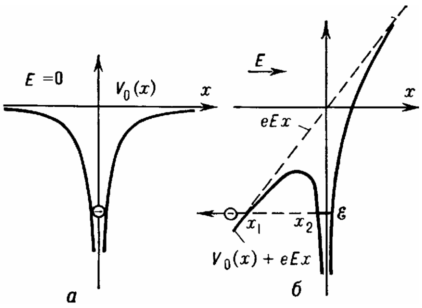

Fig. 1.2. Diagram of electron potential energy in free space without field (a) and with field (б).

FI is better investigated closer to the metal surface. FI is more probable on the metal surface than in the free space with the same field strength. This is determined by the action of electrostatic force "representation" which diminishes the potential barrier. However, FI on the metal surface is possible only when the distance between the atom and the surface does not exceed the critical state x_{cr}. It is connected with the fact that for tunnel electron transformation into the metal at a regular temperature it is necessary to raise the basic energy level of the electron in the atom with the help of electrical field up to the Fermi level in the metal (Fig. 1.3). If the atom approaches the surface at $x<x_{cr}$, then the energy level of the electron in the metal is lower than Fermi level in metal and W will dramatically decrease. On the other hand, the process when we move the atom away from the surface of the metal at $x>x_{cr}$ also leads to abrupt decreasing in W. That is why FI has practical use in the certain sphere near x_{cr}. Half width of this sphere is 0.02–0.04 nm when it is under operation condition of the field ion microscope

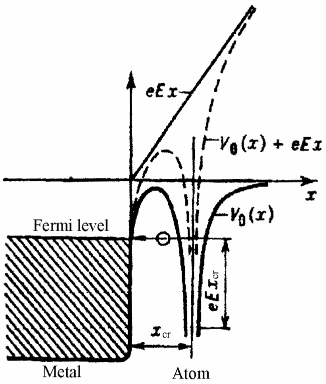

Fig. 1.3. Diagram of the electron potential energy in high electrical field close to the surface of the metal

In addition to field ion microscopes, FI is used to create ion sources for ion guns and mass-spectrometers. The advantage of such sources is the absence of high temperature electrodes and the possibility to avoid molecules dissociation. Besides, with the help of such ion sources one can observe peculiar chemical reactions which occur only in the high electrical field.

1.2.2 Electron emission (EE)

EE is electron emission from the surface of the condensed medium and by the solid surface in particular. EE occurs when some part of electrons situated in the near-surface area of the solid as a result of some outside influence obtains energy sufficient for overcoming the potential barrier on the interface between the solid and vacuum, or if the outside electrical field makes its potential barrier "transparent" for some part of electrons. EE is observed when the solid body is under some influence. There are different types of influence. From the diagnostics point of view the following types of influence and emissions are the most interesting ones:

1) heating of solids – *thermoelectron emission* (TEE);
2) electron bombardment of the surface – *secondary electron emission* (SEE);
3) ion bombardment of the surface – *ion electron emission* (IEE*)*;
4) surface exposure to electromagnetic radiation – *photoelectron emission* (PEE);
5) creation of the highest electrical field (10^7 V/cm) near the surface – *field electron* (*or autoelectron*) *emission* (PEE).

Thermoelectron emission (TEE)

TEE is electron emission produced by heated solids (emitters) into vacuum or some other environment. Only those electrons that get an additional energy needed for potential barrier overcoming can leave the solid body. The minimum energy needed is called *work function* and is defined by the ratio:

$$\Phi = e(\varphi_{\text{sample}} - \varphi_{\text{vacuum}}) - E_F\ , \tag{1.7}$$

where e is the electron charge, φ_{vacuum}, φ_{sample} are electrostatic potentials in vacuum and volume of the solid, E_F is Fermi energy. The number of electrons, which are able to leave solid boundaries in the conditions of thermodynamic balance according to Fermi – Dirak distribution at the temperature ~300 increases slowly and exponentially with the increase in the temperature. That is why TEE current is noticeable only when the solid is heated. In the absence of the field that extracts eliminated electrons they form emitter negative space charge which limits TEE current near the surface. If such field exists, then, according to Langmuir theory, when the tension is low $V<V_0$ between the emitter and the anode TEE current density is $J \sim V^{3/2}$. Under $V>V_0$ the space charge "revolves" and current gets the density of $J=J_0$ and under following increase V shoots up slowly (Fig. 1.4.). Current tension density J_0 can be calculated by Richardson-Deshman formula:

$$j_0 = AT^2 \exp(-\Phi / kT)\ , \tag{1.8}$$

$A=A_0(1\text{-}r)$, r is the energy averaged coefficient of electron reflection from the surface; $A_0=4\pi ek^2m/\hbar^3$ = 120.4 A/cm^2K^2 where e – electron charge, m – electron mass; Φ – work function. Formula (1.8) was obtained based on the assumption that the emitter surface is uniform and that the electronic gas is in the conditions of thermodynamic balance. But in reality such balance is disturbed by current turnover and penetration of the external electrical field into the emitter and also by Φ being dependent on A. That is why Φ and A found from the dependence $j(T)$ cannot be considered as constant substances. For the majority of pure metals the responsiveness of the mentioned factors leads to A notion from 15 to 350 A/cm^2 K^2.

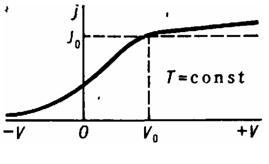

Fig. 1.4. Tension dependence of thermo electronic current j on V tension between emitter and anode

Formula (1.8) can be applied to the description of TEE both out of metals and semi-conductors (SC). However, the influence of temperature, electrical field, admixtures in the emitter, etc. on the emission current and on such values as Φ and A is different in semi-conductors and in metals. Such difference appears because of small amount of conductive electrons and existence of localized surface electron conditions influencing Fermi level E_F position for semi-conductor surface up to its “fastening” in some place of the forbidden area. At that neither E_F being on the semi-conductor surface nor Φ depends on E_F in volume (i.e. on the type and concentration of doped impurity). Such fixing is usually implemented in crystals with covalent bond (Ge, Si, etc.); in this case the nature of TEE is the same as made from metal. On clean surfaces of ion crystals the structure of surface property is in such condition that the Fermi level on the surface can move inside the forbidden area following its position in the structure. That is why when the type and admixture concentration in volume PP is changed; Φ and the barn-floor value TEE are changed too. Besides, the electrical field in such PP is not screened by the charge of surface properties but it penetrates into emitter on the considerable depth. The surface of big number of emitters is heterogeneous; there are “spots” on them with different work function. Between them the contact potential and the electrical fields of spots appear. These fields create an additional potential barrier for emitted electrons and this leads to stronger barn-floor dependence on anode voltage and temperature.

On the work of TEE the thermoelectronic cathodes of electron guns is based (section 3.2.2), they are used in electrovacuum and gas-discharge devices, in industrial plants.

Secondary electronic emission (SEE)

SEE – emission of electrons (secondary) by solids and liquids over bombardment by electrons, which are called *principal electrons.* The time interval between principal electrons input into the target and secondary electrons output is not more than $10^{-14} - 10^{-12}$ s. If radiation thickness by the primary electrons target is less than the run of primary electrons, then secondary electrons are emitted from both sides: the bombarding surface (SEE "for radiation") and its reverse side (SEE "for shooting"). Fig. 1.5 shows typical energetic spectrum of secondary electrons: it can be seen that it has an unbroken character from energy E=0 to energy E_p of primary electrons. In general current of secondary electrons one can conditionally note down the following 4 parts (Fig. 1.5):

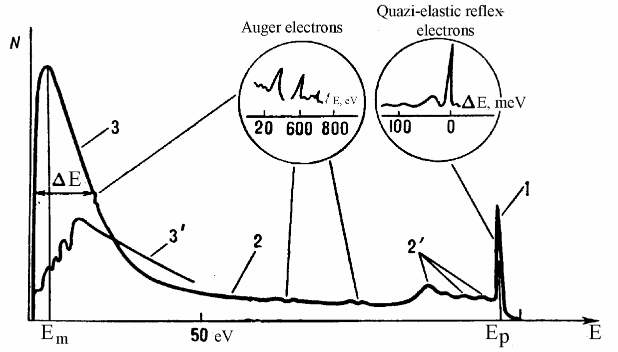

Fig. 1.5. Energy spectrum of secondary electrons: 1 – low-loss and quasi-elastic reflected electrons; 2 – non-elastic reflected electrons (including those with characteristic energy losses – 2′); 3 – true secondary electrons; 3′ – example of spectrum of true secondary electrons for plane (100) of monocrystal W obtained in narrow spatial angle.

1) *primary electrons elastically reflected from the surface;*
2) *quasi-elastic reflected electrons* (i.e. which had some characteristic energy losses up to hundreds of eV on the excitation of lattice oscillations)*;*
3) *primary non-elastically reflected electrons* (E>50 eV);
4) *true secondary electrons (*E≤50eV).

The latter represent the electrons of the substance, whose energy received from primary and non-elastically reflected electrons is sufficient for vacuum yield, i.e. exceeding the work function. The most probable energy of true secondary electrons for metals is E_m~2÷4.5 eV and maximum half-width is ΔE_m~12÷15 eV. For non-conductors it is E_m~1 eV and ΔE_m~1.5÷3 eV.

The electronic spectrum fine structure shown on the incisions of Fig. 1.5 is caused by Auger electrons and distinctive energy losses at the atom excitation of the substance. It contains information concerning elemental structure of the substance, chemical relations and atoms interposition. The spectrum fine structure of true secondary electrons emitted from monocrystals and registered and irradiated in the narrow solid angle reflects the distribution of electron condition density, which is higher than the Fermi level.

SEE is quantitatively defined as SEE coefficient

$$\sigma = I_1/I_2 = \delta + \eta + r\,, \tag{1.9}$$

where I_1, I_2 – primary and secondary electrons current, δ, η, r – true SEE coefficient of elastic and non-elastic reflected primary electrons. Coefficients δ, η, r are the values averaged on the big number of elementary emission operations caused by the separate primary electrons. If $P(n)$ – target emission probability (n=0, 1, 2, 3, ...) of secondary electrons under the influence of one primary electron; then we have $\sigma = \sum_{n=0}^{\infty} nP(n)$. At primary electron energy E_p<100 eV – $\sigma = \delta + r$, and at E_p >100 eV – $\sigma = \delta + \eta$. Coefficients σ, δ, η, r depend on E_p, primary electron angle φ, atomic number Z and substance structure, surface state, temperature (in case of SEE non-conductors), and surface edge indices $\{hkl\}$ in case of monocrystals.

Primary electrons elastic scattering is defined by energy band structure of the emitter near-surface region, elastic resonance scattering at collective and single threshold excitation of solid electrons, and by non-elastic channels opening, and in case of monocrystals by electron diffraction.

Electron non-elastic scattering is defined by dispersion and primary electron breaking when moving inside the emitter. The non-elastically scattered electron flow consists of diffusely scattered electrons and of dispersed electrons along big and small angles. The latter possess greater energy than those that diffusely scattered. The contribution of these electron groups into SEE strongly depend on E_p of primary electron angle φ emitter, atomic number Z. Non-elastically scattered electrons come out from different depths d up to

$$d_{max} = 3 \cdot 10^{11} A/\rho Z\, E_p^{\,1,4}\ м\,, \tag{1.10}$$

where ρ – emitter substance density in kg/m^3 ; A – mass number, E_p – primary electron energy in keV.

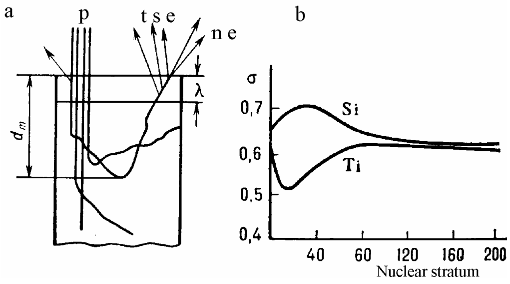

Fig. 1.6. a: The table of secondary electron emission formation: p – primary electrons; ne – non-elastically scattered electrons; t, s, e – true secondary electrons;
b: Electron emission coefficients dependence on primary electrons penetration depth d_m over Si on Ti and Ti on Si coating.

At $E_p \geq 1$ *keV* the average energy of non-elastically scattered electrons is $\langle E_a \rangle = (0.31 + 2.5 \cdot 10^{-3} Z) E_p$. When Z decreases, E_a increases due to d_{max} growth.

True secondary electrons are emitted from near-surface layer with the thickness λ (Fig. 1.6, a) under the influence of primary electrons and non-elastically scattered electrons, that is why $\delta = \delta_0 + \delta_1 = \delta_0 + k{\cdot}s{\cdot}\eta$, where δ_0 and S – electrons quantity formed by one primary electron and one non-elastically scattered electron, $k = d_m/(d_m + \lambda)$. For metals at $E_p > E_{pm}$ $\lambda << d_{max}$ and $\delta_1 = s{\cdot}\eta$. At $E_p < E_{pm}$ the depth output λ does not depend on E_p, but δ_0 and S decrease when E_p increases. Work function decrease results in greater growth of δ_0 and s rather than δ. Since non-elastically reflected electrons pass over a longer way if compared to primary electrons, when crossing the outlet area at different angles, then $\delta_0 < s$. For all metals $s/\delta_0 \sim 3 - 9$, a $\delta_1/\delta_0 \sim 0.2 - 4$. Despite similar σ implications, s and δ_0 implication difference results in $\sigma(d)$ dependence having extremes over $d \sim \lambda$ of antipodal features (Fig. 1.6. b) – maximum for Si and minimum for Ti, when silicon (Si) is applied to titanium (Ti) or Ti to Si (δ_0 and s for Si is more than for Ti).

As a result of interaction, metals with true secondary electrons, which have the conduction electron, lose such amount of energy so that they cannot leave the emitter. They are defined by the little significances λ (~30Å) and do not depend on E_p, Φ and φ, $\sigma_{max} \sim 0.4 - 1.8$.

Ion-electron emission (IEE)

IEE – electron emission by the solid body during its ion bombardment. There exist potential electrons emission from the surface (potential IEE) and their kinetic dislodging (kinetic IEE). Such potential emission is connected with the energy target transmission to electrons. The energy emits at the transmission of bombarding ion into the main atom state. As a rule, such transmission is carried out by Auger neutralization. If the ion approaches the metal surface and the non-occupied energy level of this ion is lower than the electron Fermi level in the metal, then, one of the conduction electrons will pass to the non-occupied ion level. Such transmission is shown with number 1 in Fig. 1.7, a. As a result, the ion is neutralized and the released energy is transmitted to another metal electron (2 in Fig. 1.7), which gets the opportunity to leave the metal. Under the following boundary condition the IEE can be observed: $\varepsilon_i > 2\Phi$, where ε_i – atom energy ionization, ions of which are being observed, Φ – metal work function. For non-metals instead of Φ the boundary condition includes energy of the highest level filled with electrons (e.g. this is the valence band “absolute limit” for intrinsic semiconductors).

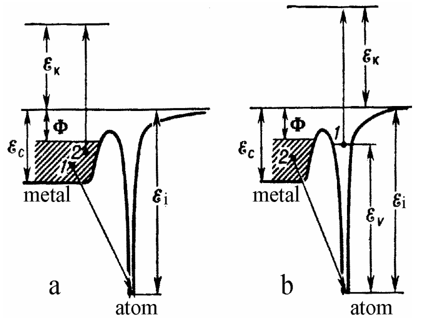

Fig. 1.7: a – Auger neutralization of positive ion on metal surface: ε_i – ionization energy; Φ – metal work function; ε_c – conduction area bottom; ε_κ – electron kinetic energy in vacuum; b – Auger deactivation.

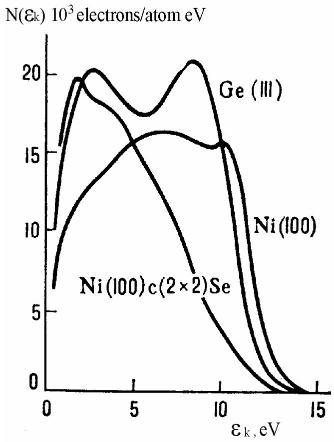

Fig. 1.8. Electron energy spectra at potential ion equalization He^+ with energy of 5 eV from various targets (written above the curves). Inscription Ni (100) with (2x2) Se means that on the edge (100)Ni Se is adsorbed, which forms cubic lattice (c) of 2x2.

The coefficient of the potential emission γ_p equal to the medium of the electrons per 1 ion departing to the vacuum increases when ε_i becomes higher and it grows up to dozens of percent for monovalent ions of rare gases. In case of multicharged ions the electrons capture by ion is carried out in series with gradual descending of ion charge repetition factor up to 0. At that γ_p may exceed 1. When ions energy $E_0 \leq 1$ keV – γ_p slowly decreases at E_0 growth. When E_0 is high γ_p quantities go down to 0.

In such cases, when ions neutralization in the excited state of the atom (and not in its normal state) is possible, the process of electrons emission is carried out by Auger deactivation (Fig. 1.7, b). The energy emitted when the target electron (2, Fig. 1.7, b) had changed into the excited atom state is transformed to electron 1 on the excited level. Here emission occurrences are the following: $\varepsilon_v > \Phi$, where ε_v – atom excitation energy. Auger deactivation–induced emission is fulfilled mostly under rare gas ions radiation of the refractory metal target. Here, γ_n from one to dozens of keV in the interval E almost does not depend on E. When ε_i is close to 2Φ or ε_v is close to Φ then the coefficient γ_p may notably depend on target temperature T. When the target is monocrystal γ_p is considerably defined by the edge crystal structure and in this case IEE can be observed. The energy spectrum shape of the emitted electrons (Fig. 1.8) depends on energy electron distribution in metal conduction band (or in semiconductor valence band) and can be used for its determination. Maximum energy in spectrum is close to $\varepsilon_i - 2\Phi$. Kinetic dislodging is caused by atoms ionization by collision of the target surface layer and impinging particles. Its common feature is the energy threshold E_{0th} (type of energy, under lower level of which emission cannot be observed) (Fig. 1.9). In

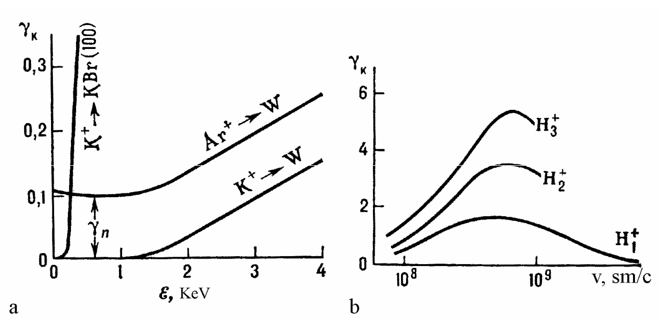

Fig. 1.9. a – view of the dependence of kinetic dislodging coefficient γ_K on ions energy Ar and K for W and KBr; b– is the same as "a" when Cu is bombarded by hydrogen isotope ions.

ion bombardment of refractory metals Li^+ is heavier E_{0th}>1кeV; in non-conductors, for example, alkalihalogen crystals, E_{0th}~0.1–0.2 keV. When energy E_0 is higher than the threshold the kinetic dislodging coefficient $\gamma_к$ increases, comes out into the plateau, and decreases (Fig. 1.9, b). For isotope ions H^+ the maximum emission is observed when E_0=100 keV, under such energies of available ions the peak value $\gamma_к$ for metals is ~1,5. For heavier ions when E_0 is about MeV the meaning $\gamma_к$ may run up to few dozens and depends on surface condition. Both electrons of target atoms and impinging particles themselves come out into the vacuum. Some number of electrons is excited by the fast recoil atom. When we talk about a monocrystal $\gamma_к$ are different for different edges and none monotonously depend on the ion angle. Energy distribution of emitted electrons under kinetic dislodging has maximum (~1–3eV) distant wane where peaks and generations are pointed out and connected with Auger change in collided particles and other processes (Fig. 1.10).

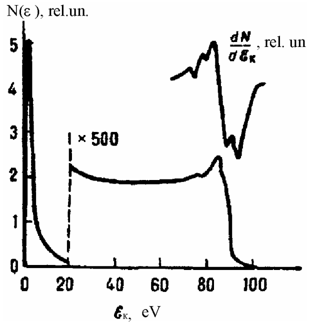

Fig. 1.10. Energy electrons spectrum on kinetic dislodging.

Potential and kinetic IEE of metals are separated in space and time. At ions approaching the surface at first they are neutralized and they irradiate electrons determining potential IEE. After the atomic particles collision the electrons appear which determine kinetic IEE. Usually both IEE are additive, i.e. $\gamma=\gamma_p+\gamma_к$, however, such additive property is not always observed, e.g. it may not occur in nonconductors and Thin films of compound composition.

At surface bombardment by the intensive ion beam initial heating of metal may take place, as well as surface and films charging, and so on. These processes in addition to IEE lead to the appearance of thermoionic and field electron emission.

Photoelectron emission (PEE)

PEE – particular case of photoeffect known from the university program of general physics of photoeffect, namely, *extrinaic photoeffect* – electron emission by solids and liquids under the influence of electromagnetic irradiation into vacuum or some other environment. PEE has some practical use from solids into vacuum. The basic PEE rules include: 1) the number of emitted electrons is proportional to the radiation intensity; 2) for each substance under stated conditions of surface and temperature T=0 K there exists a threshold – minimal frequency ω_0 (or maximum wave length λ_0) of radiation; under such circumstances PEE does not appear; 3) maximum photoelectron kinetic energy increases linearly with the radiation frequency ω and does not depend on its intensity.

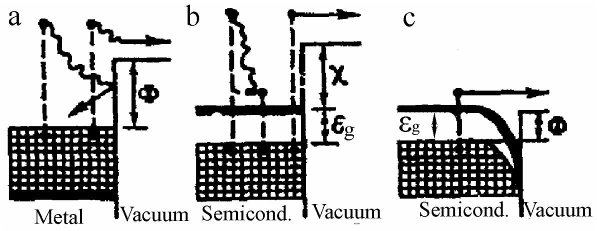

Fig. 1.11. Photoelectron emission energy diagrams: a – from metal; b – from semiconductor with $\chi>2\varepsilon_g$; c – from semiconductor, the surface of which is treated to the negative electron affinity ($\chi<\varepsilon_g$). In the area of strong internal energy field the energy bands are curved; cells show occupied electrons conditions; thick line – conduction band bottom.

PEE is the result of three consecutive processes: a) photon absorption and appearance of the high energy electron (if compared to the average one); b) motions of this electron towards the surface, on which some energy can be wasted; c) electron output to other environment via interface. Quantitatively PEE is defined by photoresponse Y – number of outgoing electrons per one photon hitting the surface. The quantity Y depends on solid features, its surface condition and photon energy. Let us illustrate the processes of PEE formation with the help of energy diagrams (Fig. 1.11). PEE appears from metals if photon energy $\hbar\omega$ exceeds metal work function Φ (Fig. 1.11 a). For clean surfaces the majority of metals have Φ>3 eV, that is why PEE from metals (if Φ is not brought down by special surface coatings) can be observed in visible and ultraviolet (UV) spectrum range. Close to the threshold PEE for the majority of metals is $Y \sim 10^{-4}$ photon/electron. Such insignificant value Y is determined by light penetration into the metal at the depth $\sim 10^{-7}$ *m* and it is absorbed there as well. Photoelectrons interact with the conduction electron while moving from the volume to the surface. In metals there are a lot of such electrons, which scatter the energy obtained from the photon very fast. The energy sufficient for the work function fulfillment is kept only by those electrons which were formed near the surface at the depth of not more than 10^{-9} m. Besides, such insignificant value of metals is caused by the fact that metal surface strongly reflects visual and short-range UV radiation.

When photon energy increases the metal photoeffect Y increases slowly with the $\hbar\omega$ growth up to $\hbar\omega$ =15 eV. When $\hbar\omega$=15 eV the metal surface reflection coefficient R sharply decreases (up to ~5%) and the electron energy inside the metal that absorbed photons increases. That is why Y increases with the great speed obtaining the value of 0.1–0.2 electron\photon for some metals (Pt, W, Sn, Ta, In, Be, Bi). Accidental contamination can significantly bring down F, as a result of which PEE threshold moves towards longer waves (from UV to the visual area) and Y in this area may increase greatly. Sharp increase in Y and threshold shift of PEE metals into the visible spectrum range can be achieved by covering the clean metal surface with the monatomic layer of electropositive atoms or molecules (Cs, Rb, Cs_2, etc.) that form the dipole electric layer on the surface.

In semi-conductors and dielectrics (Fig. 1.11, b) the PEE threshold: $\hbar\omega_0 = \varepsilon_g + \chi$, where ε_g – width of the forbidden zone, parameter χ – *affinity with electron – represents the potential barrier height for conduction electrons.* In weakly alloyed semi–conductors there are not many conduction electrons, that is why in contrast to metals photoelectron energy scattering on the conduction electrons does not play any role. In these materials the photoelectron looses its energy interacting with valence band electrons (at the same moment the collision ionization of core atoms may occur), or with lattice thermal vibrations (*photons* formation). Energy scattering speed and depth, at which photoelectrons can enter the vacuum depend on quantity χ and ratio ε_g and χ. If $2\ \varepsilon_g < \chi$, then the photoelectron with primary kinetic energy $\geq \chi$ creates an electron-hole pair. The path length per energy scattering in such an act (~1÷2 *nm*) is less than the penetration depth of radiation into the crystal (0.1÷1 μm). In this case, the majority of photoelectrons when moving towards the surface loose energy and do not come out into vacuum. In such materials PEE threshold close to the threshold is $Y \sim 10^{-6}$ electron\photon, and even at relatively large distance from the threshold ($\hbar\omega = \hbar\omega_0 + 1$ *eV*) still does not exceed 10^{-4} electron/photon.

If $\varepsilon_g > \chi$, and optical phonon energies in a solid $\sim 10^{-2}$ eV, then photoelectrons waste the energy for optical phonons formation, and photons energy scatters in semi-conductors at the path length l of only ~15-30 nm. That is why even if we bring down χ of semi-conductor to 1 eV, PEE close to the threshold is still not sufficient. In dielectric crystals of alkali-halogen compounds with the path length of 50–100 nm, χ is not too large, that is why Y increases sharply from PEE threshold and achieves a great value.

Semi-conductor surface cleaning in ultrahigh vacuum, coating of atoms or molecules monolayers, which decrease χ , and special type of alloying create the strong intrinsic electric field in the Thin surface, which accelerates photoelectrons and decreases the work function so that $\varepsilon_g > \Phi$. Here the surface potential barrier height χ may become lower then the bottom conduction zone level in the crystal volume (Fig. 1.11, c). That provides the outlet of significant number of thermalized electrons from the great depth $\sim 10^{-6}$ m.

Field Electron Emission (FEE)

FEE (synonyms: *autoelectron, electrostatic, tunnel emission*) – it is electron emission by conductive solid and liquid bodies under the external electric field E influence of rather high intensity ($E \sim 0.1$–1 V·Å^{-1}). It was found in 1929 by R.U. Wood. Classical theory wasn't able to explain FEE. Quantum mechanics methods were first applied in FEE from metal in 1928 by R. Fowler and L. Norheim. Their theoretical explanations of FEE were based on the tunnel effect. The simplified conception of FEE and tunnel effect can be obtained by observing a potential the electric field (Fig. 1.12). The energy of the highest occupied level in the metal counted off from energy diagram for electrons in the metal bordering with it in vacuum in the presence or absence of the potential minimum is called Fermi energy E_F and equals electrons chemical potential in metals μ.

The difference between Fermi energy and potential electron energy in vacuum is thermoelectron work function Φ. Electrons that occupy the states of the conductivity band under Fermi level form Fermi liquid. The state density on the "surface" of this liquid is higher than at the bottom of the conductivity band, so it may be considered that the majority of electrons are located at energy levels near E_F. Basically, the tunneling process starts from Fermi level. In the absence of the external field electrons are kept in the metal by the half-infinite potential barrier that is why the electron can leave the metal provided it passes over the barrier. The presence of the electrostatic field F on the surface and close to it causes this barrier width change as it is shown on Fig. 1.12. So, electrons close to the surface meet the depressed and narrowed potential barrier $u=V-E$; that is why the process of tunneling can take place. The probability of passing through the barrier is

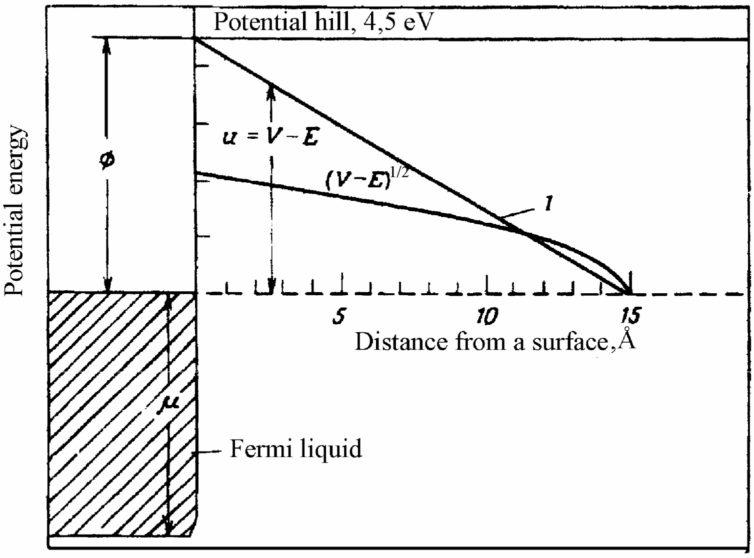

Fig. 1.12. Potential energy in metal in the presence and absence of the external field. The surface is supposed to be clean and image potential is neglected, ϕ – work function; μ – chemical potential; E – kinetic energy, V – potential energy; *1* – resulting potential. Applied field F = 0.3 V·Å^{-1}

$$P = const \cdot \exp[-(2^{3/2} m^{1/2} / \hbar)\int_0^l (V-E)^{1/2} dx], \qquad (1.11)$$

where m – particle mass; $\hbar$ – Planck's constant; E and V – kinetic and potential energies; l – barrier width. Fig. 1.12 shows that multiplier describing the barrier equation $(V\text{-}E)^{1/2}$ approximately has the triangle shape hence its corresponding area equals

$$A \approx \frac{1}{2}\phi^{1/2} \cdot \phi / F \approx \frac{1}{2}\phi^{3/2} / F\,. \qquad (1.12)$$

For the electrons located on the Fermi liquid surface the probability of passing P equals

$$P = const \cdot \exp[-(2^{3/2} m^{1/2} / h)\phi^{3/2} / F]\,. \qquad (1.13)$$

Multiplication P by the number of electrons falling to surface unit area within the time unit produces field emission current density J. As a result, strict consideration of the current density dependence on the field strength is obtained:

$$J = 6{,}2 \cdot 10^{-6} (E_F / \phi)^{1/2} (E_F + \phi^{-1} F^2 \exp(-6{,}83 \cdot 10^7 \phi^{3/2} / F)) \qquad (1.14)$$

The simple model presented in Fig. 1.12 and formulas (1.11) – (1.14) can be improved by considering the mirror view forces, which influence the electron leaving the metal both for clean and filled with adsorbate surfaces (Fig. 1.13). The mirror view force potential reduces the barrier height due to the work function decrease per value $e^{3/2}F^{1/2}$ (this value is called Schottky correction). By including this correction into the exponential part of the equation (1.14) the following expression for current density can be obtained:

$$J = 1{,}54 \cdot 10^{-6} (F^2 / \phi) t^2(y) \cdot \exp[-6{,}83 \cdot 10^7 \phi^{3/2} f(y) / F], \qquad (1.15)$$

where $f(y)$ and $t(y)$ – slowly changing elliptical functions of non-dimensional parameter

$$y = e^{3/2} F^{1/2} / \phi, \qquad (1.16)$$

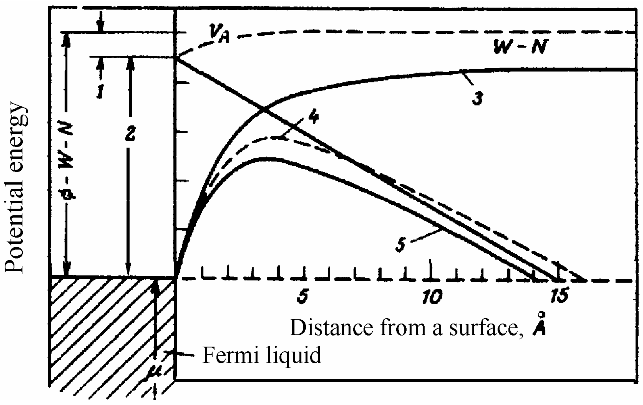

Fig. 1.13. Potential energy and image potential for electrons in the metal in the presence and in the absence of the external field. The barriers for clean metal and metal with a dipole layer of atoms of adsorbed gas are shown. ϕ – work function; μ –chemical potential; V_A – presents dipole layer contribution to compound potential; 1 – contact potential; 2 – clean W work function; 3 – mirror view force potential; 4 – W – N system effective potential; 5 – W clean surface effective potential.

functions $f(y)$ and $t(y)$ are tabulated.

Equation (1.16) was experimentally checked in the wide range of J values and was verified numerically. It can be written as

$$I / V^2 = a \exp[-b\phi^{3/2} / (cV)], \qquad (1.17)$$

where *a, b* and c – constants, *I* – emission current, *V* – applied potential connected with *F* ratio *F= cV.* It is obvious that the dependence diagram ln(I/V^2) on *I/V* must be linear and its inclination should be proportional to Φ^2 (it is often called s Fowler-Nordheim diagram).

Such graphical dependence was examined in many field emission experiments and formed the basis for field methods of the work function measurement. Though the experimental results confirm the validity of ratio (1.5), it can only be applied only to the clean emitting surface.

When the adsorbate is present the triangular or pseudo-triangular barrier must be modified by inclusion of the additional potential well into it in order to take into consideration the adsorbate presence on the surface. This sum is solved in PEE one-dimensional model of metal with free electrons in the presence of both charged and neutral adsorbate on the surface (Alferiev and Dick model). Emission of the metal in the presence of adsorbate is viewed in this model with potential usage and it is depicted in Fig. 1.14. This model is interesting because it predicts some unexpected effects, namely, resonances in the emission probability in the

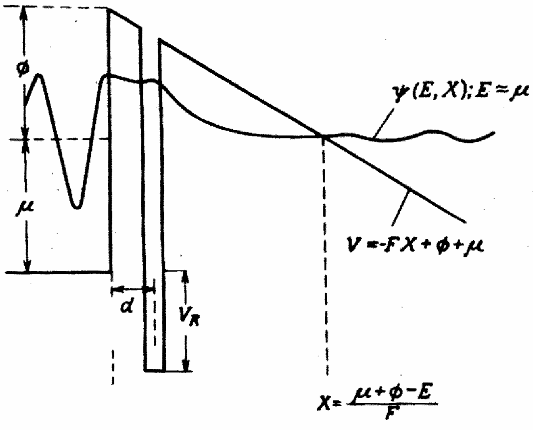

Fig. 1.14. One-dimension single-electron pseudo-potential is used when we describe metal field emission in the presence of the adsorbed atom, *d* – distance from the atom to the surface: V_R – potential drop between zone bottom of the conduction band and general adsorbed atom condition: $\Psi(E, X)$ – electron wave function at the distance *X* from the surface.

presence of metal adsorbate. All this leads to the additional peak or step in the emitted electrons energetic spectrum and also to the emission current amplification and decrease in Fauler – Nordgame graph inclination when the fields $F > 0.5$ V·A^{-1}.

Neutral adsorbates can be divided into adsorbates with and without constrained conditions; the energy level of the latter is situated below the zone bottom of metal conduction. For the adsorbate of the first type the decrease in expectancy and current emission is observed along with simple scope change in the energy distribution according to Fauler-Nordgame. For the adsorbate of the second type the current decrease is observed only when the connections are weak. Strong connection leads to the current decrease and to Cthe decrease of Fauler-Nordgame graph inclination. Thus, the adsorbate can be regarded as energy supply (sink) for tunneling electrons. The distribution of the electron energy emitted under the field influence is undoubtedly more sensitive to the potential form near the surface than current density that is the result of integration along all energies. The observed model shows that when the coming out to the metal boundary electron has the energy equal to the virtual energy level (atomic zone) of adsorbed atom then in this case tunneling electrons passing will occur resonantly when there is a field emission.

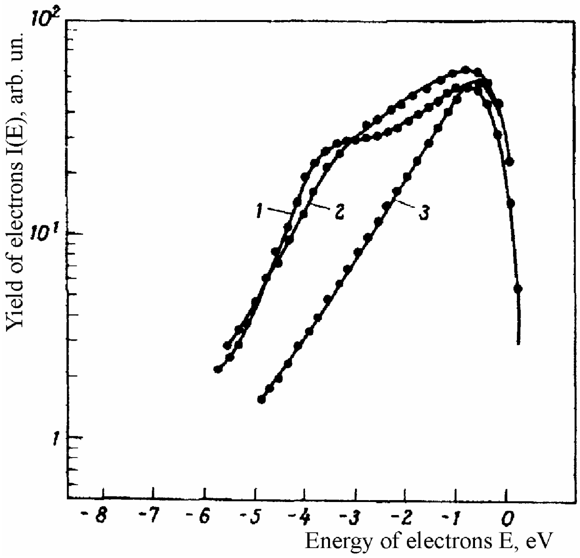

Fig. 1.15. Comparison of the experimental energy spectrums from the emitted electrons $I(E)$ when PEE from the surface W(100) that reveals contamination influence; 1 – clean surface; 2 – after CO adsorption with the temperature 77 K; 3– the same after heating up to 300 (hump disappearance can be observed).

A very important implication of the above given theory consists in the fact that instrumentation of the complete electron distribution, emitted under the field influence, according to the energy, give information about “virtual levels” of adsorbed atoms One of the examples of such instrumentation type is shown in Fig. 1.15.

2. Surface Structure

This part reveals some general information concerning crystal and electronic structures of the surface necessary for mastering the terminology used in surface analysis methods.

2.1 Crystal structure of the surface

2.1.1 Basic notions of crystallography

To understand the research methods of crystal structure of the surface it is necessary to familiarize yourself with the classification and description of its symmetry properties, i.e. to learn the basics of crystallography. Assuming that the reader is acquainted with this science, we would like, however, to remind of its main notions.

Lattice – parallel location of points where the interval between the points is equal.

Crystal structure – a system of grid and atom points where certain group of atoms (which is called *basis*) is connected with every point of the grid; all groups are identical according to their content, location, and attitude.

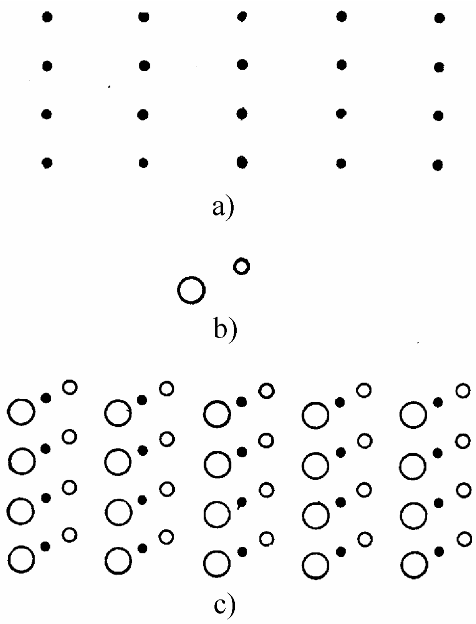
a)

b)

c)

Fig. 2.1. a – space lattice; b – basis, consisting of two different atoms; c – crystal structure: integration of b – basis with every point of the a-space lattice.

Fig. 2.1 illustrates the difference between the lattice and the crystal structure.

Perfect crystal is the result of construction by means of infinitely many occurrences of the same structural element ("brick") in space, called *the unit cell.*

Crystal symmetry – a definite property of a crystal that allows coinciding in turnings, reflections, parallel shifts, as well as in some parts in combinations of these actions. Symmetry means the possibility of object transformation to combine with itself.

Due to the perfection and symmetry of a crystal there exist three vectors: **a**, **b**, **c** that are called *the elementary translation vectors.* Examining the lattice from any arbitrary point **r'**:

$$\boldsymbol{r'} = \boldsymbol{r}+n_1\boldsymbol{a}+ n_2\boldsymbol{b}+ n_3\boldsymbol{c}, \qquad (2.1)$$

where n_1, n_2,, n_3 – arbitrary whole numbers. Elementary translation vectors are considered to be *basic* if the structure atom position examined from any two points **r** and **r'** is the same, and satisfies the proportion (2.1) under arbitrary choice of numbers n_1, n_2, n_3. Basic translation vectors **a, b, c** are chosen as unit vectors of the coordinate system connected with *crystallographic axes. Crystallographic indices* – three whole numbers, defining the location of crystal faces and atomic planes in a space (Miller indices), as well as directions in crystal and crystal edge directions (Weiss indices) relative to crystallographic axes. The straight line and parallel edge, determined by Weiss indexes p_1, p_2, p_3 (are marked as [p_1, p_2, p_3] or [h, k, l]) pass from coordinate origin O to A point, determined by vector p_1**a**+ p_2**b**+ p_3**c,** where a, b, c – lattice spacing (Fig. 2.2). P plane that cuts off segments p_1a, p_2b ,p_3c on axes, has Miller indices h, k, l determined by the attitude of entire quantities opposite to indexes p_1, p_2, p_3, т. е. h:k:l = (1/p_1):(1/p_2):(1/p_3), that are marked as (h, k, l). When one or two

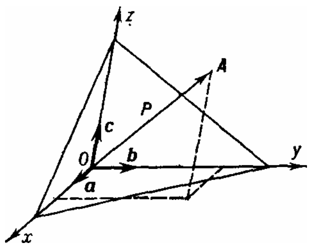

Рис. 2.2. Straight line OA with Weiss indices [2,3,3] and plane P with Miller indices (4,3,6); *Ox, Oy, Oz* crystallographic axes; *OA⊥P.*

Miller indexes equal zero, planes are considered to be parallel to one of the crystallographic axes. The negative value of Miller indexes corresponds to the planes that cut coordinate axes in negative directions. The system of symmetrical edges of one simple crystal is marked as $\{h, k, l\}$.

Translation is a transition of a crystal as a whole parallel to itself, described by vector

$$\boldsymbol{T} = n_1\boldsymbol{a} + n_2\boldsymbol{b} + n_3\boldsymbol{c}. \qquad (2.2)$$

Group of translations – a system of actions, the elements of which are different in a set of whole numbers n_1, n_2, n_3.

Vectors **a** and **b** presented in Fig. 2.2 can be regarded as vectors of two-dimensional lattice. Parallelogram which was formed by these vectors is called *the primitive cell* (only points of the lattice are in the angles), which is considered to be a part of *the unit cell.*

Point group – a system of symmetrical operations with any point of the body, in the result of which the body returns to its original position. There exist the following symmetrical operations of two-dimensional crystallographic point group: single, double, thrice-repeated, fourfold, and sixfold turns around the point, specular reflection in the plane transversely to the surface and glide reflection (particularly, the reflection relative to the straight line with the following translation along this straight line divided by translation period). *N*-numbers are used to denote turns and their multiplicity, while *m*-symbol denotes specular reflection. Only turns with $n = 1, 2, 3, 4, 6$ together with the translation symmetry requirements are used for the lattice (1.1). This requirement restricts all possible turns and translations compatible with the given turn so that various combinations of possible turns and reflections are reduced to *ten different two-dimensional point groups* permissible for two-dimensional crystal. These groups are marked with the following symbols:

1, 2, 1*m*, 2*mm*, 4, 4*mm*, 3, 3*m*, 6, 6*mm*.

The first index refers to the turn around the point so that, for example, point group 4 consists of fourfold turns.

The second index denotes the presence of the reflection action relative to the straight line transverse to *ox* axis as well as the presence of other lines of specular reflection connected with the given turn. The third index denotes the presence of other lines of specular reflection connected with each other by the symmetry conditions but having no lines of specular reflection within the limits of the first system. Crystals of the given point group constitute *the crystal class.*

2.1.2 Crystal structure of the surface and its description

The surface of the solid body represents a fault (fracture) of the solid boy crystal lattice disturbing three-dimensional translation symmetry of its volume structure. The surface, however, preserves two-dimensional periodicity, which is considered to be its major feature. Thus, *the notion of two-dimensional crystals* is connected with the basic translation vectors **a** and **b**. The structure of the solid body close to the surface is implied under the notion of the "surface structure". The part of the solid body close to the surface is called *the ridge*. Hence, the “surface” is presented in the form of the *carrying base* (three-dimensional periodic volume structure) and several atomic layers of the ridge. It is obvious that in the direction parallel to the surface there is a transformation of the three-dimensional periodic volume structure, and the distance between layers according to the normal towards the surface will be different from the lattice parameters of the carrying base volume. As a whole, the ridge is two-dimensional periodic crystal structure. The above mentioned proves that the periodicity of the surface differs from the periodicity of the carrying base, though these periodicities are *coherent*.

The given notions belong only to working surfaces, and the surface structures we are interested in contain *adsorbate.* The notion of *adsorbate structure* that implies the presence of localized excess of extraneous particles coming either from outer environment or from the solid itself is used for the description of surface layers over the ridge. It is obvious that the presence of adsorbate can significantly change the structure of the ridge as there is a possibility of the highest surface layers (adsorbate structure) to contain both new dockages and particles of the working surface.

Further, the notion of the Bravais lattices will be used.

The analysis of symmetry properties of two-dimensional lattices (grids) results into *only five lattices different in symmetry that are called the Bravais lattices* (let us remind that there are 14 of them in three-dimensional lattices): 1) hexagonal lattice with 6th degree rotation axis; 2) square lattice with 4th degree rotation axis; 3) primitive rectangular lattice; 4) centered rectangular lattices, which are *two* symmetrically non-equivalent lattices characterized by bilateral symmetry; 5) oblique lattice having none of these elements. Let us point out that only centered rectangular lattice is considered to be non-primitive. Alignment of any other two-dimensional lattice leads to the lattices, which may be characterized by primitive lattices of the same symmetry. Combining five Bravais lattices with ten different point groups causes 17 possible two-dimensional special groups. Thus, only 17 types of surface structures different in symmetry are fulfilled.

Planes are marked within either round or curly brackets (for example, (111) or {111}) depending on whether they define particular chosen plane of the given crystal or one of the planes belonging to a certain class in crystals with the specified type of symmetry. The symbols of crystallographic directions are defined similarly, either in square or broken brackets (for example, [111] or <111>).

Let us note that even in case of unconstructed working surface the surface unit cell is not necessarily a simple projection of three-dimensional unit cell on the surface plane. Let us consider, for example, plane (100) of the face-centered crystal (i.e. one of the surface planes parallel to the set of planes). Top view of such surface (i.e. volume projection on the surface) is schematically shown in Fig. 2.3. Atoms of the top layer and all the odd layers are marked with crosses, while atoms of even layers including following the top one layer are marked with circles. This surface has a square symmetry as both "the surface" and the volume have 4th degree rotation axis transversely to this surface. However, the surface Bravais lattice is described by the primitive square unit cell on the right. The projection of three-dimensional face-centered unit cell on the left constitutes centered square unit cell with the area twice as large as the original one. As we can see, centered square cell is symmetrically identical to the primitive square one. However, it would be wrong to use it for the description of the surface symmetry. Such kind of difference in the surface description using either two-dimensional or three-dimensional unit cells occurs in the description of two-dimensional structure of three-dimensional space non-primitive unit cell (which is not symmetrically equivalent to the two-dimensional structure cell). These can lead to the confusion of definitions.

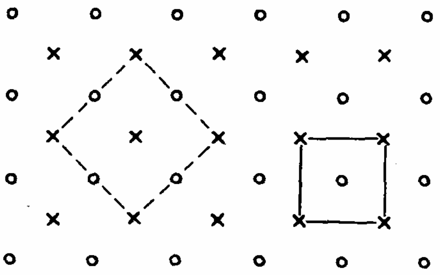

Fig. 2.3. Scheme of the solid surface (100) with body-centered cubic lattice structure.

The description of surface crystal structure

When surface layers of the solid body represent either a new-build ridge or adsorbate, or even both, the structure might be either disordered or ordered, but in any case coherent with the carrying base or ordered but incoherent with a carrying base in case when adsorbate has its own structure. The first case is easy to describe connecting the adsorbate Bravais lattice with the Bravais lattice under the carrying base. Usually one method suggested by Park and Madden is used here. It includes simple vector structure. If **a** and **b** - measuring translation vectors of the carrying base lattice, and **a'** an **b'** – measuring translation vectors of the adsorbate or the ridge, they may be connected by

$$\boldsymbol{a}'=G_{11}\boldsymbol{a} + G_{12}\boldsymbol{b}, \tag{2.3}$$

$$\boldsymbol{b}'=G_{21}\boldsymbol{a}+G_{22}\boldsymbol{b}, \qquad (2.4)$$

where G_{ij} – four coefficients that form the matrix so that

$$G=\begin{pmatrix} G_{11} & G_{12} \\ G_{21} & G_{22} \end{pmatrix}, \qquad (2.5)$$

the cells of the adsorbate and the carrying base are connected by the following proportion

$$\begin{pmatrix} a' \\ b' \end{pmatrix}=G\begin{pmatrix} a \\ b \end{pmatrix}. \qquad (2.6)$$

One of the other properties of the matrix is that the determinant (det G) is the relation of spaces of two cells at issue as the area of the unit cell of the carrying base equals to $|\,\boldsymbol{a}\times\boldsymbol{b}\,|$. This gives the following convenient classification of the surface structures:

a) det G – *an integer, and all the matrix components are integers*; two cells are *connected identically,* where the adsorbate cell has the same translation symmetry as the whole surface;

b) det G – *is a rational fraction* (or det G – *an integer, and some of the matrix components are rational fractions*); two cells are *connected relatively.* In this case the structures are still commensurable, but the real surface cell is larger than either the adsorbate cell or the ridge cell. The size of such surface cell is defined by the distance at which two cells coincide through regular intervals. That is why such structures are called structures with *coincident lattices.* In this case measuring translation vectors of the objective surface cell $\boldsymbol{a}''$ and $\boldsymbol{b}''$ are connected by cell vectors of the carrying base and adsorbate through *P* and *Q* matrixes:

$$\begin{pmatrix} a'' \\ b'' \end{pmatrix}=P\begin{pmatrix} a \\ b \end{pmatrix}=Q\begin{pmatrix} a' \\ b' \end{pmatrix}, \qquad (2.7)$$

moreover, det G and det Q are chosen to represent the least possible integers and to be connected by the proportion

$$\det G=\frac{\det P}{\det Q}; \qquad (2.8)$$

c) det G – *is an irrational;* two cells are incommensurable, and the true surface cell doesn't exist. This means that the carrying base serves as a flat surface where the adsorbate or the ridge can form their own two-dimensional structure. Such situation may occur when, for example, the bond adsorbate - adsorbate is much stronger than the bond adsorbate – carrying base, or when adsorbate particles are of a very large size to "feel" the grain effect of the carrying base.

The following definition of the surface cells is widely used. Period relations of the surface and the carrying base cells as well as the angle to which one of the cells is to be turned to place along one line both couples of the measuring translation vectors are set. Then, if A adsorbate on the {*hld*} surface of X material forms the structure with the measuring translation vectors with the length of $|\boldsymbol{a}'|=\mathrm{p}|\boldsymbol{a}|$ и $\boldsymbol{a}'=\mathrm{q}|\boldsymbol{b}|$ and angular displacement of the unit cell φ_0. The given structure can be written as

$$X\{hkl\}p\times q-R\,\varphi_0-A \quad \text{или} \quad X\{hkl\}(p\times q)R\,\varphi_0-A. \qquad (2.9)$$

This definition was given by Wood. It can be used only when angular displacements of both couples of the measuring vectors of the surface and carrying base unit cells are identical. Consequently, such definitions are suitable for such systems where the surface and the carrying

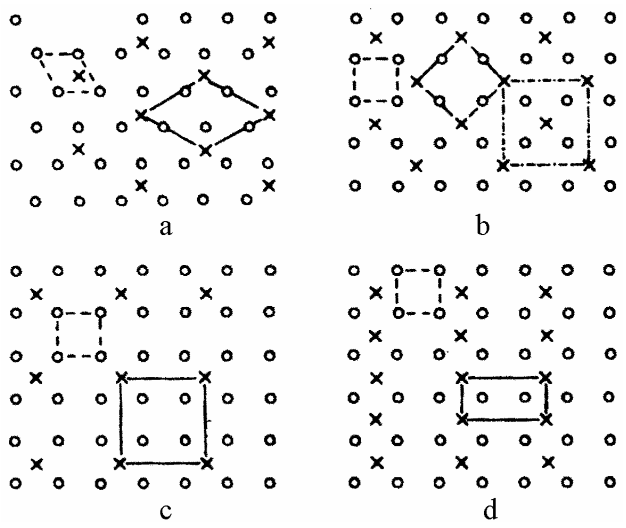

Fig. 2.4. Example of high layer structures

base unit cells have the same Bravais lattice or when one of the lattices is rectangular and the other one is square. In general, definition (2.9) is not suitable for cells with mixed symmetry, and there is a need to use the above considered matrix definitions. Working unreconstructed surface Ni{100} [defined as Ni{100} (1×1)] can be an example of (2.9) definition. At the same time the structure formed by the oxygen adsorption (O) on this surface is Ni{100} (2×2)–O. Contrary to this, Si{100} is usually transferred to Si{100}(2×1), and the atomic H adsorption cannot "change" the surface leading to Si{100}(1×1)–H structure. Examples of some surface lattices are shown in Fig. 2.4. Periodically placed atoms of the carrying base, adsorbate, or ridge are marked with circles and crosses. Dashed and firm lines are used for Bravais lattices of the carrying base and the whole surface correspondingly. **a** – structure $\left(\sqrt{3}\times\sqrt{3}\right)R30^0$ on the hexagonal carrying base, its matrix definition $\begin{pmatrix} 2 & 1 \\ -1 & 2 \end{pmatrix}$; **b** – structures (2x2) or $\begin{pmatrix} 2 & 0 \\ 0 & 2 \end{pmatrix}$, **c** – $\left(\sqrt{2}\times\sqrt{2}\right)R45^0$ or $\begin{pmatrix} 1 & 1 \\ -1 & 1 \end{pmatrix}$, **d** – (2x1) or $\begin{pmatrix} 2 & 0 \\ 0 & 2 \end{pmatrix}$. Dash and dotted lattice (*b*) is centralized, but not turned towards the unit cell of the carrying base. This structure is often described as c(2x2), which makes the definition p(2x2) for *c*-structure necessary.

One of the examples of definitions shown in Fig. 2.4 – the structure $\left(\sqrt{2}\times\sqrt{2}\right)R45^0$ on the square grid – is the most general for cubic surfaces {100}. However, in this case centered structure c(2x2) was accepted to describe the structure. It is $\sqrt{2}$ twice larger then the unit cell $\left(\sqrt{2}\times\sqrt{2}\right)R45^0$ and not expanded relatively to the carrying base cell. These causes the need to use definitions p(2x2) for true square structure (2x2) (Fig. 2.4, b). It is known that there is no centered square Bravais cell is different in symmetry from the primitive square cell, but nevertheless, this definition is widely used.

2.2 Electron structure of the surface

A number of methods of the electron surface spectroscopy is aimed at the investigation of energy state of electrons on the surface (i.e. the investigation of the electron structure of the surface).

The major objective of this study is the answer to the following vital physical questions:

1. Is there any difference between the electron state in the volume and close to the surface?
2. What is the charge density in the area of crystal border with the vacuum?
3. How do chemical connections restructure in some first atom planes after the cleft?
4. What is the electrostatic potential that surface atoms "feel"?
5. The progress of modern high technologies depends on the answer to these questions.

2.2.1 Surface states

More than 70 years ago, in 1932 I.Y. Tamm published an article "About the possible connection of electrons on the crystal surface". It was mentioned that the border of the perfect crystal lattice can serve as a source of a peculiar electron state located close to this border. Such surface states that were later called "Tammov's states" split off from the permitted spectrum area and settle inside the prohibited zone. They are very similar by nature to usual connected state studied in quantum mechanics course. For example, both of them are characterized by the energy located in the spectrum area inaccessible for "free" particle: both of them are described by the exponentially damped wave function.

With the beginning of the surface state notion it became clear that the crystal surface plays a role of *its independent subsystem where its belonging electrons also move in the periodic (two-dimensional) field. I.e. a part of the electrons is connected to the surface of the solid body migrating along it.* Now it is possible to speak about such mixed structures as metal with dielectric surface or, on the contrary, dielectric, on the surface of which two-dimensional crystal is placed. The crystal model with the superconducting surface was also discussed. However, it is very difficult to create a crystal with the surface close to the perfect one. That is why mentioned exotic structures have not been observed yet. Though, a great part of this system, called the surface phenomenon belongs to Tamm's and surface states of a different type. Theoretically the issue of surface state is considered in the following way.

Since the crystal is a system of numerous particles containing movable nucleuses and electrons, the state of these particles is described by *complete* many-particle Schredinger equation. Using Born-Oppengeimer approximation, nuclear and electron parts are singled out from this equation. By that we can come into a many-electron Schredinger equation, which represents many-electron wave equation describing the movement of electrons in the fixed nucleus field. Using the model of independent particles within the limits of Hartry-Foke method, i.e. assuming that every electron experiences statistic nucleus potential and the effect of the *middle* field of other electrons, many-electron Schredinger equation is reduced to the single-electron type. In that way, the analysis of the electron properties of crystal surface leads to the solution of the single-electron Schredinger equation together with the boundary conditions meeting the requirements of the considered system. There are various kinds of methods used here, which won't be considered in this part. Instead, let us consider some research results of surface state for semi-conductors obtained by now (to illustrate some general features of surface state).

Basic energy values used to describe surface state properties are shown in Fig.2.5. The following scheme corresponds to *p*-type crystal ($p_{\text{ь}}>n_{\text{ь}}$) with the spent layer ($p_b >p_s$ и $p_s> n_s$). Here $p_{\text{ь}}$, $n_{\text{ь}}$, p_s and n_s denote respectively cubic density of holes, cubic density of electrons, surface density of both holes and electrons. Similar diagrams can be considered for *p*-type crystal with the enriched layer ($p_{\text{ь}}<p_{\text{s}}$ и $p_{\text{s}}>n_{\text{s}}$) or for p-type crystal with the inverting layer ($p_{\text{ь}}>p_{\text{s}}$, $p_{\text{s}}<n_{\text{s}}$).

The same consideration can be directed at *n*-type crystal with spent, inverting, and enriched layers. Energy definitions and proportions described below do not greatly depend on the choice of the particular case mentioned above. Diagram on the right shows flat metal tip. If such tip really exists the external field can be applied to the surface of semi-conductor. It is supposed that the investigation of working surfaces provides separation of semi-conductor from the plate (tip) by vacuum interval (in case with contact conditions it can be oxide level).

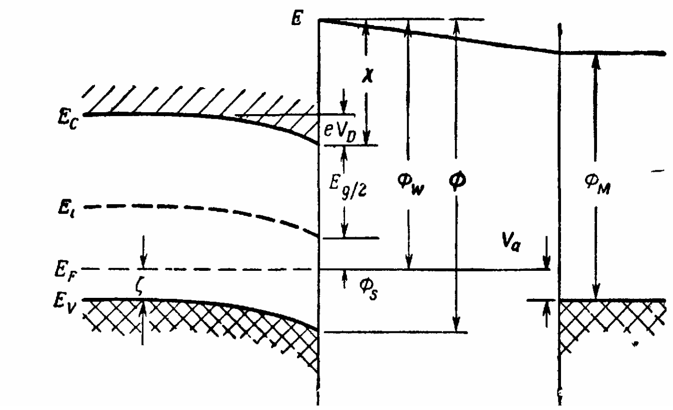

Fig. 2.5. Parameters describing space charge in p-type semiconductor. With the lack of the applied external field and surface states the curved band eV_{D}.

There exist the following typical energy types: vacuum reference level E', conduction band border E_{c}; valence band border E_v; intrinsic level $E_{\text{i}}\approx(E_{\text{c}}+E_{\text{v}})/2$; energy gap $E_{\text{g}}=E_{\text{c}}-E_{\text{v}}'$, Fermi energy E_{F}; photoelectric work function $\phi_{\text{w}}=E'-E_{\text{F}}$; photoemissive threshold (extrapolated by cubic dependence) ϕ, which, as a rule, corresponds to valence bond border of the surface (Φ corresponds to the crystal potential of ionization); electron affinity χ, doping parameter $\zeta=E_{\text{F}}-E_{\text{v}}'$, band deformation eV_{D}; surface potential ϕ_{s}; photoelectric work function of the flat metal tip ϕ_{m} and applied voltage V_a. Doping parameter for p-type extrinsic semi-conductor roughly equals to

$$\zeta = kT \ln \frac{N_v}{N_A}, \tag{2.10}$$

where N_A – acceptor center density, N_v – effective state density of the valence band (for states within the interval ~kT close to area border), k – Boltzmann constant, and T – temperature. Let us write some proportions between stated energy parameters for p-type sample (supposing that Φ corresponds to the valence band border):

$$\Phi = \chi + E_g, \tag{2.11}$$

$$\phi_w = \chi - eV_D + E_g - \zeta, \tag{2.12}$$

$$\phi_s = \frac{1}{2} E_g - eV_D - \zeta. \tag{2.13}$$

In accordance with Fig. 2.5 V_D is a positive value in equalities (2.11)–(2.13). Lack of surface state and the external field $V_D=0$ makes the zones flat up to the surface itself. In case of photoemission measuring operations from surface states Φ doesn't correspond to the valence band border, and instead of (2.11) we have $\Phi \leq \chi + E_g$. χ value depends on the geometry of crystal surface, and on the doping type and degree; that is why equalities (2.11)–(2.13) are often used for preliminary consideration of surface states. By excluding χ parameter from equalities (2.11) and (2.13) we have

$$eV_D = \Phi - \phi_w - \zeta. \tag{2.14}$$

Hence, by measuring photoemission threshold, photoelectric work function, and the doping degree we can get a band zone with the lack of external fields, i.e. the value satisfied with the mentioned requirements. It is clear that these considered proportions should be different for n-type samples due to the fact that ζ is counted from the conduction band border in the samples of this type. The replacement of $\zeta \rightarrow (E_g - \zeta)$ in (2.11) – (2.14) gives appropriate proportions in case with n-type semi-conductors.

If $V_D \neq 0$, this implies the existence of the surface states. Photo-electromotive force testing where the energy light $hv > E_g$ and I intensity cause high concentration of free electron-hole pairs on the surface gives the spontaneous method of V_D definition. This leads to the leveling of the band form. Usually the graphical chart ΔV as I function under this curve saturation $V=V_D$ is build. Here the field, appearing due to the diffusion of electrons and holes into the volume created by light, and having various mobility functions, should be considered.

Another method of V_D definition is the *conduction* measurement along the surface. It is based on the supposition that the surface state current is relatively stiff, and the volume zone provides the conductivity.

Thus, if measurements on the working surface provide some zone flexure under the lack of adsorption and external fields, surface states *should* exist. However, there is a need for complicated analysis and experimental equipment to answer the question of the quantity of existing surface states and the distribution of their energy. Let us briefly consider these issues.

2.2.2 Surface state distribution

If $V_D \neq 0$, then surface states should exist. How to obtain a surface state distribution using experimental results? There is no simple answer to this question due to Fermi statistics peculiarities. Only those states can be easily investigated, which are located on the Fermi surface or close to it. For example, electron states located on some electron-volt higher than the conductivity metal or semi-conductor area can be investigated using light absorption or hot electron dispersion testing. Thus, this issue is not investigated enough yet. Only if we managed to “scan” the energetic zone structure with Fermi level (by changing Fermi energy), and if the testing could be performed in a wide range of temperatures, the problem will be solved. Surface state structure could be defined unambiguously. In practice, however, we are only able to change a small value of the Fermi level, and the temperature interval remains narrow, received data are limited, received information on surface states is incomplete.

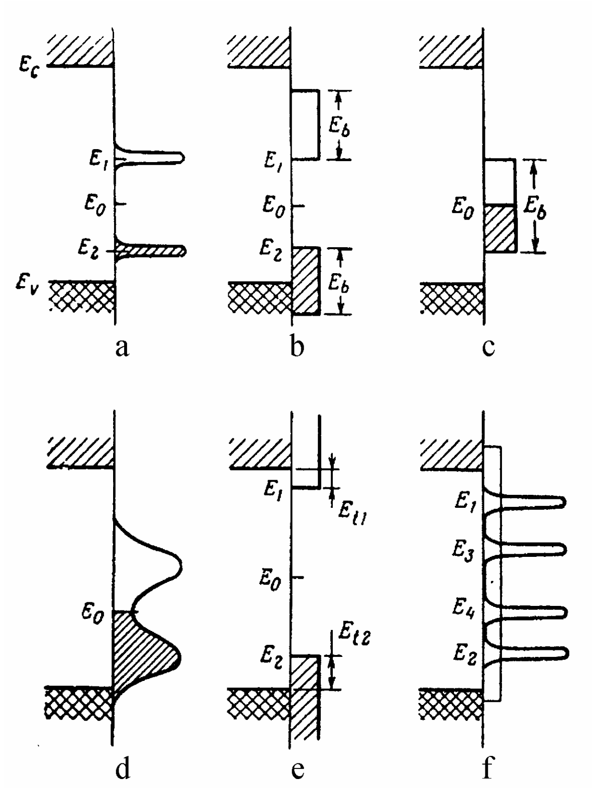

Fig. 2.6. Some useful models of proper surface states: **a** – two discrete levels; **b** – two bands; **c** – combined zones; **d** – ch-like zones; **e** – ion type bands; **f** – possible distribution of improper states.

Another reason for small width of the energetic layer, which could be scanned with E_F Fermi level, is that the whole number of surface states (both charged and neutral) is often characterized by a bottom limit E_F. Let us consider the surface state models to explain these statements.

Similar to cubic impurity states, surface states can be considered to be either “acceptor-like” or “donor-like” states. By the data, acceptor-like states are neutral if they are free; and negatively charged if only one electron is present. Donor-like states are positively charged when they are empty; and neutral if only one electron is present. Acceptor-like states are similar to the electron trap (to the neutral trap when lacking of electrons and to the negatively charged trap when at least one electron is present). Donor-like states are equivalent to the hole trap (to the neutral trap when there is no hole in it and to the positively charged when there is one trapped hole). It seems that such location, when the acceptor levels (electron traps) are situated higher than the donor levels (hole traps) is typical for surface states. Minute donors are located a bit below the conduction band, and minute acceptors – above the valence band. It is different from the proper surface states (pure surface without adsorbents): acceptor-like (donor-like) states are usually located below (above) the conduction band (valence band limit). Due to this fact, the following conclusion can be made: surface states are not similar to volume minute donors and acceptors. This is applicable only for *proper* surface states. The above mentioned statements could be changed if *improper* surface (with adsorbent) states are present. Some surface states can be located beyond the forbidden zone.

Let us consider as an example the *a*- model of *two discrete levels*, which is shown in Fig.2.6. Let N_1 (N_2) be a number of acceptor (donor) type obtainable surface states, and Q_1(Q_2) – negative (positive) charge connected with filled (empty) acceptor (donor) states. Their corresponding energies are E_1 and E_2. Taking into account Fermi statistics and single statistical weight the total charge of surface states $Q_{ss}=Q_1+Q_2$ equals to

$$Q_{ss}=-eN_1\left(1+\exp\frac{E_1-E_F}{kT}\right)^{-1}+eN_2\left(1+\exp\frac{E_F-E_2}{kT}\right)^{-1}. \qquad (2.15)$$

Let us assume that $N_1=N_2=N$, and besides this, according to the definition:

$$E_0=(E_1+E_2)/2,\quad \Delta E_F=E_F-E_0,\quad E_{sg}/2=E_1-E_0=E_0+E_2. \qquad (2.16)$$

New values E_0 and ΔE_F determine the neutral state energy level (when $Q_{ss}=0$), and the location of the Fermi level relative to this one. Hence, instead of (2.15) we have:

$$-\frac{Q_{ss}}{eN}=\left(1+\exp\frac{E_{sg}/2-\Delta E_F}{kT}\right)^{-1}-\left(1+\exp\frac{E_{sg}/2+\Delta E_F}{kT}\right)^{-1}, \tag{2.17}$$

which can be written like

$$-\frac{Q_{ss}}{eN}=\frac{sh(\Delta E_F/kT)}{ch(E_{sg}/2kT)+ch(\Delta E_F/kT)}. \tag{2.18}$$

Function $-Q_{ss}/eN$ describes standardized negative charge of surface states. When $\Delta E_F < ½(E_{sg})$, the function is close to the hyperbolic sine, and when $\Delta E_F > ½(E_{sg})$ it tends to saturation.

The diagram of Q_{ss}/N on ΔE_F dependence is shown in Fig. 2.7, when T=75, 300 or 1200 K. The energy gap between surface states E_{sg} is considered to be not temperature depended. In the following Figure it equals to 0.25 electron volts. Such value is typical for Si. Taking into account the fact that ΔE_F and $½(E_{sg})$ are a part of the expression together with temperature as $\Delta E_F/kT$ and $½(E_{sg})/kT$ ratios, it is possible to unify typical temperatures and energies, i.e., for example, energy gap value can be written using the value of temperature: E_{sg} equals to $40kT$ when 75K, $10kT$ under indoor temperature (300 K) and $2,5kT$ – under 1200 K.

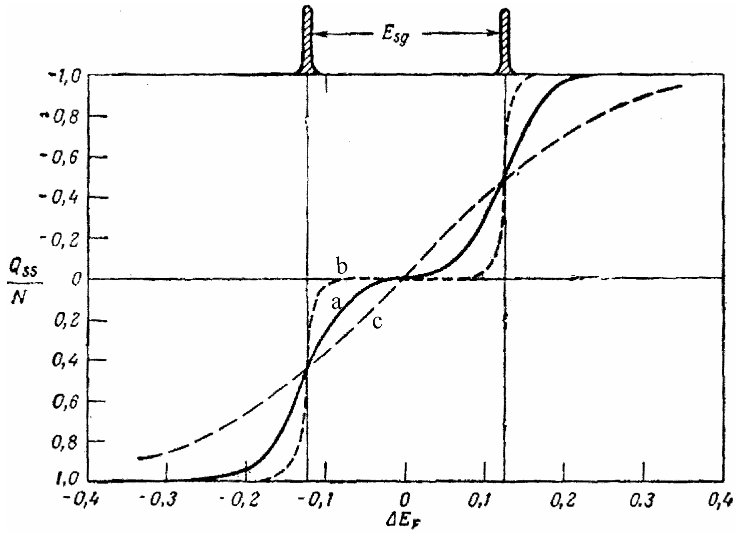

Fig. 2.7. Surface states charge as a function of the Fermi level location and temperature in two discrete levels of the model: **a** – T=300 K; **b** – T=75 K; **c** – T=1200 K.

As results from Fig. 2.7, there is a considerable change of Q_{ss} charge measurable value as a function and temperature in case with simple distribution model (*two discrete levels*). Finally, it is determined by the penetration of Maxwell exponential “tail” behind the surface state energy level. Within the limit of high temperatures Q_{ss} linearly changes from ΔE_F and, most likely, does not depend on the discrete nature of surface states responsible for the originating charge. The inclination increased in E_0 point together with temperature; this dependence can be obtained from (2.18):

$$-\left(\frac{\partial Q_{ss}}{\partial \Delta E_F}\right)_{E_0}=\frac{eN/kT}{1+ch(E_{sg}/2kT)}. \tag{2.19}$$

The inclination value is closely connected with carrier mobility within the external field.

3. Experimental Features of Surface Diagnostics

3.1 Requirements for experimental conditions

The experiment on carrying out surface analysis with the use of any methods of nuclear physics is basically very easy. Conventionally it may be divided into following stages: 1) *production of any action on the surface* (by electron, ion, atomic, molecular, γ-quantum beams, etc.); 2) *realization of action*; 3) *analysis of surface response*, that is analysis of characteristics of secondary or reradiated (reflected) electron, ion, atomic, molecular, γ-quantum flows. However, the need to use the ultrahigh vacuum method, low temperatures and special conditions of sample preparation, make surface diagnostics laborious, interesting and expensive. The necessity to use ultrahigh vacuum method is *firstly* conditioned by the necessity to exclude from external environment atoms and molecules coming to the surface during the entire time of an experiment (in practice this requirement, due to the inability to fulfill it, is replaced by the requirement to have equal surface conditions during the entire time of an experiment). *Secondly* the method of creating influence on the studied surface (including the influence of electron and ionic beams) and the method of registration and analysis (electrostatic, magnetic and other particle analyzers, detectors, etc.) also require ultrahigh vacuum.

3.1.1 Ultrahigh vacuum and surface purity

The notion ‘pure surface’ implies, first of all, that it does not contain impurities that are not ncluded into the solid limited by this surface. To obtain pure surface the following main techniques are used:

1. Chipping.
2. Heating.
3. Ionic bombardment (usually by inert gas ions).
4. Chemical treatment

The first technique involves cleaving of a relatively massive sample in ultrahigh vacuum. The main drawback of this technique is that a separate sample (for example a long bar) can usually be split only several times; consequently the surface cannot be prepared repeatedly. Besides, many materials can significantly change their surface properties (for example, adsorptive) when exposed to repeated chipping.

Surface heating involves purification of surface by means of thermal desorption of adsorbed particles. In most cases, however, due to very close connection of the adsorbate with the surface it cannot be removed by heating at the temperatures, lower than the temperatures of sample melting. This method of purification is used for refractory materials from which surface oxides are removed at the temperature lower than the melting temperature. However, even with these materials, the use of this method is considered doubtful for removing such admixtures as C, which together with backing material forms compounds (carbides) with very strong bonds.

At the same time purification by heating may be convenient for regeneration of pure surface after the adsorptive experiment with loosely bound adsorbates.

Purification by ionic bombardment involves removing surface layers by means of dispersion.

For metal surfaces the method of argon ion bombardment Ar^+ with the energies of 0.5–10 keV is most commonly used. Later we will discuss physical background of ionic dispersion in relation to its other applications in a more detailed way. From the viewpoint of structural analysis, one of the drawbacks of ionic bombardment is significant surface damage (at large doses) with intrusion of Ar atoms, so that for restoration of ordered structure surface annealing is required.

Chemical method of purification involves low-pressure delivery of gases into the vacuum system. These gases react with surface admixtures and form loosely–bound adsorbates, which in turn can be thermally desorbed. This technique is most commonly used for removing carbon from the surfaces of refractory metals. When these surfaces are exposed to O_2 at increased temperatures, C is removed in the form of desorbed CO, which then evaporates from the oxidized surface, and this surface may then be afterpurified by heating only.

Determination of the notion "pure surface in the experimental process" depends on the definite experiment. In structural analysis where the methods of electronic spectrometry are used, the following purification criterion may be considered as reasonable: within the time of measurement (approximately one hour) the number of atoms settled on the surface from the gas phase is not more than several percent of the monolayer. When analysis involves the usage of ion beams to probe the surface, atoms settled from the gas phase may be removed by probing ions. Therefore purification requirements in this case can be formulated with respect to the balance of velocity of atoms coming to the surface from the gas phase, and velocity of removing atoms from the surface by the probing beam.

Velocity of atoms coming from the vacuum to the surface can be easily estimated taking into account kinetic theory of gases:

$$\frac{dN_a}{dt}=\frac{1}{4}n\langle v\rangle\ . \tag{3.1}$$

Here n – concentration of residual gas atoms in the vacuum camera, $\langle v\rangle$ – average atom velocity. Equating the kinetic energy of a particle with mass m with the root-mean-square velocity $\bar{v}_{sq}$ of its thermal energy, which is determined by absolute temperature T and Boltzmann constant k, we have

$$\bar{v}_{\kappa\text{в}}=3kT/m\ . \tag{3.2}$$

Using the ratio between $\langle v\rangle$ and $\bar{v}_{sq}$:

$$\langle v\rangle=\sqrt{\frac{8}{3\pi}}\,\bar{v}_{sq}\ , \tag{3.3}$$

and the fact that pressure P is determined as $P=nkT$, we have the expression for the velocity of coming particles.

$$\frac{dN_a}{dt}=P\sqrt{\frac{1}{2\pi kTm}}\ . \tag{3.4}$$

If P is expressed in millimeters of mercury, T in Kelvins, and m is substituted for molecular mass M by means of multiplication by atomic mass unit, expression (3.4) may look as follows:

$$\frac{dN_a}{dt}=3{,}51\cdot 10^{22}\,P/(TM)^{1/2}\ . \tag{3.5}$$

Here dN/dt has the following number of dimensions: *molecule*$\cdot$*cm*$^{-2}$*s*$^{-1}$. For example, for nitrogen molecules (M =28) at room temperature (T=293 K) and pressure 1 *mm of mercury* advance speed is equal to 3.88 $\cdot 10^{20}$ *molecules*$\cdot$*cm*$^{-2}$*s*$^{-1}$. For air at T=273°K we have:

$$\frac{dN_a}{dt}=3{,}95\cdot 10^{22}P\ \textit{molecules}\cdot cm^{-2}s^{-1}. \tag{3.6}$$

In practice it is often necessary to correlate the time of monolayer adsorption to the sample surface with the pressure value in the vacuum camera. It is thought that a monolayer (one atom thick complete layer) consists of approximately 10^{15}–$2\cdot 10^{15}$ *atom*$\cdot$*cm*$^{-2}$ and that all molecules coming to the surface adhere to it (otherwise it is necessary to introduce the so-called adhesion coefficient). Therefore it is easy to estimate that the time of nitrogen monolayer adsorption accounts approximately for $3\cdot 10^{-6}$ at the pressure of 1 *mm of mercury*, and almost 1 *h* at the pressure of 10^{-9} *mm of mercury.* This means that at adopted assumptions, within one hour several percent of monolayer is created in vacuum with maximum pressure 10^{-10} *mm of mercury.* Adopted assumptions concern the least favorable cases, for example the analysis of surfaces easily reacting with H and CO- gases which are the main partial components of ultrahigh vacuum.

Consider the case when together with vacuum adsorption, surface bombardment by accelerated ions takes place.

At the bombardment of a target by ion flows with the current density j=1 *mA/cm*^{2}, the number of ions hitting in 1 *cm*^{2} of the surface within 1 *s*, accounts for

$$\frac{dN_u}{dt} = 6{,}25 \cdot 10^{15}\, j \;\; ion{\cdot}cm^{-2}{\cdot}s^{-1} \tag{3.7}$$

The number of dispersed particles of the target leaving 1 *cm*^{2} of the irradiated surface within 1 *s,* is equal to the number of particles which hit the surface multiplied by the dispersion coefficient [see (1.3)]:

$$\frac{dN_p}{dt} = S \cdot 6{,}25 \cdot 10^{15}\, j \;\; particles \;{\cdot}cm^{-2}s^{-1} \tag{3.8}$$

where S is dispersion coefficient, which depends on the ion-target combination and ionic energy. The target surface is considered ‘dynamically pure’ if $(dN_p/dt)>(dN_a/dt)$. The estimations show that at the pressure relevant to the typical conditions in which the analysis is carried out (10^{-7}-10^{-9} *mm of mercury*), j~ 0.01 - 1 *mA/cm*^{2} is required for efficient target purification.

So, ultrahigh vacuum requirements for surface analysis consist in keeping the surface in pure or any other clearly defined and already obtained conditions. This also concerns the case when layer-by-layer analysis (profiling) of element concentration in surface layers is carried out. This analysis involves removal of the large number of monolayers by means of dispersion by the ion beam, with the simultaneous analysis of these layers by any of the following methods: (SIMS, SIEMS, EAS, XPES, etc). Here the sample is analyzed without preliminary purification; so that its surface composition is determined by the pollutions caused by air treatment, and does not depend on the quality of ambient vacuum in the analytic camera. However, after removing surface layers in the process of layer-by-layer analysis, ‘the freshly treated surface’ becomes sensitive to new pollutions, and this is to be taken into account in the analysis process.

The above stated ultrahigh vacuum requirement for surface analysis places strict limits on the production technology of equipment in vacuum. First of all this relates to the materials and the quality of their treatment while manufacturing ultrahigh vacuum cameras and units placed in these cameras. Contemporary surface investigations use the same ultrahigh vacuum camera for several various methods any of which can be very complicated. To achieve this, elements used for the implementation of every method are assembled on *a separate stainless steel flange connected with the stainless steel camera through the copper or aluminum seal*, which results in greater flexibility of the experiment and facilitates dismantling.

Despite the fact that modern vacuum pumps are used which are capable of creating the pressure equal to 10^{-10}–10^{-11} *mm of mercury*, the main constituent part for ultrahigh vacuum obtaining is that the entire ultrahigh vacuum system should be annealed. The case is that the pressure value in the absolutely hermetic ultrahigh vacuum system is limited by gas separation from the inner walls and surface of the equipment located inside the camera, what is mainly caused by the desorption of the gases adsorbed from these surfaces. When these surfaces are heated, desorption speed increases and filling of the surface by adsorbates reduces, which consequently leads to decrease in desorption speed when cooled to room temperature. In the analysis process this allows to reach lower pressure values in the ultrahigh vacuum systems. Usually ultrahigh vacuum cameras together with all the equipment are heated for approximately 12 hours at temperature 200 °C. This evidently means that all the vacuum camera components should resist heating up to 200 °C. The additional requirement is that all the components should be non-magnetic as almost in all methods of surface investigation moving charged particles are used which are deviated by weak electrostatic and magnetic fields. Currently the production technology is well established which meets these requirements and includes mainly the use of stainless steel, refractory metals and special ceramics for electric or thermal isolation. Plastic materials used in "high vacuum" (up to ~10^{-6} *mm of mercury*), as well as compactors like rubber or viton are unsuitable for ultrahigh vacuum.

3.2 Major units of analytical plants

3 major instrumental groups, necessary to conduct the experiment of surface diagnostics can be distinguished:

1. influence sources (electron and ion guns or accelerators, sources of X-ray, ultraviolet and other γ-quanta);
2. analyzers;
3. detectors of surface response;
4. electronic appliances providing functioning of the 3 groups mentioned above.

Let's briefly view the working principles and construction of the appliances from the instrumental groups mentioned.

3.2.1 Electron and ion optics

The appliances that have very simple construction called *electron- or ion- optic* (including electron and ion *lenses*) and used to control the movement of charged particles (both primary and secondary; both ions and electrons) are the major units of analytical plants for surface studies. The main purpose of these appliances is to focus or, on the contrary, to disperse flows of charged particles. Hence we have the term 'lens' borrowed from optics. The similarity of terms here is not accidental: it is caused by the fact that moving electrons and ions (as well as light) possess corpuscular and wave properties. Therefore the branch of physics dealing with movement of charged particles through the appliances creating electric and magnetic fields of given configurations is called *electron* (*ion*) *optics*. For calculations of particles trajectories in electron- and ion-optic appliances the following basic regulations and rules are used: 1) the 2-nd Newton's law; 2) equations (3.9) and (3.10); 3) Maxwell's equations; 4) data on initial energies and directions of charged particles. The main ratio for calculations is the equation for the force $\boldsymbol{F}$ affecting the charge q moving with the speed $\boldsymbol{v}$ in crossed (in general case) electric and magnetic fields. This equation is known from general physics.

$$\boldsymbol{F}=q\boldsymbol{E}+q[\boldsymbol{vB}]\,. \tag{3.9}$$

In many important cases moving charges create significant fields themselves. This effect is called *spatial charge*. Fields created by the spatial charge are calculated with Poisson's equation, which in one-dimensional case looks as:

$$\frac{d^2V}{dx^2}=-\frac{\rho}{\varepsilon_0}\quad , \tag{3.10}$$

here V – electrostatic potential created by moving charges with current density $j=-\rho v$, $v=(2K/m)^{1/2}$, v – speed of charges movement, K – kinetic energy, ρ – number of charges in the volume unit.

Let's demonstrate the working (and calculation) principle of electron- and ion- optical systems on the example of an electron lens. We will call *the electron lens* the combination of electric and magnetic fields focusing the electron beam. Focusing effect of the lens is caused by the force included into the ratio (3.9); it may be calculated without using data on wave properties of electron beams, that is the field of geometrical optics. However, for calculating focus distances, aberrations and other properties, the calculations of the most probable trajectory of the wave packet instead of the trajectory of the classical charged particle are required. This is true only for the case when fields $\boldsymbol{E}$ and $\boldsymbol{B}$ do not change significantly along the length of the wave packet which is always accomplished in laboratory-scale fields.

Figure 3.1 shows the influence of electric field on the electron movement. Fig. 2 represents thin nets, located under potentials V_1 and V_2, and discriminating zones of the constant electrostatic potential V_1 and V_2. The electron trajectory is represented everywhere, except the internet zone, as a straight line. In this zone speed component v_x increases while v_y remains invariable as field ***E*** does not have a component along y-axis. Let's assume that electrostatic potential vanishes at the point where electron kinetic energy $K = mv^2/2$ is equal to zero. Then

$$mv_1^2/2=eV_1, \quad mv_2^2/2=eV_2, \quad v_1/v_2=(V_2/V_1)^{1/2}.$$

Let's rewrite these expressions using the geometry shown in the picture through dip θ_i and reflection θ_r angles. Now we have:

$$\sin\theta_i= v_y/v_1, \qquad \sin\theta_r= v_y/v_2, \qquad \sin\theta_i/\sin\theta_r=(V_2/V_1)^{1/2}. \tag{3.11}$$

Thus refraction occurs in accordance with the law looking in the same way as Snell's law for optical refraction at the boundary of two mediums. Electron trajectory deviates in the direction of normal towards equipotential surface if V increases. If we put V=0 in the point where K=0, we will get the common optical law with the only difference that the index of medium refraction is substituted for $V^{1/2}$. The same result is achieved if electrons are replaced with wave packets.

The presented case of electron ray deviation in the direction of normal towards equipotential surface at increase in V, makes it possible to understand the principle of electrostatic focusing. Besides, expressions (3.11) create the basis for numerical calculations of electron trajectories in the domains of constantly changing V.

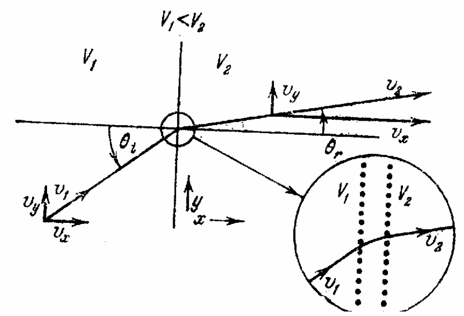

Fig. 3.1. Refraction of the electron's trajectory after its transmission from the potential domain V_1 into the domain with higher potential V_2. The inset on the right shows the trajectory curve in the section between the closely set nets.

The electrostatic lens used in practice is schematically shown in fig. 3.2. Two coaxial round cylinders are at potentials V_1 and V_2. Equipotential surfaces are located symmetrically to the surface going between the cylinders. The refraction of electron trajectories on the right is less than that on the left, as the average value V on the right is higher. Therefore the given difference ΔV between two equipotential surfaces V' and V'' corresponds to the smaller ratio $(V''/V')^{1/2}$. To show it in a different way let's note that electron energy (and consequently its impulse) is higher in fig. 3.2, so the electron deviation in the same field is smaller. Thus, the double-cylinder lens influences electrons in the same way as in optics the combination of strong positive and weak negative lenses influences the light beam, and as a result reduces divergent beams back into the focus. This result is true for all the electrons flying out of any point of the object surface. However, the picture quality decreases when object dimensions become comparable with the cylinders' diameters.

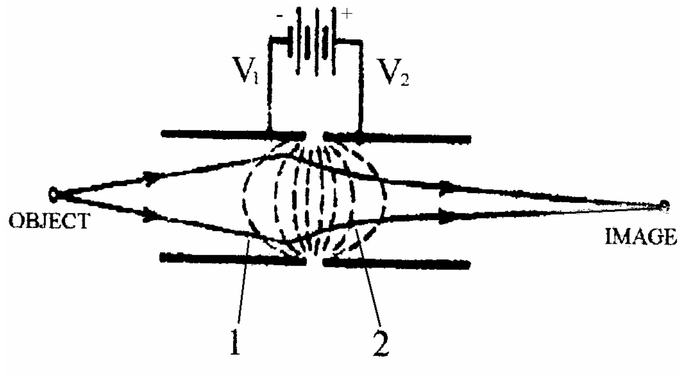

Fig. 3.2. The electrostatic lens composed of two coaxial cylinders. Electron trajectory bends in the direction of normal towards equipotential surfaces (marked with dotted lines): 1 – converging strong-focused slow electrons; 2 – divergent loosely-defocused fast electrons

Fig. 3.3. shows the scheme of the thin magnetic lens to demonstrate how magnetic field devices function. Equipotential surfaces are marked by dotted lines; magnetic field force lines are perpendicular to these surfaces. Incoming electrons accelerate in the azimuth direction. Azimuth speed component (rotation round the symmetry axis) creates the force directed to the axis. Since this force is proportional to the distance of the electron from the axis, focusing is achieved. On the left incut the force $\boldsymbol{F}=-e[\boldsymbol{vB}]$ is perpendicular to the draught surface and is directed upwards; on the right incut $\boldsymbol{v}$ has the component perpendicular to the draught surface and directed upwards, so $\boldsymbol{F}$ lies in the draught surface and is directed to the axis. To obtain high values of $\boldsymbol{B}$ at a relatively short part along the axis, the crossover coil is almost surrounded by iron. When an electron enters the lens it is affected by accelerating force, in this case outwards, as it is shown on the left incut. This force rotates every falling electron clockwise (if we look to the right along the system's axis). Thus, the electron acquires azimuth speed component, directed at the right angle towards $\boldsymbol{B}$, as a result of which the force emerges directed along the lens axis. In this way focusing is achieved. The general property of all magnetic lenses is image rotation with regard to the object, which is caused by the azimuth speed component mentioned above. The long solenoid functions in the same way as the short magnetic lens.

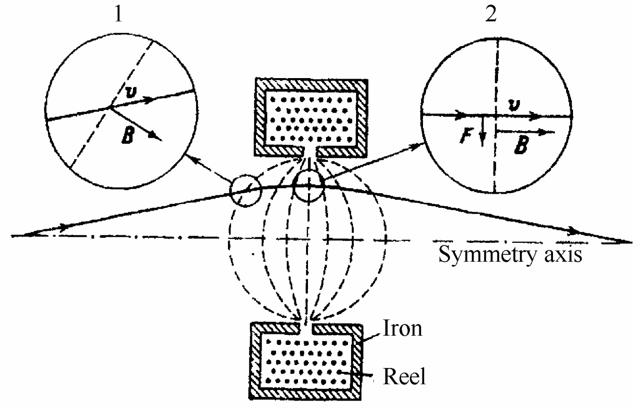

Fig. 3.3. Working principle of the thin magnetic lens.

3.2.2 Electron and ion guns

Electrons and ions influence the surface by means of devices called electron and ion guns respectively. These devices form beams of charged particles with given parameters. The main general requirements for the parameters of electron and ion beams designed to influence the surface for conducting its analysis are as follows:

1) minimal energy scattering;
2) minimal spatial divergence;
3) maximal stability in the time of current density in a beam.

Constructively (and conditionally) two blocks may be distinguished in electron and ion guns: *emissive block* (*or the source of charged particles*) designed to create charged particles (cathodes in electron guns, ionization cameras in ion guns), and *beam formation block* consisting of the elements of electronic or ionic optics designed for acceleration and focusing of particles. Fig. 3.4 shows the simplest scheme of the electron gun.

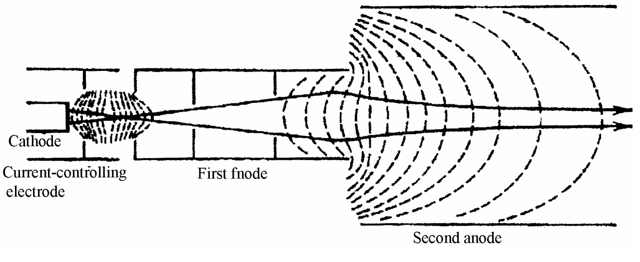

Fig. 3.4. The simplest scheme of the electron gun with cylindrically-symmetrical electrodes. Equipotential surfaces are marked by dotted lines.

Electrons flying out of the cathode are focused depending on their initial speeds, all their trajectories, however, cross near the cathode. The lens effect created by the first and the second anode gives the picture of this crossing point in another remote point. Potential change on the controlling electrode changes the net current in a beam by altering the depth of potential minimum of the spatial charge near the cathode. Refractory metals and oxides of rare-earth metals are used as cathodes of low-power electron guns (those obtaining electrons by thermoelectronic and autoelectronic emission. The phenomena of autoelectronic and explosive emission are used for obtaining powerful electron beams.

For surface diagnostics, ion guns with the following electron-obtaining methods are used: electron impact; vacuum spark method; photoionization, exposure to strong electric fields; ion-ion emission; interaction of laser radiation with the solid; as a result of electron adhesion to atoms and molecules (for obtaining negative ions); due to ion-molecular reactions; due to surface ionization.

In addition to the sources of the above-mentioned ionization techniques, arc and plasma ion sources are sometimes used. Often such sources are used which combine field and electron impact ionization. The scheme of such source is shown in Fig. 3.5. Gas comes to the source through the delivery pipe. The current leads of the emitter and the ionization camera are fastened on the ceramic washer. In electron impact ionization mode, cathode glow switches on, and electrons accelerate into the ionization camera due to the potential difference between the cathode and the camera. Ions are drawn from the ionization camera by the drawing electrode. The focusing electrode is used for focusing the ion beam. Beam collimation is performed by collimating electrodes, and beam correction in horizontal and vertical directions is performed by correcting electrodes. Accelerating potential is delivered to the ionization camera. At high-voltage field ionization, accelerating potential is delivered to the emitter. Three types of emitters may be used in the source: point, comb and thread. To illustrate this we will give definite voltage values used in the working ion gun. When the thread functions, standard electrode potentials are equal to: emitter + 4kV; ionization camera – 6–10 kV; drawing electrode from –2.8 to +3.8 kV; correcting plates from –200 to +200 kV and from –600 to + 600 V; slit diaphragms 0V.

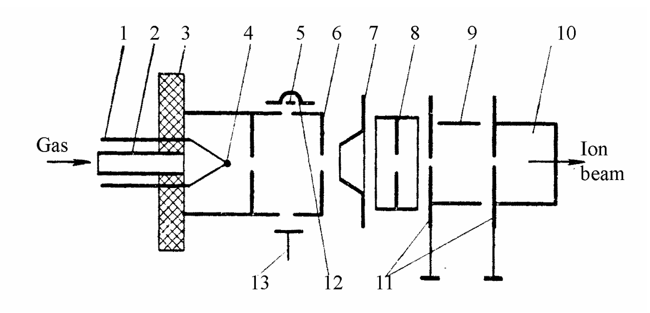

Fig. 3.5. The scheme of ion sources with ionization by field and electron impact: 1 – current leads; 2 – pipe for gas delivery; 3 – ceramic washer; 4 – emitter; 5 – cathode; 6 – ionization camera; 7 – drawing electrode; 8 – focusing electrode; 9, 10 – correcting plates; 11 – collimating plates; 12 – reflecting electrode; 13 – electron collector.

3.2.3 γ-quantum and photon sources

X-ray range

In usual sources of X-ray radiation, X-ray beams are emitted at bombardment of the solid target (anode) by high energy electrons. The radiation from these targets consists of distinctive lines connected with filling of the gaps in spanning levels created by the beams of falling electrons. These lines are laid on the constant background of deceleration radiation stretching up to the energy of falling electrons. In most cases electron energy is selected in such a way that it is bigger than binding energy of K-coating of target atoms. Therefore in the spectrum lines connected with gap-filling in K-coating prevail.

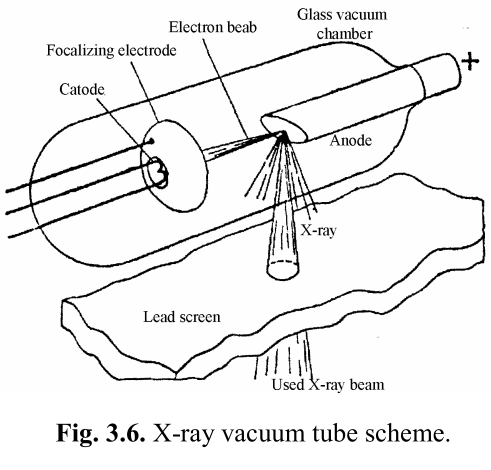

Fig. 3.6. X-ray vacuum tube scheme.

To obtain X-ray, *X-ray vacuum tubes* are usually used. Their typical scheme is shown in fig 3.6. Between the thermionic cathode (red-hot tungsten thread) and the anode, potential difference of 50 *kV* and more is maintained. Due to the reasons mentioned below, metal is usually selected as anode. Anode must have water cooling as due to the significant volume value, electron currents even of several milliamperes evolve on the power anode about hundreds of Watts in the form of heat.

If we need useful information on the *surface obtained* *with the help of emitted electrons* our photon source must probably be more monochromatic. If this is the X-ray source, which has been mentioned above, the substance for its anode should have the low background of deceleration radiation and narrow characteristic radiation lines among which the only line is preferably domineering. The fact that a great amount of heat is evolved on the anode, which requires its good thermal conductivity, entails the necessity to use metals as a cathode. The anode low temperature is of special importance, if the source should be "bare" in the vacuum system of the ultrahigh vacuum analytical camera, as during the process of work gas separation from the anode may cause unacceptable pressure increase. *Magnesium* and *aluminum* are preferable as anode material since they most fully meet the above mentioned requirements

The refraction index of X-ray in all substances is close to 1. Therefore the diffraction lattice should be used for measuring wave-lengths of X-ray. Such measurements are rather difficult, as wave-lengths of X-ray are very small (approximately from 0.1 to 1 Å) if compared to the smallest constant of the lattice which can be manufactured (approximately10000 Å). For such measurements we should use the diffraction lattice with the distance between the marks of approximately 1 Å. Since this value is of the same order as the size of the atom, the distance between the atoms in the crystal lattice of the solid is so big that the crystal represents a natural diffraction lattice for X-ray. Besides, the atoms form the right structure with the constant distance between the knots. Therefore the usage of crystals is considered the most convenient way to measure the wave-lengths of X-ray.

The alternative to the above mentioned source of X-ray is *synchrotron radiation* that is radiation accompanying the movement of the charged particles with relativistic velocities in accelerators of charged particles. This radiation always accompanies acceleration of charged particles in annular accelerators (which is basically deceleration radiation) and is the main source of energy losses by the charged particles in these plants. Attraction of synchrotron radiation for surface investigation is determined by the following factors. *Firstly,* the charged particles accelerated in the synchrotron radiate the spectrum in the form of polarized continuum concentrated precisely in the accelerator's plane. *Secondly*, synchrotron radiation may be obtained as a by-product from the accelerator designed for investigations in the domain of high energy physics, although by the present moment many electron storage rings have been created which are used mainly as a source of synchrotron radiation. *Thirdly*, synchrotron radiation has a wide spectrum of "plateau" type, which enables to evolve X-ray with different wave-lengths but with the same intensity. *Fourthly*, the intensity is by several orders higher if compared to other sources. *Fifthly*, synchrotron radiation is polarized.

Ultraviolet (UV) *range*

For surface investigation both close (400–200 nm) and remote (vacuum) range (200–10 nm) of the ultraviolet (UV) spectrum are used. Any of the UV sources mentioned below may be used. For example, the spectrum of solids heated up to ~3000 K contains a significant amount of UV spectrum, which intensity increases together with temperature increase. Any high temperature plasma may be a more powerful source. For surface analysis, mercury, xenon and other gas-discharge lamps are used. The openings of these lamps (or the entire retorts) are made of ultraviolet-transparent materials (usually quartz). It is also possible to obtain intensive synchrotron radiation of continuous UV spectrum. There exist lasers radiating in UV range; the smallest wavelength is emitted by the laser with frequency multiplication.

3.2.4 Analyzers

Analyzers are the key components of the plants for surface diagnostics. These devices are designed for analyzing surface response. The term "analysis" in the *instrumental – methodical plan* implies discrimination of differential characteristics from integral ones (or decomposition of integral characteristics into differential ones which is basically the same). In this case we consider decompositions of the general flow of electrons, ions, γ-quantums, etc., emitted by the surface (reflected from the surface) into the spectrum according to energies, along the flight angles (reflections), masses (for ions only). Consequently, the following types of analyzers are distinguished: *energetic analyzers* (they are also called *energetic filters* and *energetic separators* since their function is not to let particles with the smaller energy spread); *angle analyzers* (including goniometers and other sample manipulators); *mass analyzers* (also called *mass filters* and *mass separators*). Decomposition of particles characteristics into spectrums and recording of these spectrums is called *spectroscopy.* Further numerical processing of the obtained spectrums in order to get necessary information (together with spectroscopy) is called *spectrometry.* For that reason analyzers are usually called spectrometers. Various spectroscopy methods have various historical roots, and due to this fact there is a wide range of analyzers. To compare data obtained in different plants, it is necessary to understand the reasons for advantages and disadvantages of the analyzers used. Thus it is essential to discuss some major peculiarities of different analyzers. First, consider the most widespread electron energy analyzer-electron spectrometer.

The main purpose of any electron spectrometer is, as it has been mentioned before, discrimination from electrons entering the spectrometer with the wide range of energies and angles (due to the divergence of the source-emitting surface) only those electrons whose energies are confined within the definite narrow domain (regardless of the entrance angle). Ideally this can be achieved when several types of energy analyzers with high energy resolution are used, or with the help of the simpler analyzer and subsequent processing of the output signal. For surface investigation *the analyzer with the inhibiting field* is most commonly used as a wide-band high-aperture filter

Energy resolution and collection angle (input angle) are the two main parameters taken into account while constructing and choosing analyzer for each definite application. Both parameters characterize the device’s sensitivity. Energy resolution in all the appliances is connected with their physical size.

Analyzer with inhibiting field (AIF)

Popularity of the analyzer with the inhibiting field is explained by the fact that it was first used for the investigation of slow electrons diffraction – one of the most widespread methods of surface diagnostics. The simplest AIF scheme is shown in fig. 3.7. The sample is placed at the collection centre of concentric spherical sectoral nets. When this scheme is used for slow electrons diffraction, the first net closest to the sample is at the same potential (ground) as the sample. Due to this fact electrons leaving the sample are distributed in the direction of the net in the field-free space thus providing radial geometry of the experiment. The next net is at the smaller potential than that of the electron gun cathode, thus all the electrons with the energies smaller than the energies of the electrons falling at the sample, decelerate and fail to go through the last acceleration stage towards the luminescent screen. Thus in a usual experiment on slow electrons deceleration nets are used only as a high-aperture analyzer which absorbs only elastically scattered electrons. However, if inhibitory nets are at lower potentials, all the electrons with the energies that are greater than the energy corresponding to this potential, reach the luminescent screen which in this case is used as a simple current collector. Thus if electron distribution according to energy is described by the function $N(E)$, and the inhibitory potential is equal to V_0 and corresponds to the minimum value of adsorption energy $E_0=eV_0$, current entering

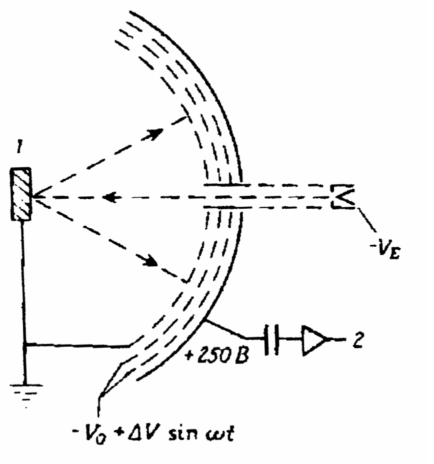

Fig. 3.7. AIF scheme used in slow electrons diffraction. When the modulated inhibiting potential is used (as it is shown in the figure) the modulated component of the signal received by the detector increases and is registered by the simultaneous: 1 – sample; 2 – to the simultaneous detector.

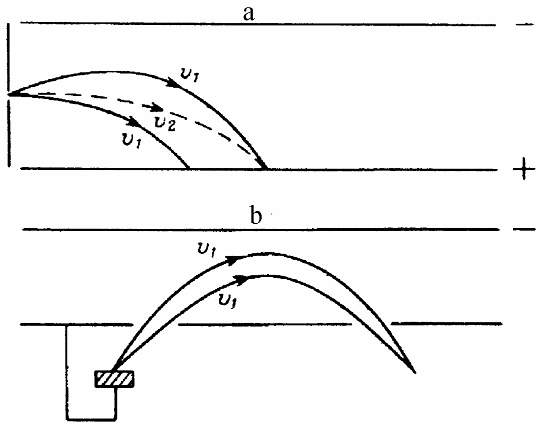

Fig. 3.8. Trajectory of electrons in the flat condenser: **a** – electrons are injected perpendicularly to the field, at $v_2>v_1$ deviation is less noticeable, however, the electrons with the initial speed v_1 may reach the same point as the electrons with the speed v_2, if they are injected at the necessary angle towards the main direction
b – scheme of the flat mirror analyzer used in the focusing configuration.

the collector is equal to $\int_{E_0}^{\infty} N(E)dE$. Since the maximum energy of the electrons emitted by the sample cannot be higher than that of the electrons in the primary beam E_p the upper integration limit is to be changed. As a result the current becomes equal to $\int_{E_0}^{E_p} N(E)dE$. It is clear that if we differentiate this current we will get the distribution of electrons according to energy $N(E)$, which we have been looking for. The easiest way to conduct differentiating is to simulate the inhibiting potential V. The difference between the currents entering the collector at potentials V_0 and $V_0+\Delta V$ accounts for $\int_{E_0}^{E_0+\Delta E} N(E)dE$, and if the value $\Delta E = e\Delta V$ is small, the currents difference is equal to $N(E_0)\Delta E$, that it is proportional to the desired distribution according to energy. The use of such type of simulation entails the necessity to seek compromises between the signal value and resolution: the resolution determined by ΔE decreases linearly with ΔV while the signal $N(E)\Delta E$ increases with the growth of this value. This compromise is found at high resolution (ΔV value is small) when the imperfections conditioned by nets non-spheresity and penetration of the field between them limit the resolution usually up to 1 eV.

The inhibiting potential V_0 is usually simulated sinusoidal (that means that voltage $V_0+\Delta v\sin \omega t$) is applied. Using decomposition into Taylor's series it is possible to show that collector current at such simulation may be presented as the sum of sinusoidal components. In practice the amplitude of the second sinusoidal component ($\sin 2\omega t$) is usually measured, which may be obtained with the help of the simultaneous detector, which in its turn may be regarded as variation of the method of registration of the signal simulated by the net with duplicated frequency. The amplitude of this component at the first approximation is proportional to the derivative of the function of electron energy distribution $N'(E)$. The work with the second sinusoidal component is preferable as the sought function structure $N(E)$ is often feebly marked (weak peaks at the background with high intensity). *Differentiation eliminates constant background and allows to use higher acceleration.*

Thus, the main advantages of AIF are as follows: *simplicity of design, big collection angle (usually approximately π steradian), absence of aberrations connected with the angle divergence.* The main disadvantage of AIF is its *bad signal/noise ratio* caused by the fact that all the electrons with the energy greater than the inhibiting potential reach the collector and generate *shot noise.* In addition to restrictions connected with simulation amplitude, analyzer's resolution is restricted to non-sphericity and sizes of the nets, as well as the distance between the nets; and that affects the degree of the field penetration into the high-aperture filter. Resolving capacity of the typical analyzer with the curvature radius of approximately 50 mm, distance between the nets approximately 2-3 mm and with two inhibiting nets to minimize the field's penetration accounts for $E/\Delta E \approx 100–200$.

Deviating electrostatic energy analyzers

The use of the analyzer with high energy resolution is considered to be a much more convenient way to estimate the number of electrons with the energies within the given range. This device relies on the use of both electrostatic and magnetic fields. In this chapter we are going to discuss only electrostatic deviating analyzers, as they are the most frequently used in the plants for surface diagnostics. If the energies of charged particles correspond to those which are used in most methods of electron and ion spectroscopy, these devices are easy- to- operate, compact and may be used in ultrahigh vacuum systems.

A couple of parallel plates at different potentials are the example of the simplest electrostatic deviating system. The field emerging in such system has flat, parallel, equidistant equipotential surfaces. If we direct electrons to this field they will deviate; and the highest deviation level at the given distance will be observed with electrons with the lowest energies. If we make a hole (exit aperture) in the plate with high potential, the electrons with the energies located at the certain interval will come out through this hole. The range of this interval is the function of the aperture size and the field strength. At the same time, if electrons are injected into the field perpendicularly but with different dispersion angles around the main direction, electrons with the same energy will apparently deviate in a different manner depending on the injection angle. This means that in the electron current which has passed through the exit aperture, energy scattering will be revealed which is connected with angle diversity of the falling electrons (fig. 3.8. a). As a result of angle diversity, both energy resolution and passing capacity of the analyzer decrease. It is evident that a properly designed analyzer should focus on the exit aperture particles injected with the same energy but at different angles. In the considered case this may be achieved when electrons are injected at the relevant angle. This focusing range is shown in fig 3.8, b. Here focusing is achieved when such an average injection angle is chosen that the electrons coming at the large angle and thus requiring greater deviation passed a longer way in the deviating field. This requirement is met only under strictly limited circumstances, so focusing is never perfect. Ideally the focus position shouldn't depend on the injection angle relating to the central trajectory. In the case of flat analyzers it is possible to approach this ideal with the help of laborious procedure of selection of geometrical conditions. Therefore, the most frequently used are the analyzers which basic types are presented in fig 3.8, b.

They include: a 127° cylindrical analyzer with parallel plates (fig. 3.9, a) where the full deviation angle accounts for either 45° (second-order focusing) or 30° (first-order focusing); a concentric semi-spherical analyzer with deviation angle 180° and first-order focusing; the analyzer of "cylindrical mirror" type (fig. 3.9, c). The latter device consists of concentric cylinders and at the entrance angle concerning the analyzer axis equal to approximately 42° has the second-order focusing. The two latter types of analyzers are most commonly used for surface investigation as they to some extent represent the highest rate of design optimization, and therefore we will discuss them in a more detailed way. However, the analyzers of the first type are rather convenient for investigations with angular resolution as they can be extremely small and simple in design.

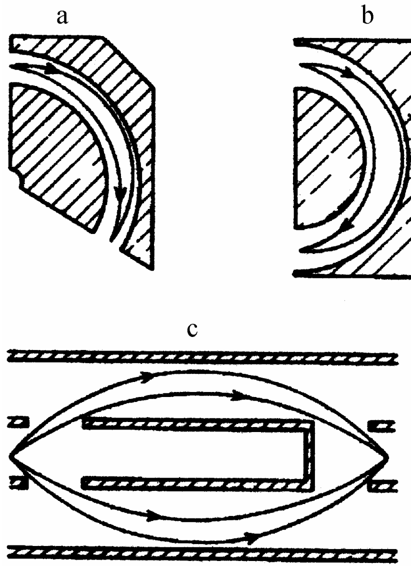

Fig. 3.9. Schemes of electrostatic analyzers and electrons trajectories: **a** – 127° analyzer with cylindrical electrodes; **b** – 180° spherical sector or concentric semispherical analyzer; **c** – analyzer of "cylindrical mirror" type.

If we determine resolving capacity as $E_0/\Delta E$, the resolving capacity of each appliance may be given by the ratio of its physical size (or the full length of electrons distance in the analyzer) to the size of the driving diaphragm (aperture). Thus for the semi-spherical analyzer this value can be expressed as $2R_0/s$, where R_0 – radius of the central distance through the analyzer, s – the size of the entrance (and exit aperture). For the analyzer of the "cylindrical mirror" type resolving capacity accounts approximately for 5,6R_1/s, where R_1 – the radius of the internal cylinder, s – the size of the driving aperture (not the internal cylinder aperture which is usually large, but the aperture between the internal cylinder and the points of the source and the image location). Usually the real entrance aperture is absent, so its dimensions are determined by the dimensions of the charged particles source.

It is evident that the given formulas for the resolving capacities of the semi-spherical analyzer and the analyzer of the "cylindrical mirror" type are similar, which provides close value characteristics if the dimensions of both analyzers are similar. The semi-spherical analyzer usually uses circular aperture which contracts the source full angle up to 5° and less; thus the full solid collection angle is less than 10^{-2} *Sr.* The analyzer of the "cylindrical mirror" type can register all the electrons whose speed vectors lay within the solid angle between the cones with half-angles 42.3 + 6° and 42.3–6° at any horizontal angles. The full solid collection angle accounts in this case for approximately 1 *Sr.* Thus the full solid collection angle for the analyzer of the "cylindrical mirror" type may be 100 times as much as the one for the semi-spherical analyzer. It is obvious that the greater collection angle should increase the signal and improve the signal/noise ratio.

However, the semi-spherical analyzer has certain advantages over the analyzer of the "cylindrical mirror" type. If electrons decelerate before the injection into the analyzer, the analyzer's effective resolving capacity may be improved. This is caused by the fact that when aberrated members are excluded the resolving capacity $E_0/\Delta E$ is determined by the system geometry; so if energy E_0 decreases, ΔE decreases as well. If the real energy of electrons before deceleration is equal to γE_0, where γ – some constant ($\gamma>1$), the effective resolving capacity is $\gamma E_0/\Delta E$. This estimation is rather simplified, as angular divergence is changed in the deceleration process, what results in the increase in analyzer's aberrations. This effect for any optical system can be described by Helmholz-Lagrange equation:

$$\alpha_0^2(\gamma E_0) = \alpha_1^2 E_0 M^2,$$

where α_0 – divergence at the initial energy (γE_0), and α_1 – divergence after deceleration up to energy E_0. One more variable with the help of which the design of the electron-optic system of preliminary deceleration may be optimized is the system increase (M), which is determined as the ratio of the picture size to the object size. With the use of this parameters system, significant growth of efficient resolving capacity may be obtained despite the aberrations. The semi-spherical analyzer is especially suitable for such working mode. Since the entering electron beam has a cylindrical or conical form, for obtaining the required preliminary deceleration either flat nets closing the entrance aperture or the systems of electrostatic lenses simultaneously creating the picture of the electron source on the entrance aperture can be used. Having chosen proper electron lenses we can get a significant flange local distance between the analyzer and the sample. On the other hand, the entrance configuration of the "cylindrical mirror" analyzer does not enable to use usual electron lenses. However, it can function in the preliminary deceleration mode, when concentric spherical sector nets are installed before the analyzer, and the centre of these nets coincides with the location of the source spot on the sample. One of the drawbacks of the "cylindrical mirror" analyzer is a relatively short flange local distance, and therefore though it collects electrons in a broad solid angle, the most part near the sample surface is shaded by the analyzer. In these conditions the electron beam exciting electron emission is to be put at the angle of slide towards the sample.

Let us view the above-mentioned considerations quantitatively. The typical "cylindrical mirror" analyzer with the external cylinder diameter about 100–150 mm can efficiently function without preliminary deceleration, with resolving capacity of approximately 200 and flange local distance of approximately 5 mm. The semispherical analyzer of the comparable size equipped with the preliminary deceleration device can function properly with resolving capacity 1000–2000 and flange local distance 25–50 mm.

While comparing the "cylindrical mirror" analyzer and the semispherical analyzer we would like to note that the "cylindrical mirror" analyzer is usually (but not exceptionally) used in appliances with low resolution and high efficiency of electron collection. Here a certain inconvenience is observed connected with the small value of the flange local distance. The semispherical analyzer is an analyzer with low collection efficiency which can work with high resolution and, if necessary, with relatively large flange local distances. Certainly, not all the cases of usage of the semispherical analyzer and the "cylindrical mirror" analyzer correspond to this simple classification. Another essential difference of these analyzers concerns directly the collection angle which may be required during the experiment. It is clear that if the experiment with angle resolution is to be carried out, the semispherical analyzer is preferable.

In conclusion let us consider the working modes of the analyzers mentioned above which are important for the comparison of results. In the mode without preliminary deceleration (the usual mode of the "cylindrical mirror" analyzer usage) energy scanning is carried out by changing the potential on the external deviating cylinder and consequently is estimated by the change of E_0. Since value $\Delta E/E_0$ is constant, this means that ΔE is proportional to E_0, so if energy distribution of electrons entering the analyzer is equal to – $N(E)$, the analyzer output signal is proportional to $EN(E)$. On the other hand, at the preliminary deceleration mode the analyzer can function both at the fixed deceleration coefficient γ, when transmission energy is changed and value $EN(E)$ is measured, and at the constant transmission energy E_0 and the changing deceleration coefficient γ. In this case E_0 and consequently ΔE are constant (except for the changes caused by aberrations), and $N(E)$ is measured in the constant resolution mode. Both operation modes have their evident advantages. However, when we compare the results obtained from different analyzers, it is necessary to take into account their operation modes. It should also be mentioned that when AIF is used in the differential modulation mode, energy resolution in most experiments is set by the value (constant) of the modulating voltage, so at the output we have $N(E)$ but not $EN(E)$. This difference is significant when comparing, for example, the spectrums of Auger electrons obtained with the help of AIF and SSA (semi-spherical analyzer) which are the most frequently used types of analyzers in surface investigation.

3.2.5 Charged particles and photons detectors

Secondary-electron multipliers (SEM) and photo-electron multipliers (PEM) are the most frequently used detectors of charged particles and photon fluxes. In these appliances the phenomena of photo-electron (PEM) and secondary electron (SEM and PEM) emissions are used. These phenomena help obtain a photo electron or a secondary electron and increase the number of

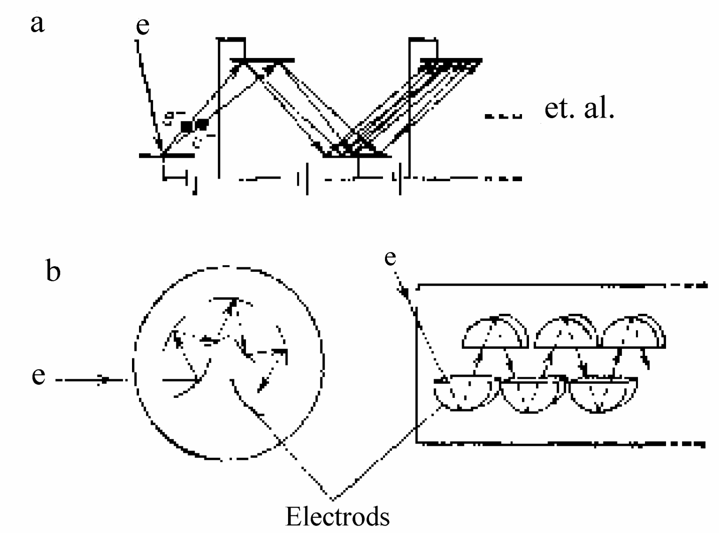

Fig. 3.10. Electron multipliers: *а* – equivalent diagram; *б* – shape and location of electrodes providing maximum efficiency for electrons collecting at secondary emission; *е* — electron beam

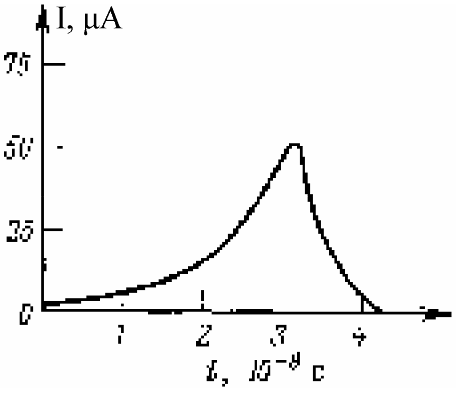

Fig. 3.11. The shape of the current impulse at the output of the electron multiplier. The current increases approximately in accordance with exponential law.

electrons in a beam spreading under certain conditions. Here the possibilities of increasing the number of electrons are virtually unlimited. To get high electron multiplication it is sufficient to create the conditions in which secondary electrons accelerate through passing great potential difference, so that they could cause further secondary emission. This process may repeat many times. Fig. 3.10 shows that at any stage of multiplication (it is supposed that at all stages the potential differences are the same) each electron falling to the metal surface causes the same multiplication. Therefore the common multiplication coefficient M for n stages is given by the expression $M=\delta^{n}$, where δ– the number of secondary electrons created per one falling electron. Hence, if one electron falls at the first out of ten multiplication cascades and $\delta=4$, we will get 10^6 electrons from the last cascade. Evidently we deal with the simple and relatively efficient charge amplifier with high amplification factor. Indeed there exist multipliers with amplification factor 10^6, although for that we should provide not only high coefficient of secondary emission (i.e. use materials with low photoelectric function) but also low losses of electrons in the process of cascaded multiplication with the help of either electrostatic or magnetic focusing.

Consider some other characteristics of the electron multiplier. For example, the time during which the impulse of the amplified charge is formed when a separate electron falls at the first electrode. To simplify the calculation we assume that the distance s between the electrons is equal to 1cm, and the difference of potentials between them 100 V. Then the time of flight t between the neighbouring electrodes can be determined from the approximated expression: $s=at^2/2$, where a – acceleration. Thus:

$$t=\sqrt{2s/a}=\sqrt{2sm/qE}=\sqrt{\frac{2\cdot 1\cdot 10^{-2}\cdot 10^{-30}}{1{,}6\cdot 10^{-19}\cdot 10^{4}}}\approx 3\cdot 10^{-9}\,c.$$

The full time of flight for ten-cascade electron multiplier will account for approximately 30 ns. It is clear that as charges move from one cascade to another, the current must increase. Since the number of electrons at each cascade increases approximately in accordance with expression $\Delta N/\Delta t\approx(\delta-1)N$, we can expect that current impulse will increase exponentially (fig. 3.11). Let's calculate the maximum current which flows when the charge moves from the last but one cascade of multiplication to the last one. As a rough approximation, it is equal to the ratio between the value of the charge coming to the last cascade and the time of flight: $I\approx q_t/\Delta t=10^6\cdot 1.6\cdot 10^{-19}/(3\cdot 10^{-19})=50$ *mA*. This rough estimation can be specified taking into account the real configuration of the field. However, this will give us only approximate result; for the exact calculation it is necessary to know the range of the value of time of flight which in its turn depends on the detector's dimensions.

The same method of multiplication is mostly used in devices called *photo-electron multipliers* (PEM) (fig. 3.12). In PEM the first cascade of electrons is set by light instead of electrons. Here the process at which the metal sample is given the energy of electromagnetic radiation, light radiation in particular, takes place. Light waves represent transverse vibrations of electrical and magnetic fields which are able to transmit the kinetic energy which is sufficient for electrons to fly out of metal. The process resembles of thermo- electron emission mentioned above. This similarity is clearly observed and can be used in practice even without preliminary basing of reasonableness of such approach (which should be done by all means).

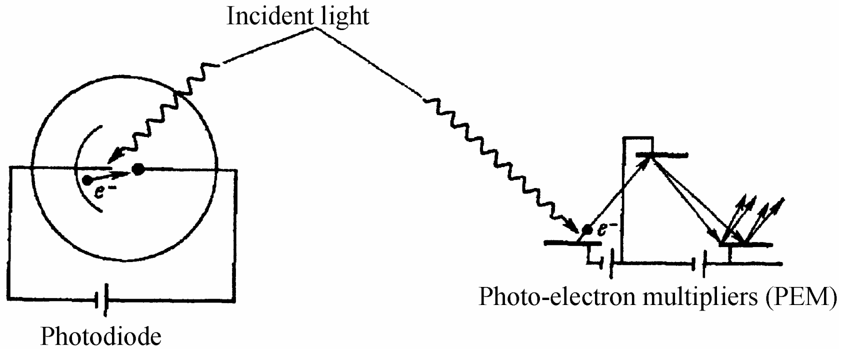

Fig. 3.12. Photodiode and PEM schemes.

We clearly see from the experiment that if we apply substance with low photoelectric work function (for example alkali natrium metal) on the cathode surface in the usual vacuum diode and radiate the cathode with visible light, electric current will flow from the cathode to the anode. Since the cathode emits only electrons, the current may flow only in one direction. Such device is called *photodiode* (fig. 3.12) by analogy with vacuum diodes with incandescing cathodes. Using the photodiode as the first cascade of the electron multiplier, we turn the latter into a photoelectron multiplier whose light sensitivity is several times as much as the one of the photodiode. The above mentioned types of photoelectron multipliers do not have positional sensitivity.

3.2.6 Microchannel plate

In the late 1960-s we witnessed the significant advancement (both in the methods of detecting weak flows of charged particles and the methods of image amplification in electron and ion microscopes). This was made possible due to the appearance of the device called microchannel plate (MCP). Besides, MCP has the same multiplication factor as an ordinary electron multiplier and even provides spacious resolution of ~50 μm. The design and the working principle of MCP are shown in fig. 3.13. It represents the plate of semi-conducting glass 2 mm thick and with the diameter 40–80 mm. This plate has perforated microscopic channels (capillaries) with the diameter 15–50 μm. The channels cover near 60 % of the plate's area. Thus, the plate with the diameter 75 mm has 2 million capillaries. The distance between the channels varies from 20–60 μm. The difference of potentials along the channels accounts for approximately 1000 V. Incident radiation causes the emergence of the cascade of secondary electrons moving along the channels. The primary electron is created either as a result of clashing with the channel wall or from the electron transformer located before the system of capillaries. The electrons from the device's output can be directed immediately at the luminescent screen, thus obtaining visible image of the source or in additional MCP to get the general multiplication factor up to 10^7 and more, and then use the standard methods of signal processing.

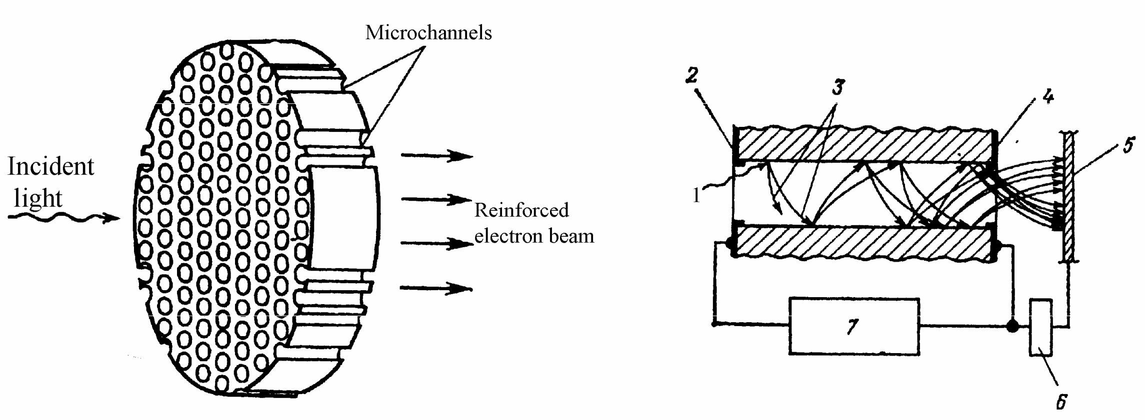

Fig. 3.13. Design (on the left) and working principle (on the right) of the microchannel plate: 1 – incident light; 2 – input electrode; 3 – secondary electrons; 4 – output electrode; 5 – anode system or luminescent screen; 6 – collector feed circuit; 7 – high voltage source.

Due to small length of channels and high voltage, the full time of flight is significantly shorter if compared with the ordinary electron multiplier with the same multiplication factor. The characteristic time of impulse increase accounts for less than 10^{-9} *s*, and its time spread is 10^{-10}. Therefore, MCP may be used as a device with extremely high time resolution.

4. Theoretical Basics of Ionic Spectroscopy Methods

As it was mentioned in the introduction, the basics of the methods of ionic spectroscopy include processes, which proceed in the reaction of the accelerated ionized atomic particles with the sub-surface layers of the solid. These processes are so various and complex that there is hardly a theory which could systematically describe them from a common point of view. That is why by now a number of theories have been developed, each of which describes a separate process or a limited set of processes. In the present part the major statements and conclusions of some generally recognized theories, which were fundamental for the rise of analysis methods, are being examined. These are the following:

- *atomic collisions theory*;
- *theory of atomic particles passage through the substance;*
- *theory of surface sputtering by ions;*
- *theory of interaction of atom with the surface;*
- *theory of excitation and ionization of the secondary atomic particles.*

The major attention is paid to the theory of ionic sputtering, which is the basis not only for such methods as energy-mass-spectrometry of secondary ions and ionic-photon spectroscopy, but also for the methods of the level-by-level analysis.

Due to ionic sputtering, the level-by-level analysis becomes practically possible by any other methods of surface diagnostics.

4.1 Elements of Atomic Collisions Theory

In the present part the major statements and conclusions of the theory of atomic collisions necessary for understanding the processes and theories (in particular the theory of surface sputtering by ions), which lay the basis of the methods of ionic spectroscopy.

Basic signs, accepted in the present part (Fig. 4.3.): E_0, M_1 – the energy of ions in the beam (synonyms: flying, bombarding, probe, and primary ions), E_1 – the energy of flying ions after collision with the target atom, E_2 – energy, transmitted by the primary ion to the target atom after the collision, M_2 – mass of target atoms, θ_1 – deviation angle of the flying ion from the initial direction after collision with the target atom, θ_2 – angle between the initial direction of the flying ion and the direction of movement of the target atom (recoil atom) after the collision

4.1.1 Cross-section of collisions

We'll remind you, what cross-section of collisions is. The process of the atomic collision of two particles, flying (1) and resting (2), may be characterized by a parameter σ, which means that in general *the share of particles type* 1, falling to the target with the thickness x, which consists of particles of type 2, dispersed with the density N (per volume unit), *which takes part in collisions*, *equals* the product

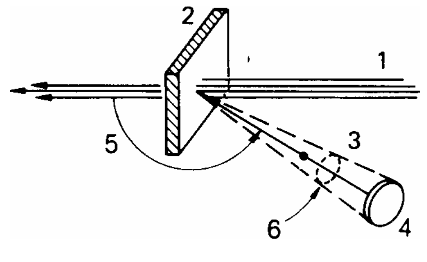

Fig. 4.1. Illustration of the notion of the scattering differential section. The only particles registered are the ones scattered within the limits of solid angle Ω, determined by the inlet of detector: 1 – incident beam of particles; 2 – target, containing N_s atoms/cm^2; 3 – scattered particles; *4* – detector; 5 – angle of scattering θ; 6 – solid angle Ω capture of the detector.

$$N \cdot x \cdot \sigma. \tag{4.1}$$

In other words: cross-section of collision σ – is the potential measure of reaction between two atoms (one – in a beam, and the other – in a target), which is determined by the following equation

$$\sigma = \frac{Число\ актов\ взаимодействия}{Число\ падающих\ частиц} . \tag{4.2}$$

If the target contains N_s atoms for the unit of area and is positioned perpendicular to the beam of particles with the intensity I, the number of reaction acts within a time unit equals $I{\cdot}\sigma{\cdot}N_s$. For the fine target with the thickness t, containing N atoms/sm^3, $N_s=N{\cdot}t$.

Value (4.1) is also the probability that the atom of type 1 collides with the evenly arranged atoms of type 2 during passing the short pathway x in the homogeneous substance. This statement is true only when $Nxa < 1$.

We will deal with the cross-sections of elastic collisions, when the kinetic energy is transmitted from atom 1 to atom 2 and also with the cross-sections of non-elastic events (excitation of plasmons, excitation and ionization of atoms, etc.)

For the elastic events it is more convenient to use the *differential cross-section,* determined as follows

$$d\sigma(E_0, E_2) = \frac{d\sigma}{dE_2} dE_2 , \tag{4.3}$$

where E_0 – the energy of the flying atom, and E_2 – energy, transmitted in one collision. Full and differential cross-sections are, obviously related by the correlation

$$\sigma_{полн} = \int d\sigma(E_0, E_1) \cdot \tag{4.4}$$

4.1.2 Collision cross-section and impacted parameter

The differential cross-section of scattering $d\sigma/d\Omega$ for the particle moving by the target atom to the element of the solid angle $d\Omega$ is written in the following equation:

$$\frac{d\sigma(\theta)}{d\Omega} \cdot d\Omega \cdot N_S = \frac{Number of\ particles scattering in\ d\Omega}{Полное\ число\ налетающих\ частиц} \tag{4.5}$$

thus, the average differential cross-section of the scattering $\sigma(\theta)$ is

$$\sigma(\theta) = \frac{1}{\Omega} \int_{\Omega} \frac{d\sigma}{d\Omega} \cdot d\Omega , \tag{4.6}$$

which is usually called scattering cross-section. For a small detector with the inlet area A which is remote from the target at the distance l, the solid angle Ω equals A/l^2 Sr.

In the experiment with geometry, shown in Fig. 4.1. number N_s of the target atoms on 1 sm^2 is

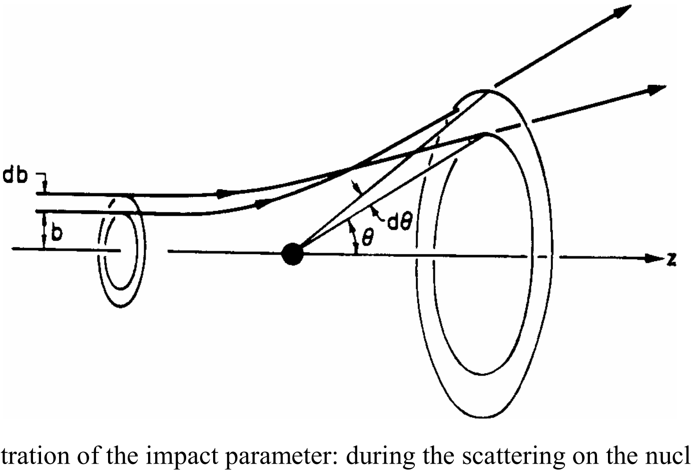

Fig. 4.2. Illustration of the impact parameter: during the scattering on the nucleus, particles with the impact parameters from b to $b+db$ are deviated into solid angle $2\pi\ \sin\theta d\theta$

related to the yield of scattering Y or with number Q_D of registered particles (in the ideal detector with 100% efficiency and with the solid angle of capturing Ω) by the following correlation

$$Y = Q_D = \sigma(\theta) \cdot \Omega \cdot Q \cdot N_S, \tag{4.7}$$

where Q – full number of flying particles. Value Q is determined by the integration in the time of the flow of charged particles, falling to the target. From the equation (4.7) it can be easily noticed that the term "cross-section" is fully justified by the fact that it has dimension of the area.

Impact parameter b (Fig. 4.2.) – distance between the trajectory of the flying particle and right line parallel to it, which passes through the center of the nucleus of the target atom. Particles with impact parameters between b and $b + db$ are scattered at the angles from θ up to $\theta+d\theta$. By definition, the cross-section of the distance is the constant of proportionality between the impact parameter and the scattering angle: $2\pi b db = -\sigma(\theta) \cdot 2\pi \sin\theta d\theta$. If the forces between the flying atom and the target atom are central ones, there should be a full symmetry regarding the rotation around the beam direction. In this case $\sigma(\theta)$ combines the initial homogeneous scattering of the impact parameters of the flying particles with the final angular distribution. The sign "minus" means that the increase in the impact parameter results into the decrease in the scattering angle, because the force, action to the particle decreases.

4.1.3 Elastic collisions

Despite the fact that the atoms in the solid are interrelated, the kinetics of the initial collision of the ion with the surface atom is described in details as a simple two-particle collision of free atoms. The duration of the collision is small, the energy of interrelation is great, and the local combining forces are small. Thus, it can be easily shown on the basis of the laws of energy and impulse conservation, that if the flying ion with the energy E_0 and the mass M_1 collides with the surface atom with the mass M_2 and scatters within the angle θ_1 (in the laboratory reference system, Fig. 4.3.), the scattered ion has energy E_2, which is determined by the following equation:

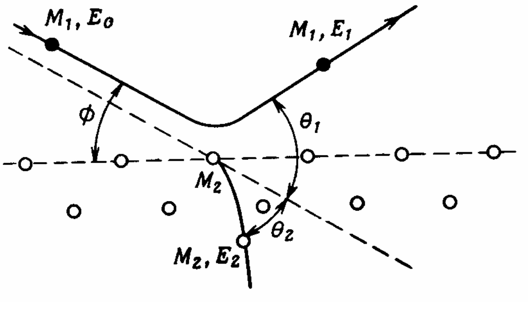

Fig. 4.3. Scheme of the process of ion scattering on the atom, positioned on the surface.

$$\frac{E_1}{E_0} = \frac{1}{(1+A)^2}\left[\cos\theta_1 \pm \left(A^2 - \sin^2\theta_1\right)^{1/2}\right]^2, \tag{4.8}$$

where $A=M_2/M_1$ and sign "plus" corresponds to $A>1$, and both signs – to $A<1$. At the same time, the surface atom acquires the energy, and if initially it was resting, now it bounces off with the energy E_2 under the angle θ_2 regarding the trajectory of the falling ion. Thus

$$\frac{E_2}{E_0} = \frac{4A}{(1+A)^2}\cos^2\theta_2 \cdot \tag{4.9}$$

The energy conservation law requires the following correlation to be fulfilled $E_0=E_1+E_2$, and thus provides univocal correspondence of θ_2 and θ_1. Particular values of these two angles are determined by the precise trajectory of the bombarding ion. Let's point out that the energy of scattered ions for the determination of the outlet angle (scattering) is determined only by the correlation of target mass (scatterer) and the scattered particle. Thus, the study of the scattered ions and their energy creates a potential possibility of the analysis of the surface content.

The maximum energy E_{2m}, which can be transmitted by atom 1 with the energy E_0 to the atom 2, which had zero energy before the collision, with the central (synonyms: head-on collision with zero impact parameter) collision can be described in the following way:

$$E_{2m} = \gamma E_0 = \frac{4M_1M_2}{\left(M_1 + M_2\right)^2} E_0 \ . \tag{4.10}$$

Scattering of the probabilities of energy transmission E_2 is determined by equation (4.10) and cross-section $d\sigma(E_0, E_2)$. In case of Rutherford scattering, i.e. when the powers are high enough to make scattering depend on the Coulomb repulsion of the nucleus:

$$d\sigma(E_0, E_2) = \pi \frac{M_1}{M_2} Z_1^2 Z_2^2 e^4 \frac{dE_2}{E_0 {E_2}^2}; \quad 0 \le E_2 \le E_{2m}, \tag{4.11}$$

where Z_1e and Z_2e – charges of nucleus. This cross-section is characterized by the dominating role of the collisions with small amount of energy transmitted ($E_2 << E_{2m}$); moreover, it decreases along the absolute value with the decrease in E_0 and best describes the experiment when the following condition is satisfied:

$$\varepsilon = \frac{M_2E_2}{M_1 + M_2} \frac{a}{Z_1Z_2e^2} >> 1, \tag{4.12}$$

$$a \approx 0{,}085 a_0 \left(Z_1^{2/3} + Z_2^{2/3}\right)^{-1/2}; \quad a_0 = 0{,}529\,\text{Å}, \tag{4.13}$$

i.e. when the powers are strong enough, when the nucleus are approaching each other and the distance between them is less than the radius of screening a. The characteristic values of this energy, standardized for parameter ε for various combinations “the flying particle – target” are described in table 4.1.

When the powers are weak ($\varepsilon \le 1$) screening of the Coulomb interaction is desirable; in this case the cross-section may be roughly written down in the following way

$$d\sigma(E_0, E_2) \approx C_m {E_0}^{-m} {E_2}^{-1-m} dE_2, \tag{4.14}$$

$$C_m = \frac{\pi}{2} \lambda_m a^2 \left(\frac{M_1}{M_2}\right)^m \left(\frac{2Z_1Z_2e^2}{a}\right)^{2m}, \tag{4.15}$$

where a λ_m – dimensionless function of parameter m, slowly changing from $m=1$ in high energies [i.e. such energies where (4.14) transforms into (4.11) and $\lambda_m = \lambda_1 = 1/2$] up to $m \approx 0$ in very low energies (table 4.2). Equation (4.14) is deduced on the basis of classical theory of collisions with the use of interatomic interaction potential of the type $V(R) \sim R^{-1/m}$, where R – distance between the colliding atoms

Table 4.1. Energy of Tomas-Fermi in the units ε : $E_{TF} = E/\varepsilon$

Element	M_2 A.E.M.	Ион	H	He	Ne	Аг	Кг	Xe	U
		M_1 A.E.M.	1	4	20	40	84	131	238
H	1		0.0869	0.494	15.33	63.6	324	850	3120
C	12		0.414	1.087	13.86	46.8	200	498	1710
Si	28		1.163	2.68	23.8	68.0	254	585	1910
Cu	64		2.93	6.30	44.1	107.0	338	722	2130
Ag	108		5.46	11.45	72.0	160.0	453	903	2260
Au	197		10.75	22.2	128.4	266	676	1250	3060

Table 4.2. Value λ_m in formula (4.15)

m	1.000	0.500	0.333	0.191	0.055	0.000
λ_m	0.500	0.327	1.309	2.92	15	24

Although this conclusion is possible only when there are minor deviations from the Rutherford interaction ($m \cong 0.2$), equation (4.14) may be used also when the value of m is less, when the cross-section stops depending on the initial energy:

$$d\sigma(E_0, E_{2m}) \approx \frac{\pi}{2} \lambda_0 a^2 {E_2}^{-1} dE_2; \quad 0 \le E_2 \le E_{2m} \tag{4.16}$$

when $m \approx 0$. Let’s note down, that even in this case “remote” collisions are dominating ($E_2 << E_{2m}$).

The significant characteristic of the elastic events is the average energy, which is lost by the particle, when it passes distance x. On the basis of equations (4.1) and (4.14) and using the definition of average value, we have:

$$\overline{\Delta E} = Nx\int d\sigma(E,T)\cdot T = NxS_n(E) \ , \tag{4.17}$$

where $S_n(E)$ – cross-section of (nuclear) inhibiting action:

$$S_n(E) = \frac{1}{1-m}C_m\gamma^{1-m}E^{1-2m} \ . \tag{4.18}$$

Let’s note down that in equation (4.17), as in many other following correlations, the limits of integration are not stated. They are omitted because the integration element is included into the differential cross-section, where the tolerance range of integration variable E_2 is stated [see, for example, (4.14)].

It can be easily seen that at low energies ($m\approx 0$) value $S_n(E)$ increases proportionally to E, at intermediate energies ($m\approx 1/2$) it goes on the plateau and at high ones($1/2<m<1$) decreases. Such nature of dependence may be described by more convenient formula

$$S_n(E) = 4\pi a Z_1 Z_2 e^2 \frac{M_1}{M_1+M_2} s_n(\varepsilon) \ , \tag{4.19}$$

where $s_n(\varepsilon)$ – universal function, which depends on the precise type of screened Coulomb potential, being used. Some proposed variants are shown in Fig. 4.4. Energy variable ε in this figure is determined by relation (4.12). The curves correspond to various functions of Coulomb interaction screening between two colliding atoms. Curve 1 corresponds to the Tomas-Fermi potential; using it during the ionic scattering of the surface, we get the excessive values of scattering coefficient. Curve 2, which corresponds to Lenz-Yensen potential, decreases the stopping cross cross-section. Curve 3 corresponds to Bohr potential. The accuracy of the above given equations is maximum (few per cent) in the field of weak screening ($\varepsilon>>1$, $m\approx 1$) and minimum in the field of strong screening ($\varepsilon<<1$, $m\approx 0$), where it best equals 100%.

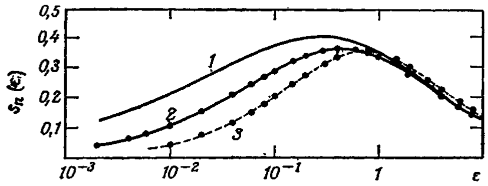

Рис. 4.4. Cross-sections of nuclear inhibiting action in Thomas-Fermi's variable. See the text.

4.2 Elements of the theory of the accelerated particles passing through matter

For the description of particles penetration into the substance the following parameters are included (Fig. 4.5): **v** – initial velocity of an ion, E – its energy, θ – ion incidence angle to the target surface, R – length of the path in the substance, R_p – projective range, x – penetration depth.

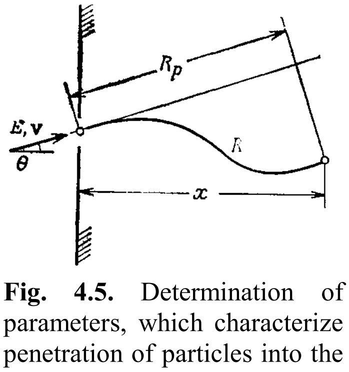

Fig. 4.5. Determination of parameters, which characterize penetration of particles into the substance.

Average energy, lost on the unit of path by the particle, moving in the homogeneous substance, is calculated by the equation (4.17) and equals:

$$\frac{dE}{dx} = -NS_n(E) \ . \tag{4.20}$$

Average range $R(E)$ of the particle in the substance before its stoppage may be calculated in the following way

$$R(E) = \int_0^E \frac{dE'}{NS(E')} \ . \tag{4.21}$$

If all the energy of the particle is lost in the elastic collision, equations (4.18) and (4.21) give:

$$R(E) \approx \frac{1-m}{2m}\gamma^{m-1}\frac{E^{2m}}{NC_m} \ .$$

Generally speaking, the average projective range $R_p(E)$ is less than value $R(E)$ due to the scattering of particle falling in the substance. Fudge factor of the range $R_p(E)/R(E)$ is much less than "one" when $M_1 << M_2$ ($\varepsilon \leq 1$) and approaches to "one" when $M_1 >> M_2$ and when $\varepsilon >> 1$. In the domain of applicability of equation (4.14) and in the absence of the electronic deceleration this value depends on the correlation of masses M_2/M_1 and on the parameter m, but there is no obvious dependence on energy.

Distribution $F_R(x,E,\theta)$ of particles ranges over the target depth x depends on angle θ between the direction of the initial beam fall and a perpendicular to the surface. This definition is generally characterized by the average value of x

$$x(E,\theta) = R_\varphi(E)\cos\theta \qquad (4.22)$$

and corresponding root-mean-square deviation.

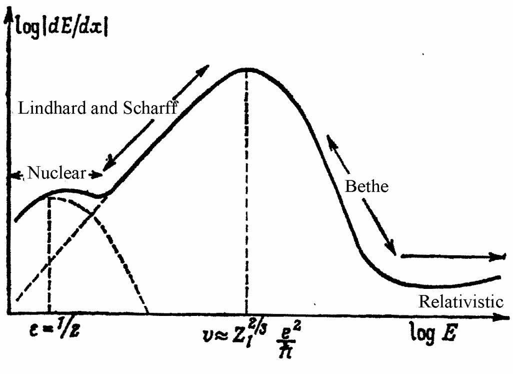

Fig. 4.6. Approximate graphic chart of average specific losses of ion energy from depending on energy.

The deceleration of ions especially at high velocities of falling particles ($\varepsilon >> 1$) is determined by the energy losses, the electron excitation, and the scattering on electrons is not significant due to their small mass. That is why in case of values E_0, typical for the scattering, out of all the parameters of interaction with the electrons we are interested only in the cross-section of nuclear inhibiting action. In Fig. 4.6 the approximate course of change of this value in different energy bands is shown. In the lowest energies [$\varepsilon \approx 1$, equation (4.12)], for heavy ions and ions of average masses atomic deceleration prevails, and for light ions there are other types of deceleration. In this field the observed particles are predominantly neutral. Behind the maximum of average energy losses (field $v >> e^2/\hbar$) function S_e is approximated by Bethe formula:

$$S_e = \frac{4\pi e_1^2 Z_2 e^2}{mv^2}\left(\ln\frac{2mv^2}{1} + correctionterm\right), \qquad (4.23)$$

where e_1 – particle charge (if it is considered as point charge), e – electron charge, I – average ionization potential; correction terms are introduced in correspondence with a specific situation.

Equation (4.23) can be applied outside the field, where usually those experiments are carried out, which deal with scattering of the surface with ions; here the particles are usually ionized. When the velocity approaches the velocity of light, average energy losses pass through the shallow minimum and then increase in the utter relativist case.

In low velocities ($v \leq Z_1^{2/3} e^2/\hbar$) we can use the formula of Lindhard and Shaarf:

$$S_e \approx \xi_e 8\pi e^2 a_0 \frac{Z_1 Z_2}{Z}\frac{v}{e^2/\hbar}, \qquad (4.24)$$

where $Z = (Z_1^{2/3} + Z_2^{2/3})^{1/2}$ and ξ_e – function of atomic number Z_1.

It was experimentally determined, that ξ_e oscillates relatively to expected dependence $\xi_e \sim Z_1^{1/2}$. Equation (4.24) is less accurate, than (4.23), but is turns to be a satisfactory approximation in the theory of scattering due to the direct knocking-out from the equilibrium positions, where it is used as adjustment.

4.3 Elements of ion sputtering theory

4.3.1 Classifications of sputtering mechanisms

All the processes of ion sputtering may be divided into 3 types:

1. Sputtering due to the atomic collisions, which is typical mainly of metals.
2. Sputtering due to the electronic processes of target excitation, which is typical mainly of dielectrics.

3. Sputtering due to the chemical reactions.

During the sputtering of the 1st type 3 regimes are possible (Fig. 4.7). Their realization in specific situation depends on the correlation of masses of atoms, bombarding particles, and the target, and also on the primary particles energy:

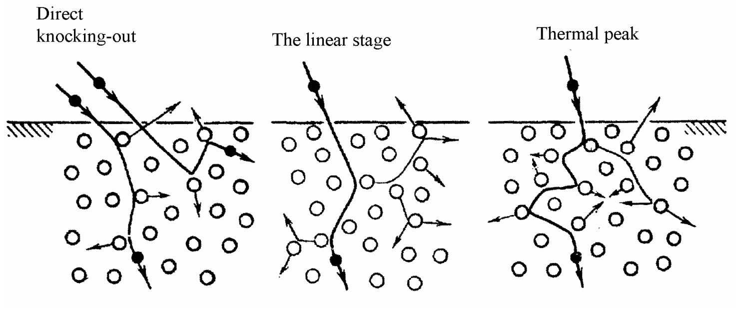

Fig. 4.7. Sputtering regimes due to atomic collisions

Regime of an initial direct knocking-out is characterized by such correlation of ion-target masses and by such value of primary ion energy, that only a small number of collisions of initially dislodged atoms with target atoms, leading to its dislodging outside the target limits, are possible. Thus, in this case, the atoms, dislodged from the equlibrium positions due to the ion-atomic collisions, acquire the energy, sufficient for their scattering but insufficient for cascade of dislodged atoms. Such condition may be realized in one of three cases: 1) during sputtering of any targets by any ions with energy close to the *sputtering threshold* (*sputtering threshold* – minimum energy E_{0min}, where sputtering is still possible); 2) during sputtering of the targets, consisting of heavy elements; 3) during sputtering of any targets by light ions with the energy, equaling to hundreds of eV.

Regime of linear cascades is characterized by the fact that the initially dislodged atom acquires the energy, sufficient for the cascade of dislodged atoms, and at the same time the spatial density of moving electrons is small. This condition is realized predominantly in case of sputtering of the target, consisting of elements with average masses by any ions, except for the heaviest and molecular ones with energies from1to 100 keV.

Regime of thermal peaks, unlike the condition of linear cascades, is characterized by great spatial density of atoms, moving as a result of elastic phenomena. At the same time the density of atom sputtering is so high that the majority of atoms within some range are moving. Thermal peaks are typical of bombardment of any targets by heavy, more than 100 a.m.u., and by molecular ions with energies 1–100 keV. Thermalization of atoms inside the peak as a result of energy transmission from the area of higher density embedded energy to the surrounding areas of the target and through the surface to the external environment, results into the emergence of the hot spot with linear sizes with the degree of primary ion range at the surface. From the field of such spots and especially from the field of their overlapping, with the sufficient density of primary ions flow evaporation of target atoms is possible.

The description of all mentioned conditions of type 1 sputtering is possible in the framework of the unite theory, based on the examination of atomic collisions cascades. The basics, conclusions and limitations of this theory in some of its mathematical interpretations will be described later.

Unlike sputtering of type 1, for the description of sputtering of type 2 there is no adequate theory, although the reasons for such sputtering are understandable, especially in case of nonmetals. The point is that in this case a considerable part of primary ion energy is used for the excitation of electronic sub-system of the target material. As life span of luminous electron condition in dielectrics is high, the excitation may diffuse towards the surface and decay, transmitting the released energy to the surface atom. If electron excitation decays not at the surface, the sputtering may take place with the flaw, which emerges as a result of decay of excitation, which diffused to the surface.

Similarly to type 1, in type 2 we distinguish also 3 conditions of sputtering, depending on the primary ions energy: *condition of separate ionization acts, condition of linear cascades of ionization, and condition of dense ionization peaks.*

For the development of any of the processes (types) of sputtering the definite time interval is required, moreover there is a possibility for such situations when all the described processes are realized in one act of sputtering. This served as the basis for the classification of sputtering according to time. This classification may be introduced in the following way.

Let's consider time from the very outset of interaction of primary ion with target atoms before the moment of relaxation of volume excitation, "disturbed" by the primary ion. Let the interaction start at the moment t=0, thus the following processes may take place depending on t:

1) during $10^{-15}<t<10^{-14}$ s fast collision processes of sputtering take place, including direct and almost direct ion-atom and atom-atom interactions, as a result of which some of the atoms leave the target;

2) during $10^{-14}<t<10^{-12}$ s (according to some data $10^{-13}<t<10^{-11}$ s) energy of the primary ion is distributed among the recoil atoms through direct collisions, the *cascade of collisions* is in progress, the flow of *displaced atoms*, the outlet of sputtered atoms and their energy spectrum are described by the linear cascade theory;

3) by the moment $t\sim10^{-12}$ s the flow of fast thermal processes is coming to an end. The energy of primary ion and moving recoil atoms becomes less than the energy of atoms displacement from the lattice points; in some limited amount, in which the collision cascade took place, all the atoms are on the move and finally are thermalized. There emerges some hot area of range, which is called *heat* or *thermal peak*, or *elastic peak*, or *thermal wedge*. The lifetime of this range acoording to various data is the following 10^{-11}– 10^{-10} s, 10^{-13}–10^{-11} s, 10^{-12}–10^{-11} s. [1];

4) when $t>10^{-11}$ s or $t>10^{-10}$ s slow thermal processes take place or the later stage starts. In case with metal these processes are characterised by the fact, that the thermal peak, reaching the target surface , warms it up to the melting temperature (thus the *hot spot* appears at the surface) and due to this *evaporation of atoms* takes place. When we deal with semi-conductors the processes of sputtering take place due to *electron excitation*. Here we should also include little-studied processes of chemical sputtering, and the mechanisms of sputtering of "*coulomb explosion*" and "*shock waves*" types

For the metals processes 3), 4) may take place only in special conditions, which presuppose high density of energy, absorbed by the target. The critical parameters of these conditions are masses of primary particles and target atoms (should be high), low value of surface binding energy; primary ions energy should correspond to the maximum stopping ability of the target.

4.3.2 Theory of sputtering by the atom collisions cascades

The works of P. Sigmund, and others represent the most advanced variant of theory of sputtering by the cascades of atom collisions. The significant contribution to this theory was made also by Russian researchers, such as Yu.V. Martynenko, and V.V. Pletnyov.

The simplest variant of the theory of sputtering by the cascades of atom collisions is the theory of sputtering by linear cascades of collisions (we will further use the abbreviation LCTS – linear cascade theory of sputtering).

LCTS is closely concerned with the theory of particles passing through the substance and its consequence - theory of radiation damage, the latter two are based on the theory of atom collisions and transmission theory; *kinetic Boltzmann's equation* creates the basis of the theory. In LCTS, as in the theory of particles passing through the substance, the Boltzmann's equation is used for description of target atoms movement, caused by the penetration of bombarding particles into the target.

Let's call the range of all the processes, which take place from the moment of outset of primary ion interaction with target atoms up to the moment of target volume relaxation, excited as a result of the time of primary ion penetration, the *act of sputtering* if as a result of this range at least one target atom escapes the limits of the target. *Another pivotal process in the act of sputtering, in accordance with LCTS, is the cascade of atom collisions.* It is possible to formulate the following

---

[1] Differences in terminology and lifetime are related to the delicacy of process understanding by various authors and obviously will soon be avoided.

general concept of the cascade: the falling ion upsets the atoms balance, thus recoil atoms are being formed – the initially upset atom (IUA), moving in the target substance; these atoms collide with other atoms (in the condition of linear cascades they collide only with stationary atoms) and if the energy of collision is high enough, they replace them; this process continues up to the time, when the energy of displaced atoms is high; in definite conditions some part of the atoms may leave the target.

The notion of cascade generation is frequently used: primary recoil atoms, i.e. the atoms created by the primary ion, are called the zero cascade generation; recoil atoms, created by the atoms of zero cascade generation, are called first cascade generation and so on. Cascade generations emerge naturally in the approach to the solution of Boltzmann's equation, which implements the transition from usual integro-differential form of this equation to the integral one. The notion of *cascade branches* is also used: these are the successions of collisions, which form separate chains; in case of monocrystals cascade branches may form crowdions and focusons (branches, which are spread into definite crystallographic directions).

Integro-differential form of transference equation allows to immediately define the most important properties of LCTS: *average number of atoms, participating in cascade; density of atoms, whose balance was upset; average number of atoms, moving in the definite moment of time in the definite energy interval, and, finally, atom flow density, differentiated along the energy and direction.*

The integral form of the transmission equation allows estimating the density of the atoms, taking part in the cascade in the form of the convergent functional series, the n-term of which may identify the density of atoms, belonging to n-generation cascade.

The mathematical part of the LCTS is explicitly described in great number of publications. Let's consider only those moments, which are vital for understanding the issues connected with ion spectroscopy methods.

Before coming to the conclusions of LCTS, let's consider the suppositions, which form its basis and also limitations and drawbacks of this theory, related to these suppositions. At the same time let's proceed from interpretation of P. Zigmund, because only in this interpretation we can find relatively simple analytic forms of sputtering characteristics through the parameters of primary ions and target atoms measured in the experiment.

In LCTS the following characteristics are taken into account (determination of angles properties is shown Fig.4.8):

– *Coefficient of sputtering* (*S*), determined as an average number of atoms, removed from the solid as a result of one primary ion influence;

– *Angular distribution of sputtered particles* $W(\theta,\varphi)=\dfrac{d^2S}{d\theta\cdot d\varphi}=\dfrac{d^2S}{d^2\Omega}$,

where θ, φ – are azimuth , measured from the external perpendicular to the surface, and horizontal angle, measured from the sputtered atom velocity vector projection on the surface, in the rectangular frame of reference *XYZ*, plane *XOY* of which is superposed with the target surface, and positive direction of axis Z coincides with the external perpendicular to the surface (Fig. 4.8);

– *Energy distribution of sputtered atoms* $N(E)=\dfrac{dS}{dE}$ *on the whole area over the target surface;*

– *Energy distribution of sputtered atoms in the element of solid angle*:
$W(E,\theta,\varphi)=\dfrac{d^3S}{dEd\theta d\varphi}=\dfrac{d^3S}{dEd\Omega},(d\Omega=d\varphi dCos\theta)$.

General assumptions in interpretation of LCTS by P. Zigmund during the determination of these characteristics using the steady-state kinetic equation of Boltzmann are the following:

– *Linear character of cascades*;

– *Isotropy of cascade*;

- *Absence of surface influence on the process of cascade development*;
- *Absence of volume constraint forces influence on the cascade energy*;
- *Absence of orientation effects, related to the presence of crystal structure*;
- *Disregard of faults as a result of cross-sections and interaction potential approximations, used for the description of elastic and non-elastic sputtering of the atoms.*

Taking into account the influence of cascades anisotropy, presence of surface and volume atomic binding energy on the results of some sputtering characteristics is done by introduction of special allowances into the final forms of these characteristics based on the possible effects, conditioned by factors, which were not taken into consideration at the starting point of calculations.

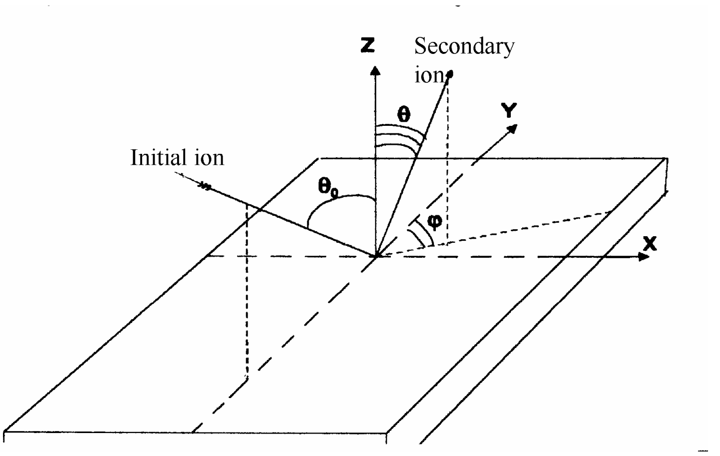

Fig. 4.8. For the definition of typical angles, considered in LSTC: "Initial ion" – direction of initial ions beam, "Secondary ion" – direction of secondary ions outlet.

While solving the transport equation by the alternative way by its reduction to the integral equation for the distribution function, the effects of non-linear character of the cascades influence of the surface on the cascades development, and effects of anisotropy are immediately taken into consideration. However, such account of above mentioned effects is possible in the special target setting, which presupposes more limited ranges of initial ions and target ions parameters, than in the given approach. That is why the results of calculations S and $N(E)$, obtained in the alternative approach, are more precise in quantity, than in the above mentioned calculations, but only for the limited number of "ion-target" pairs.

Let's consider some conclusions of LCTS, concerning above-mentioned characteristics.

<u>Sputtering coefficient</u>

In compliance with LCTS, in the condition of linear cascades

$$S = \Lambda \cdot F_D, \tag{4.25}$$

where

$$F_D = (\frac{dE_0}{dx})_n \cdot \alpha(\frac{M_2}{M_1}, \theta_0, E_0) = \alpha\left(\frac{M_2}{M_1}, \theta_0, E_0\right) \cdot N \cdot S_n(E) \tag{4.26}$$

and

$$\Lambda = \frac{\Gamma_m}{8(1-2m) \cdot N \cdot C_m} \cdot \frac{1}{U_0^{1-2m}}, \tag{4.27}$$

here F_D – primary ion energy, absorbed by the target on the depth unit of the sputtered layer (in calculations we use the value of distribution function of energy, absorbed according to the depth, taken in zero) $(dE_0/dx)_n$ – average energy, lost by the primary ion in the target on the path unit, α – dimensionless function of the ratio of target atoms mass (M_2) to primary particle mass (M_1), reference angle θ_0 and primary ion energy E_0 (there are tabulated numerical values α); Λ – constant, depending on material properties; U_0 – potential surface barrier; N – target atoms density; m and C_m – cross-section parameters of nuclear inhibiting action, in case of Coulomb interaction:

$$C_m = \frac{\pi}{2} \cdot \lambda_m \cdot a^2 \cdot (\frac{M_1}{M_2})^m \cdot (\frac{2Z_1 \cdot Z_2 \cdot e^2}{a})^{2m}, \tag{4.28}$$

m – index in the equation of interatomic interaction potential of the type $V(R) \sim R^{-1/m}$ (R – distance between centers of colliding atoms); m –slowly changes from 1 when energies of colliding particles is high and up to 0 when the energies are very low; λ_m – dimensionless function of parameter *m;* $Z_1\cdot e$, $Z_2\cdot e$ – charges of nucleus of colliding atoms, *a* – screening radius, $\Gamma_m = m/(\psi(1)-\psi(1-m)), \psi(x) = d[\ln\Gamma(x)]/dx,$ $\Gamma(x)$ – gamma function.

For sputtering of targets with great atomic number by light ions, simple equations are obtained, which describe S through the cross-section values of ion-atom and atom-atom collisions, energy of target atoms bonds, average energy of recoil atoms.

It has to be mentioned that there is a great number of empirical and semi-empirical equations to calculate S in definite ranges of primary ions energies, correlations of ion-target masses, etc.

Energy and angular distributions of sputtered atoms in LCTS.

Let's use the following abbreviations: EDDA – energy distributions (or spectrums) of displaced (sputtered) atoms, ADDA – angular distributions of displaced (sputtered) atoms. In the analysis of EDDA and ADDA the main attention will be paid to the correlation of parameters of these characteristics with the physical properties of targets. Such accentuation is due to the importance of these characteristics for ion spectroscopy.

In LCTS the following equations are obtained for EDDA and ADDA above the target surface:

$$W(E,E_0,\theta_0,\theta,\phi)=F_D(E_0,\theta_0,\theta)\cdot\frac{\Gamma_m}{4\pi}\cdot\frac{1-m}{N\cdot C_m}\cdot\frac{E}{(E+U_0)^{3-2m}}\left|Cos\theta\right|, \qquad (4.29)$$

where *E* – kinetic energy of atoms sputtered above the target surface (*Z*=0). Parameter *m* in this case is a slowly changing energy function *E,* decreasing from $m\approx 0.2$–0.3 when *E*=1keV up to *m*=0 when $E\approx U_0$. Taking into consideration the influence of volume energy of atoms bonds (E_D) on the cascade development in the process of atoms deceleration results into EDDA and ADDA of this type (4.29) by changing:

$$\frac{E}{(E+U_0)^{3-2m}}\to\frac{E}{(E+U_0+E_D)(E+U_0)^{2-2m}}. \qquad (4.30)$$

Most probable energy, obtained by solving the task on the function extremum (4.29) equals:

$$E_m= U_0/2(1\text{-}m). \qquad (4.31)$$

Value E_m, obtained from (4.30), is, apparently, much higher than that of (4.29).

Equation (4.29) is obtained in the supposition of presence of flat potential barrier for the cascade atoms, crossing the target surface. Thus, in case of such barrier presence and assumptions made from (4.29) it is evident, that E_m and the form of EDDA and ADDA don't depend on primary ion type, its energy and angles $\theta_0,$, θ, φ. Indeed, correlation (4.29) doesn't give any information about the interaction of angle φ with the parameters of EDDA. Concerning correlation of parameters EDDA with θ and θ_0, as can be seen from (4.29), let's notice, that alteration of these angles affect only the intensity of EDDA, and leaves unchanged E_m and $E_{1/2}$ – width on the half altitude in the maximum of dependence *N*(*E*), fixed for the spectrum unit and asymptotic in high and low energies [from (4.29), (4.26), taking into account dependence of α on above mentioned parameters it is evident that $W(E_0,\theta_0,\theta,\varphi)\sim\frac{Cos\theta}{Cos\theta_0}$]. However, as we will see after, numerous experiments show, that, as a rule there is an obvious dependence of parameters EDDA on θ_0, θ, E_0. Thus, it is advisable to use (4.29) in practice only when $\theta_0\approx\theta\approx\varphi\approx 0$, and E_0 is in the range of keV, or, in other words, when the opportunity of registration of atoms or ions, appearing in the first cascades generations and other sputtering processes, except linear cascade, is avoided or limited. The above mentioned peculiarities of equation (4.29) should be considered as drawbacks in the aspect of its use in the ion spectroscopy, which presupposes surface sputtering where modern experiments may be carried out in different combinations of angles θ_0, θ, φ. The key reason for these drawbacks is the fact that LCTS doesn't take into account the effects of anisotropy of cascades development.

Let’s consider some opportunities of taking anisotropy into account.

One of the ways of taking anisotropy of cascade development into account is separate consideration of the anisotropic part of the cascade (from zero to second generations) and the isotropic one (generations with sequence number more than 2). The specific character of this or that part may be taken into consideration during the summation of rows, describing the density of atoms in the cascade. For the total EDDA with the presence of spherical potential barrier we get:

$$N(E)=\delta(E+V_0-T_0)+2T_0/(E+V_0)^2, \tag{4.32}$$

with the presence of flat barrier

$$N(E)=\delta(E+V_0-T_0)+2T_0E/(E+V_0)^3, \tag{4.33}$$

where T_0 – energy of IUA, and delta-function describes the contribution of IUA into EDDA. It is obvious, that when the energy is high enough, non-isotropic contribution into the highly energetic part of EDDA should be made not only by IUA but also by atoms, of at least 1^{st} or 2^{nd} cascade generation. The analytical theories don’t give any description of this contribution yet. It can be easily seen that equations (4.32) and (4.33) don’t provide any information about dependence of $N(E)$ on θ_0, θ, φ. In order to identify this dependence, peculiarities of EDDA and ADDA formation are related directly to *the impulse*, transmitted by the primary ion to the target atoms. The analysis shows, that function of impulse distribution is much more complicated, that the function of absorbed energy distribution, moreover an average cascade impulse “remembers” the impulse direction of the particle, which created this cascade. As a result, the cascade should be dissymmetric, i.e. it should be enriched by the atoms in the direction of movement of the particle, which initiated it, and depleted in the opposite direction. Thus, correct calculation of EDDA and ADDA should be based not only on full energy, brought into cascade by the primary particle, but also from the details of primary particle sputtering and IUA on the target atoms. Three possible scenarios of cascade development with the participation of the primary particle, which result into deviation from the cosine EDDA and ADDA type (4.29) are considered: I) cascade is created by the primary displaced atom, which got the impulse, whose direction is essentially different from that of primary particle; 2) the sputtered primary particle creates the cascade in the direction, absolutely different from its own initial direction and with the energy different from the initial one E_0; 3) the primary particle, elastically sputtered backwards, creates the cascade in the direction towards the surface, at the same time its energy is the same as E_0.

Detailed consideration of the above mentioned cases resulted into the following equation for EDDA:

$$W(E_0,E,\theta_0,\theta,\varphi)\sim B(E_0)\cdot Cos\theta\cdot$$
$$\cdot\left[\frac{E}{2\cdot(E+U_0)^3}+C(E)\cdot\frac{E}{(E+U_0)^3}\cdot\begin{Bmatrix}-Cos\theta_0\cdot\left(E\cdot Cos^2+U_0\right)^{1/2}+\\ E^{1/2}\cdot Sin\theta_0\cdot Sin\theta\cdot Cos\phi\end{Bmatrix}\right] \tag{4.34}$$

$$\left.\begin{aligned} \text{where }C(E)&=(\gamma\cdot E_0)^{-1/2}, && \text{in case 1}\\ &=\left(\frac{M_1}{M_2}\right)^{\frac{1}{2}}\cdot E_0^{-1/2}\cdot g(E_0,T_0) && \text{in case 2,}\\ &=\left(\frac{M_1}{M_2}\right)\cdot E_0^{-1/2} && \text{in case 3}\end{aligned}\right\} \tag{4.34a}$$

$$g(E_0,T_0)=\frac{M_1+M_2}{2M_1}+\frac{M_1-M_2}{2M_1}\left(\frac{\gamma\cdot E_0/T_0-1}{\gamma\cdot E_0/T_0-1-\gamma\cdot\ln\gamma\cdot E_0/T_0}\right), \tag{4.34б}$$

$$\left.\begin{aligned} B(E_0) &= N^{3/2}\cdot C_1(E)\cdot \ln(\gamma E_0/\ T_0), && \text{for } m=1 \quad \text{in case 1} \\ &= N^{3/2}\cdot \frac{C_m(E_0)}{1-m}\cdot\left((\gamma\cdot E_0)^{1-m}-T_0^{1-m}\right), && \text{for } m<1 \quad \text{in case 1} \\ &= N^{3/2}\cdot C_1(E_0)\cdot\left(\frac{E_0}{T_0}-\frac{1}{\gamma}-\ln\frac{\gamma\cdot E_0}{T_0}\right), && \text{for } m=1 \quad \text{in case 2,} \\ &= E_0 && \text{in case 3} \end{aligned}\right\} \tag{4.34в}$$

$$\gamma = \frac{4M_1\cdot M_2}{(M_1+M_2)^2}\ . \tag{4.34г}$$

In compliance with equations (4.34) parameters EDDA in all three cases depend on E_0, θ_0, θ, φ; moreover, the deviations of EDDA (4.34) from EDDA (4.29) are usually determined by the second component in square brackets (4.34). The last condition determines the fact that deviations EDDA (4.34) from (4.29) become noticeable when the secondary atoms energies are low, that is in the range between 0÷10 eV. Calculations of EDDA based on equations (4.34) provided that one of the angles θ_0, θ, φ changes, and the rest two are fixed, reveal the deviations of most probable energies and changes of spectrums half-widths in this or that side, depending on $C(E_0)$ (4.34, a). So, for instance, in case 3 when θ_0=70°, θ=45° are fixed, increase in φ causes the decrease in spectrum intensity, E_m, $E_{1/2}$; and in case 1 when θ_0=10°, φ=0° are fixed, increase in θ_0 causes shifting of EDDA into the side of high energies with simultaneous increase in E_m, $E_{1/2}$.

The qualitative compliance of equation (4.34) with the experiment for the diaposone of not very big angles θ_0, θ, φ was noticed in some works, devoted to the examination of these compliances.

4.3.3 Patterns of thermal peak, hot spot and shock waves

When the density of energy, extracted in the target as a result of primary particle deceleration, is high, dissipation of this energy is not the same as in case of linear collisions cascades, as all the atoms or their major part is on the move in the limited part of the target. For heavy monoatomic or molecular ions with the energy of about several keV, the value of average energy, transmitted by the target atoms is about several eV for an atom. With such value of average atoms energy the crystal structure of the target doesn't remain. In this case there appears a so-called thermal peak (let's choose for the further use this term, as during the description of this condition of sputtering we need to use the notion of local field with the increased temperature in the equlibrium or non-equilibrium sense). The process of peak initiation might be presented as a result of linear cascade development – overlapping of separate branches of the cascade (sub-cascades), without participation of linear cascade (in case of non-metals from the moment of primary particle interaction with the surface, many-particle processes with electron participation might start).

There is a number of thermal peak concepts, which describe deviations of experimental results along the measurement of S and EDDA from those, which are forecasted by LCTS (such deviations are called non-linear effects of sputtering). All the designed concepts are postulating the existence of the peak (some of them also describe its evolution), without saying a word about its formation. As regards the last one it is supposed that the thermal peak is either the last stage of development of atomic collisions cascade (i.e. the stage of thermalization), or just a simple highly intensive thermal impulse, which is forming along the track of the primary particle.

All the concepts of thermal peak existing today may be symbolically divided into *two groups: equilibrium* and *non-equilibrium.* In compliance with equilibrium concepts, provided that the density of energy absorbed in limited target volume is high, the thermodynamic balance is obtained very fast, and it is characterized by Maxwell's distribution of atoms according to their velocities. The volume center (or nucleus) is placed under the surface on the distance of average range of primary particles. Then the form of volume is postulated (orb, cylinder, ellipsoid), the profile of temperature distribution along the volume (Gauss's distribution with the maximum at the center of volume or proportional one). The given hot volume is intersected by the target surface; hence from the section plane the atoms are evaporated with Maxwell's energy distribution, where the equilibrium temperature of the peak, which is calculated by this or that method depending on the amount of energy absorbed, is used as a temperature. By postulating the law of evaporation, we calculate evaporation velocity – the flow of evaporated particles within the time of such peak existence, i.e. the coefficient of thermal sputtering S_{therm}. The consistence of the peak in this very conseption represents, as a rule, a flux, or dense liquid.

Non-equilibrium conceptions are used for the description of more realistic peak, than the above mentioned method, based on the consideration of irreversible transition of energy from the area of high energy density to the surrounding target areas and through the surface to vacuum. For the description of energy transition the following equation of thermal conductivity is used:

$$\frac{\partial T}{\partial t} = div(\kappa \cdot gradT), \tag{4.35}$$

where T – temperature in the sence which it has in thermodynamics of irreversible processes, κ – coefficient of temperature conductivity, in general $\kappa=\kappa(T)$. In the simplest pattern s the dependence $\kappa=\kappa(T)$ is not taken into consideration, assuming that $\kappa=const$ and using the value of κ for the crystals of corresponding targets. Another serious simplification of such pattern s is approximation of initial temperature distribution (required for the determination of temperature profile at the surface on the basis of equation (4.35)) by the gaussian with parameters, chosen on the basis of conclusions. If it is posiible to determine the surface profile of the peak temperature (to be more precise, the profile of temperature in the hot spot, which was created by the surface peak) on the basis of all simplifications, mentioned and others, concerning the equation (4.35), by integrating the evaporation rate on the surface and according to the temperature we can calculate S_{therm}. At the same time to determine the evaporation rate it is assumed, as a rule, that the process of evaporation is the same as the one, when the solid is in balance with its vapor.

Let's consider more developed conceptions of thermal peak in details. In one of such conceptions we consider the cylinder peak at the early stage of its development and the possibility of the orb form on the later stage (when the radius of the hot spot on the surface becomes comparable with the average range of primary particle in the target) due thermal transference. The target surface crosses the cylindrical peak perpendicular to its axle. The aggregative state of the target substance in peak volume is a dense ideal gas. Thus, a popular dependence $\kappa=\kappa(\text{T})$ upon the kinetic theory of gasses is used. Having in mind the described conceptions of cylinder peak, we use the equation of heat conduction, designed by L.D. Landau and P.L. Kapitza while assessing the thermal emission of electrons, initiated by α-particles. In both cases the solution is obtained in the following form of functional dependence $T = T(\rho, \kappa, F'_{\text{D}}, t)$, ρ – peak radius, t – time, F'_{D} – energy contribution into the peak for the unit of length of primary particle trajectory. At the same time the differences between the obtained values of S_{therm} are inessential. Knowing the temperature profile along the peak radius in the time, it is easy to calculate S_{therm} from the following correlation

$$S_{therm} = \int_{t_0}^{\infty} dt \int_{0}^{\infty} 2\pi\rho d\rho \left[\Phi\left((T_a + T)\right) - \Phi(T_a)\right], \tag{4.36}$$

where $\Phi(T)$ – evaporation law; T_a – temperature of the target, surrounding the peak; T – temperature, induced by the primary particle, which depends on ρ and T in accordance with the equation of thermal conductivity $T=T(\rho, \kappa, F'_{\text{D}}, t)$. The first member of the equation in the square brackets (4.36) describes the evaporation from the peak, the second – evaporation outside the peak at temperature T_a. In the equation (4.36) from integration along ρ and t we may come to the integration along T in correspondence with the law $T=T(\rho, \kappa, F'_{D}, t)$. Using this law in the form proposed by P.L. Kapitza we may have:

$$S_{therm} = \frac{F'_D}{8\pi\Lambda' C_V}\int\limits_0^{T_0}\frac{dT}{T}\left(\frac{1}{T^2}-\frac{1}{T_0^{\,2}}\right)\left[\Phi(T_a+T)-\Phi(T_a)\right], \qquad (4.37)$$

where $\Lambda' = \kappa \cdot C_V$ – coefficient of target thermal conductivity; C_V – thermal capacity; $T_0=T(\rho=0, t=0)$ – initial temperature in the peak nucleus:

$$kT_0 = {F'_D}\Big/{2\pi N < \rho^2{}_0 >}, \qquad (4.38)$$

where k – constant of Boltzmann, $<\rho_0{}^2>^{1/2}$ – initial width of the peak.

A detailed consideration of four integrals, which are easily seen in (4.37) results into the differentiation between *two stages* of peak evaporation (or peak development): *early* (*high temperature*) with the temperature of evaporation close to T_0 and *late* (*low temperature)* with the temperature of evaporation close to T_a. The concrete definition of the law $\Phi=\Phi(T)$ and substitution at the late stage of law $T=T(\rho, \kappa, F'_D, t)$ for the cylinder on the law $T = T(\rho, \kappa, E_0', t)$ for the orb (E_0 – energy, put into the center of the orb by primary particle) results into two various equations S_{therm}. We will not describe these equations here, instead we will consider the equation for EDDA, obtained in the framework of described formula, because, first of all, integration of these equations along the corresponding variables leads to S_{thern}, and secondary, these equations differ significantly from general Maxwell's distributions, which were proposed as EDDA in the condition of thermal peaks.

EDDA in the condition of thermal peaks

Common pattern of cylinder thermal peak, described above, with the concrete definition of evaporation law in the form of:

$$\Phi(T) = N\left(kT/2\pi M_2\right)^{1/2}\cdot\exp\left(-U_0/kT\right), \qquad (4.39)$$

which follows directly from the law of Maxwell-Boltzmann for the evaporation of ideal gas of constant temperature, limited by flat potential barrier U_0, leads to the expression of EDDA of the following type:

$$W(E,\theta)dEd^2\Omega = 0{,}0688\lambda_0 a^2 F_D'^{\,2}\frac{EdE}{(E+U_0)}\cdot f\left(\frac{E+U_0}{kT_0}\right)\cdot Cos\theta' d^2\Omega', \qquad (4.40)$$

where $f(\xi)=\left(1+\xi+\frac{1}{2}\xi^2\right)\cdot\exp(-\xi)$ – tabulated function of non-dimensional parameter; θ' – angle of cone gap of the solid angle Ω'; λ_0= 24, a = 0.219 Å – constant of Born-Meyer, taken from LCTS.

On the basis of the same preconditions as in the equation (4.40), except the differences in the form of dependences $T = T(\rho, \kappa, F'_D, t)$ and $\Phi = \Phi(T)$, we may get:

$$W(E,\theta)dEd^2\Omega = 0{,}0153\frac{\lambda_0 a^2 F_D'^{\,2}}{(kT_0)^2}\cdot\left(1+\frac{T_a}{T_0}\right)^2\cdot\frac{EdE}{(E+U_0)^2}\cdot\exp\left(-\frac{E+U_0}{k(T_0+T_a)}\right)\cdot Cos\theta' d^2\Omega'. \qquad (4.41)$$

In the low temperature condition, i.e. at the late stage, EDDA doesn't differ in form from (4.41).

In conclusion of this part let's cite some general observations, concerning the above mentioned conceptions.

Let's consider some small surface volume δV of the target, in which primary particle passing results into release of heat with the intensity I_Q^{in}. In case of the massive target we may consider that the volume surface δV is supported in some definite thermodynamic conditions, which are determined by the properties of the target material and in turn which determine the rate of heat dissipation through the volume surface $\delta V - I_Q^{in}$. Depending on correlation of values I_Q^{in} and I_Q^{out}, in correspondence with the theory of thermal conductivity, the following situations are possible:

1) $I_Q^{in} << I_Q^{out}$ –no thermal peak occurs;
2) $I_Q^{in} \leq I_Q^{out}$ – non-equilibrium thermal peak may occur with the impulse character I_Q^{out};
3) $I_Q^{in} \geq I_Q^{out}$ – equilibrium thermal peak may occur;
4) $I_Q^{in} >> I_Q^{out}$ – everything may result in some thermal explosion.

The above described conceptions encompass, apparently, only first three situations; situation 4 is not developed yet at all.

4.3.4 Mechanisms of sputtering due to electronic processes and chemical reactions

An electronic process in ion sputtering is a relatively new field of fundamental investigation of sputtering, which recently attracts more and more attention. The fact that these processes may play a pivotal role in the majority of cases of ion sputtering became obvious only in the past 15-20 years. In a more detailed way the electronic mechanisms of sputtering are studied on the haloid compounds and oxides during their irradiation by low-energy ions, low- and high-energy electrons and photons. The fast progress in the understanding the role of electronic processes in sputtering of these very materials (due to more that half a century researches) is conditioned by abundant information about mechanisms of formation and evolution of lattice excitation, and point defects in the crystals of these materials. The mechanism of defects formation and sputtering turned to be identical.

As regards the occurrence of electronic processes in EDDA at present we know only the following: metal component of haloids and oxides sputtering always has thermal energy distribution; during sputtering of oxygen haloids in some cases there is a epithermal component.

When we talk about chemical sputtering, we should definitely understand the differences between sputtering as a result of chemical reactions at the target surface (proper chemical sputtering) and changes of physical sputtering, conditioned by defecation of chemical composition of the surface in the process of sputtering. In the first case we mean an independent mechanism of erosion, which presupposes the formation of the molecule on the surface with low binding energy (the content of these molecules includes chemically active atoms of the primary beam (H , C , O , N and others)), and desorption of these molecules or of their fragments at the surface temperature. In the second case we mean the influence of formed chemical compositions on the process of physical sputtering by changing binding energies and masses of atoms, participating in collision processes of sputtering.

The classical example of proper chemical sputtering should be, obviously, the sputtering of graphite by atomic and ionic beams of hydrogen with the energies from heat type up to tens of kiloelectron-volts. *Chemical sputtering differs from other types by experimental characteristics: high coefficient of sputtering in comparison with its value for the other ion-target combinations wit atomic masses, close to the considered ones; strong dependence of the sputtering coefficient on temperature; absence of strict sputtering limit along the primary particles energy; Maxwell's distribution along the secondary particles energies.*

4.3.5 Peculiarities of multicomponent targets sputtering

Talking about multicomponent targets we mean *single-phase* and *multi-phase* alloys and compounds. Here single-phase targets are those, where the components (elements) are *evenly distributed along the target volume*, and multi-phase are those, which consist of *grains of various chemical composition and with various crystal structure*.

Recently the multi-component targets attract more and more attention, first of all, due to their broad practical use and secondly, due to great number of unsolved issues of radiation stimulated transition of the substance in the process of preferential sputtering.

By preferential sputtering we imply disproportion of outlet (*or the coefficient of sputtering*) *of separate target components to their volume and surface concentration.* We have to clearly distinguish between preferential sputtering and *selective* one. By the latter we imply the different rate of various phases (grains) etching in the content of multi-phase targets.

For the description of multi-component targets sputtering we should include at least three different notions of sputtering coefficient, defining them in the following way:

1) *partial coefficient of sputtering for i-component* S_i – average number of sputtered atoms *i*-elements, for one primary ion;
2) *full sputtering coefficient* – $S = \sum_i S_i$;
3) *sputtering coefficient of component i* – $S_i^c = S_i / C_i$, where C_i –surface concentration of *i*-component in the process of sputtering.

Among the effects, which accompany multi-component target sputtering, we may distinguish two groups: 1) primary or dynamical effects in the sputtering process, which are examined in the flow of sputtered particles and connected with redistribution of intensity of emission of target components atoms, with the alterations of angular and energy distributions; 2) secondary, which are the result of sputtering and which lead to the changes in the surface content and to formation of changed layer, including both chemical and phase content change. It is obvious, that both primary and secondary effects are the result of combined action of sputtering mechanisms and transition of target substance close to the surface in the process of sputtering. At present there is no complete theory, which would describe the above mentioned effects. The development of concepts about them goes in the framework of patterns, based on the above viewed theories, taking into consideration values of masses and binding energies of various multi-component target atoms. To be more precise, the conceptions about primary effects develop in this way, and the attempts are made to describe the changes in surface content under sputtering, because only these effects may be approximately considered basing on one sputtering act (i.e. from the point of view of proper preferred sputtering). When we talk about formation of the altered layer, together with preferred sputtering we have to involve the processes of transition. The following transition processes are considered as the most effective ones: *diffusion, segregation* (*including their radiation accelerated variants*)*, implantation of recoil atoms and cascade interfusion.* Despite the understanding of the role of these processes (in many cases it is very concrete) in the formation of the altered layer, hardly any pattern could be named, which can predict the results of continuous sputtering of the optional two-component target, not to mention more complicated objects. On the other hand, it is almost impossible up to now to define any common experimental regularities of multi-component target sputtering, concerning both primary and secondary effects, although for some class of materials we may talk about some tendencies. Let's point out only two moments, which are of greater importance from the point of view of ionic spectroscopy, and which are related to two-component target sputtering and are grounded both experimentally and theoretically. This is *first, surface enrichment in continuous sputtering by light component* in the condition of insignificant difference between the values of binding energies of components, and also the *enrichment of surface by component with higher binding energy* in the condition of approximate equality of component masses. *Second, for the formation of stationary altered layer we need to sputter the layer with the width not less than projective range of the primary ion.*

4.3.6 Computer simulation of sputtering processes [1]

As it has been already mentioned above, currently there is an intensive development of methods of numerical simulation of sputtering processes. Numerical simulation often allows to calculate many parameters of sputtering, including EDDA, more realistically than by analytical methods. It was especially clearly seen in the recent works, when the study of EDDA started using more versatile experiment geometry. As a result, various peculiarities in EDDA are revealed connected with different sputtering mechanisms which are impossible to describe by analytical theories. At present in order to familiarize oneself with experimental data, concerning EDDA, we should know the principles of their numerical simulation, as often only simulation gives an opportunity to describe the experimental specters. In this conncetion let's consider the modern algorythms of numerical calculations of sputtering parameters in details.

Modern programs of numerical computer-aided calculations are based on two approximations of atomic collisions processes in the solid: 1) *many-particle, or else called molecular-dynamical approximation* (*MDA*); 2) *two-particle, or the approximation of pair collisions* (*APC*). Both types of approximations are the distribution of methods of numerical calculations of radiation damages on the sputtering, whose development dates back to early 1960s. The basics of the calculations and specific programs are described in special literature in details that is why we will restrict ourselves only to the most general observations, concerning the *sputtering act simulation* in MDA and APC.

In MDA, whose field of application is limited by the diapason of low energies of colliding particles and by high density of collisions (i.e. in the conditions, partially corresponding to the conditions of thermal peak), the crystallite of the solid, which includes a limited number of atoms (from hundreds to thousands) is considered. Each crystal atom interacts with another one by conservative central forces, so that the force, influencing the definite atom, equals the simple sum of pair forces. If these forces are the repulsive ones, the forces of elastic type are required in order to keep the atoms of the crystallite together, i.e. to create conditions of crystallite stability. The repulse potentials with limited conditions for crystallite and gravities with free or fixed boundary conditions, and also the combination of both types of forces and conditions are used in the definite programs.

Sputtering act simulation in MDA algorithms is made in the following way. The chosen atom of the crystallite is set in motion in the commanded direction with the commanded kinetic energy (both are commanded by the bombarding conditions) and classical equations of motion are integrated for all crystal particles up to the time, when one atom leaves the solid or it becomes obvious that no atom can leave the solid. As we have to integrate $6N_a$ (N_a – number of atoms in the crystallite) of the classical equations of motion with fine pitch, we face big difficulties, concerning computer memory and time of calculations: this often limits the number of cascades, able to be calculated. In order to avoid these difficulties the researchers have to use simplifications, one of which is the lack of requirement for stability of numerical crystallite. In the framework of metastable patterns for this reason we use so-called eroded interatomic potentials, and in the framework of quasi-stable patterns the numerical crystallite cannot be fixed at all; at the same time lattice atoms needed for integration are generating along the tracks of different displaced atoms.

In literature we may often meet just the name of the program without explanation of its specific character. The most common programs, which implement algorithms of MDA are GRAPE, COMENT, ADDES.

More economical ones, and thus more wide-spread are the algorithms, based on APC. In this approximation we can trace the development of the primary ion and recoil atoms trajectories, due to the sequences of pair collisions of the primary ion with stable target atoms, and of moving recoil

---

[1] The questions concerning this part of the book are stated in more details in the articles of P. Zigmund and I.P. Biersack in the monograph "Fundamental and applied aspects of ionic sputtering". – M.: Mir, 1989. – 349 c. And also in the monograph "Sputtering by Particle Bombardment I". – Edited by R. Behrish // Translated from English by V.A. Molchanov.- M.: Mir, 1980.- 336 pages.

atoms of any cascade generation with motionless particles. The particle is considered to be moving if its kinetic energy is more than some minimal value $E^{\min}$. Integration of classical equations of motion is reduced in this case to sputtering integrals calculations. Only those collisions are calculated, whose parameters are less than value p^c, which corresponds to energy value E^c, if it is less the particle is considered to have left the cascade. Specific implementations of APC differ significantly depending on the pattern of the solid used in calculations. For the solid with the ordered placement of atoms the basic realization of APC is the program MARLOWE. In case of the amorphous solid (unordered gas-like structure) more developed variants of APC implementations; apparently, algorithms TRIM, TRIM SP are used. The major difference between the above mentioned implementations of APC, concerning the cascade simulation, lies in the procedure of search for the next partner for collision after the act of sputtering. In MARLOWE this procedure lies in the choice of a partner from the basic group of atoms, which reproduces all possible spatial relations between atoms of the solid and the moving atom. After having chosen a partner for collision the parameters of collision are determined geometrically; then the sputtering integrals are calculated including the scattering angle. In TRIM the parameters of collision and sputtering integrals are calculated using the notion of free path, which is determined as the value reciprocal to the cube root of the material average density. Parameters of collision and scattering angle are in this case random values, which are chosen from distributions, constructed in this or that way. Thus, algorithms TRIM, TRIM SP are based on the simulation method of Monte-Carlo; that is why they are close in their physical sense to the analytical calculations on the basis of Boltzmann equation, to be more precise, to LCTS.

The possibility of calculation majority of sputtering characteristics in case of multi-component metals has to be regarded, obviously, as the most important achievement of the recent years in the sphere of computer simulation of the sputtering processes. Although the programs, which allow making these calculations, as the majority of analytical theories, do not take into consideration the processes of substance transmission in the subsurface layer, they are of great importance for the fundamental researches of the vital sputtering characteristics.

Major difficulties in simulation of multi-component target sputtering are, first of all the necessity of taking into account various results of collisions in the atoms combinations: “light-light”, “light-heavy”, “heavy-heavy”; secondly, necessity to take into account the concentration differences; and thirdly, necessity to take into account various surface binding energies. Ways of overcoming these difficulties and also general descriptions of programs for studying the sputtering by method of Monte-Carlo and some results of these researches are discussed in the works, cited in the reference note on the previous page.

4.4 Ionization and excitation theories in ionic spectroscopy

In atomic physics and physics of atomic collisions by the term “excitation’ we imply, as a rule, any energy conditions of atoms, different from the basic one, including the state of ionization. By now, it is stated, that all the same processes are responsible for ionization and excitation of secondary particles. That is why the terms, “excitation” and “ionization”, used in this part, should be considered as synonyms, if there are no indications. At the same time we have to distinguish between terms “ionization” and “ion formation”. The latter implies the unity of the excitation processes (ionization) and excitation relaxation (neutralization), which lead to registration of the atomic particles in the ionized condition in the experiment. The terms "de-excitation", "excitation relaxation", "neutralization" should be interpreted as synonyms, if there is no concrete definition in the text.

4.4.1 On the classification of theoretical patterns for ion formation

So, ion formation is the overall result of influence of mechanisms of excitation and excitation relaxation on the atom in the processes of its collision with other atoms in the solid and while moving close to the surface during the sputtering and scattering. Existing classifications of ion formation mechanisms consider only the case of sputtering due to the linear cascades of atomic collisions, and this leads to neglecting the possibility of ion formation, for instance, in the condition of thermal peaks. The peculiarities of excitation in the condition of direct dislodging and the actions of other primary ions sputtering and scattering mechanisms are also not taken into account. Thus, full classification should take into account the above mentioned moments, including all possible micro-processes during the interaction of primary and secondary atomic particles with the sub-surface field of the analyzed volume and with the surface. At first, however, let's try to systematize the conceptions about ion formation processes in the conditions of cascade sputtering mechanism.

4.4.2 Microprocesses, responsible for ion formation

For the ease of explanation let's accept the following scheme (Fig. 4.9).

Let's symbolically break the space, where the processes, responsible for ion formation, take place, into 4 fields: A – near-surface field of solid volume, in which the collisions cascade is developing; B – solid surface (by the term "surface" in this part we will imply the plane, which passes through the balance centers of nucleus of the atomic layer); C – near-surface field of the vacuum (~ 10 Å); D – vacuum.

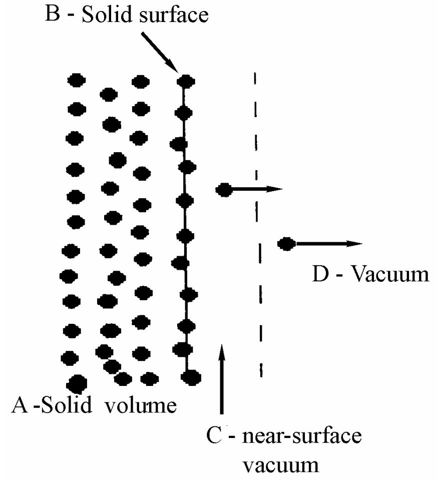

Fig. 4.9. Scheme of the typical fields of ionization processes.

The process of ion formation includes several stages, each of which comprises microprocesses, which differ significantly in each A–D fields. Let's state peculiarities of each field A–D, significant for micro processes: <u>*Field A:*</u> excitation of atoms is possible as a result of non-elastic atom-atom and electron-atom interactions; <u>*Field B:*</u> the collisions cascade is finishing, the excitation is possible as a result of last pair interaction; <u>*Field C:*</u> as a result of electron interaction of surface with the leaving particle the condition of the latter may change; <u>*Field D:*</u> atoms doesn't interact with anything, although the spontaneous decay of excited atom and multi-atomic ions conditions is possible together with the decay of cluster and molecular ions with the formation of mono-atomic excited and ionized particles.

It is obvious that each of these fields has its specific character depending on the type of bonds in the solid (metal, semi-conductor, dielectric). Microprocesses, which are being considered in this part, usually refer to metals. The fragmentation of the complex process of ion formation on the microprocesses and stages is one of the existing ways of describing this phenomenon, and due to the fragmentation of the ion formation process into its components, each possessing its formalities, let's call this phenomenon *differential*. Using another approach the task of ion formation description is solved in the framework of a single formality, which takes into account the simultaneous action of microprocesses. As the microprocesses are generalized (summarized), let's call this approach *integral*.

During the cascade mechanism of sputtering the primary ions are moving in sequence through the fields A–D. It is obvious that in each of the fields they are exposed to electromagnetic influences of various configurations from environment. These influences may result into alterations of atom conditions at the definite moments. Possible microprocesses, which result into the change of the atom condition in each of the mentioned fields might be classified in the following way:

Microprocesses in field A (*inside the solid near to the surface*).

By now the following possible processes may occur in this field:

A1. Formation of the hole on atoms internal shells. It is considered that this microproces is the beginning of so called *kinetic ionic emission*. Its essence is that the atom with the hole on the internal shell (with the relatively long lifetime) may leave the boarders of the solid together with the conduction electron, which neutralizes it. After that in field D the relaxation of the hole wit the conduction electron may occur. Thus, the process equal to Auger process - in the atom of the solid, is happening in field D. The energy, extracted during the relaxation might be transmitted to another atom electron, as a result of which ionization of atom outside the metals takes place.

A2. The processes of atoms excitation in the cascades of collisions as a result of non-elastic *atom-atom* and *electron-atom* interactions. There is a number of grave theoretical arguments against possibility of observation of such processes impact into the secondary atoms excitation. The most fundamental are the following: a) the radius of the excited atom is too big to correspond to the inter-lattice radius; б) excitations (especially the short-living ones) are quickly removed as a result of Auger relaxation. Both these arguments make the theorists either transmit the feeding point to the distances close to the surface and to the surface or observe the transmission process from the first generation cascades (where due to the greater relative energy of the colliding atoms the probability of excitation is higher, than in the following generations) towards the final collision. Such process may be carried out through the chain of quasi-molecular conditions, which occur as a result of succession of collisions in the separate cascade branch.

Microprocesses in field B (*on the surface*).

This group of processes is conditioned by the succession of binary and ternary collisions of surface atoms, primary ions, and atoms of collisions cascade in the subsurface field.

B1. In the non-elastic binary collision of the cascade atom with the surface atom the last gets the impulse from the cascade atom in the direction surface → vacuum, as a result of which it leaves the solid in the excited state. The description of the process itself is complicated by the “ambiguity” of the surface atom condition (it’s neither in the solid nor in the vacuum), so the excitation is described on the basis of the results of excitation probability examination in the non-elastic collisions in gas phase. At the same time we assume that changes in the internal state of the colliding particles are the result of electron exchange in the process of collision.

There is also interpretation of ion formation as a result of the collision, due to which the ion leaves just because according to the pattern of the solid by Zommerfeld all atoms inside the solid are ionized. The formation of neutral particles and a very small number of ions among the sputtered particles are explained by the fact that probability of ion neutralization in the field B is close to one. (Fig. 4.9), as the ion creates a potential well without the barrier for electrons of metal conductivity in this field. The problem of ion neutralization near the surface of metals is considered in details in part 6.3.

B2. This is the process, where the impulse of the cascade atom is transmitted simultaneously to two adjacent surface atoms, so that they enter vacuum in the bound state. By now, concerning the formation of excited and ionized atoms, this process is not studied well enough, although it is obvious that it might be described in approaching of molecular orbitals (as the breakdown of the quasi-molecule in the vacuum) or in approaching of pair collisions in the gas phase.

B3. This is the process, where the primary dislodged atom leaves the vacuum, being sputtered on the one of the adjacent target atoms. This atom excitation is possible both in the process of interaction with the primary ion and in the process of scattering. In the last case the description is the same as in B1.

The interaction of atom with the surface and microprocesses in field C (*near surface field of the vacuum*)

Cascade atom, which enters vacuum from the internal or subsurface layer of the solid, while passing through the surface gets to the field, which is characterized by special configuration of electromagnetic fields. The specific configuration of fields is conditioned by the forces of interaction between atom (or ion) and the surface, they are: а) *forces of mirror image*; б) *forces of Van der Waals* (*orientation, induction, dispersion*); в) *forces, conditioned by exchange and correlation interaction of electrons* at such distances between the atom nucleus and the surface, when there is no full detachment of the complex system "atom+surface" into two systems (atom and surface).

For the definite atom in various distances from the surface the relative influence of these forces is different. The values of these forces depend on peculiarities of electron structure of the surface and on the electron structure of the atoms shells. The major difficulty of formation of excitation and ionization theory lies in the great variety of electron structure of surfaces and atoms. The fact that sputtered particles have a wide energy spectrum (from hundredth parts up to hundreds and even thousands of electronvolts) plays an important role in the emergence of great variety of patterns of excitation and ionization in the field C. This role is determined by the correlation of sputtered particle rate and electrons rate on the Fermi level of the solid, i.e. by the "adiabatic" movement of sputtered particle. If the atom rate is much less than “Fermi rate” its electron shell transforms entirely according to the changing distance from the surface. Then electron configuration of the atom may be considered as an independent one from the atom’s rate, here people say that adiabatic conditions of movement are fulfilled. The wide spectrum of kinetic energies (rates) of the secondary atoms results into the need to take into consideration the wide spectrum of excitation probabilities depending on the adiabatic movement of atoms.

Logically, we should start theoretical description of atoms movement in the field C from the consideration of electron configuration of the atom, which is near the solid surface, to be more precise, from the electron configuration of the system “surface + atom” Let’s discuss the modern solution of this problem in details.

Main properties of an atom, interacting with the surface on the fixed distance, are estimated by the method of density functional, which is used in the theory of non-homogeneous electron systems. A well-known pattern of jelly is accepted as a surface, i.e. it is considered that the atom interacts with homogeneous infinite gas with the density which is equal to the density of the solid. The equations of the system condition, which include both electrostatic and exchange and correlation forces are solved self-consistently. The calculations have approved the before known affirmation that the discreet levels of the atom, interacting with the system, whose electron conditions represent continuum, also become continuum, widening in their resonance. The form of the continuum for three atoms, varying by their electronegative character, is represented in Fig. 4.10. It can be seen that, for instance, conditions, corresponding to *3p*-resonance of chlorine, are placed under the level of Fermi and thus should be occupied, and conditions, corresponding to *2s* - resonance of *Li* should be empty. *3p* - resonance of silicon is close to Fermi level, that is why this resonance swings the Fermi level, which facilitates formation of more covalent bonds of silicon with metal, than of ion ones, unlike chlorine and lithium, which either repulse

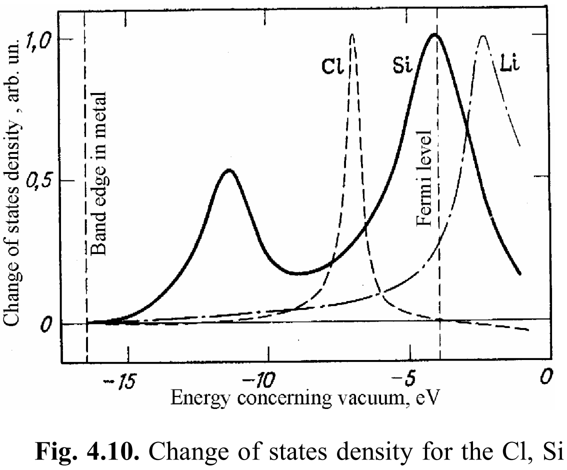

Fig. 4.10. Change of states density for the Cl, Si and Li atoms during their adsorption on the jelly. On the curve for Si we can see resonance levels, induced both by 3s- and 3p-conditions.

(lithium) or attract (chlorine) the electron of a metal.

In Fig. 4.11 we can see the outlines of constant electron density, which crosses the metal surface at right angle at the center of the atoms of *Li, Si, Cl,* which characterize three types of fundamental bonds. In the upper row there are outlines of electron density for three systems. The differences of the curves of equipotential lines of *Li* and *Cl* are attracting much attention. Lithium, having small electro negativism, attracts the electrons, which results in bending the equipotential of metal electrons towards lithium atom. The opposite is true for chlorine. Silicon is characterized by greater penetration of equipotentials bound with the atom into metal, in comparison with lithium and chlorine. All three cases are characterized by the fact that the outlines are acquiring purely metallic features at the distances, which don't surplus the atoms sizes.

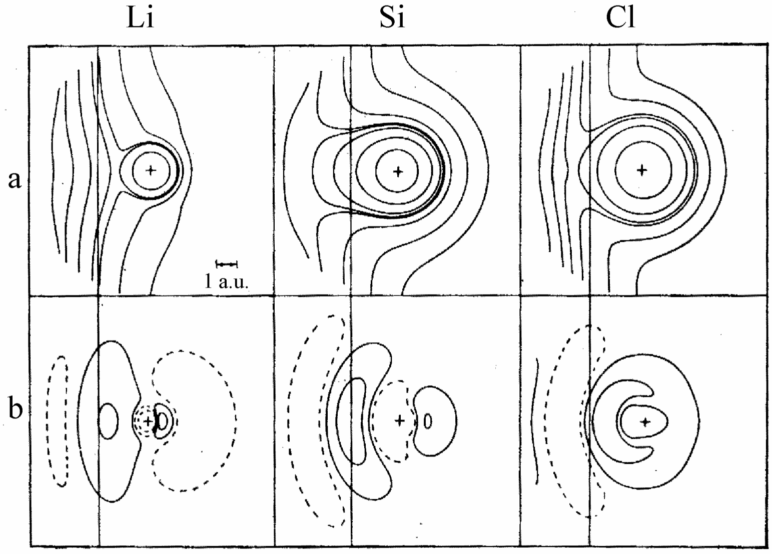

Рис. 4.11. Lines of constant charge density during the adsorption of atoms of Cl, Si and Li on the jelly: *a* – full charge; *б* – induced charge. Solid (dotted) lines indicate the surplus (lack) of electrons.

The charge transformation, concerning the "atom-surface" interaction can be seen in more details in the lower row of the figures, which represent the outline maps of the difference between electron density of the "metal-atom" system and super-position of densities of the metal and the atom (i.e. they illustrate only those atomic electrons, which shifted from the vacuum into the field between the metal and the atom). The outlines, indicated by solid lines, show the fields of charge accumulation, and the dotted ones – the fields of charge depletion.

The above mentioned illustrations make it obvious that the details of microprocesses of electron exchange between the atom and the surface should greatly depend on the definite combination "solid-secondary atom", which in turn determines the details of the theoretical description of the ion formation process (which represent the disregard of some microprocesses for the others). Among the microprocesses of electron exchange the non-radiation Auger- and resonance processes are of special importance. These processes are classified in the works of Hagstrum. It is assumed that the intensity of these processes to a first approximation don't depend on the atom rate (v). That is why it is considered that the atom is at some distance l from the surface. If ε_0 – is the major state of the atom, ε_f - the metal energy of Fermi, ε_i – the energy of excited state, so under the condition $\varepsilon_0 < \varepsilon_f < \varepsilon_i$ the following processes are possible:

1c) Resonance ionization (RI) of the atom by tunneling the electron from the excited level ε_i of the particle to the vacant level of the metal conductivity zone;

2c) Resonance neutralization (RN) of the ion – tunneling of the electron from the occupied level of the metal to the level ε_0 of the atom major state;

3c) Auger-neutralization (AN) of ion – transition of the electron from the conductivity zone on the level ε_0 of the atom with the transmission of liberated energy to the other electron;

4c) Auger relaxation of atom excitation (AD) with exchange – transition of the electron of the metal conductivity zone to the level ε_0 of the atom with the transmission of liberated energy to the electron at the excitation level ε_i;

5c) Auger relaxation of atom excitation without exchange, i.e. non-radiative transition of the atom from ε_i to ε_0, and transmission of the energy surplus to the electron of the metal conductivity zone.

For ion-photon emission the following microprocesses, taking place in the final distances between the atom and surface, might be of great importance:

6c) transition of the electron from the metal conductivity zone to the excitation level of the atom;

7c) transition of the electron from the atom major state to the excited one.

Microprocesses in field D

After the discontinuance of electron interaction between the atom and the surface, i.e. after the transition of the atom from field C into field D (Fig. 4.9), the spontaneous processes of relaxation of secondary particles excited states become possible together with electron and photon emissions, the breakdown of molecular and cluster complexes. Let's distinguish only those microprocesses, which may lead to formation of ionized atoms:

1d) Auger-relaxation of overexcited atom;

2d) ion dissociation of diatomic and of more complex molecules and clusters.

4.4.3 Patterns of secondary atoms ionization in the conditions of sputtering due to the atom collisions cascades

In this part we consider the ways of designing patterns, which are to describe the ion formation process when the atoms leave the surface due to the electron exchange in the conditions of cascade sputtering. Such patterns explain a great number of well-examined laws of metals and semiconductors SIE. It particularly concerns the dependences of ion formation probability upon the electron work function (φ), upon the atom rate, and emission angle.

The problem of ion formation in such patterns is considered in two aspects: first, there is a need to describe the process of charge exchange between the atom and the surface in order to determine the ion formation probability, second, there is a need to take into account the influence of surface excitation due to secondary ions activity on the ion formation probability. These aspects are interrelated, as a result of which serious problems are emerging while solving the task of ion formation. A significant success has been achieved in understanding the process of charge exchange, but the second aspect is taken into account only as simple corrections in the form of surface distortion. Let's consider in details the most wide-spread and the most general for metals and semiconductors approach to the description of ion formation probability, as a result of electron exchange in the system "leaving atom – surface". Later for brevity let's call the patterns, based on such approach, the patterns of electron exchange (MEE). The basic suppositions for designing MEE (not taking into account the effect of surface excitation by the primary ions) are the following:

I. The metal (semiconductor) surface is supposed to be smooth without transverse heterogeneities. Electron gas (for the description of the solid the Sommerfeld pattern is used) is characterized by the Fermi level ε_f (for metals) or by the energy value of the level, which corresponds to the bottom of conductivity zone (for semiconductors). The work function of outlet Φ is determined as the difference between ε_f and vacuum level. All electron excitations of the surface, generated by primary ions, are supposed to dissipate fast, so that electron temperature is equal to zero.

II. The sputtered atom is supposed to be a single-level one with level energy ε_a, which is ionization (or valency) level for the positive ion or the level of electron affinity for the negative one. Due to electron metal screening, level ε_a is shifted up or down according to its position in the free atom, depending on the electronegative character of the element and is widened.

III. Electron exchange in the system "atom-surface" is considered with the use of various modifications of time dependant electron Hamiltonian, without taking into account the exchange and correlation forces. The failure to take these forces into account is the weak point of this theory and presents the difficulty which hasn't been overcome yet. In the concepts of secondary quantification the electron Hamiltonian of the system may be written down in the following way:

$$H(t)=\sum_k \varepsilon_k n_k+\varepsilon_a(t)n_a+\sum_k\left[V_{ak}(t)c_a^{+}c_k+c.a.\right], \tag{4.42}$$

where the first and the second components represent the energies of the electrons in the solid and in the atom correspondently, the third – is the energy of interaction between the atom and the surface. Indexes k and a correspond to the levels $|k\rangle$ and $|a\rangle$, $n_k=c_k^{+}c_k$, $n_a=c_a^{+}c_a$ – the operators of electron number at the levels $|k\rangle$ and $|a\rangle$, *c.a.* –complex affinity.

The probability of positive ion formation (α^{+}) is calculated in the following way: one minus probability of level filling $|a\rangle$ (i.e. of the ionization level) during the time of interaction between the atom and the surface. The probability of negative ion formation (α^{-}) is calculated as the probability of filling of the level of atomic electron affinity during the time of interaction.

IV. The electron may pass from the level $|k\rangle$ in the solid to the level $|a\rangle$ in the atom with the probability, determined by the value of the matrix element

$$V_{ak}(z)=\langle k|V|a\rangle, \tag{4.43}$$

z – distance between the atom and the surface, V – interaction potential. The value of level widening $|a\rangle$ is determined by the lifetime (τ) of the electron at this level. In accordance with the principle of uncertainty the half-width of the level $|a\rangle$ might be determined as

$$\Delta(z)=\pi\sum_k |V_{ak}|^2\,\delta(E_k-E_a(z)) \quad . \tag{4.44}$$

Good approximation for $\Delta(z)$ may be presented by such dependence

$$\Delta(z)=\Delta_0 e^{-(\gamma\pm)z}, \tag{4.45}$$

as the wave function $|k\rangle$- of the condition decreases exponentially with the distance. Here $\gamma\pm$ is constant, which characterizes the interaction length between the atom and the surface during the formation of positive (+) and negative (-) ions, the order of magnitude γ~10^{-10} m. Δ_0~1 эВ – the level width in the desorbed condition of the atom. The probability of transition $|k\rangle \rightarrow |a\rangle$ is the value reciprocal to time $\tau(z)$ and is calculated in the following way

$$w(z)=1/\tau(z)=2\,\Delta(z)/\hbar\,, \tag{4.46}$$

V. The trajectory approach in the consideration of atom movement close to the surface is used in the calculations. However, introduction of the parameter t instead of parameter z significantly facilitates the calculations. Transition from z to t is accomplished with the help of correlation

$$z(t)=v_{\perp}t,$$

where $v_{\perp}$ - component of the atoms rate, perpendicular to the surface. This correlation doesn't take into account the influence of the surface real repulsive potential on the atom's trajectory. Taking into account this potential we have the following dependence:

$$z(t) = vt + \frac{1}{\gamma^{-}} \ln \frac{\left[1 - k' \exp\left(-\gamma^{-} vt\right)\right]^{2}}{\text{Б}} \tag{4.47}$$

where
$$\text{Б} = \frac{2k'mv^{2}}{\Phi - A + \varepsilon_{\epsilon}(0)} \tag{4.48}$$

$$k' = 1 - \frac{v(\sqrt{m^{2}v^{2} + 2m(\Phi - A + \varepsilon_{\epsilon}(0))} - mv)}{\Phi - A - \varepsilon_{\epsilon}(0)} \tag{4.49}$$

where A – energy of electron affinity for this atom, Φ – work function of electron leaving the surface.

VI. Dependence of the potential of interaction between the atom and the surface on the distance between them is represented by time dependence, usually in the following way

$$\begin{array}{lll} V(t)=VU(t) & t \geq 0 & \text{(4.50a)} \\ V(t)=V & t < 0\,. & \end{array}$$

If the trajectory (4.24) is used in calculations the $U(t)$ is presented by the exponent:

$$U(t)=exp[-\gamma^{\pm}z(t)]=\exp(-\gamma^{\pm}v_{\perp}\, t) \tag{4.50б}$$

VII. Depending on the distance between the atom and the surface, the displacement of energy of level $|a\rangle$ is assigned in the form of linear function when considering the positive ion formation:

$$\varepsilon_{a}(z)=\varepsilon_{F}+b(z-z_{c}) \tag{4.51}$$

or in the following form

$$\varepsilon_{a}(t)=\varepsilon_{a}(\propto)+[\varepsilon_{a}(0)-\varepsilon_{a}(\propto)]\exp(-2\gamma^{+}vt), \tag{4.52}$$

where b – is constant, which determines the inclination of the atom trajectory towards the axis z; z_{c} – coordinate z of the point of intersection of level $|a\rangle$ with the Fermi level. While considering the negative ion formation in the number of articles the following function was used

$$\varepsilon_{a}(z)=-(\Phi-A+\varepsilon_{a}(0))\exp(-\gamma^{-}z)+(\Phi-A)\,, \tag{4.53}$$

where A – is the energy of electron affinity to the atom.

For calculation of $\alpha^{\pm}$ taking into consideration the factors, mentioned in points 1-7 various semi-classical methods of calculations, the device of time-dependent perturbation theory, and the device of secondary quantification are used. The possible processes *at small distances* between the atom and the surface (i.e. when $\varepsilon_{a}<\varepsilon_{F}$) are resonance transitions from conditions $|k\rangle$, which are positioned below the Fermi level, to the web level $|a\rangle$ (as all conditions $|k\rangle$ are occupied). *At the greater distances* the tunnel transitions $|a\rangle \rightarrow |k\rangle$ are possible. At distances $z<z_{c}$ ($\varepsilon_{a}>\varepsilon_{F}$) nonadiabatic transitions from the atom level to the un-occupied levels $\varepsilon_{k}>\varepsilon_{F}$ are possible; at the distances $z>z_{c}$ ($\varepsilon_{a}<\varepsilon_{F}$) resonant filling of unoccupied positions $|a\rangle$ may happen. Imposing definite requirements for the parameters values ε_{k}, ε_{a}, V_{ak}, Δ at the point z=0 (or t=0), we may calculate the probabilities of ion formation with the presence of some combination of microprocesses, described above (see "microprocesses in field "C""), neglecting the others. In the considered patterns, as a rule, we neglect the probability of high-energy excitations, i.e. Auger processes. Such neglect in favour of resonance processes and the use of dependences (4.44), (4.45), (4.50)–(4.52) result into the following equation for the ionization probability.

$$\alpha^{\pm} = \exp\left(-\frac{2\Delta(z_c)}{\gamma^{\pm} v_{\perp}} \right). \tag{4.54}$$

The pivotal role in (4.54) is played by the value $\Delta(z_c)$ – the resonance width of ionization level in the moment of intersection of $\varepsilon_a(z)$ with Fermi level.

If the sputtered atom on the infinity has the valence level with energy I lower than the vacuum one and if it is at the same time in non-interaction condition $I>\Phi$, then

$$\varepsilon_a(\infty) - \varepsilon_F = I-\Phi \tag{4.55}$$

However, as the image forces in this case lift the ε_a close to the surface, the following equation (written down in atomic units) becomes true:

$$\varepsilon_a(z) - \varepsilon_F = \Phi - I + \frac{1}{4(z - z_{im})}, \tag{4.56}$$

where z_{im} is the coordinate of the image plane.

Taking into consideration (4.56) we obtain:

$$\alpha^{+} = \begin{cases} 1 & \Phi \geq I \\ \exp[-\mathit{Д} \exp(-\frac{\gamma}{4(I-\Phi)})], & \Phi < I \end{cases}, \tag{4.57}$$

where $\mathit{Д} = 2\Delta_0(\gamma v_{\perp})^{-1} \cdot \exp(-\gamma z_{im})$. Equation (4.57) is a simple generalization of equations (4.44), (4.46), (4.50), (4.54), (4.55), (4.56).

If parameters Φ, I, A, ε_F are determined with respect to the vacuum level, then in the generalized form the probabilities of atom's acquiring the charge may be approximately written down in the following way:

$$\alpha^{+} = \exp[-(I-\Phi)/\varepsilon_0], \tag{4.58}$$

$$\alpha^{-} = \exp[-(\Phi-A)/\varepsilon_0], \tag{4.59}$$

where $\varepsilon_0 \sim v(z_c) \cdot \mathrm{Cos}\,\theta$.

Consideration of surface distortion

Effects of surface distortion during the ion bombardment include the displacement of atoms in the surface layers, generation of electron excitation, and also physical and chemical consequences of the atom leaving the surface. Electron excitations, generated by the ion bombardment in the solid, occur, first as a result of Coulomb interaction of the primary atom with electron system of the solid, and second, as a result of atomic collisions in the cascades. By now the attempts have been made to take into consideration the influence of electron excitations and atoms movements on the ionization probability. Let's take the series of Shroubeck's articles as an example. In present articles for the description of electron gas an additional parameter, corresponding to the temperature of electron gas – T_s is introduced. For the description of ionization probability semi-classical method, based on the use of interaction potential the same as in (4.42) is used, and for the description of temporary dependence of charge value (p) on the atom (in case of positive ion formation) the relaxation equation of the following type was used:

$$\frac{dp}{dt}=\frac{[p(t)-p_0(t)]}{\tau(t)}\,, \tag{4.60}$$

where $\tau(t)$ –time of relaxation –identical to lifetime in (4.23):

$$\tau(t)=(h/2\Delta)\exp(2\gamma vt), \tag{4.61}$$

$$p_0=\exp[-(\varepsilon_F-\varepsilon_a(t))/kT_s]. \tag{4.62}$$

Meaning of p_0 – value of equilibrium positive charge at the time t. The solution of equation (4.60) results into:

$$p(\infty)=\alpha^+=\left(\frac{\hbar\gamma v}{\Delta}\right)^{a\delta/\,2\gamma vkT_s}\exp\left[-\frac{\varepsilon_F-\varepsilon_a(0)}{kT_s}\right], \tag{4.63}$$

where $\delta=\varepsilon_a(0)-\varepsilon_a(\infty)$. Correlation (4.63) is derived by neglecting the nonadiabatic transitions and provided that

$$\begin{array}{ll} \varepsilon_a(t)=\varepsilon_a(0) & t<0 \\ \varepsilon_a(t)=\varepsilon_a(0)-[\varepsilon_a(0)-\varepsilon_a(\infty)]at & 0\le t\le 1/b \\ \varepsilon_a(t)=\varepsilon_a(\infty) & t>1/b. \end{array} \tag{4.64}$$

At high temperatures T_s

$$\alpha^+=\exp[-(\varepsilon_F-\varepsilon_a(\chi_0))/kT_s], \tag{4.65}$$

where $$\chi_0=\frac{1}{\gamma}\ln\left[\frac{\Delta_0}{\hbar\gamma v}\right].$$

The difference between the resonance-exchange pattern, described above, and Shroubeck's pattern consists in the following:

First, dependence α^+ on v, in correspondence with (4.65), is described as

$$\alpha^+\approx v^{[\varepsilon_a(\infty)-\varepsilon_a(0)]\Gamma/\gamma kT}, \tag{4.66}$$

here Γ^{-1} – distance at which ε_a changes from $\varepsilon_a(0)$ to $\varepsilon_a(\infty)$. Thus, Shroubeck's pattern presents power dependence α^+ on v, which at real rates of v is not worse than exponential dependence, corresponds to the experiment.

Second, in Shroubeck's pattern the adsorbed atoms field is interpreted as the energy step. If for the measurement of Φ we introduce the layer of adsorbed atoms with the width $(\Gamma')^{-1}$for some value $\delta\Phi$, then α^+ from $\delta\Phi$ will be changing in the following way:

$$\alpha^+\sim\exp\left[\frac{\delta\Phi\Gamma'}{\gamma kT_s}\ln\left(\frac{2\Delta_0}{\hbar\gamma v}\right)\right], \tag{4.67}$$

i.e. in the same way as in resonance-exchange pattern.

Third, α^+ in the Shroubeck's pattern depends on the size of the sputtered atom, similar to the resonance-exchange pattern (the size of the atom is directly related to the energy of electron affinity). If we assume that in resonance-exchange pattern condition ε_a, crossing ε_F, is not occupied, then at $T_s=0$ values α^+ coincide in both patterns. Thus, in this case resonance-exchange pattern represents an extreme case of Shroubeck's pattern at $T_s=0$. In case when ε_a is occupied, we can't establish the relation between these patterns. Shroubeck's pattern doesn't conform to the experiment (unlike the resonance-exchange one) in the part, which concerns probability α^- ; since formation of α^- in this pattern is entirely equal to the formation of α^+, if we consider hole excitation instead of electron excitation.

A direct experimental fact, which proves the influence of excited surface on $\alpha^{\pm}$, is dependence of $\alpha^{\pm}$ on the energy of primary ions E_0. Strong dependence α^+ on E_0 was observed in the number of experiments for the Si^+ ions from silicon and Ga^+, As^+ ions from gallium arsenide. This dependence for metals is weak. This can be explained by the fact that electron-hole excitations in semi-conductors have the energy, higher than that in metals.

Calculations T_s, on the basis of excitations in the cascade of atomic collisions give greater value than that of metals. However these calculations give practically no dependence of T_s on E_0; according to them T_s is not homogeneous in the field of cascade development. Thus, the problem of influence of substrate excitation on $\alpha^{\pm}$ is far from being solved.

Summarizing all above mentioned we have to emphasize that the theory of formation of $\alpha^{\pm}$ on the basis of the conception about electron exchange between the leaving atom and the surface requires for its accomplishment, firstly, taking into consideration the correlation and exchange interaction of electrons, secondly, taking into consideration the influence of surface distortions on $\alpha^{\pm}$, which are caused by ion bombardment. At the same time, taking into account the results of multifold testing of the above mentioned patterns, we may state that these patterns give right dependences of ionization probability on such important experimental parameters as sputtered atom rate, work function of the electron outlet from the surface, potential of atom ionization.

4.4.4 Pattern of bond breaking

In the previous part the surface of the solid was considered as gas of free electron. This implies that electron exchange pattern s may be used only for the analysis of ion formation in case of metal and semiconductors sputtering with the low bond ionicity. For the description of ion formation during sputtering of compounds with predominantly ionic bonds a pattern, based on concepts of bond opening between sputtered atom of the metal and its bond partner – electronegative atom, which is placed on the surface of such compounds, was proposed in middle 1960s. This pattern was called "Pattern of bond breaking" (PBB). Initially PBB was proposed for the description of chemical effect in the secondary ionic emission. Let's consider the last developments of this pattern in details.

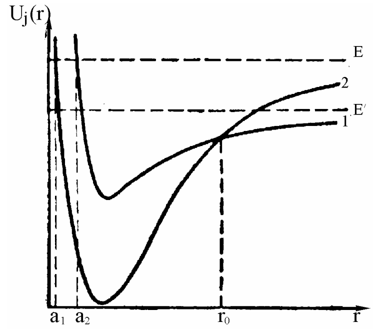

Рис. 4.12. Curves of a potential energy for two electronic terms of a molecule

The description of the mechanism of bond opening is based on the analysis of the process of charge exchange during atomic collisions. At the same time technique, proposed by L.D. Landau in 1930-s is used, it was modified for the case of bonds "surface- atom" and "surface–ion" and is based on the analysis of changes of the states of diatomic molecule.[2] The essence of this technique consists of the calculation of probability of change of the molecule states, including bound and unbound states (i.e. probability of molecule dissociation). For visualization we use the pictures of curves crossings of potential energy dependence on the distance between the nuclei for the molecule electron terms. (Fig. 4.12).

The probability of change of the state, which is characterized by one of the above mentioned

---

[2] You can find out more about this technic from the fundamental course: L.D. Landaw, E.M. Lifschitz //Quantum mechanics. - M.: Science. – 1974. – 752 p.

curves, into the state, which is characterized by other curve, is calculated in the cross point of these curves (if there is any) using the methods of excitation theory. The general formula for this probability is the following

$$w = \frac{2\pi}{\hbar}\left|\int \chi_2^* V(r)\chi_1 dr\right|^2, \tag{4.68}$$

where $\chi = r\cdot\chi_{\text{nucl}}$ (χ_{nucl} – wave function of nuclei radial motion); χ_1, χ_2 depend on the rate of radial relative motion of nuclei of the atoms in the molecule in the cross point $r=r_0$, (see Fig. 4.12) terms 1 and 2; $V(r)$ – excitation energy.

By analogy with the above said the bond opening and ionization of the atom sputtered on the surface is considered in the following way. Let us have a sputtered neutral atom M^0 and a positive ion M^+, which abandon surface X. We will consider charge exchange between M^0 (or M^+) and X as taking place in the crosspoint of the potential energy curves of the system M^0+X^0 (curve 1 Fig. 4.12) and M^++X^- (curve 2 Fig. 4.12). Symbol X^- corresponds to the vacancy on the place of the abandoned sputtered atom, which captivated its (of the sputtered atom) electron, as the result of which there was atom tonisation X^0 symbolizes surface condition if there is no ionization of the sputtered atom. In other words, the ionization of the sputtered atom can be described as the transition of the "atom-surface" system from state $|1\rangle$ into state $|2\rangle$ under the influence of some perturbation, which can be compared, according to the results of the perturbation theory, to such matrix element of transition H_{12}, that probability of the mentioned transition (that is probability of sputtered atom ionization) might be calculated in the following way:

$$\alpha^+ = \exp(-2\pi H^2_{12}/v|\xi|), \tag{4.69}$$

where v – velocity of the sputtered atom in point r_0; $|\xi|$- difference of the first derivatives $U(r)$ along r in point r_0. Subsequent calculations of value α^+, is theoretically multiversion. Let's be logical. Since covalent forces between neutral atom and the surface are short-term ones, in point r_0 we can admit that U does not depend on r (curve 1, Fig. 4.12). Forces, that form curve 2, are the forces of the Coulomb attraction between M^+ and negatively charged vacancy M^-. On the infinity ion curve 2 s above covalent bond of curve 1, whereas energy difference between them equals value $I\text{-}A^v$, where A^v- electron affinity of cationic vacancy. The given energy difference in point r_o compensates the Coulomb potential (i.e. in point r_o if U doesn't depend on r for covalent curve 1 there exists an obvious balance of $I\text{-}A^v$, on the one hand and energy of Coulomb attraction between M^+ and X^-, on the other hand. Hence, distance r_o in atomic units is expressed as $(I\text{-}A^v)^{-1}$. For the sputtered atom with mass M_2 and kinetic energy E_κ, v and $|\xi|$ have in point r_o the following values (in atomic units):

$$v(r_0)=[2(E_\kappa+I-A)/m]^{1/2},\ |\xi|= r_0^{-2} \tag{4.70}$$

Taking into account the above said the matrix transition element may be chosen in the following way:

$$H_{12} = \frac{r_0}{8}\Psi_1\left(\frac{r_0}{2}\right)\Psi_2\left(\frac{r_0}{2}\right), \tag{4.71}$$

where Ψ_1, Ψ_2 – normalized wave functions of electron in conditions $|1\rangle$ and $|2\rangle$, which correspond to curves 1 and 2 in Fig. 4.12. The electron condition in the neutral atom corresponds to function Ψ_1, electron in the cationic vacancy corresponds to function Ψ_2. If to consider metals atoms as sputtered particles, than, due to the fact that external electrons of the metals atoms are *s*- electrons, we may use water-like wave functions as Ψ_1, expressed in the form, which permits the introduction of ionization potential for atom I:

$$\Psi_1(r)=2\kappa^{3/2}e^{\text{-кг}}\text{, где }\kappa^2=2I\,. \qquad (4.72)$$

As we know very little about vacancies during sputtering, than for the first approximation for Ψ_2 we may use a combination of spatial dependence of the wave function of electron, which belongs to a negative ion, in the field of a positive ion, and of amplitude parameter C:

$$\Psi_2(r)=\left(\frac{R}{R-r}\right)^{1/\gamma_\kappa} C\frac{(2\gamma_\kappa)^{1/2}}{r}\exp\left(-\gamma_\kappa r-\frac{r}{R\gamma_\kappa}\right), \qquad (4.73)$$

where R – distance between sputtered atom and its vacancy, $\gamma_\kappa^2=2$ Å.

It can be easily seen that formulas (4.69)–(4.73) allow to calculate α^+ on the stipulation that we know the values of parameters C and A^v.

Formula (4.69) is true in that case if states $|1\rangle$, $|2\rangle$ are not degenerated, in other case this formula should be written down in the following form

$$\alpha^+=G\exp\left(\frac{-2\pi H_{12}^2}{v|\xi|}\right)_{r_0}, \qquad (4.74)$$

where $G\approx g_+/g_0$; g_+, g_0 – degrees of degeneration of states $|2\rangle$ and $|1\rangle$ correspondingly.

While comparing PBB with an experiment we may mention sufficient correspondence of this pattern to such dependencies as $\alpha^+(E)$ and $\alpha^+(I)$, and also to the dependencies of chemical and isotopic effects in the secondary ion emission. Values of parameters *C and* A^v, defined by method of adjustment, for such elements as B, Mg, Al, Nb, Mo and elements of the 4th period of the periodic table with external 4-s electrons, are close to values A=1.463 (value of the electron affinity of oxygen), and C=0.25.

4.4.5 Thermodynamic description of ionization and excitation processes.

The question of excitation and ionization of secondary particles in conditions of thermal peaks is related to the thermodynamic approach (TDA) to the excitation and ionization in the secondary ionic and ion-photon emission, which started its development earlier without relation to mechanisms of sputtering.

By now in the applied and fundamental works, which are based on the implementation of TDA we may distinguish 4 directions, which differ by the details of the used conceptions. Let’s analyze these directions and show that they all are exploiting the ideas of the non-equilibrium statistical physics.

Direction 1.

The beginning of TDA implementation in the problems of the secondary ion emission is usually related to the works of 1973, where on the basis of observed dependence of the secondary atoms (α^+) ionization degree on their ionization potential (I), which is expressed in the following way $\alpha^+\sim\exp(-I/K)$ (K – constant), for the description of the secondary ions outlet it was proposed to use Sakha’s equation, which describes ionic balance in hot plasma:

$$\frac{N^+N_e}{N_0}=\left(\frac{2\pi}{\hbar^2}\cdot\frac{M^+M_e}{M_0}kT\right)^{3/2}\frac{B^+B_e}{B_0}\exp\left(-\frac{I}{kT}\right) \qquad (4.75)$$

or the Sakha-Erger equation, which differs from (4.75) by the substitution of $I\to I+\Delta I$ (ΔI – normalizing of Debai-Khunkel). In (4.75) N^+, M^+, N_e, M_e, N_0, M_0 – are concentrations and masses, of correspondingly ions, electrons, and neutral atoms in plasma; *h, k* – Plank and Boltzmann’s constants; B^+, B_e, B_0 – statistical sums of ion, electrons, and neutral terminals states, T – plasma temperature. Implementation of (4.75) for the explanation of values α^+ and the number of regularities of their changes resulted into the necessity to use the idea of formation (in the process of interaction of primary ion with surface) of plasma-like local equilibrium state in the limited subsurface area. Hence there was a need to consider N_e and T as adjustment parameters, and their values remained so, that this plasma had to be dense (N_e~10^{23} sm^3) and hot (T_0~10^4 K). The above mentioned idea together with (4.75) comprised the basis for such called pattern of local thermodynamic balance (LTB) in the secondary ionic emission. This pattern was many times successfully examined and implemented in the problems of secondary ionic and ionic photon emission. For ionic photon emission (4.75) is easily transformed into ratio:

$$J_{qp} = A_{qp}\hbar\nu_{qp}N_b g_q Z^{-1}\exp\left(-E_q/kT\right), \tag{4.76}$$

where J_{qp} – intensity of atomic spectral line, A_{qp} – probability of transition from level q on the higher level p; $hV_{qp}=E_p-E_q$; E_p, E_q – energies of the levels; N_b – density of the excited atoms; g_q – degeneracy of level q; Z – statistical sum of the atoms conditions.

Direction 2

Established in 1950's fact of dependence of α^+ on the electron liberation from surface (φ) in the form $\alpha^+ \sim \exp(\varphi/K_1)$ (K_1 –constant) paved the way to using (4.75)instead of Sakha and Lengmur formula, which describes the process of surface ionization:

$$\alpha^+ = \frac{g_i}{g_a}\cdot\exp\left(\frac{\varphi - I}{\kappa T_e}\right), \tag{4.77}$$

where g_i and g_a – full statistical sums of the ions and atoms conditions. In some variants in (4.77), as in (4.75) there is a substitution $I \to I+\Delta I$, where ΔI is given the meaning of amendment I on the value of image forces energy. Formula (4.77), in contrast to (4.75), doesn't involve concepts of hot plasma, but requires thermodynamic balance between the atom abandoning the surface and the surface itself (to be more precise, between the electrons of the abandoning atom, electron gas of the solid and matrix array of the solid).

The given variant of TDA was many times subject to criticism, which stemmed from the proof of both the impossibility of the above mentioned balance in conditions of ionic bombardment of the surface, and the impossibility of temperature (T_e) increase up to several thousands degrees. At the same time T_e implied the temperature of the electron sub-system of the solid in the field of primary ion penetration. Acting in advance, let's point out that we can agree with this criticism concerning the impossibility of that kind of balance, but it is difficult to agree with the impossibility of values T_e ~$(1–10)\cdot 10^3$ K. The last is proved by the number of new works, in which the mentioned orders of values T_e are obtained on the basis of strict theoretical consideration of electron processes in atomic collisions cascades.

In the number of articles the attempts to develop directions 1 and 2 have been made by means of concretization of the spatial domain of plasma like state of the substance and those processes, which are responsible for LTB of this state. Thus we introduce near-surface range with linear dimensions 10–20 Å in which, according to the authors, such processes take place which form substance state, which information is held in parameters of the secondary ionic and ionic photon emission. Thus the possibility of special substance, which is called "quasi-free ("dense") ionic plasma", in the mentioned field is proved (taking into account the processes of defects formation in dielectrics). Its balance (or "quasi-iquilibrium") is guaranteed by competition between processes of generation and recombination of defects in the atomic collisions cascade. During cascade development the process of "adhesion" and "detachment" of free cascade atoms to the opened bonds may happen several times, and at the same time it may transform from kinetic state to the potential state of energy quantum, which equals to the binding energy of atom's in the lattice (E_b), that is why we can talk about temporal homogeneity of the process. Energy E_b according to the authors might be viewed as characteristics of the process, similar to equilibrium temperature in case of plasma or gas, and might be used for description of ionization degree, substituting kT for E_b in the equation of Sakha-Ergert. Numerator of the exponent in (4.77) is modernized according to the considered processes so that finally α^+ turns to be expressed through electronegativeness (X) and through the energy of the electron affinity (χ) of the atom:

$$\beta^+ = \frac{\alpha^+}{\alpha^+ + 1} = \frac{g_i}{g_a} \exp\left[-\frac{2(\chi - X)}{\alpha E_{св}} \right] \tag{4.78}$$

where $\alpha \sim 0.3 \div 1$ is the fudge factor for the renormalization of the chemical bonds. In other variant α^+ (of the occupancy of the levels) is determined by the processes of non-elastic electron-atomic collisions between the "thermal component" of electron ionic emission (EIE) and sputtered atoms, since the output of the very thermal component of EIE and sputtered atoms during the ionic bombardment coincide in time. The above mentioned range is located near the surface from the side of the vacuum so that the excitation and ionization processes in it are the same as if the gas of electrons with MAXWELL'S distribution along velocities was crossed by the sputtered atoms beam (distribution of atoms along velocities in this case is not defined concretely).

Direction 3

On the basis well-known empirical dependence α^+ on I and D_0 (D_0 –atomization energy) the best formula for quantitative analysis by means of mass-spectrometry of the secondary ions was proposed. Moreover it is more acceptable in the view of Non-equilibrium Statistical Thermodynamics. According to this formula:

$$\alpha^+ = \frac{g_i}{g_a} \cdot \exp\left(-\frac{I}{\kappa T_e} + \frac{D_0}{\kappa T_a} \right) \tag{4.79}$$

where T_a and T_e – correspondingly are the temperatures of sputtered substance atomization and registered atom ionization, introduced by analogy with quasi-equilibrium pattern for description of ionization in spark discharge plasma and laser torch.

Direction 4

This direction is based on the ideas of Non-equilibrium Statistical Physics.

Further we will talk not about, but about secondary atoms excitation, implying, that ionization is the excitation of atom in the continuous spectrum. So, coming in (4.79) from ionization probability α^+ to the relative occupancy of the levels (i.e. to the function of electron distribution along the atom's energy states), let's rewrite (4.79) into

$$f_n = f_0 \cdot \exp\left(-\frac{e_n}{T_e} + \frac{D_0}{T_a} \right), \tag{4.80}$$

where ε_n – energy of the level n, f_0 – normalization factor, which includes statistical sums of atoms states. Boltzmann's constant in (4.79) is omitted for brevity.

Let's compare (4.80) with non-equilibrium distribution function, which is widely used for description of occupancies of oscillating levels of the molecules in molecular kinetics, and in particular in non-equilibrium gas of the molecules

$$f_n' = f_0' \cdot \exp\left(-\frac{nE_1}{T_k} + \frac{nE_1 - E_n}{T_t} \right) \tag{4.81}$$

Distribution (4.81) is known as Treanor's distribution.

Comparison of (4.80) and (4.81) shows the coincidence of distribution functions along form, and, obviously, not along parameters meaning, including temperature ones. Distribution (4.81) presupposes the consideration of totality of energy levels of molecules as an independent sub-system with temperature T_k, which is located in thermostat, due to which molecule gas is emitted, which is understood as a hole with temperature T_t. Parameters E_1, E_n – are energies of the 1st and n-level of oscillator correspondingly, which pattern s the molecule, n – number of quantum, which are located in n-level.

Let's use the above mentioned coincidence of distributions (4.80) and (4.81) for formation of non-equilibrium pattern of secondary atoms excitation and ionization using the analog approach, but first and foremost let's make some explanations.

Non-equilibrium distributions with 2 temperature parameters in non-equilibrium chemical kinetics were obtained on the basis of kinetic equations solutions for the function of distribution in non-equilibrium conditions. Later, we found out, that they might be obtained also from canonical distribution of Gibbs. Both methods are general for the implementation of this function for description of any statistical systems, and not only of gases. Using the above mentioned generality of the distribution function (4.81), let's try to develop on its basis non-equilibrium statistical pattern of secondary atoms excitation.

So let's consider as *statistical system* the totality of atoms of atomic collisions cascade, initiated by the primary ion, and as *quasi-particles* the excitation quantum of cascade atoms, which happen in every atom collision. Thus, atomic collisions cascade is a thermostat with temperature T_a, excitation quantum is sub-system of quasi-particles with temperature T_e. According to great canonical distribution of Gibbs, probability to find system with n quasi-particles and energy E_n is the following:

$$W(n,E_n) \sim \exp\left(\frac{\mu n-\varepsilon_n}{T_a}\right), \tag{4.82}$$

where μ – chemical potential of quasi-particles. Turning to the relative occupancies of the atoms levels, we have

$$f_n'' \sim f_0'' \exp\left(\frac{\mu n-\varepsilon_n}{T_a}\right). \tag{4.83}$$

Let's point out that on the one hand we have ratio (4.82), obtained theoretically, and on the other hand we have formula (4.80), obtained empirically. It is obvious that (4.80) and (4.83) have the same meaning on conditions that

$$\mu = \frac{D_0 \cdot T_a}{n \cdot T_e}. \tag{4.84}$$

Analogue of Treanor's distribution from (4.83) is true if

$$\mu = E_1\left(1-\frac{T_a}{T_e}\right). \tag{4.85}$$

Equating right parts of (4.84) and (4.85), we have:

$$D_0 = nE_1\left(\frac{T_e}{T_a}-1\right). \tag{4.86}$$

I.e. the meaning of parameter D_0, obtained from theory, as ratio (4.86) shows, is not the same as those of (4.79), (4.80). Assuming that D_0 is an adjusting parameter and omitting it by substitution of (4.86) into (4.80), we have:

$$f_n = f_0 \cdot \exp\left(-\frac{\varepsilon_n + nE_1}{kT_e}+\frac{nE_1}{kT_a}\right) = f_0 \exp\left[-\frac{\varepsilon_n}{kT_e}+nE_1\left(\frac{1}{kT_a}-\frac{1}{kT_e}\right)\right]. \tag{4.87}$$

When we formulated (4.87) it was assumed that amortization temperature coincides with the temperature of the atomic collisions cascade and the temperature of ionization (excitation) coincides with the temperature of excitation quantum in the cascade (quasi-particles). This assumption is justified by the affinity of physical meanings of these parameters.

Calculations of α^+ and of probability of excitation with the use of (4.87) were done in assumption that the temperature of quasi-particles during the development of cascade coincides with the temperature of the electron sub-system $T_e \sim (1\text{-}10)\cdot 10^3$ K. Cascade temperature was determined in the non-equilibrium sense as $T_a = dE/dS$. Free energy accretion dE was considered to equal the energy of the primary ion E_0. Enthropy accretion dS, according to the formula of Boltzmann was calculated as $dS = k\cdot\ln[N!/(N-n')!n'!]$, where N – overall number of atoms inside volume with the sizes as run of an initial ion, n' – overall number of atoms in the cascade. Number of quasi-particles n was assumed to equal the number of collisions in the cascade with the energy more than 100 eV. Parameters n and n' were calculated on the basis of cascade theory of sputtering. The results of the calculations correspond well to the experiment.

5. Theoretical Basics of Electron Spectroscopy Methods

5.1 Electron outlet depth and investigated substance volume

There is a need to determine *electron outlet depth* for surface quantitative analysis by electron spectroscopy methods: the distance starting from the surface up to the depth of a sample, which electrons of a definite energy E are able to pass without any loss of energy (Fig. 5.1). The incident radiation energy used in the electron spectroscopy methods concerning either photons or electrons is sufficiently great for its penetration into the solid far beyond the outlet limits of the investigated electrons with their characteristic energies. Electrons that come over non-elastic collision and δE energy loss leave the solid with smaller energy and contribute to the signal background while moving from their initiation point (ionization point) to the surface.

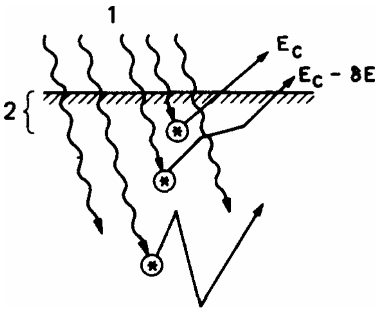

Fig. 5.1. Characteristic electrons initiation scheme in the depth of the solid with the high energy photon drop on the surface: 1 – overlapping photons; 2 – characteristic electrons outlet depth.

Let us imagine the substance as the electron-emitting source with the flux level I_0 and strongly defined energy E_c, and consider imaginary thin getter film on the substance surface, which is traversed by the secondary electrons outgoing current. Any non-elastic film collision removes electrons from the particle group with E_c energy. Let the non-elastic collision cross-section equal to σ, and in $1\ cm^3$ of the film contain N' scattering centers. If I is defined as the electron flux film level then σI electrons leave the initial group counting on one scattering center, and the electron loss dI on the layer with the thickness dx equals to

$$dI = -\sigma I N' dx, \tag{5.1}$$

that gives

$$I = I_0 e^{-\sigma N' x}. \tag{5.2}$$

The average free path length (λ) is connected with the dispersion cross-section by the following proportion

$$1/\lambda = N'\sigma, \tag{5.3}$$

which allows to rewrite (5.1) as

$$I = I_0 e^{-x/\lambda}. \tag{5.4}$$

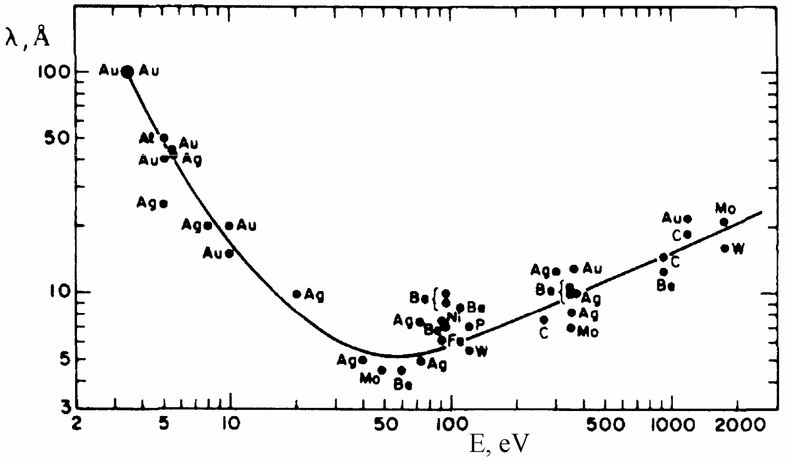

Fig. 5.2. Universal curve of λ - free electron path dependence on E - energy.

Thus, the number of electrons, which are able to go beyond the getter film limits, is exponentially vanishing with the film thickness. The average free path length is regarded as the outlet depth synonym, and both values are marked with the same symbol λ. The electron outlet with the intended energy E_c of the solid uniformly excitable at the depth, is set by the integral $\int I(x)dx = I_0\lambda$, so that substance thick layer proves to be non-absorbing target with λ thickness.

The signal monitoring of the electrons formed in the carrying base as a thickness function of the applied external layers of various metals is carried out to determine the electron flow loss.

Such monitoring results correspond to the average free path length value and to other measuring results of these values, which are shown in Fig. 5.2.

Experimental data prove that the average free path length is energy dependent and has a slanting minimum located close to 100 eV. The average free path length is to some extend insensitive to the substance, in which the electrons are moving. Such diagrams of the average free path length dependence are called “the universal curves”.

5.2 Non-elastic electron-electron collision

The non-elastic electron-electron collision cross-section can be obtained using the theory of charged particle dispersion in the central power within the impulse approach field. In the given approach for the distribution on minor angles for particles with similar charges Z_1=Z_2=e and similar mass M_1=M_2=m, moving with v speed the electron transfers an impulse to the electron target, which equals to

$$\Delta p = \frac{2e^4}{bv} \quad , \tag{5.5}$$

where b – impact parameter.

Let T be the energy transferred from the electron moving with the kinetic energy $E = mv^2/2$ ($E = mv^2/2$ target atom), then

$$T = \frac{(\Delta p)^2}{2m} = \frac{e^2}{Eb^2} \quad . \tag{5.6}$$

Differential cross-section $d\sigma(T)$ of energy transfer within the limits of T up to T+dT is determined by the following formula

$$d\sigma(T) = -2\pi b db \cdot \tag{5.7}$$

As follows from (5.7): $2bdb = -(e^4/ET^2)dT$, i.e.

$$d\sigma(T) = \frac{\pi e^4}{E} \cdot \frac{dT}{T^2} \, . \tag{5.8}$$

Full energy transfer cross-section from the moving electron within the limit of $T_{\min}$ up to T_{max} equals to

$$\sigma_e = \int\limits_{T_{\min}}^{T_{\max}} d\sigma(T) \, , \tag{5.9}$$

$$\sigma_e = \pi \frac{e^4}{E} \left(\frac{1}{T_{\min}} - \frac{1}{T_{\max}} \right) \quad . \tag{5.10}$$

For electrons with E energy of some hundreds eV and higher, the maximum energy transfer ($T_{\max}$=E when M_1=M_2) is greater than $T_{\min}$. That is why

$$\sigma_e \cong \frac{\pi e^4}{E} \frac{1}{T_{\min}} = \frac{6{,}5 \cdot 10^{-14}}{ET_{\min}} cm^2 \, , \tag{5.11}$$

where the value e^2 = 14.4 eV·Å is used and energy E and $T_{\min}$ should be measured in eV.

5.3 Cross-section of electron ionization by collision

Cross-section of electron ionization by collision σ_e can be evaluated according to formula (5.11), assuming that $T_{\min}=E_{\mathrm{B}}$ – cohesive energy of the orbital electron:

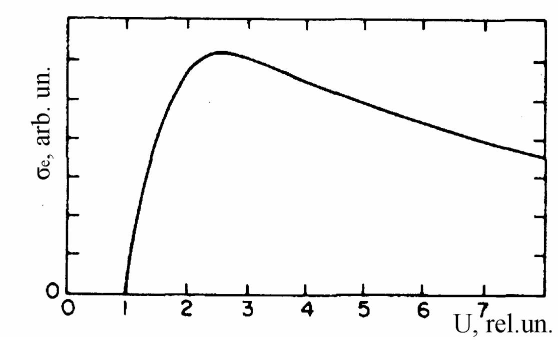

Fig. 5.3. Dependence of collision ionization cross-section on the basic energy.

$$\sigma_e = \frac{\pi e^4}{EE_B} = \frac{\pi e^4}{UE_B^2}, \qquad (5.12)$$

where $U = E/E_{\mathrm{B}}$. With the flying particles energy less than E_B, i.e. under $U<1$, ionization cross-section should equal to zero. The real cross-section as a U function is shown in Fig. 5.3. Ionization cross-section maximum is present with basic energy values U~3–4. When $E_{\mathrm{B}}=100$ eV $U=4$ the cross-section equals to $1.6 \cdot 10^{-18}$ cm^2. This value corresponds to the experimental values of ionization by collision cross-section maximum (measured about $U=4$).

5.4 Plasmons

Plasmons are quanta of plasmic oscillations of electron conductivity (electron gas and electron jelly), their energy is $\hbar\omega_{\mathrm{p}}$ about 15 eV. Plasmon excitation in the solid by primary electrons results in discrete peak in the loss of the electron energy.

From the classical view point plasma frequency is determined by gas oscillations in valence electron present in metal relative to positively charged atom frame (Fig. 5.4).

If gas, as a result of fluctuations, transfers from its balanced position r (i.e. from some volume $4\pi r^3/3$) to some dr value, then the electric field E_p occurs in spherical shell containing $\delta n = 4\pi r^2 \delta r$ electrons:

$$E_p = \frac{e}{r^2} \cdot \delta n = 4\pi n e \delta r, \qquad (5.13)$$

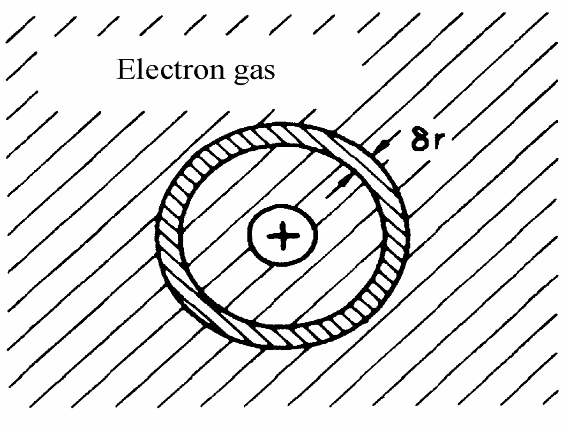

Fig. 5.4. Electron gas from electrons of the positive frame experiences radial compressibility δ*r*.

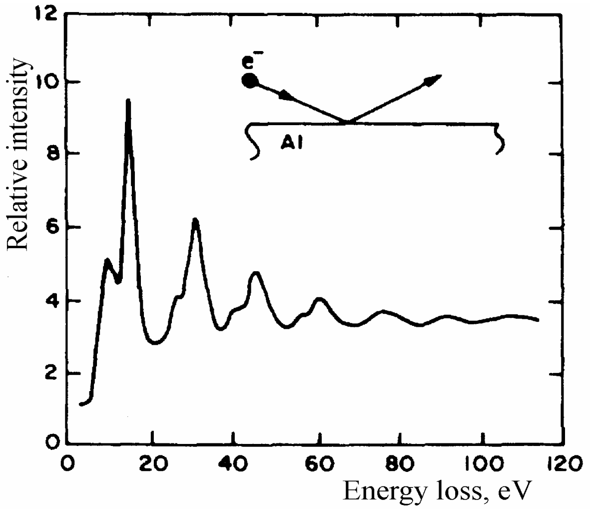

Fig. 5.5. Electron energy loss spectrum for reflected from aluminum. The initial electron energy equals to 2 kilo electron volts. The loss peaks correspond to the excitation of surface and volume plasmon combinations.

some power affects the electrons

$$F = -eE_p = -4\pi e^2 \delta r n, \tag{5.14}$$

harmonic oscillation frequency affected by this power equals to:

$$\omega_p = \left(\frac{4\pi e^2 n}{m} \right)^{1/2}, \tag{5.15}$$

where m – the electron mass. The electron gas density for metals $n \sim 10^{23}$ cm^{-3} results in the oscillation frequency $\omega_p = 1.8 \cdot 10^{16}$ s^{-1} and energy $\hbar\omega_p = 12$ eV. Plasma frequency can be regarded as the "natural" one of the electron-ion system excitable by the external charged particles. Measured plasmon energy values comprise 10.6 eV for Mg and 15.3 eV for A1. Fig. 5.5 shows electron energy loss spectrum reflected from the aluminum film. The loss peaks fall at volume plasmon combination with energy $\hbar\omega_p = 15.3$ eV and surface plasmon with energy 10.3 eV. Surface plasmon frequency $\omega_p(s)$ is connected with volume plasmon frequency by the following proportions:

$$\omega_p(s) = \frac{1}{\sqrt{2}} \omega_p. \tag{5.16}$$

It has been stated that the given proportion is applicable for numerous metals and semi-conductors.

5.5 The average length of the electron free path

The average length of the electron free path in a solid can be assessed by n electron content in one cubic unit within the general theory of the energy loss in solid bodies:

$$-\frac{dE}{dx} = \frac{4\pi e^4 n}{mv^2} \ln B, \tag{5.17}$$

where B is the relation of the particle energy to the excitation one. The dominant part of the electron energy loss in the solid falls at plasmon excitation via further collisions. Energy losses happen in discrete portions, which are equal to quantum value $\hbar\omega_p$. Thus,

$$B = \frac{2mv^2}{\hbar\omega_p} \tag{5.18}$$

using (5.15), energy losses can be define in ω_p:

$$-\frac{dE}{dx} = \frac{\omega_p^2 e^2}{v^2} \ln \frac{2mv^2}{\hbar\omega_p}. \tag{5.19}$$

If plasmons are the major cause of the energy loss while defining the average electron free path length λ, then

$$\frac{1}{\lambda} = \left(-\frac{dE}{dx} \right) \cdot \frac{1}{\hbar\omega_p}, \tag{5.20}$$

whence

$$\frac{1}{\lambda} = \frac{\omega_p e^2}{\hbar v^2} \ln \frac{2mv^2}{\hbar\omega_p}. \tag{5.21}$$

For example, determined according to this formula λ value in A1 equals to 9.2 Å for electrons with the energy 350 eV ($\hbar\omega_p$=15 эВ, $u^2 = 2E/m = 1.23 \cdot 10^{18}$). The given value corresponds to data shown in Fig. 5.2.

5.6 The range of primary electrons in solids

In the material analysis accelerated electrons are used to create vacancies on the inferior envelope atom of the solid, the completing of which is accompanied by Auger emission or X-ray. The detection of characteristic X-ray (electron microanalysis) deals with near-surface layer

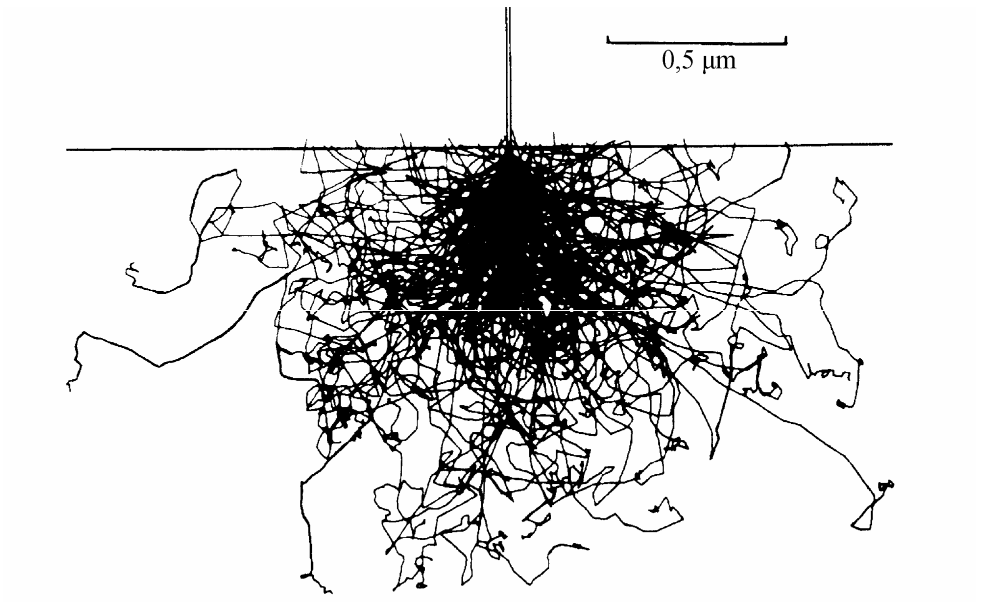

Fig. 5.6. Electron trajectory obtained using Monte-Carlo method for a beam with the energy 20 keV in case of its normal fall on Fe. Volume density of trajectory gives pictorial presentation of the elastic scattering.

thickness, within the limits of which X-ray is generated. The situation is more complicated concerning probing electrons with energy varying from 1 to 50 keV than for heavy ions with the same energies, which locus is relative to the straight line during the greatest part of the range. Significant deviations from the direction of incidence caused by the elastic scattering occur concerning some electrons. Fig. 5.6 shows some calculating results of primary electrons locus in iron (E_0=20 keV) using Monte-Carlo method.

The elastic scattering includes both collisions with large deflection angles and multiple collisions with minor deflection angles resulting in significant changes of the electron direction.

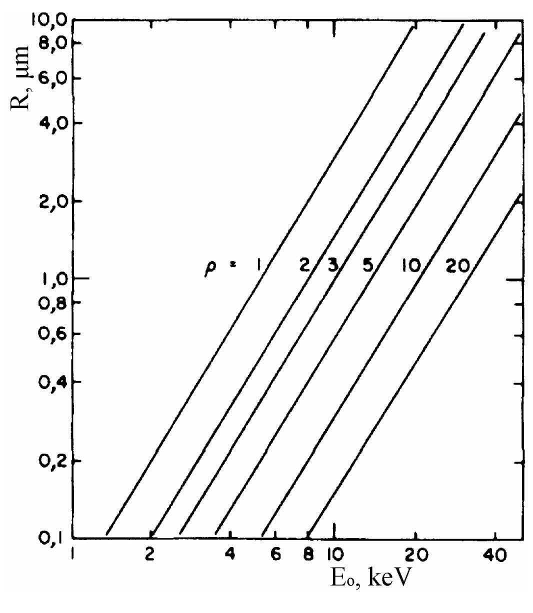

Fig. 5.7. Range *R* dependence on the initial electron energy at different density levels ρ of a substance.

The electron range *R* is defined as a complete distance passed by the electron in a sample along its locus, and can be written in the following way:

$$R = \int_{E_0}^{0} \frac{dE}{dE/dx}, \tag{5.22}$$

with the energy loss $\frac{dE}{dx} \sim \frac{NZ_2}{E} \ln\frac{E}{I} \sim \frac{\rho}{E} \ln\frac{E}{I}$, (5.23)

where *N* – atom concentration, and due to this NZ_2 value is proportional to ρ, and *I* – the average ionization energy: $I \sim 10Z_2$ (eV). The observed range dependence on the initial energy is as follows:

$$R \cong \frac{K}{\rho} E_0^{\gamma}, \tag{5.24}$$

where ρ – density (grams/cm^3), *K* – independent of the substance constant, index γ has a value between 1.2 and 1.7. It is favorable to carry out mass range ρR, which in its first approximation is independent on the target substance. Electron range *R* as the energy function is shown in Fig. 5.7 for K=0.064 and γ=1.68.

Mass electron range ρR_x regarding characteristic X-ray generation is less than the value of mass range ρR because characteristic X-ray is excitable only when the electron energy is higher than the critical excitation energy or cohesive energy E_B of the orbital electron. Mass range regarding the characteristic X-ray generation is determined by the following formula:

$$\rho R_x = K\left(E_0^{\gamma} - E_B^{\gamma}\right). \qquad (5.25)$$

Observed K and γ parameters approximation gives the following formula:

$$\rho R_x = 0{,}064\left(E_0^{1{,}68} - E_B^{1{,}68}\right), \qquad (5.26)$$

where E_0 and E_B – in keV, ρ – in grams/cm^3, R_x – in μm. Fig. 5.8 shows the electron range R in aluminum, range R_x regarding the drive line $A1K_\alpha$ and CuK_α in aluminum containing copper, and range R_x regarding drive lines CuK_α and CuL_α in pure copper. Ranges regarding X-ray depend on the matrix density (ρ_{Al} = 2.7 *grams/cm^3*, ρ_{Cu} = 8.9 *grams/cm^3*) and on the cohesive energy E_B (E_B = 8.98 keV for CuK_α; E_B=0.93 keV for CuL_α).

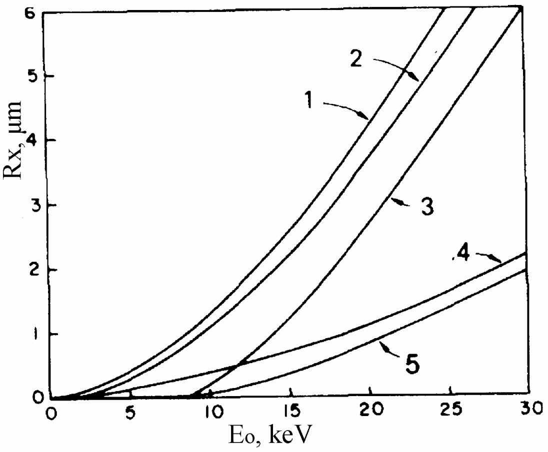

Fig. 5.8. Effective electron range in Cu and A1 regarding X-ray generation. The ranges indicate electron penetration point in characteristic radiation generation: 1 – range in aluminum; 2 – range in A1 regarding line $A1K_\alpha$ generation; 3 – range in A1 with copper admixture regarding line CuK_α generation; 4 – range in Cu regarding line CuL_α generation; 5 – range in *Cu* regarding line CuK_α generation.

5.7 Bremsstahlung

According to classical physics, the charge, moving with acceleration is the source of electromagnetic radiation. Corresponding energy losses are called radiation losses. Charge acceleration is caused, for example, by electron deviation in atom field during its movement in a substance. Since the acceleration is determined by relation of electrostatic force to the mass, the radiation loss component is of a greater significance to electrons than to heavy particles. As it shown further, bremsstahlung generates photon spectrum stretching up to the initial energy of the flying electron. Bremsstahlung is of a great interest to the material analysis as it is able to create noticeable background lower than the characteristic radiation spectrum in those investigation methods where characteristic photons are registered. Elastic scattering cross-section of a charged particle Z_1 on a nucleus charge Z_2 is presented in the following formula:

$$\frac{d\sigma}{d\Omega} = \left(\frac{Z_1 Z_2 e^2}{4E}\right)^2 \frac{1}{\sin^4 \theta/2}, \qquad (5.28)$$

where θ – scattering angle. The following scattering cross-section can be presented in the corresponding impulse Δp values:

$$\Delta p = 2p \sin \theta/2$$

$$d\Omega = 2\pi \sin\theta d\theta = \frac{2\pi\Delta p d\Delta p}{p^2}. \qquad (5.28a)$$

Then the impulse Δp cross-section transmission equals to

$$\frac{d\sigma}{d\Delta p} = 8\pi\left(\frac{Z_1 Z_2 e^2}{\upsilon}\right)^2 \frac{1}{(\Delta p)^3}. \qquad (5.29)$$

Classical electrodynamics tells that total energy emitted within the frequency unit interval and with the expectation of one collision is determined by the following formula:

$$\frac{dI}{d\omega}=\frac{2}{3\pi}\frac{(Z_1e)^2\Delta p^2}{m^2c^3}, \tag{5.30}$$

where m – mass of a deviated particle. The given formula is obtained in non-relativistic approach and within low frequencies limit ω. The given differential radiation cross-section can be presented in the form of photon radiation probability and hw energy corresponding to Δp impulse transmission per Δp impulse transmission probability product:

$$\frac{d^2X}{d\omega d\Delta p}=\frac{dI}{d\omega}\frac{d\sigma}{d\Delta p}, \tag{5.31}$$

or obviously

$$\frac{d^2X}{d\omega d\Delta p}=\frac{16}{3}\frac{Z_2^2e^2(Z_1^2e^2)^2}{m^2v^2c^3}\frac{1}{\Delta p}. \tag{5.32}$$

To identify the radiation spectrum using frequency the following expression should be integrated over all possible impulse transmissions, starting from Δp_{min} up to Δp_{max}:

$$\frac{d^2X}{d\omega d\Delta p}=\frac{16}{3}\frac{Z_2^2e^2(Z_1^2e^2)^2}{m^2v^2c^3}\ln\frac{\Delta p_{макс}}{\Delta p_{мин}} \tag{5.33}$$

To define the relation of $\Delta p_{max}/\Delta p_{min}$ there is a need to consider the kinematics of the process. Let us write the energy and impulse conservation law like

$$E=E'+\hbar\omega, \tag{5.34}$$

$$(\Delta p)^2=(p-p'-k)\approx(p-p'), \tag{5.35}$$

where E, p – energy and impulse before collision; E', p' – after collision; k – Bremsstahlung photon impulse, which can be neglected. From proportions (5.34), (5.35) we have

$$\frac{\Delta p_{\max}}{\Delta p_{\min}}=\frac{p+p'}{p-p'}=\frac{\left(\sqrt{E}+\sqrt{E-\hbar\omega}\right)^2}{\hbar\omega}, \tag{5.36}$$

so, (5.33) can be written as

$$\frac{d^2X}{d\omega d\Delta p}=\frac{16}{3}\frac{Z_2^2e^2(Z_1^2e^2)^2}{m^2v^2c^3}\ln\frac{2-\hbar\omega/E+2\sqrt{1-\hbar\omega/E}}{\hbar\omega}. \tag{5.37}$$

The function shown in Fig.5.9 decreases as lп($E/\hbar\omega$) under minor $h\omega/E$, then comes closer to the linear, and cuts under $E = h\omega$. The following spectrum was obtained by Bete and Gaitler in 1934.

According to (5.30) Bremsstahlung is significant for light particles (electrons) in substances with great atom number.

Total energy loss on radiation for moving particles with N atoms in cubic unit equals to

$$\frac{dE_{rad}}{dx}=N\int_0^{\omega_{\max}}\frac{dX(\omega)}{d\omega}d\omega, \tag{5.38}$$

let us introduce the following value $z=h\omega/E$, and consider the proportion (5.37) and equality

$$\left(\frac{1+\sqrt{1-z}}{\sqrt{z}}\right)^2=\frac{2-z+\sqrt{1-z}}{z}, \tag{5.39}$$

then we can obtain the following formula for radiation losses

$$\frac{dE_{rad}}{dx}=\frac{16}{3}\frac{Z_2^2e^2(Z_1^2e^2)^2}{m^2v^2c^3}\int_0^1\ln\left(\frac{1+\sqrt{1-x}}{\sqrt{x}}\right)dx\,. \qquad (5.40)$$

Integral in (5.40) equals to one, so radiation losses are energy independent. The relation of radiation and non-radiation losses $dE_{\text{rad}}/dE_{\text{non-rad}}$ for electrons can be determined by the following expression:

$$\frac{dE_{rad}}{dE_{non-rad}}\approx\frac{4Z_2}{3\cdot137\cdot\pi}\left(\frac{v}{c}\right)^2 \qquad (5.41)$$

which is of a minor state when $v < c$.

It is necessary to remember that in electron spectroscopy the deceleration photon can distort the characteristic line in a spectrum. Rough evaluation of the radiation cross-section relation to the ionization cross-section comprises $Z_2(v/c)^2/137$, which equals to ~ 0.01 for electrons with the energy of 100 keV and under $Z_2/137$ it comprises 0.25. Particularly this fact defines element frequency limit in methods using X-radiation recording. This limit equals to approximately 1% of the admixture content in the solid matrix.

5.8 Transition probability between atom energy states

5.8.1 Time-independent perturbation theory

Surface electron spectroscopy methods are based on the use of energy difference in atom transition between the energy levels. Electron Auger-spectroscopy (EAS) (includes the creation of a hole in atom inferior envelope, one atom transition to fill this hole and the second one for the following Auger-relaxation excitation) can serve as an example of method that uses two atom transitions. Procedures similar to Auger-process are used in X-ray fluorescence (target excitation using X-ray, and in the analysis according to characteristic X-ray) as well as in electron microanalysis (excitation by electrons, the analysis according to X-ray). X-ray photoelectron spectroscopy can serve as an example of the method that uses one atom transition: the creation of a hole in the inferior envelope and the creation of a photoelectron with greater energy. Issues connected with these processes and necessary to understand the electron spectroscopy methods are considered within the course of quantum mechanics. The given part of this manual includes some basic ideas and conclusions of quantum mechanics concerning the above mentioned processes. To calculate transition probability a well-known quantum-mechanical *time-dependent perturbation theory* is used, which basic conclusions, necessary for atom transition description, are listed in section (5.8.2). Let us begin with *time-independent perturbation theory*.

In the first order of perturbation theory the interaction of atom system with the external field is described by the application of an additional component equivalent to the external field potential into the Hamiltonian of this system. Thus, atom Hamiltonian interacting with the stationary field can be written like

$$H=H_0+H', \qquad (5.42)$$

where H_0 – non-perturbed atom's Hamiltonian (there is a Schredinger equation salvation), and H' – additional potential created by the applied electric field.

The solutions of the equation $H_0u_n = E_nu_n$ form a number of proper functions. Transition probability into the time unit from the initial state m into its final state k is given by the following expression

$$W=(2\pi/\hbar)\rho(E)\left|\langle\psi_k|H'|\psi_m\rangle\right|^2\,. \qquad (5.43)$$

Here $\rho(E)$ – final state density in the unit energy interval

$$\langle\ \psi_k | H' | \psi_m \rangle = \int \psi_k^* H' \psi_m d\tau = |H'_{km}|, \tag{5.44}$$

where ψ^* — complex-conjugate function relative to ψ, $d\tau = r^2 dr \sin\theta d\theta d\varphi$ – three-dimensional differential of volume, *a* wave function ψ_m equal to

$$\psi_m = \exp(i\omega_m t) u_m \cdot \tag{5.45}$$

Expression (5.43) is well-known in quantum mechanics as the "Fermi golden rule". The greatest advantage of this rule is that there is no need to be aware of the true potential wave functions H_0+H', the salvation of H_0 is only needed. Let us note that W has dimensionality $(time)^{-1}$.

5.8.2 Time-dependent perturbation theory

Time-dependent perturbation theory allows to obtain the basic formula for transition probability in quantum system and to calculate process cross-section used in the analysis methods. The essence of these calculations is as follows.

Let us consider a system with Hamiltonian H determined by expression (5.42). Let H' be *time-dependent* excitation, some alternating electric field, for example. Wave function ψ_0 satisfies Schredinger equation

$$i\hbar \frac{d\psi_0}{dt} = H_0 \psi_0 \cdot \tag{5.46}$$

As H_0 is time-independent, we can write

$$\psi_0 = u(x, y, z) e^{it_0 i/\hbar} \tag{5.47}$$

or

$$\psi_0 = \sum_n a_n^0 u_n^0 e^{-iE_n^0 t/\hbar}, \tag{5.48}$$

where $u^0{}_n$– orthonormalized proper vectors satisfying the equation

$$H_0 u^0{}_n = E^0{}_n u^0{}_n, \tag{5.49}$$

$a^0{}_n$ – time-independent constants. For perturbed Hamiltonian the Schredinger equation can be written as

$$H\psi = i\hbar \frac{\partial \psi}{\partial t} = (H_0 + H')\psi \tag{5.50}$$

and

$$\psi = \sum_n a_n^0 u_n^0 e^{-iE_n^0 t/\hbar}, \tag{5.51}$$

where components $a_n(t)$ are now time-dependent. By substituting (5.51) for (5.50) and multiplying by the complex-conjugate function $(u^0{}_s)^*$, considering ortonormalization we have

$$\frac{da_S}{dt} = a_S \frac{i}{\hbar} \sum_n a_n(t) H'_{sn}\, e^{i(E_S - E_n^0)t/\hbar}, \tag{5.52}$$

where

$$H'_{sn} = \int (u_s^0) * H' u_n^0 d\tau \tag{5.53}$$

– space integral. Let us note that under small disturbances there is a slow time change $a_n(t)$. In this case we can get an approximate solution assuming that $a_n(t) \simeq a_n(0)$:

$$a_S(t) - a_S(0) = -\frac{i}{\hbar} \sum_n a_n(0) \int_0^l H'_{sn}(l) e^{i\omega_{SN} t} dt, \tag{5.54}$$

where $h\omega = E^0{}_s - E^0{}_n$

One particular case that is worth mentioning is when during the moment of time $t=0$ the system is in the state of $a_n(0)=1$, and the values of other components equal to zero. Then for $s \neq n$ the expression (5.54) changes into

$$a_S(t) = \frac{i}{\hbar}\int_0^i H'_{sn}(t)e^{i\omega_{sn}t}dt \cdot \tag{5.55}$$

Perturbation *H' (t)* can cause transitions from *n* state into any other state *s*. The probability of a system occurs in *s* state during the moment of time *t* equals to $|a_s(t)|^2$.

If *H'* is time-independent, then

$$a_S(t) = -H'_{sn}\frac{(e^{i\omega_{sn}t}-1)}{\hbar\omega_{sn}} \tag{5.56}$$

and

$$|a_s(t)|^2 = 4\frac{H'^2_{sn}\sin^2(\omega_{sn}t/2)}{\hbar^2\omega^2_{sn}}, \tag{5.57}$$

which is right until $|a_s(t)|^2 < 1$.

In many practical exercises a particle transfers into the continuous state continuum as a result of perturbation, i.e. becomes free particle (ionization – electron leaves the atom). In this case instead of the intended final state it is appropriate to consider final states density. Let $\rho(E)$ be the final states density (a number of energy levels per unit energy interval) assuming that H'_{sn} is similar for all final states.

Transition probability $P(t)$ is presented by the following expression

$$P(t) = \sum |a_s(t)|^2 = 4|H'_{sn}|^2 \sum \frac{\sin^2(\omega_{sn}t/2)}{\hbar^2\omega^2_{sn}}. \tag{5.58}$$

In case of transition into the continuum we replace the sum by the integral taking into account that the number of states in the energy interval *dE* equals to $\rho(E_S)dE_S$, hence

$$P(t) = 4|H'_{sn}|^2 \int_{-\infty}^{\infty} \rho(E_s)\frac{\sin^2(\omega_{sn}t/2)}{\hbar^2\omega^2_{sn}}. \tag{5.59}$$

The main contribution into the integral is made when $\omega_s = 0$, assuming that $\int(\sin^2\alpha x/x^2)dx = \pi\alpha$, we have

$$P(t) = 4|H'_{sn}|^2 \rho(E_n)\frac{\pi t}{2\hbar}, \tag{5.60}$$

so that transition speed *W* equals to

$$W = \frac{2\pi}{\hbar}\rho(E_n)|H'_{sn}|^2 \cdot \tag{5.61}$$

Thus, the "Fermi golden rule" (5.43) in time-dependent situation is given in (5.61).

5.8.3 Transition probability in the oscillating electric field

An important supplement to time-dependent perturbation theory is the disturbing field phenomenon having time-dependence in the form of $e^{i\omega t}$. Let us consider as an example the oscillating electric field directed along the *x* axis:

$$\mathcal{E} = \mathcal{E}_0\cos\omega t = \frac{\mathcal{E}_0}{2}(e^{i\omega t} + e^{-i\omega t}) \tag{5.62}$$

and

$$H'(t) = \frac{e}{2}\mathcal{E}_0 x(e^{i\omega t} + e^{-i\omega t}) \cdot \tag{5.63}$$

Substitution of *H'(t)* into (5.55) gives

$$a_s(t) = \frac{i}{\hbar} e \frac{\mathcal{E}_0 x_{sn}}{2} \int_0^t \left(e^{i(\omega_{sn}+\omega)t} + e^{i(\omega_{sn}-\omega)t} \right) dt \tag{5.64}$$

when the average integral value equals to zero. If $\omega_{\mathrm{sn}} = \omega$, we have

$$\left| a_s(t) \right|^2 = \frac{e^2 \mathcal{E}_0^2}{\hbar^2} \left| x_{sn} \right|^2 \frac{\sin^2 \left[(t/2)(\omega - \omega_{sn}) \right]}{(\omega - \omega_{sn})^2}, \tag{5.65}$$

where $|x_{sn}| = \int u_s{}^* x u_n{}^* d\tau$. As $\varepsilon_0{}^2/2$ is the density of the electric field energy $\rho(\omega)$, then the transition probability equals to

$$T_{ns} = \left| a_s(t) \right|^2 = 2e^2 \left| x_{sn} \right|^2 \int_0^\infty \frac{\sin^2 \left[(t/2)(\omega - \omega_{sn}) \right]}{\hbar^2 (\omega - \omega_{sn})^2} \rho(\omega) d\omega \,. \tag{5.66}$$

Let us assume that spectral distribution $\rho(\omega)$ changes more slowly than the function multiplied by $\rho(\omega)$ in the integration element. In the narrow interval of w values, the integration element of which is different from zero, $\rho(\omega)$ is almost a constant magnitude. That is why $\rho(\omega)$ can be replaced by its value when $\omega = \omega_{\mathrm{sn}}$, and can be taken outside the integral without any significant accuracy loss. Further, using the following substitution $z = (\omega - \omega_{\mathrm{sn}})t'/2$ let us rewrite (5.66) as:

$$\left| a_{sn}(t') \right|^2 = \frac{e^2 \rho(\omega_{sn}) \, | x_{sn} |^2 \, t'}{\hbar^2} \int_{-\infty}^{\infty} \frac{\sin^2 z}{z^2} dz \,. \tag{5.67}$$

Taking into account the integral value $\int_{-\infty}^{\infty} \frac{\sin^2 z}{z^2} dz = \pi$, the transition probability equals to

$$T_{sn} = | a_{sn}(t') |^2 = \frac{\pi e^2 \rho(\omega_{sn}) \, | x_{sn} |^2 \, t'}{\hbar^2}, \tag{5.68}$$

where $x_{sn} = \int u_s{}^* x u_n{}^* d\tau$. Expression (8.63) is applicable for irradiation polarized along x axis. In general, when irradiation falls on the atom from all directions with chance polarization, T_{sn} should include equal contributions of x_{sn}, y_{sn} and z_{sn}, hence

$$T_{sn} = \frac{\pi e^2 \rho(\omega_{sn}) t'}{3\hbar^2} \left| < \psi_s \,|\, r \,|\, \psi_n > \right|^2, \tag{5.69}$$

multiplier 3 is introduced into the denominator because every polarization direction contributes to the intensity. The expression

$$\left| < \psi_s \,|\, r \,|\, \psi_n > \right|^2 = | r_{sn} |^2 = | x_{sn} |^2 + | y_{sn} |^2 + | z_{sn} |^2 \tag{5.70}$$

is called the dipole coefficient function, and (5.69) – dipole approximation for transition probability.

5.8.4 Spontaneous transitions

Transitions that occur with the absence of external field are called spontaneous transitions. The calculation of such transitions is based on the method introduced by Einstein in 1917. This method allows to calculate the speed of spontaneous transitions using certain speed of induced transmissions, the calculation of which is represented in the previous section (5.8.3).

Let us have a group of atoms in thermal equilibrium, every atom radiates and absorbs radiation with similar speed. Let P_{ns} be the probability of that fact that atom transfers from one state n into the other state s during a little period of time dt. P_{ns} probability should be in proportion to P_{n} probability of atom occurrence in its initial state n multiplied by T_{ns} probability transition from n state into s state:

$$P_{\mathrm{ns}} = T_{\mathrm{ns}} \cdot P_{\mathrm{n}} \,.$$

Taking into account (5.69) we can rewrite this expression as

$$P_{ns}=A_{ns}\rho(\omega_{ns})P_n dt, \qquad (5.71)$$

here $\rho(\omega_{sn})$ earlier determined spectral density, dt replaces t' as a time interval, and A_{ns} corresponds to the multiplier of expression (5.69):

$$A_{sn} = \frac{\pi e^2}{3\hbar^2}\left|\psi_n\middle|r\middle|\psi_n\right|^2$$

Transition probability from the upper state s into the lower state n can be written as $P_{sn}=A_{sn}\rho(\omega_{sn})P_s dt$. From the expression symmetry leading to (5.69) we know that $A_{sn}=A_{ns}$ and $\omega_{sn} = \omega_{ns}$, that is why:

$$P_{sn}=A_{ns}(\omega_{ns})P_s dt. \qquad (5.72)$$

Let us note that P_{ns} is not equal to P_{sn} because $P_n>P_s$ as n level has low energy and great occupancy in accordance with Bolzman law under thermal equilibrium.

As the whole system is in the equilibrium, the full number of transitions from n into s state should be equal to the full number of transitions from s into n. As the induced transition probabilities are not equal ($P_{ns}\neq P_{sn}$), some additional transitions from s into n state should exist, which are spontaneous transitions. According to the definition, spontaneous transition probability doesn't depend on the energy density of the external field; this probability can be written as $B_{sn}\cdot P\cdot dt$, where B_{sn} – spontaneous transition probability. A and B coefficients are called the Einstein coefficients.

Hence, full transition probability from s into n state equals to $P_{sn}+B_{sn}P_s$. The same value should be equal to transition probability from n into s state. Thus, from equations (5.71) and (5.72) we have

$$\rho(\omega_{ns})P_n A_{ns}=\rho(\omega_{ns})P_s A_{ns}+P_s B_{sn} \qquad (5.73)$$

or

$$B_{sn} = \rho(\omega_{ns})A_{ns}\left[\frac{P_n}{P_s}-1\right]. \qquad (5.74)$$

State occupancy with E energy is proportional to Bolzman factor $e^{-E/km}$, and P_n/P_s relation can be written as

$$\frac{P_n}{P_s} = e^{(E_s-E_n)/kt} = e^{\hbar\omega_m/kT}. \qquad (5.75)$$

Hence

$$B_{sn} = \rho(\omega_{ns})A_{ns}(e^{\hbar\omega_m/kT}-1)\cdot \qquad (5.76)$$

Multiplier $\rho(\omega_{ns})$ in expression (5.76) should be removed as, according to the definition, B_{sn} doesn't depend on the energy density of the radiation field. It is removed using the expression for the energy density inside the close cavity (i.e. using the model of the ideal black body). The Plank law for thermal radiation results in the following dependence

$$\rho(\omega) = \frac{\hbar\omega^3}{\pi^2 c^3(e^{\hbar\omega/kT}-1)}\cdot \qquad (5.77)$$

The substitution of this expression into the equation (5.76) leads to the expression for B_{sn}, containing A_{ns} and known constants:

$$B_{sn} = \frac{\hbar\omega_{ns}^3}{\pi^2 c^2}A_{ns}\cdot \qquad (5.78)$$

So, spontaneous transition speed from the filled state into the non-occupied state equals to

$$W = \frac{4}{3}\frac{e^2}{\hbar}\left[\frac{\omega_{ns}}{c}\right]^3\left|<\psi_s\,|\,r\,|\,\psi_n>\right|^2\cdot \qquad (5.79)$$

This expression can be written as

$$W=0.38\cdot 10^{16}(\hbar\omega)^3 \cdot|<\psi_s|r|\ \psi_n>|^2, \qquad (5.80)$$

where $\hbar\omega$ is expressed in eV, coefficient function has dimensionality $(A)^2$, and $e^2=14.4$ eV·Å Typical value W equals $10^{15}\ s^{-1}$ for elements in the middle of the D.I. Mendeleyev periodic table.

To sum up everything mentioned in the given part let us write the most vital expressions for transition speeds:

– *for stationary perturbation* [(5.43) and (5.61) proportions]:

$$W=\frac{2\pi}{\hbar}\cdot|H'_{sn}|^2\ \rho(E_n);$$

– *for time-dependent perturbations* $H'=\varepsilon_0\cos\omega t$ [(5.69) proportion]:

$$W=\frac{\pi e^2\rho(\omega_{sn})}{3\hbar^2}|r_{sn}|^2;$$

– *for spontaneous transitions* [(5.79), (5.80) proportions].

$$W=\frac{4}{3}\frac{e^2}{\hbar}\left[\frac{\omega_{ns}}{c}\right]^3|r_{sn}|^2.$$

6. Ion Spectroscopy Methods

The phenomena of ion emission considered in chapter 1.2.1. form the basis for the methods of electron spectroscopy. In chapter 4 we discussed in detail many processes and their models which are necessary to describe the phenomena occurring during interaction of ions with surface. The current chapter views definite applications of phenomena involved in ion scattering and ion emission. This is necessary for studying properties of surface and near-surface layers of solids.

6.1 Analysis of ions scattered by the surface

6.1.1 Shading and neutralization effects. Element analysis

Methods of ion spectroscopy, which study scattered primary ions, may be subdivided into two major groups:

1) methods using scattered ions with high energies (from 10 keV to 2 MeV and more) which provide data about the surface only under specific conditions of the experiment (we are not going to discuss them in this chapter);

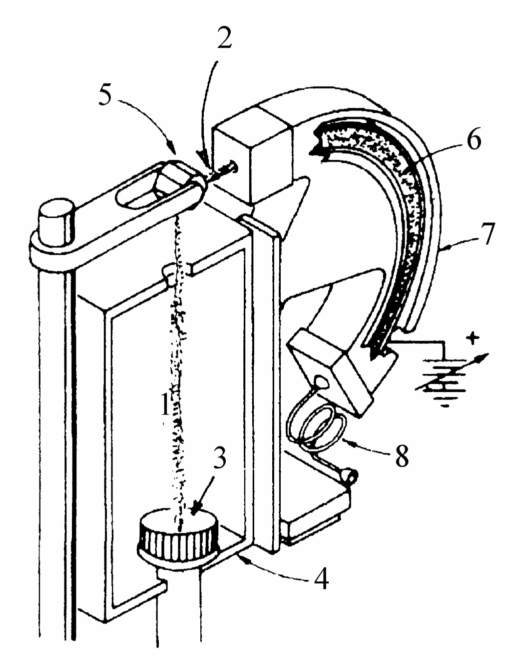

Fig. 6.1. The diagram of registration system applied in scattering of ions with low energies: 1 – flying ions; 2 – scattered ions; 3 – ion gun; 4 – screen; 5 – set of targets; 6 – trajectory of positive ions in the energy analyzer; 7 – energy analyzer with 127-degree turn of a beam; 8 – channel electron multiplier.

2) methods using slow ions (the ones whose kinetic energy is less than 10 keV). They are usually called methods of slow ions scattering (SIS) or ion scattering spectroscopy (ISS). The theoretical basis of these methods is represented by ratios (4.8), (4.9) (chapter 4.13).

The principle of analysis is very simple the surface is exposed to almost monoenergetic ion beam, usually He^+ or Ne^+ with energy ranging from 0.5 to keV(in some cases up to ~ 10 keV). Fig. 6.1 shows the possible scheme of the experiment: ion gun 3 creates an ion beam with low energies 1 which are scattered on the studied samples 5 at angle of 90° and analyzed in the electrostatic analyzer 7 with 127 -degree turn of ions. The directions of falling and scattering are well-known, so values E_0, M_1 and θ_1 in equation (4.8) are fixed. Therefore, the measured energies E_1 of scattered particles allow determining the mass of scattering atoms M_2 located on the surface. The typical energy spectrum of scattered ions is shown in Fig.6.2. There are surface atoms near peak vertexes due to which peaks in the spectrum appear. Mass resolution is determined by energetic width of the peaks which in turn depends on the energy and angle resolution of the experimental plant. Big collection angle and improperly collimated falling beam result in inaccuracies in determining θ, and consequently, in widening of scattering peaks. For the detector with relatively small collection angle mass resolution capacity ($M_2/\Delta M_2$) is determined by energy resolution capacity. These values are connected by the following ratio:

$$\frac{M_2}{\Delta M_2}=\left(\frac{E_1}{\Delta E_1}\right)\frac{2A}{A+1}\left[\frac{A^2+\sin^2\theta_1-\cos\theta_1(A^2-\sin^2\theta)^{1/2}}{A^2-\sin^2\theta_1+\cos\theta_1\left(A^2-\sin^2\theta_1\right)^{1/2}}\right] \tag{6.1}$$

Fig. 6.3 shows the dependence charts of *($M_2/\Delta M_2$)* upon scattering angle θ_l for several values of A and energy resolution capacity equal to 100. We see that at small scattering angles resolution is poor, as energy losses are insignificant, and all the peaks will concentrate near E_0. The best mass resolution is obtained when the value of A is small. On the other hand, when A decreases the range of possible scattering angles decreases either. For example, in the simplest case when θ_1=90° the equation (4.1.) looks as follows:

$$\frac{E_1}{E_0} = \frac{A-1}{A+1}, \tag{6.2}$$

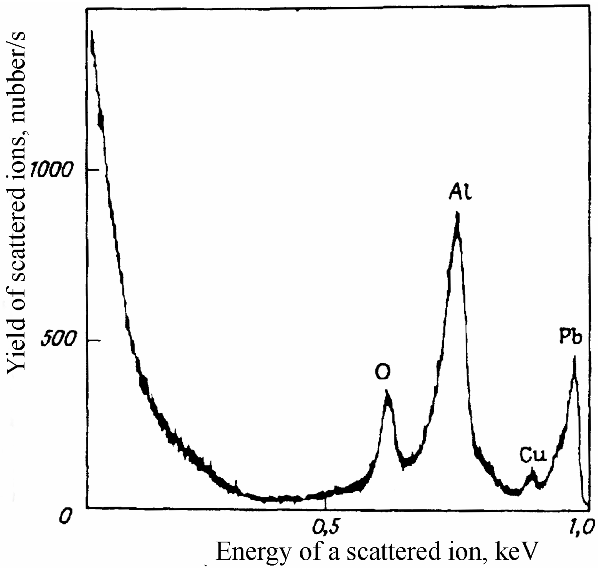

Fig. 6.2. Energy spectrum of the 90^0 scattered He^+ ions from the surface of the dirty alloy. Ions energy – 1 keV, current density in beam – $3.5 \cdot 10^{-7}$ A/cm^2.

which doesn't have any solutions at $A<1$. Thus, when at this angle we choose a heavy falling ion for resolution optimization in case of heavier atoms of the target ($A>1$), we exclude from analysis all the lighter atoms of the surface. For smaller values of θ_1, the minimum value of A at which measurements are possible is less than 1.

While the energy of the scattering process does not depend on the nature of interaction potential of the ion and the atom $V(r)$ in terms of correlation between the values E_1/E_0, A and θ_1, the scattering cross-section do depend on this potential. Indeed, for any potential there is an unequivocal correspondence between the scattering angle and the aiming parameter b for any separate trajectory of falling ions. For the separate scattering act in approximation of the mass centre the scattering angle is represented by the following expression:

$$\theta_{цм} = \pi - 2\int\limits_{r_{мин}}^{\infty} \frac{bdr}{r^2\left(1 - \frac{b^2}{r^2} + \frac{V(r)}{E}\right)^{1/2}}. \tag{6.3}$$

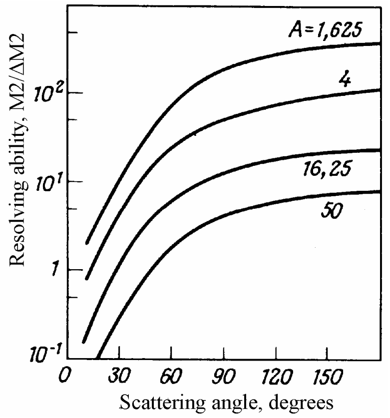

Fig. 6.3. Dependence of the mass resolution value upon the scattering angle in laboratory system of coordinates.

This expression allows to calculate the full scattering cross-section, bigger than θ_{cm}, which is given by the area πb^2, and differential cross-section of scattering to the angle $\theta_{c.m.}$ (with some variation of $d\theta$) which is determined by $\sigma = 2\pi bdb$. The choice of the potential $V(r)$ is poorly determined; it is usually represented as a repulsion potential between the nuclei, which to some extent takes into account electron screening. It is exactly this potential which is used in Molier's approximation for Thomas-Fermi screening functions at interaction of atoms with atomic numbers Z_1 and Z_2:

$$V_M(r) = \left(\frac{Z_1 Z_2 e^2}{r}\right)\phi\left(\frac{r}{a}\right), \tag{6.4}$$

where in this case the screening function is given by the expression

$$\phi\left(\frac{r}{a}\right) = 0.35y + 0.55y^4 + 0.1y^{20}, \tag{6.5}$$

$$y = \exp(-0.3\, r/a), \tag{6.6}$$

here c – characteristic length equal to Firsov constant:

$$a=0.88534a_B Z_1^{1/2}+Z_2^{1/2})^{-1/3}, \qquad (6.7)$$

where a_B – Bohr radius. However, neither this form of screening nor the potential itself is exact enough, and the problem of proper choice of the potential remains one of the challenges of numerical description of SIS. For example, Born-Mayer potential is also used which can be compared with (6.4) according to suitability:

$$V_{BM}(r)=Ae^{-Br}. \qquad (6.8)$$

Suitable values of A and B for different combinations of atomic numbers of flying ions and scattering atoms are tabulated. The differential cross-sections calculated with the use of this method are often twice as much and differ from the calculation results with Molier potential.

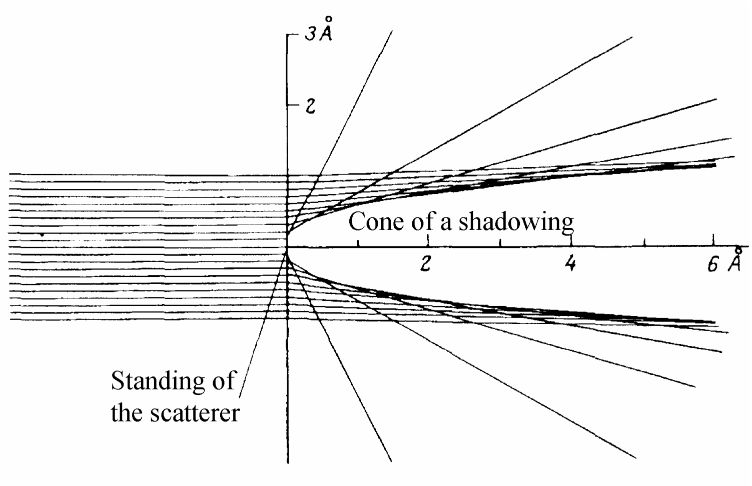

Fig. 6.4. Formation of "shadowing cone": scattering trajectories of He^+ ions with energy 1 кэВ on atom O located at the origin of the coordinates (Thomas–Fermi–Molier potential) are shown.

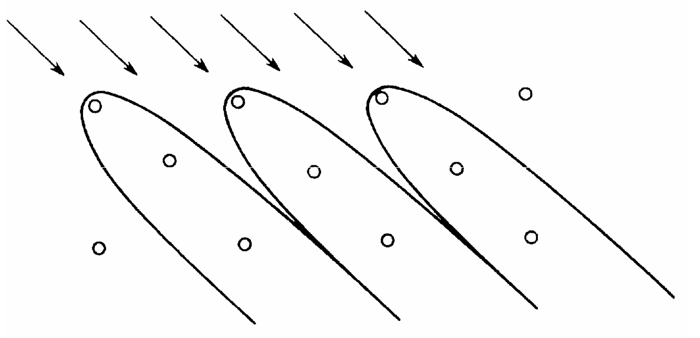

Fig. 6.5. Cones of a shadowing for ions He^+ with energy 1 keV from high layers atoms of surface Ni {100}, designed on more low - laying atoms.

Using any of these potentials it is possible to calculate the correlation between the scattering angle θ_1 and the aiming parameter b. Fig. 6.4 shows the set of ion trajectories obtained from the set of experimental data when Molier potential was used for describing interaction of He^+ ion with energy 1keV, with scattering atom O located at the coordinate origin in the diagram. Each trajectory is presented as two straight lines joined in the same scattering junction. Strictly speaking, a certain curvature should be taken into account, especially near the angle; this detail, however, does not affect the overall picture. The picture proves the existence of the "shade cone" behind the scattering atom which makes the part of the space for the ions falling in this direction invisible. Thus if any other scatterer lies within this cone, it will be shaded and will not be able to participate in the scattering process. For the conditions, which correspond to the case shown in Fig. 6.4, we can see that at the typical distance between the atoms of the solid ~2Å the width of the shading cone behind the scatterer accounts for 1.5 Å, i.e. it can be compared with typical interatomic distance. That means that when ion scattering at the surface under these conditions is studied the upper layer of atoms usually shades the second layer and deeper layers of atoms. Fig. 6.5 shows the shading cones for He^+ ions with energy 1keV around the atoms of the upper layer at the surface of Ni(100), which in the chosen azimuth direction completely shade the deeper layers. Thus we can see that shading at elastic scattering is the main reason for surface sensitivity of SIS. Here only the phenomena occurring in the upper atomic layer participate in forming useful signal. In this connection SIS method may be regarded as a more sensitive to the surface than most methods of electron spectroscopy in which the contribution of consecutively located layers decreases exponentially and in which the average length of free path accounts approximately for two distances between atomic layers. We can get some idea of the dimensions of the shading cone and scattering cross cuts depending on the energy of the flying ion and the type of scatterer when we calculate the aiming parameter for the small scattering angle under changing conditions. We can see from the figure that the bombarding ions possessing very low energy ”feel” the surface much better than the heavy ions possessing higher energies. However, the scattering results of heavy ions allow obtaining more detailed information about the surface if compared to scattering of light ions. On the other hand, heavy ions with higher energy will cause much greater deformations of the surface than lighter low-energy ions with comparable shading cones and scattering cross-sections.

It has been supposed up to now that interaction of bombarding ions with surface may be described as single acts of ion scattering at isolated atoms of the surface. Experimental results such as the spectrum shown in Fig. 6.2 apparently prove the adequacy of this simple description. In fact, although the potential of interaction of the ion with the atom is greatly shielded and thus is short-ranged, there is a domain where ions simultaneously “feel” the repulsion effect from several surface atoms. While the ion trajectory “aimed” at maximum approaching the surface atom can be only slightly distorted due to the influence of the neighboring atoms, the ions at “intermediate” trajectories can have comparable scattering cross-sections at several atoms. Indeed, it is obvious that at very small angles of sliding fall, scattering at the single atom is impossible (every surface atom will be in the shading cone of the neighboring atoms. Ions, however, can “slide” on the repulsion potential of several atoms. The simplest way to evaluate some effects of repeated scattering is to conduct calculations in one-dimensional case for a linear regular “chain” of atoms. Such calculations cover many phenomena which result in emission in the plane of incidence (which is usually studied) and they are closely connected with scattering along the azimuth with low indices at the monocrystal surface. In calculations that take into account scattering from all ions of the chain (up to ten ions), the ions are viewed, "shot" along one of the parallel trajectories which build a regular net. Thus, a beam is modulated numerically which falls in the given direction. Ion emission for every trajectory may then be represented on the dependency chart of energy upon the scattering angle. The examples of such results are shown in Fig. 6.6., where the calculation results for Ar^+ ions with energy 1 keV scattered on the chain of Cu atoms with the distance between each other 2.55 A (which corresponds to the distance between the atoms in azimuth direction<110> at the surface of Cu (100) at the sliding fall angles (i. e. the angles between the surface plane and the ion fall direction) 25 and 30°. The calculation results reveal the presence of two typical “loops” of scattering. Since every point corresponds to the trajectory at the regular cell, density of points in each position on the loop indicates relative probability of this phenomenon. Besides, the presence of loops, as we can see it from the picture, causes two major features: existence of minimum and maximum scattering angles and presence of two different energy values at the same scattering angle. The minimum scattering angle is connected with the minimum value of the sliding output angle as a result of repeated (“sliding”) scattering on the way outside. Maximum possible scattering angle is affected only by the fall under the scattering angle

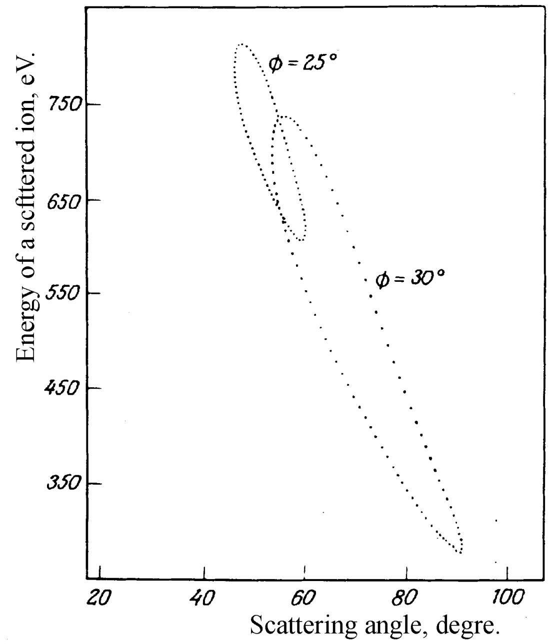

Fig. 6.6. Dependence "loops" of scattered ions energy upon the scattering angle for Ar^+ ions with energy 1 keV, scattered at the regular linear chain of atoms Si with interatomic distance 2.55 A. The calculation results refer to the sliding angles of 25 and 30°.

and great scattering which exclude the possibility of “frontal” hit into the atom causing significant angle scattering. The studies of trajectories in the scattering process show that the loop structure describes two fundamentally different types of scattering. The low-energy part of the loop corresponds to the scattering mainly on the one surface atom (pseudo-binary collisions), whereas its upper part is connected with the ions which are exposed to double collision when two atoms contribute significantly to scattering. Such act of scattering is shown diagrammatically in Fig. 6.7. It has been found that two separate acts of scattering result in less full energy loss than one scattering at the same resulting angle. Though such behavior is typical for all SIS under all conditions, the results presented in Fig. 6.7 have been obtained under extreme conditions. Importance of double collision and small width of scattering loops (at scattering angles) are typical of acute scattering (to which heavy ions with low energy make a great contribution) and of sliding fall. So, with the same calculations when Ar$^+$ ions are replaced by He$^+$ ions we will have a scattering loop without maximum scattering angle with the smallest minimum angle and significantly lesser density of points in the upper part of the loop (double scattering) with respect to the lower part. Thus, under such conditions the minimum scattering angle remains to exist, but as for the rest, the results are mainly determined by acts of single scattering. However, when Ne$^+$ and Ar$^+$ ions are scattered, the additional peak of double scattering is observed in the energy spectrum even at higher energies. Moreover, as it follows from Fig. 6.7, the density of points in certain interval of scattering angles *dθ* near the ends of the loops is high. Therefore, at the scattering on the angles close to maximum and minimum values, stronger signals are observed. Heat variations, however, reduce this effect, violating the strict periodicity of chains and resulting in scattering of points at the calculated scattering loops. In fact, repeated scattering is not limited by the plane of incidence; and, therefore, in the calculations for the real three-dimensional system, scattering along surface atom “channels” in the form of greatly broken trajectories was found.

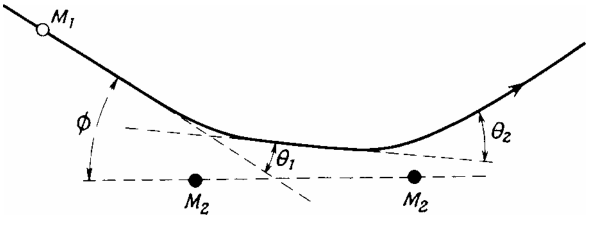

Fig. 6.7. The plan of a double scattering for bombarding ion on the next atoms of a surface in a plane of incidence; θ_1 and θ_2 - the corresponding scattering angles.

Although such calculations show that for example, in the scattering spectrums of He$^+$ ions with energy 1 keV, the structure conditioned by repeated scattering must appear much weaker than it follows from Fig. 6.7, the absence of such structure in many experiments with Ne$^+$ may be also linked with another effect- *neutralization effect.* The case is that when the flying ion of inert gas approaches or moves away from the surface, electron exchange between the ion and the surface may result in neutralization of the ion and consequently in its falling out of the registered spectrum of scattered ions. The mechanism of this process is discussed in detail in chapter 6.3. The typical value of neutralization probability P_{neutr} for scattering of He$^+$ ions with energy 1 keV at the metallic surface after taking into account possible neutralization of both the flying and the scattered ion may be 10^{-2} or less. As a result, any scattering process at which the ions are kept in direct proximity from the surface for a long time (for example, in double scattering) is connected with great increase in neutralization probability. Moreover, these high values of significantly increase surface sensitivity of the method: the ions penetrating under the upper layer of atoms are neutralized with much greater probability. Thus, the inverse dependency of neutralization probability upon speed and consequently upon energy increases surface sensitivity at low energies like in the case of shading at elastic scattering. The full detected ions yield *Y* is determined by the following expression:

$$Y = \frac{N_{\det ect}}{N_{fall}} = \sigma P_{neutr}\ , \qquad (6.9)$$

where N_{fall} – the number of falling ions. First this yield increases and then decreases as the energy grows.

Taking into account the described processes of shading and neutralization we see that intensity I_i of ions scattered from the type i scatterer into the element of the solid angle $\Delta\Omega$ is proportional to initial intensity I_0, scatterers number N_i (cm^{-2}), neutralization probability P_i, differential cross-section of scattering $d\sigma_i(\theta,\varphi)/d\Omega$ [cm^2/sr], and shading coefficient α_i for i- component at the:

$$I_i \approx I_0 N_i P_i \alpha_i \frac{d\sigma_i(\theta,\varphi)}{d\Omega}\Delta\Omega\ . \tag{6.10}$$

Thus the relative value of scattering signals (height of peaks in the energy spectrum of the scattered ions) enables to predict the relative number of scatterers. For the surface covered with adsorbate, formula (6.10) has the following form:

$$I_i(\gamma) \approx I_0\left[N_s - \alpha_i(\gamma)N_a\right]\frac{d\sigma_s}{d\Omega}\Delta\Omega P_s(\gamma) \tag{6.11}$$

indices *s* and *a* refer respectively to the substrate and adsorbate, γ is the degree of covering. We see from (6.11) that the intensity of peaks of single scattering is determined not only by the concentration of atoms at the surface but also by the shading coefficient α_i which depends on their position.

6.1.2 Structural effects in slow ions scattering

From the aforesaid we can state that due to neutralization and shading at elastic scattering SIS-method is extremely sensitive to the surface. Due to the same circumstances SIS is used for obtaining simple structural information. For example, with SIS in the conditions when only the upper layer of atoms is sounded we can distinguish whether adsorbate particles are at the surface or in the near-surface layer. It is supposed that most adsorbates are located at the surface although there exist examples of interlayer adsorption. Another example is as follows: at adsorption of CO molecule at the surface there arise questions concerning its orientation: whether this molecule stands at the surface with one of its ends (and with what end exactly), lies at the surface or dissociates. In these three cases the signals of ion scattering on the surface atoms of C and O will correlate completely differently. Of course, for determining the relative value of these signals it is necessary to introduce some corrections which take into account different sensitivities of the SIS method conditioned by the difference of cross cuts of elastic scattering and neutralization.

At adsorption which concerns only monolayer sectors the substrate atoms generally will be only partially shaded by adsorbate atoms. If we suppose, however, that the adsorbate atoms occupy well-determined adsorption positions as regards the substrate atoms, the value of substrate shading must depend on the polar and azimuth angles of ion fall and on the width of shading cone. By changing these conditions we can get shading cones which cover the substrate atoms. This enables to obtain data on the condition of the local field adsorbate-surface. Besides, on the rough surface where the adsorbate atoms may be located rather deeply as regards the surface, we can even observe directional shading of the adsorbate atoms by the substrate atoms. For example, when we study adsorption of O atoms at

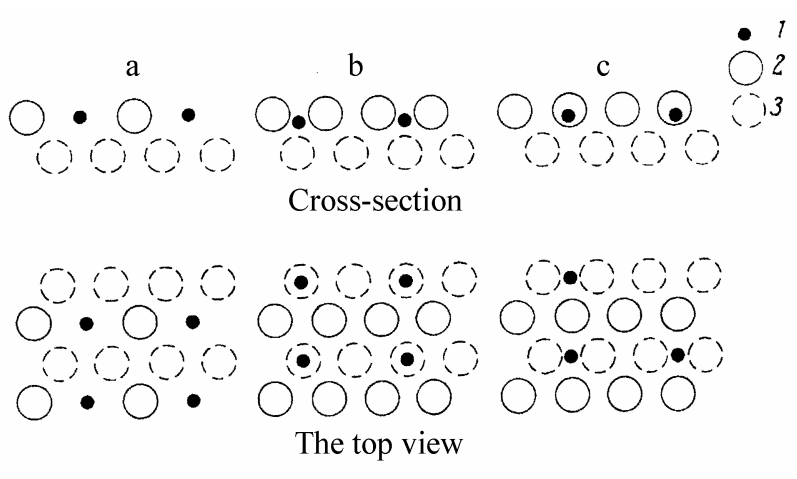

Fig. 6.8. Models of structure (2×1) at the surface {110} fcc of metal: 1 – adsorbare atoms; 2 – atom of the upper layer of the substrate; 3 – atom of the layer succeeding the upper layer of the substrate.

fcc surface {110} for obtaining the structure of the upper layer (2x1), there are three possible structure models shown in Fig. 6.8. These are either reconstruction of the upper layer when O atoms replace half of the atoms of the substrate upper layer (Fig. 6.8 a.), or adsorption of O in channels at the surface or in the places directly above the succeeding layer of substrate atoms (Fig.6.8, b), or adsorption with formation of bridge bond between these atoms (Fig. 6.8, c). Some considerations may be expressed concerning creation of bridge bond between the atoms of the substrate upper layer. In many cases azimuth anisotropy which should be expected for the scattering signals from atoms of O and of the substrate is absolutely different. For example, if atoms of O build any structure above the upper layer of the substrate, we should expect insignificant azimuth anisotropy of the signal from these atoms. If O atom is located in the hollow channels (b or c in Fig. 6.8.) under the upper layer of the substrate, acute shading of O should be expected in direction <110> (especially for model c), and it won't be observed in direction.

However, the stated qualitative conclusions are difficult to ground quantitatively, since it requires the exact width of shading cone which may vary significantly in calculations depending on the used model potential. Besides, shading depends not only on elastic scattering but also on neutralization processes which should be described on the basis of the process of local ion -atom interaction and not only ion-surface interaction. If we suppose that the dependency of neutralization speed R_n upon the distance to any atom of the surface has the form $R_n=A\exp(-as)$[1], neutralization speeds become dependant on the ion near the surface and thus result in azimuth anisotropy even if elastic shading is absent. As a result, the shading picture is created, composed of the "hard" cone of elastic shading surrounded by the "soft neutralization cloud" exponentially decreasing with distance. One of the consequences of this approach is that this broad "soft" shading may make SIS insensitive to the details of the local structure adsorbate-substrate, at least in case of high symmetry of substrate surfaces, though it doesn't decrease the value of the method from the point of view of obtaining qualitative data on the structure.

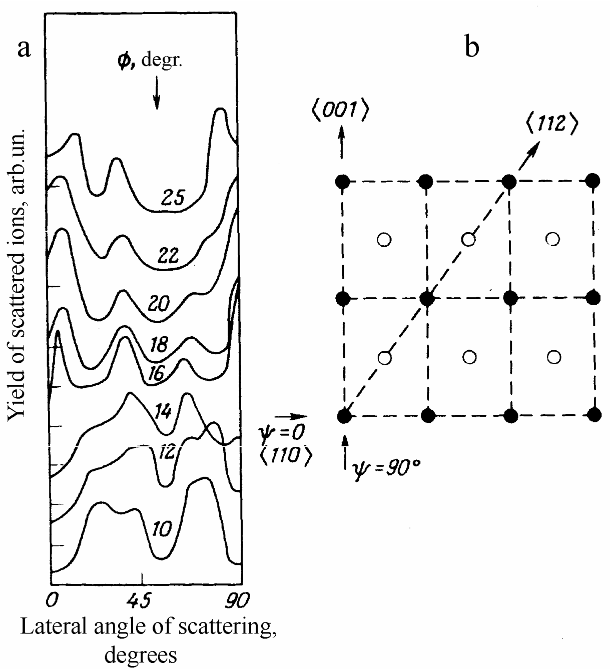

Fig. 6.9. **a** - Scatteringyield of Ne + ions with energy 5 кэВ along a normal line to surface Cu {110} depending on an azimuth of slope of an ion beam for various slip angles; **b** - the top view on a surface (light circles figure atoms of the second layer) with the indicating of some directions with the least atomic spacing in a chain.

The alternative method of obtaining structural information with the help of SIS is based on the use of the conditions under which neutralization is not a domineering process. So the effects of repeated scattering may be observed. Structural studies may be carried out with one of the two methods. When the small scattering angle is chosen (i.e. near the direction of mirror reflection) intensive peak of double scattering may be observed. It is possible to use this peak energy and its dependency upon the azimuth of fall directions for determining interatomic distance ("chain periodicity") along these directions. In such a way, for example, it is possible to note periodicity doubling due to the surface reconstruction (see Fig. 6.8, a). In contrast to it, when we observe scattered ions emitted along the normal to the surface (at relatively big scattering angles) and study azimuth effects conditioned by the difference of interatomic distances in various directions, we can study self-shading and

---

[1] For more detailed information on this dependency see chapter 6.3, formula (6.13)

"focusing" along atomic rows. This phenomenon of "focusing" is simply explained by the chart of trajectories given in Fig. 6.5. Here in the model of single scattering we see that while the ion flow coming inside the shading cone is equal to zero, the density of the flow right behind the cone's edge is much higher than that far from the cone. This is particularly true at lager distances behind the first scatterer when the increase in the density of the flow occurs due to the ions scattered by it at relatively small angels. Thus, if the second scatterer is located directly behind the shading cone, the increased signal will be observed (provided it is not rejected by neutralization), which is the signal of pseudo single and not genuinely double scattering and which, as it is seen from Fig. 6.6. may give ions with substantively different energy. Consequently, for definite interatomic distances at very small sliding angles acute shading should occur; while as the fall angle decreases, the scattering signal will give an abrupt peak at a certain critical angle before it reaches its usual value corresponding to single scattering. Of course, as we have already mentioned, the model of the shading cone refers to the single scatterer and strictly speaking cannot be applied to "chain" scattering. Nevertheless, the basic features of this model may be suitable for qualitative considering of chain scattering. Some effects of this type are seen from the results presented in Fig 6.9. It should be noted that at small angles of sliding fall the scattering signal of Ne^+ ions with energy 5 keV at the surface of Si {110} is weak in the direction of the most dense packing <100>, <110> and <211>, but at $\phi \sim 16°$ along the direction <100> the increased signal is seen connected with focusing. Most elements of the given azimuth dependences may be reproduced by simple calculations of repeated elastic scattering. Thus, the changes of these results under adsorption may be used for obtaining data on the nature of changes in structure. Moreover, investigation of the known structures of pure surfaces enables to prove experimentally some critical dimensions of shading cones, allowing to make the choice of the model potential less arbitrary. The studies that use these relatively high-energy and heavy ions still have difficulties. In particular substantial deformations of the surface occur and most of such adsorption studies involve the experiments on studying "dynamic adsorption", when the surface constantly exchanges charges with the adsorbate and the surface temperature may be increased for quick elimination of the results of destruction. In such a way stable condition may be studied.

On the other hand, the obtained structure may differ from the results of statistic studies with other methods at lower temperatures.

6.2 Energy-mass-spectrometry of secondary ions (EMSSI)

The basis of EMSSI constitutes the phenomenon of secondary ion emission (SIE) at sputtering of solids surface by ions beams. In chapters 1.2.1, 4.3, 4.4 the data are given on the nature of SIE and ion sputtering; the mechanisms causing these phenomena are considered in detail.

The particles sputtered in the process of bombardment carry the information on the structure of the material exposed to bombardment, and the masses of charged components of these particles are determined with the help of usual mass-spectrometers (magnetic or quadruple). The possibility of implementing energy analyzers into the flight channel of secondary ions (from the sputtered surface to the detector) allows to measure energy distributions of each type of ions. Joint analysis of energy and mass spectrums resulted in creation of EMSSI. Unlike the widely used method of secondary *ion mass-spectrometry*, this method is relatively new; it has been worked out within the last two decades. Fig. 6.10 shows the typical diagram of the energy-mass- spectrometer. So, if we deal only with mass-spectrum analysis of secondary ions to obtain information on element and isotope composition, we speak about secondary ion mass-spectrometry (SIMS). In this case the source of information is the spectrum of secondary ions masses obtained with mass-analyzer 10 (Fig. 6.10) under constant voltage at the energy analyzer 9.

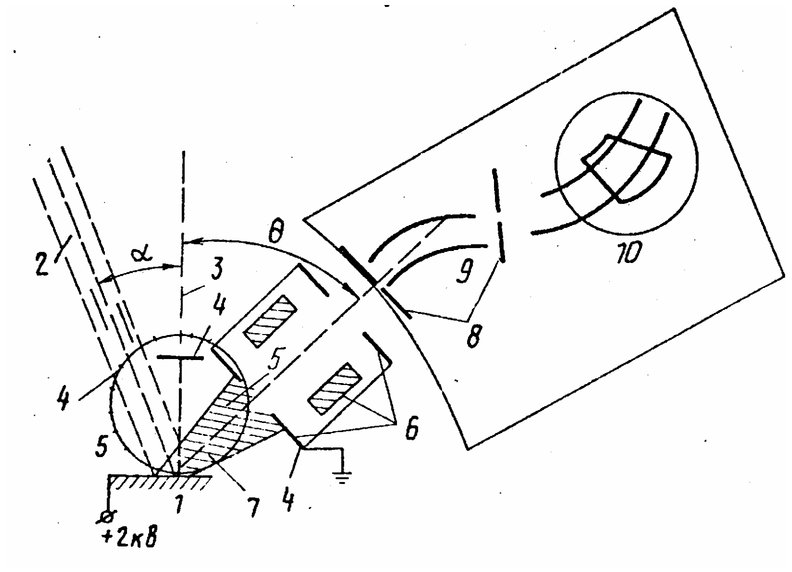

Fig. 6.10. Diagram of analytical part of energy-mass- spectrometer of secondary ions: 1 – studied sample; 2 – ion beam; 3 – normal to the surface; 4 – grounded electrodes; 5 – entrance slit; 6– 3-electrode lens; 7 – solid angle of secondary ions selection; 8 – entrance and output slit of energy analyzer; 9 – energy analyzer; 10 – mass analyzer; α and θ – falling angles of primary ions and collection angles of secondary ion respectively.

If we study surface chemical compounds and fundamental energy parameters (energy of atom's bond, electron's work function) in addition to mass spectrums energy spectrums are measured. In this case with the help of analyzer 10 the clear line of mass-spectrum is distinguished, and by varying voltage at the energy analyzer energy spectrum of ions of the type we are interested in is measured. Thus, the joint analysis of mass and energy spectrums is the essence of EMSSI. More detailed information can be obtained by analyzing mass spectrums and energy spectrums of secondary ions at different bombardment and registration angles. This method can be called EMSSI with angle resolution (EMSSI AR); currently it is being worked out in some laboratories. Generally speaking, SIMS "grew" out of EMSSI; so, first we would like to describe the possibilities of SIMS without energy analysis, and then state the method of chemical composition studies with the use of energy analysis.

6.2.1 Basic possibilities and regularities of secondary ion mass-spectrometry (SIMS)

Initial studying of SIMS was motivated not by surface studies but by the desire to get the ways of applying mass-spectrometry to composition analysis and identification of solids and to layer-by-layer analysis of thin films composition. SIMS is especially suitable for such studies, as the analyzing beam simultaneously provides the signal of SIMS and sputtering (i.e. profiling). Here the sputtered particles reflect the actual element and chemical composition of the near-surface layer of the solid. Besides, ion beams focus easily and they are easy to control, so, while scanning the surface by the beam we can obtain the maps of element and admixtures distribution characterizing the distribution of chemical composition through the surface. Thus, three-dimensional element and chemical analysis are possible. At the same time with energies and densities of the current of primary ions typical of SIMS (see below) the sputtered particles come from the upper one-, two-atom surface layers, so SIMS is a surface-sensitive method and it should provide data from the depths with the same scale as other methods of surface spectroscopy. The potential drawback of SIMS is the fact, that it is a destructive method by its nature unlike most electron methods (although they also may cause defects). On the other hand, when digital methods of registration and defocused beams of bombarding ions are used, element surface analysis may be carried out for the time corresponding to evacuation of only small part of the monolayer. This working mode is called "statistic SIMS" unlike "dynamic SIMS" which uses beams with high density of bombarding ions current. This density provides high speeds of material evacuation, which finally results in extreme sensitivity to element composition. The typical current density conditions in these two types of SIMS may be as follows: for the static one – $J=1\ nA\cdot cm^{-2}$; for the dynamic one (i.e. 10 pA in the beam with diameter 1mm) up to (i.e. 10 pA in the beam with diameter 1μm or 10 μA in the beam with diameter 1 mm. The speeds of material evacuation in these two methods account for approximately 1 Å/h and 10 μm/h respectively. Ar$^+$ ions with energies from several hundreds of eV to 10 keV are bombarding ions; though in some cases the ions of chemically active and not inert gases are used. As it has been already mentioned, the basic information obtained in SIMS experiments is the mass spectrum of secondary ions usually positive, although in many cases mass spectrum of negative ions of ionized fragments of chemical compounds may turn out to be more informative. Fig. 6.11 shows spectrums of positively and negatively charged ions obtained under sputtering of LiF surface bombarded by Ar$^+$ ions with energy 1.3 keV at low density of the falling flow. The particular feature of these spectrums is abundance of information due to the big number of various molecular ions obtained at sputtering of the surface which consists of small number of elements. On the other hand, for this material characterized by the high rate of ion chemical bond, some peculiarities are revealed in the spectrums which can be predicted. In the spectrums of positive ions electropositive Li and similar admixtures prevail which in several cases are combined with neutral clusters with space stehiometry [Li$^+$ (LiF), Li$^+$(LiF)$_2$, etc.], whereas in the spectrum of negative ions electronegative particles and similar combinations of[F$^-$, (LiF)F$^-$, (LiF)$_2$F$^-$, etc.] appear. Besides, as it is seen from Fig. 6.11, in these spectrums the sputtering process of big clusters is characterized by the significant decline of secondary ions yield as the cluster's mass increases. Besides, in the spectrums shown in Fig. 6.11 multicharged ions are not seen. Such ions are usually observed, though these could be both multicharged atom ions and multicharged molecular ions and clusters. This is illustrated by Fig 6.12, where the yields of atomic and both one-charged and two-, three-charged clusters are presented depending on the energy of primary ions sputtering silicon surface. The unique feature of SIMS if compared to most other analytic methods of surface studies is the possibility of isotope distinction. This possibility is illustrated by the mass spectrum in Fig. 6.13 which presents the record of signals from separate isotopes of Ru and Pd during the analysis of palladium by the SIMS method. It

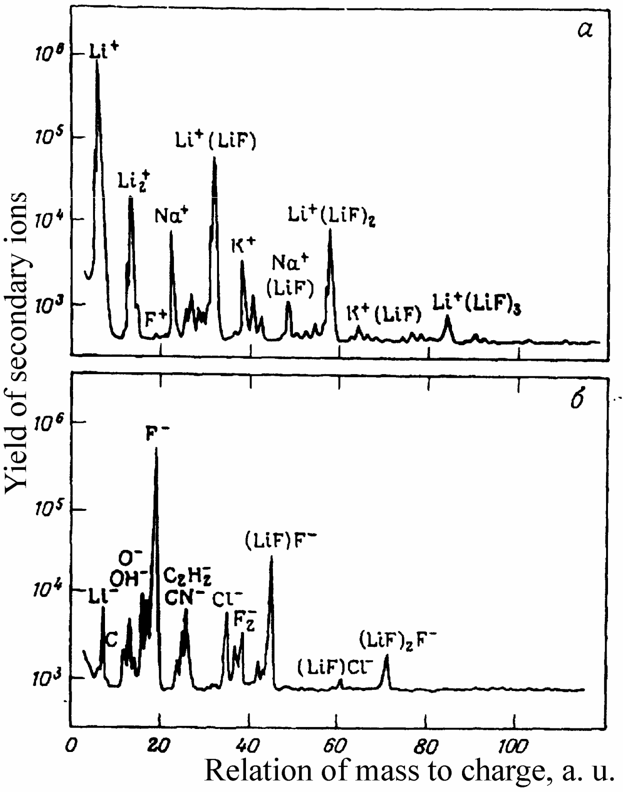

Fig. 6.11. Mass spectrums of positive (*a*) and negative *(б)* ions at bombardment of LiF surface {100} by Ar$^+$ ions with energy 1.3 keV.

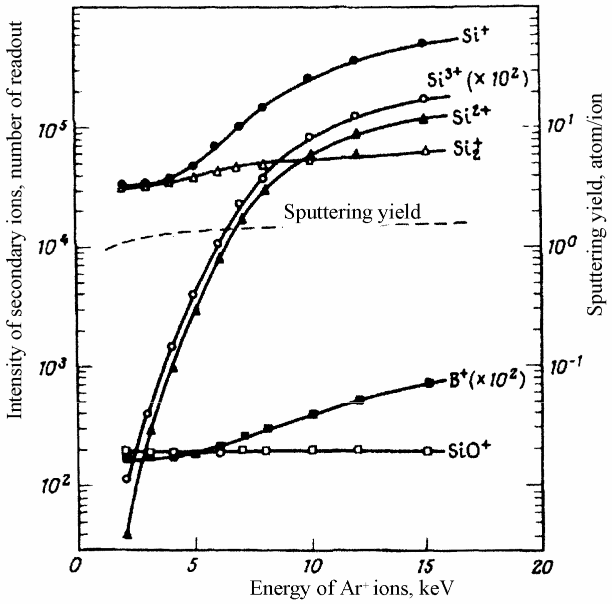

Fig. 6.12. Yield of secondary ions depending on the energy of primary Ar$^+$ ions at scattering of silicon surface.

should be noted that intensiveness correlation of isotope lines in SIMS corresponds to the proportion which follows from natural distribution of these isotopes. This peculiarity is potentially valuable for studies of surface chemical reactions with the use of "marked" chemical reagents. It should be mentioned that it is also possible to study hydrogen isotopes which cannot be studied by any other known methods of surface spectroscopy, except SIMS.

Obtaining qualitative data on the composition of the sputtered layer form mass spectrums of ions requires understanding of processes of scattering and ion-formation, whose possible mechanisms are discussed in detail in chapters 4.3 and 4.4 of the current manual. It also requires the awareness of empirically established correlation of the relative ion yield and full (ions +neutral particles) sputtering coefficient. The experiment shows that the correlation between these two values is sensitive to the type of falling ions, their energy, method of mass spectrum measurement, proportion of elements in the studied sample (matrix effect) and even partial gas pressure in the analyzing chamber. All this makes the qualitative analysis by SIMS method extremely difficult. Currently the problem of qualitative analysis is solved with the help of models when the sputtering mass spectrum of the studied sample is compared with the mass spectrum of the sample whose composition is well-known. Due to matrix effect there can't be a universal model; on the contrary, the models can be used for studying limited range of materials whose composition and properties slightly differ (for example, for stainless steel with nickel content from 5 to 20% one model is required; if the content of nickel is higher another model is used.

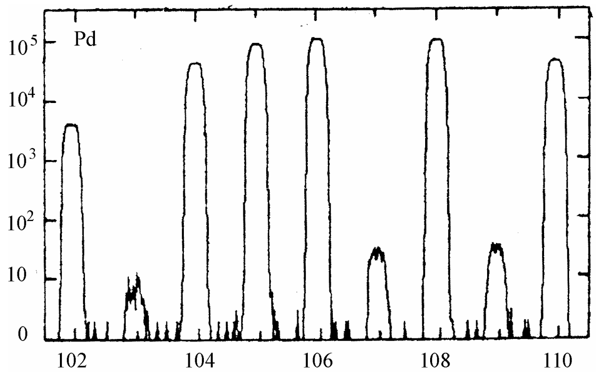

Fig. 6.13. Mass-spectrum of secondary ions of palladium isotope. Along the horizontal axis there are values of mass numbers of isotopes.

6.2.2 Layer-by-layer chemical analysis by EMSSI method

For a more detailed chemical analysis than that obtained by SIMS method (according to the fragments of chemical compounds in mass spectrums) energy spectrums of secondary ions are used. On the whole the procedure consists in the following (Fig. 6.10.)

The sample surfaces 1 are sputtered with the primary ion beam 2 with energy 1–10 keV at some angle α to the normal of the sample's surface; mass spectrums of secondary ions are registered. These spectrums are registered at constant voltage at the coats of the energy analyzer 9 which provides reliable registration of mass spectrums. In mass spectrums, ion lines of basic elements from the composition of the sputtered layer and lines of molecular ions – possible fragments of chemical compounds in the sputtered layer are distinguished. After it energy spectrums of secondary ions of basic elements discovered in mass spectrums are measured. This measurement is performed at angle θ depending on the definite mount. If chemical compounds are present in the sputtered layer, molecular fragments of these compounds may be observed in mass spectrums; and in energy spectrums of secondary ions of the definite element which is the part of several chemical compounds particular features (peaks) are observed due to the fact that ions of one and the same element, sputtered from different chemical compounds, have different energy distributions with most probable energies which are proportional to the values of formation energies (Gibbs energies) for these compound. The superposition of these energy distributions gives the registered total spectrum with separate peculiarities. According to the energies of these peculiarities when compared to the reference values of formation energies, the chemical compound is identified which sputtering resulted in this peak. Energy analyzer 9 must provide measurement of energy spectrums with resolution which enables to separate different features of the spectrum. When formation energies of separate compounds in the sample differ by several times the sufficient resolution of the energy analyzer is ΔE=1–5eV.

Then the surface layer is permanently sputtered, full mass spectrums and energy spectrums of those secondary ions which constitute the chemical compounds are registered (i.e. energy spectrums with complex structure are measured layer-by-layer) After full sputtering of the surface layer and yield of the probe beam to the substrate of the compound which is known a priori, stabilization of the compound and intensiveness of mass spectrums lines occurs together with disappearance or almost full elimination of separate peaks in energy spectrums (the latter is true if the substrate is chemically homogeneous). By observing kinetics (or dependency of intensiveness upon thickness of the sputtered layer, what is the same) of lines of molecular ions in mass spectrums and separate peaks in energy spectrums we can make conclusions about presence and relative content of certain chemical compounds in the layers.

Thus, we can increase reliability of studies of chemical composition of surface layers of metals and semi-conductors by simultaneous use of two sources of information (mass spectrums and energy spectrums) obtained as a result of one experiment.

Experiment geometry, in particular the values of angles of secondary ions selection θ (Fig. 6.10), bombardment angles α and the angle $\alpha+\theta$ play the key role in determining the structure of energy spectrums of secondary ions linked with some chemical non-homogeneities. The studies show that the peaks corresponding to certain chemical compounds in energy spectrums appear most boldly if α=0–20°, and θ=50–60°. What concerns the influence of angle α on energy spectrums the following is true: according to the cascade theory of sputtering (chapter 4.3.2), energy spectrum of secondary ions with the narrow peak in the low-energy field will be observed provided there is a small contribution of ionized recoil atoms and atoms obtained as a result of energy exchange of the primary ion within the small number of hits with target atoms (i.e. the contribution of non-cascade ions is small). Therefore, at angles α >20°, when the contribution of non-cascade ions to the energy spectrum becomes significant even for targets, non-homogenous according to their chemical composition, energy spectrums of secondary ions are have the shape of the dome which embraces energy range from several to tens and hundreds eV. Hence, we see that we cannot expect separate features linked with chemical non-homogeneity of targets at angles α larger than 20°. As an example of usage of the above mentioned method let's consider the studies of the chemical composition of anode oxide on indium arsenide. The data presented below have been obtained with the beam of primary nitrogen ions N_2^+ with energy 5 keV and current density $J\sim 5\cdot 10^{-5} A/cm^2$. The incidence angle α of the primary beam at sample 1 is $\alpha\sim 15°$, selection angle is $\theta\sim 55^0$. At sputtering of the upper layer of the oxide film on InAs the mass spectrum has been revealed composed of the lines corresponding to ions In^+, As^+, O^+, In_3O^+, In_2O^+, $In_3O_2^+$, In_3O^+, InO^+, $InOH^+$, In_2SO^+, $In_2AsO_2^+$. Then the energy spectrums of In^+, As^+, O^+ ions were measured with the resolution ~1 eV. The number of specific features was discovered in the energy spectrum of In^+ ions at sputtering the upper layer of the oxide film. Then the film was sputtered with layer-by-layer registration of mass and energy spectrums of In^+ ions. Fig 6.14 shows the energy spectrums of In^+ ions at layer-by-layer sputtering of 1200 Å – thick oxide film on indium arsenide.

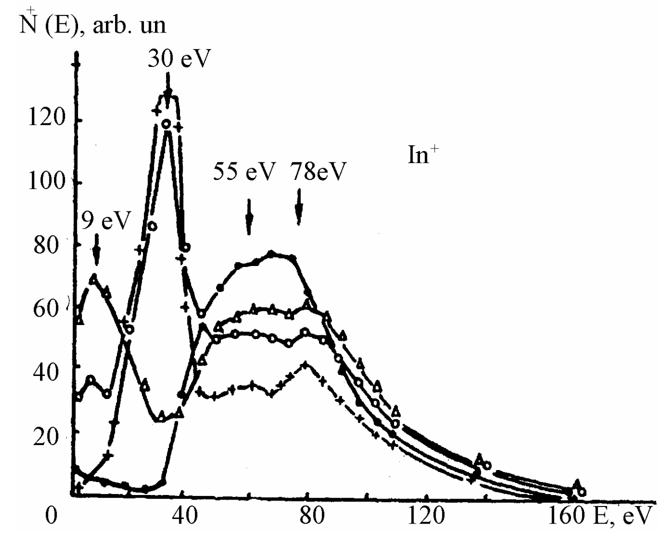

Fig. 6.14. Energy spectrums of secondary In^+ ions obtained at sputtering of oxide film on indium arsenide from different depths from the film surface. See the text.

Spectrums numbers correspond to the time since the beginning of sputtering: 9 – from 11 to 20 min, 11 – from 12 to 250 min, 13 – 330 min, 14 – 450 min. Only 4 out of 20 curves are presented, which are obtained at different depths form the film surface; the rest 16 curves characterizing intermediate sputtering stages (between the presented ones) have respectively an intermediate form between the presented curves. The depth from which a certain spectrum is obtained is determined with the following formula: $L=V_p{\cdot}t$, where t–sputtering time; V_p–average sputtering speed determined as $V_p=l/t$, where l–crater's depth measured after termination of the analysis, for example, with the profilometer–profilograph. Curve 11 obtained at sputtering of the upper layer of the film is conditioned by the ions knocked from the oxides with strong bond. These are the following oxides In_2AsO_4, $In_2O_3^+$. The low-energy peak (~9 eV) at curve 12 is created by the ions from the oxides with weak bond, and the dome within the energy range 50-80 eV is created by the same ions as the dome within this energy range at curve 11; these are the ions from the oxides with strong bond. Curve 13 corresponds to the case when the part of the probing beam comes out to the substrate of InAs. Here the ions from the oxides with strong bond (50–80 eV), from the oxides with weak bond (0–20 eV) and from the substrate (acute peak is within the range of 25–35 eV) are observed. Finally, at curve 14 obtained after prolonged etching of the sample by the probing beam only the ions from the substrate of InAs and from the oxides with strong bond are observed. Here, at the bottom of the crater the optical microscope detects mosaic islands of oxides at the substrate polished by the probing beam.

To visualize distribution of the above-mentioned compounds according to their thickness, the obtained spectrums are processed by creating intensiveness dependencies of the relevant peaks upon sputtering time (upon the thickness of the sputtered layer). All the 20 energy spectrums are analyzed as a whole. Fig 6.15 shows the dependencies characterizing, in compliance with the above-mentioned, distribution according to the film thickness of the oxides with strong bond (curves 1 and 2), weak bond (curves 3) and from the substrate (the part of curve 4 after 350 minutes of sputtering). The intensiveness dependencies of some mass spectrum lines upon the time are similar to the dependencies presented in Fig. 6.15. So, the intensiveness of mass lines corresponding to In_3O^+, In_2AsO^+, $ln_2AsO_2^+$ ions changes in a similar manner as curves 1 and 2; the intensivenesses of mass lines corresponding to InO^+, InOH ions change in a similar manner as curve 3; after the yield of the probing beam to the substrate of InAs the intensiveness of lines corresponding to In_2^+, In_3^+, $InAs^+$, In_2As^+ ions appears or significantly increase in the mass spectrum.

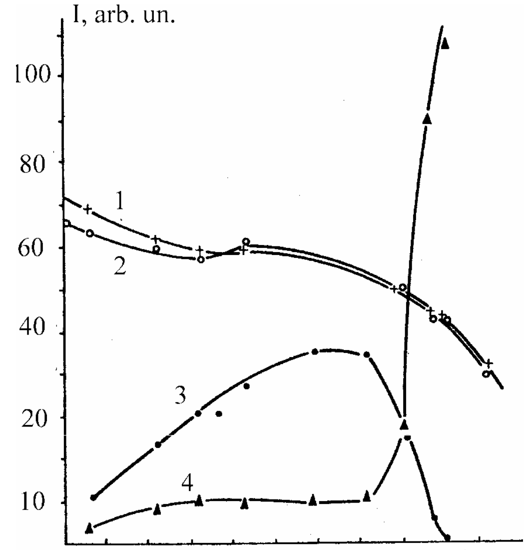

Fig. 6.15. Dependencies of In^+ ions yield from different compounds upon the time of sputtering (upon the depth of layer bedding) at sputtering of the oxide film. See the text.

Thus, in accordance with the above stated, the method of layer-by-layer determination of the chemical composition of the system "oxide on InAs" as well as other similar systems may be implemented in the following way:

1) The mass and energy spectrums of the ions of one of the basic elements of the compound of the studied sample are measured layer-by-layer (see Fig. 6.14);
2) The series of energies corresponding to the peaks in the energy spectrum of ions in Fig. 6.14 are compared to the reference series of Gibbs's energies for the compounds of the chosen element. Thus, the certain peaks are compared with the certain compounds of the film, i.e. the compounds are identified

3) Identification carried out in article 2 is proven by creation of dependencies in Fig. 6.15 or rather by mass spectrums and dependencies behavior (Fig. 6.15);
4) Besides, the curves built in Fig. 6.15 characterize thickness distribution of chemical compounds including the element chosen for the energy analysis. For the considered example: curves 1 and 2 represent distribution of oxides with strong bond (In_2O_3, $InAsO_4$ etc.), curve 3 represents distribution of oxides with weak bond (In_2O, InO), 4 – distribution of InAs.

The considered method may be implemented with the use of any mounts for mass-spectroscopy of secondary ions which permit location of the energy analyzer within the geometry presented in Fig. 6.10. This method is most efficient for complicated structures ~500–1000Å thick, as when thick structures are sputtered, the effects may be observed connected with accumulation of the high dose of interstitial primary ions. In particular, when they are used as primary chemically active ions, new chemical compounds may form whose sputtering may result in emergence of additional peaks in energy spectrums.

6.3. Ion-neutralization spectroscopy (INS)

The phenomena of charge (electron) exchange between atom moving near solid surface and the surface itself create the basis for INS. The phenomenon of this class – field ionization near the metal surface was considered in part 1.2.1. Before we start discussing the essence of INS methods let's view the processes opposite to field ionization (from the viewpoint of direction of charge exchange); these are the processes of ions neutralization near the surface or, in more general wording, the processes of charge exchange between atomic particles moving near the surface and the surface.

6.3.1 Charge exchange between ions (atoms) and the surface

Fig. 6.16 presents the diagrams of four processes with which we deal when analyzing INS. The right part of each diagram of energy levels shows the band of surface metallic conductivity filled up to Fermi level; the left part presents the localized potential pit corresponding to the flying ion. Fig. 6.16*, a* demonstrates the process of resonance charge exchange. In this case the hole condition of the ion forms the extended energy level (see below); and Fermi surface level is within it. Therefore, the electron may tunnel through the potential barrier near the metal surface to the relevant level of ion energy without changing its energy, which results in *resonance neutralization*. However, if the above mentioned state of the ion really covers Fermi level, tunneling of the electron of the flying particle into metal from the state located above Fermi level is possible, which results in *resonance ionization*. Extension of the level which makes this two-way exchange possible, at least in statistics occurs due to the fact that as the ion approaches the surface, the valency levels of the ion are covered by the valency band and hybridization occurs, i.e. the so-called molecule "surface–atom" is obtained. If the extended level and Fermi level are overlapped for the relatively long time, the balance between ionization and

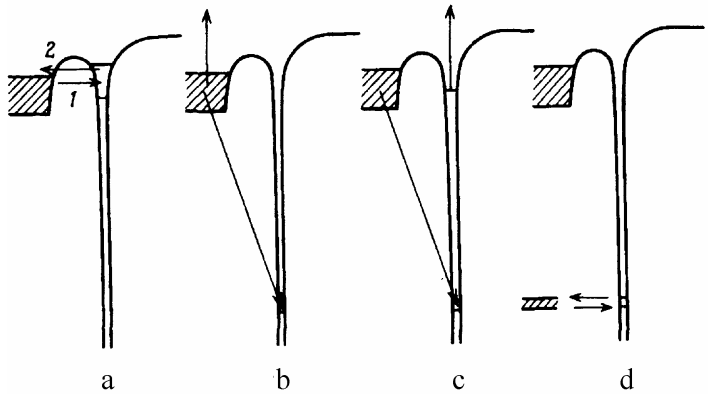

Fig. 6.16. The process scheme: a – resonance charge exchange; b – Auger-neutralization; c – Auger-relaxation; d – quasi-resonance charge exchange. The electron transfer directions at the process of neutralization and ionization are shown by arrows 1 and 2 respectively.

neutralization processes is reached; and as a result the falling particles will have a quite determined value of the average charge. If these particles were then immediately removed from the surface, their charge could be determined by the definite part of ionized and neutral particles. Implementation of these effects is possible if the flying ions have the potentials close to the value of metal work function. The ions of alkali metals usually meet this requirement.

Fig. 6.16, b shows the situation when the flying ion has the levels that according to energy are close to the filled states at the surface. In this case the electron from the zone of surface conductivity tunnels inside the potential ion pit but at the same time "falls" at the lower unfilled level giving the surplus of energy to another conductivity electron which is emitted from the solid and may be reregistered outside. This Auger-electron carries information on the density of surface states and its detecting is the essence of INS where the processes of Auger-neutralization are supposed to be domineering.

Fig 6.16, c shows the process of Auger-relaxation, when the flying particle is not an ion but an excited neutral atom. This process involves filling of the deeply-lying unfilled state of the excited atom by the conductivity electron and emission of the electron, located in the excited atom, which takes the excess energy away. The diagrams of energy levels of He and Ne atoms which have metastable excited states located near Fermi level of typical metals prove the possibility of this process.

Fig. 6.16, d shows the process at which the ions with ionization potentials corresponding to the middle of the surface conductivity band may be neutralized by the resonance. However, under these conditions resonance ionization is hardly possible, so, the exchange process becomes one-sided. The process of establishing charge balance as a result of resonance ionization will involve filling of the deeper lying unfilled level of the ion by the electron from the conductivity band.

As it has been mentioned above, at the certain stage of approaching of the ion (atom) and the surface, the changes in the energy structure (extension of atomic levels) may be interpreted from the viewpoint of creation of the molecule “surface-atom”. From the more general point of view this extension Γ may be connected by means of uncertainty principle with transition speed (possibility of transition within the unit of time) when charge exchange takes place:

$$\Gamma = \hbar R_n \, . \tag{6.12}$$

Extension and transition speed especially for large distances between the ion and the surface will be determined by overlapping the “tails” of the wave functions which may be well-approximated by the exponential function of distance from the surface s:

$$R_n = A \exp(-as), \tag{6.13}$$

where A and a – constants for the definite system surface-ion.

One of the interesting effects of INS which use ions with very low energies is that for a relatively long time most neutralization acts may take place outside the surface. This provides data that characterize the surface in a very precise way, as the neutralization acts are determined by the electron structure of the surface

The assessment of time of interaction of ions and the surface may be performed if we suppose that we deal with helium He^+ ions with energy 1 keV. It is easy to calculate that such atom passes the interatomic distance for the time equal to ~10^{-15} *s*. Such length of interaction results in extension of the level up to 1 eV in accordance with (6.12).

6.3.2 Description of neutralization processes

Studies of positive ions neutralization at the metal surface began at the end of the 1920-s. Together with these studies it was discovered that some of neutral He atoms colliding with the

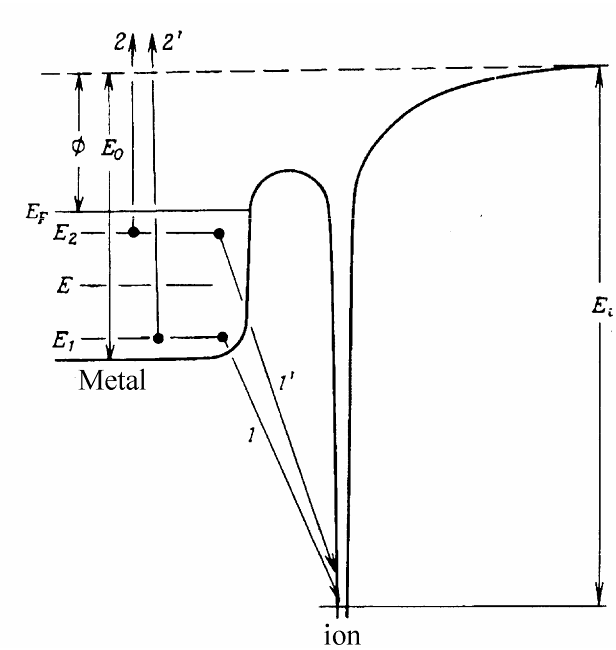

Fig. 6.17. Diagram of energy levels for the ion outside the metal surface. Pairs of electron transitions 1, 2 and 1', 2' demonstrate transitions of auger-type in the process of ion neutralization. E_i – ionization energy; Φ – work function; E_1 и E_2 – electron energies in the metal.

target caused electron emission. Later it was proven that these are the excited or "metastable" atoms of He* at the surface of Mo.

In both cases we speak about excited atoms which differ only by the time of excited states: the short one if dipole transition is allowed from the excited state and the relatively long one if dipole transition is forbidden. In the latter case excited state is called metastable. A slow ion with higher neutralization energy (ionization potential) reaching the metallic surface neutralizes as a result of two-electron Auger-process shown in Fig. 6.17. Let's consider this process in a more detailed way.

When the flying ion reaches the surface two electrons interact in the filled valency band of the metal exchanging energy and impulse. One of these electrons (the neutralizing one) tunnels through the potential barrier into the potential pit created by the ion and reaches the free level of the main atomic state whose energy is by E_i lower that the vacuum level. The energy released at this transition is transmitted to the second interacting electron which now may have sufficient energy for yield from the metal if it moves in the right direction. The latter will be true if the impulse component perpendicular to the surface is relatively high. Such transitions of Auger-type can occur from any part within the filled valency band, so, the emitted electrons have energy in the certain range of values, and they are not monoenergetic. Outside the surface this distribution of electrons according to energy may be measured. As we have already mentioned, neutralization of ions on metallic surface is a truly surface process unlike the processes taking place at some depth inside the metal. The emitted electrons appear mainly outside the metallic surface, or in extreme case in the first atomic layer of the surface. Slow flying ions involve into neutralization process those metal electrons whose "tails" of the wave functions are overlapped by the wave function of the ion. The presence of adsorbed atoms at the metal surface change electron states in the near-surface region. These changes significantly affect the energy spectrums of emitted ions. The example of the observed changes of such type is given in Fig. 6.18, where distribution of emitted electrons according to energy for He^+ ions with kinetic energy 5 eV is shown. Here the data for atomically pure surfaces of Ni{100}, Cu{100}, and Ge{111} (Fig. 6.18, a) are given and for the surface of Ni{l00}, covered by the layers of adsorbed O, S and Se (Fig. 6.18, b). The given spectrums show that the process of ion neutralization is sensitive both to the nature of the solid and to the type of chemisorbed substance. Exactly from these spectrums the data at the surface and on the layers adsorbed on it are extracted. Before considering the ways of data extraction we will give a more detailed description of the neutralization process.

The basic functions which qualitatively characterize the process of electron emission may be expressed in terms of probability of electron yield form the metal and density of metal states. (Fig. 6.19). Using Fig. 6.18, it is easy to state the limits of energy distribution i.e. minimum and maximum energies of emitted electrons. These boundary values may be simply deduced from the energy conservation law. Thus, maximum energy $E_{кmax}$, that may be transmitted to the emitted

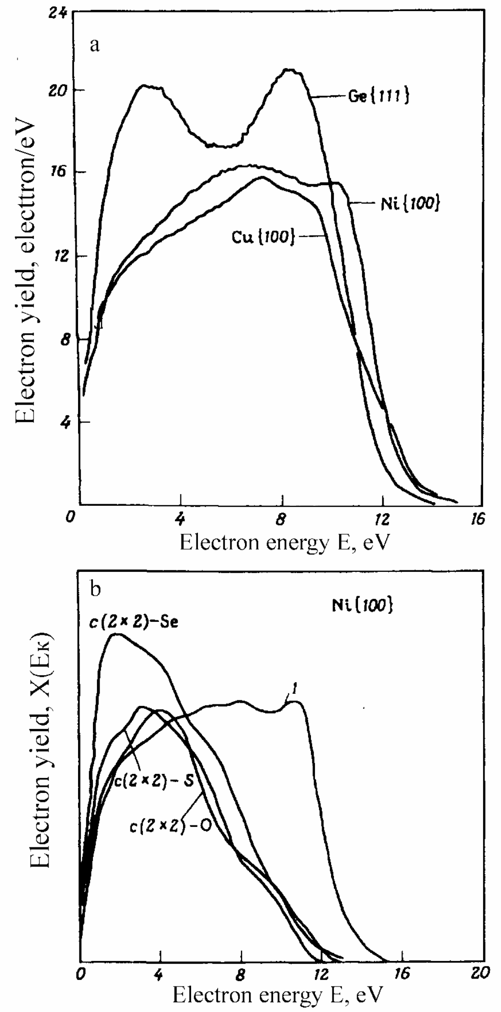

Fig. 6.18: a – Energy distribution of the emitted electrons obtained at the use of He^+ ions with kinetic energy 5 eV, falling at the surfaces of Cu, Ni and Ge; *b* – the same as a, but for the surfaces of Ni {100}, covered by the adsorbed layers of O, S or Se; 1 – pure surface.

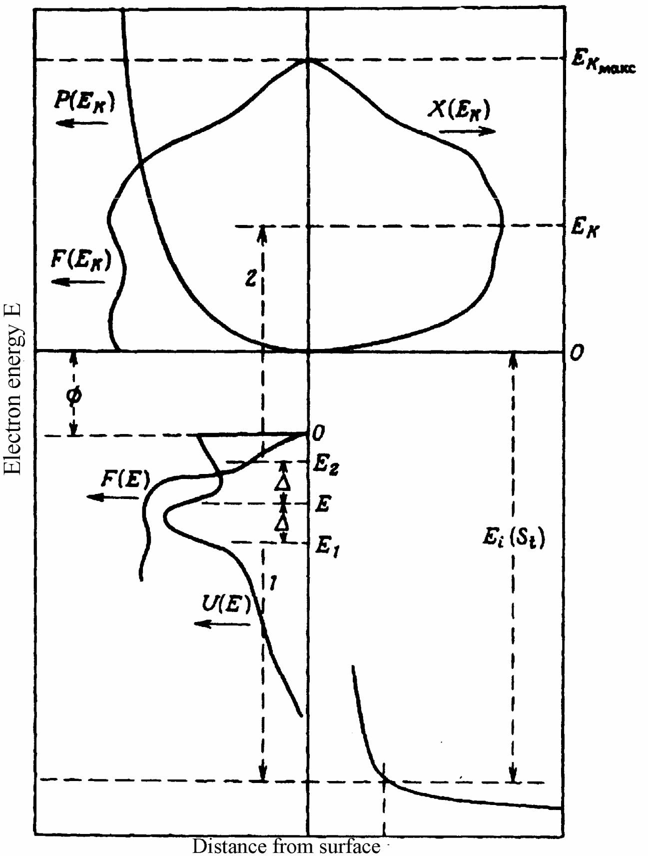

Fig. 6.19. Diagram of energy levels and functions describing the process of ion neutralization. The shape of functions *U, F, P* and *X* corresponds to the surface of Cu{111}. S – distance from the surface, S_t – distance at which electron transition occurs, E_{Kmaxc} – maximum energy of the emitted electron.

electron is determined by the expression

$$E_{Kmax} = E_i - 2\Phi , \tag{6.14}$$

where as usual, E_i – efficient ionization potential of the falling ion, Φ –metal work function. Efficient ionization potential of an atom near the metal surface is smaller than its unperturbed value. This difference is equal to classical potential of ion image. Minimum energy E_{Kmin} is determined by the expression

$$E_{K\mathrm{min}} = E_\mathrm{i} - 2E_\mathrm{F} - 2\Phi , \tag{6.15}$$

where

$$E_{K\mathrm{min}} = 0, \text{ if } E_i - 2E_\mathrm{F} < 2\Phi. \tag{6.16}$$

From (6.15), (6.16) it is clear that we should expect the shift of spectrums of emitted electrons along the axis if the work function is changed what in its turn is conditioned by chemisorption at the metal surface. In a more general case, if we ascribe energies E_1 and E_2 to electrons participating in the neutralization process, the energy of emitted electrons will be determined by the expression:

$$E_K=E_i-(E_1+\Phi)-(E_2+\Phi) \qquad (6.17)$$

While considering the process of Auger-neutralization the following simplifying suppositions are made: 1) transition probabilities for the emitted and the neutralizing electrons are supposed to be constant and do not depend on the symmetry of the valency band and electrons energy in it; 2) transition probabilities of both the emitted and the neutralizing electrons are supposed to be equal; 3) density of final states is considered constant and extension of energy levels accompanying transition is considered neglible small. As a result of such suppositions, the probability that the electron with energy in the range $E+dE$ will participate in the Auger-process is determined only by the density of initial states in the valency band $N_v(E)$. It is described by function $U(E)$ in Fig. 6.19. This function consists of two parts: $F(E)$ and $F(E_к)$ (see Fig. 6.19), corresponding to the neutralizing and the emitted electrons respectively; thus, $U(E)$ describes the distribution of these electrons according to energy inside the metal. Therefore, U(E) is used for finding energy distribution $F(E)$ of the electrons inside the metal which are excited in the process of neutralization. Emitted electrons with energy in the range dE_K near the value E_K may be obtained as result of any neutralization process, for example the one where the initial states energies of two participating electrons are located at the same distance from energy value E lying in the middle between energy E_K and the energy of atom state E_i. The values of energies E_K and E_i, meeting this requirement are determined by the proportion

$$E_K=E_i-2(E+\Phi). \qquad (6.18)$$

Equation (6.18) is obtained from (6.17) by the substitution $E_1=E_2=E.$ For initial states with energies $E_1=E+\Delta E$ and $E_2=E-\Delta E$, which are symmetrical concerning $E,$ the probability of the neutralization process which involves exactly these states should be proportional to $N_v(E+\Delta E)\cdot N_v(E-\Delta E)$, i. e. to the product of states densities at initial energies. The full probability of emergence of the excited electron with energy within the range of dE_K near E_K is described by the integral of this product over energy increment $\Delta E.$ Using the most general type of zone function $U(E)$, we can present this probability as follows

$$F(E)=\sum_{-E}^{+E}U(E+\Delta E)U(E-\Delta E)d\Delta E\,. \qquad (6.19)$$

The function of internal distribution $F(E_K)$ is obtained from function $F(E)$ by the simple substitution of E_K for E in accordance with equation (6.18) provided the given range above Fermi level is normalized at the area equal to one electron per flying ion. Function $F(E)$ is the function of density of electron pairs in the band of initial states which may give an excited Auger-electron with energy $E_K=E_i$-2$(E+\Phi)$. This function of pair density is also called self-convolution or divisible function $U(E)$. If internal distribution of excited electrons $F(E_K)$ is known, observed distribution of Auger-electrons yielding from the surface $X(E_K)$ can be obtained provided we know the probability of electron yield through the surface barrier $P(E_K)$. Here the following expression is used

$$X(E_K)=F(E_K)\cdot P(E_K), \qquad (6.20)$$

which is just the product of internal energy distribution of emitted electrons and relevant probability of their yield. Unlike $F(E_K)$, function $X(E_K)$ describes distribution of emitted electrons according to kinetic energy outside the metal.

The final purpose of INS is determination of function $U(E)$ from the experimentally measured function $X(E_K)$. For this slow (as slow as possible) flying ions are used, since energy levels of ions with higher energies are significantly extended if compared to the levels of "ideal" ions with zero energy.

6.3.3 Extraction of spectroscopic data

The procedure of extraction of spectroscopic data form the data on ion neutralization consists in the following:

1) At two small energies of flying ions the distribution functions of emitted electrons according to energy $X(E_K)$ are determined;
2) Then by means of extrapolation these distributions are used for finding the distribution for ideal flying ions with zero energy;
3) The obtained ideal distribution is then divided into function $P(E_K)$ shown in Fig. 6.20 for obtaining function $F(E_K)$. It should be mentioned that $F(E_K)$ depends on the type of the solid and does not depend on the type of the ions used;
4) Function $F(E)$, obtained from $F(E_K)$ by the substitution of the variable is exposed to deconvolution for obtaining $U(E)$- the function of transitions density.

6.3.4 Influence of adsorption on neutralization process

When foreign atoms are adsorbed on the pure metal surface the structure of electron states in the near-surface region is changed. Such changes both in states density and wave functions are most clearly seen in the immediate proximity to the adsorbed atom. This atom becomes the crossing point of great number of electron states of the system metal-atom. Discreet states of the free atom corresponding to electron configurations with lowest energy are replaced by broad energy bands where the amplitude of the wave function on the atom is larger than that one if there were no adsorbates at the metal surface. This case is diagrammatically shown in Fig. 6.21, where at energy E_A the width of the resonance connected with the adsorbate is ΔE_A.. This bound state is virtual as the electrons in it are in a very close contact with the continuum of filled electron states of the metal. Maximum module of the wave function is shifted according to energy by value D_A as regards the basic sate of the atom which is located below the vacuum level at the distance equal to the ionization potential in free space. If electrons come to non-equivalent orbitals of the adsorbed atom, several resonances may emerge.

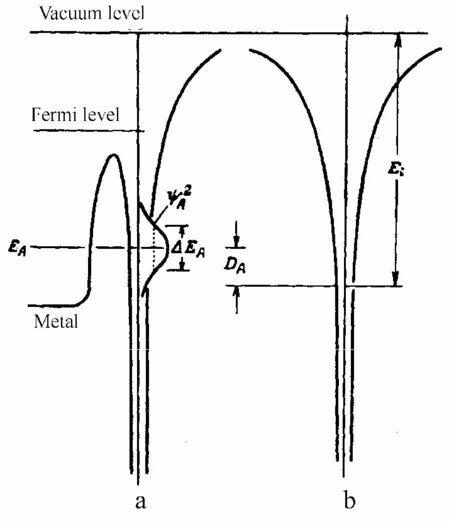

Fig. 6. 20. Diagram of electron's energy levels in the solid and in the adsorbate atom of two states of the latter: *a* – adsorbed and b – desorbed; ψ^2_A – the second degree of the module of the wave function of the surface electron orbital of the adsorbed atom

The influence of virtual bound states of the adsorbed atom on the process of ion neutralization when we deal with the electronegative atom with relatively high ionization potential in free state may be illustrated in the following way. Virtual boundary state is completely below Fermi level while the probing ion (for example, He^+ ion) creates the second potential pit outside the metal. The amplitude of the wave function on the adsorbed atom in the field of bound states is higher than when adsorption is absent, and, consequently, the amplitude of the wave function tail on the positive ion increases either. Thus, we can expect that the process of ion neutralization will be more probable if the adsorbed atom is present. This does not necessarily mean that general yield of electrons will increase.

6.3.5 INS with participation of metastable atoms

If the neutral atom in the excited metastable state reaches the metal surface it may be ionized as a result of tunneling of the excited electron to the metal. It is obvious that this is possible only when the metastable level is located above Fermi surface in the metal. In the situation when there is no suitable unfilled level, the metastable atom may interact directly with the surface in the process of Auger-relaxation. This interaction is a single-electron one and allows to obtain states density immediately without data deconvolution.

Atoms of He and Ag have suitable metastable levels located above the surface of Fermi liquids of most metals. In the case of He atoms there exist two metastable levels: the singlet one 2^1S_0 that is by 20.614 eV higher than the basic level; and the triplet one 2^3S_1 that is by 19.818 eV higher than the basic state. The lifetime of these metastable states is long enough to implement the above mentioned process. The metastable atom of *He* may transit to the basic state as a result of collision or emitting relaxation. If the pressures have been chosen properly the metastable atoms will be hitting with the surface of the metallic target more frequently than with other atoms of *He*. The radiation lifetime of the singlet metastable state accounts for 10^{-2} *s* regarding the registered two-photon process. Here the radiation with the wave length 585 Å is emitted which is capable of dislodging photoelectrons for the metal surface.

The lifetime of the triplet state is much longer (10^3 *s*), since transition to the singlet basic state is prohibited. The first short-living radiation state of *He* is state 2^1P_1 with energy 21.2 eV. We can expect photon resonance radiation to appear if the exciting potential is increased above the excitation threshold of level 2^1P_1. Therefore, working conditions must be chosen in such a way, so that they can provide a relatively large crosscut of metastable state excitation if compared to the higher excitation states.

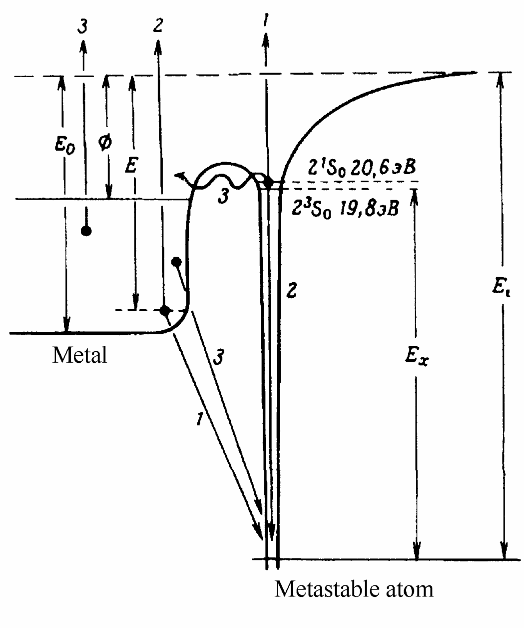

Fig. 6.21. Diagram of ion formation and its subsequent neutralization at interaction of metastable atoms of He with the surface. Electron pairs 1 and 2 illustrate the process of auger-relaxation; electron pair *3* participates in the processes of resonance ionization and auger-neutralization; E_x – energy of the metastable level.

Fig. 6.21 shows the process of ion formation and neutralization with the participation of the metastable He atom. After the first stage in which the metastable atom turns into the ion the process goes in the same way as the one for incident ions with low energies described in the previous part. Thus by using metastable atoms it is possible to obtain ions with virtually thermal energies at the metal surface. In reality, however, it does not happen exactly this way, since the influence of the potential of electrostatic image forces is not taken into account. The potential of image forces V_{im} is determined by the expression

$$V_{из} = -\frac{e^2}{4x} = \frac{3,6}{x}, \qquad (6.21)$$

here the potential is expressed in volts, and the distance *x* from the ion to the surface– in angstroms; *e* – electron charge. Of course, the value of image potential depends on the distances to the surface at which ionization and neutralization processes take place. The evaluations show that accounting of the image potential gives the ion created at the surface the value not higher than 1eV. Thus by using metastable atoms it is possible to obtain the ion beam with very low energy at the surface of the metal and decrease the extension effects of energy levels.

6.3.6 Specific requirements for experimental conditions in INS

When the INS method is used the demands placed on equipment are usual for UHV-plants. The presence of incident beam of He^+ ions or metastable He atoms does not alter these demands, as they are not bound with the target surface, except for very low temperatures. However, the plant should meet the following additional experimental requirements:

1) The source of He atoms does not contain admixtures which may gradually result in surface impurity;
2) Sufficient pumping speed is required to maintain the pressure in the chamber within the range of $10^{-9} - 10^{-10}$ *mm. of mercury* even if bombarding beam of He is present;
3) Bombarding ions must have small speeds for decreasing energy extension. Usually to obtain extrapolate distribution corresponding to relatively small energy extensions two distributions are measured corresponding to kinetic energies of ions, which are equal to, for example, 5 and 10 eV;
4) While measuring energy distribution, resolution capacity of the plant should be relatively high, since for obtaining electron distribution according to kinetic energies the dependency curve of electron current at electrode *F* (see Fig. 6.22) upon the value of retarding potential is differentiated. Resolution capacity depends on the correlation of dimensions of target G and the electron current collector. Decrease in resolution capacity which is typical of such measurements is caused by deconvolution of the measured distribution with the aperture function whose width is at half of the height $(d_G/d_F)^2/2$ where d_G is target diameter, d_F is sphere diameter. This extension may be deduced to the value 0.1 eV without great difficulties;
5) Measurement noises should be as low as possible; this especially concerns low-frequency noises, as the deconvolution procedure us to be performed by digital methods. The mode of repeated measurements with accumulation and averaging of data in the multi-channel counter is considered the most satisfying one;
6) Finally, the sample surface should have such conditions that background pressure of active gases is lower than 10^{-10} *mm. of mercury.*

All the stated requirements and restrictions must also be observed when obtaining ion-neutralization spectrums with the use of metastable excited atoms. The experimental plant used in this case should to some extent differ from the described one, as the incident beam now consists of excited or metastable atoms but not ions. Indeed, emergence of ions is an undesirable side effect when generating metastable atoms, since the latter like ions are created at the same time under bombardment by low-energy electrons. When metastable atoms of He are used, accelerating voltage that provides the balance between the yield of metastable atoms and the yield of resonance photons lies within the range of 25-30 V; though a much greater accelerating potential is usually used.

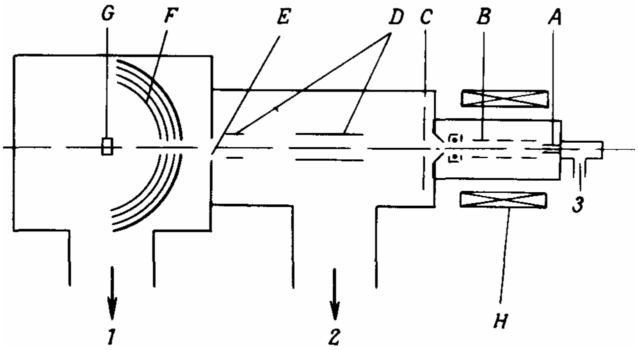

Fig. 6.22. The diagram of the experimental plant for measuring energy distributions of electrons at relaxation of metastable atoms : *A* – helium inlet valve; *B* – electron gun; C – grounded; *D* – deflectors; *E* – aperture forming the beam; *F* – semi-spherical electron collector; G – sample; H – solenoid; 1, 2 – pumping manifolds; 3 – helium inlet.

The source of metastable atoms itself contains the spiral located outside the net of the cylindrical electron collector with potential +25 V relative to the spiral. The spiral emits bombarding electrons; the source works under general pressure of He equal to 10^{-2} mm of mercury. Positively charged ions are filtered by the plates at relevant potentials. For more complicated studies of the process of electron emission one should have a more intensive source of metastable atoms. This can be implemented only by two methods used either separately or simultaneously.

In the first method maximum formation efficiency of the beam of He atoms is provided before they are excited by electron hit. The usual method of beam formation consists in using a multi-channel grid (molecular sieve) or any supersonic nozzle. The typical example of the molecular sieve is a glass washer produced by "Bendix" which has 50% transmission and consists of capillaries with diameter $2 \cdot 10^{-4}$ *sm*, length $6.3 \cdot 10^{-2}$ *sm* and proportion of the length to the diameter $3.2 \cdot 10^2$.

Further improvement of the metastable atoms source implies using the coaxial exciting electron beam instead of the transverse one. This is usually achieved by directing the beam of He atoms along the axis of the cylindrical source of electrons and using magnetic focusing for holding electrons within the limits of the beam before they reach the collector. Another approach uses the system of electron lenses for focusing the electron beam along the beam of He atoms with overlapping of the external magnetic field which makes the electrons move along the spiral. The achieved increase in the length of the electron path significantly improves the efficiency of metastable atoms formation. Since the latter are not charged they cannot be focused. As a result, preliminary collimation of the atom beam acquires great importance. The flow of metastable atoms obtained in such type of devices has the value about $5\cdot 10^{13}\,atom/(s\cdot Sr)$.

The typical layout of the knot of the experimental INS plant for measuring energy distribution of is shown in Fig. 6.22. The source of metastable atoms includes the inlet valve *A* for letting in He atoms, the electron gun *B* and the external solenoid. The generated beam containing metastable atoms, ions and photons goes through the deflector *D* which selects only ions preserving the metastable atoms and photons collimated by the aperture *E*. The formed beam after passing through the aperture in the middle of the three-net energy analyzer *F* comes to target *G*. Electrons emitted as a result of the neutralization process are analyzed according to energy with the help of RFA–F (retarding field analyzer).

The example of the plant for INS is shown in Fig. 6.23. The vacuum chamber from stainless steel is in the shape of "three-dimensional cross" formed by the pipes with diameter 16.5 *sm*. There are four removable horizontal flanges as well as one at the top and one at the bottom. The top flange has an imbedded manipulator which enables to move the sample in such a way that its surface faces any of the horizontal flanges by rotation round the axis perpendicular to the surface picture. The bottom flange is used for connecting the high-speed ion pump and the system of gas inlet. The system has an additional experimental device which enables to study the structure of the target

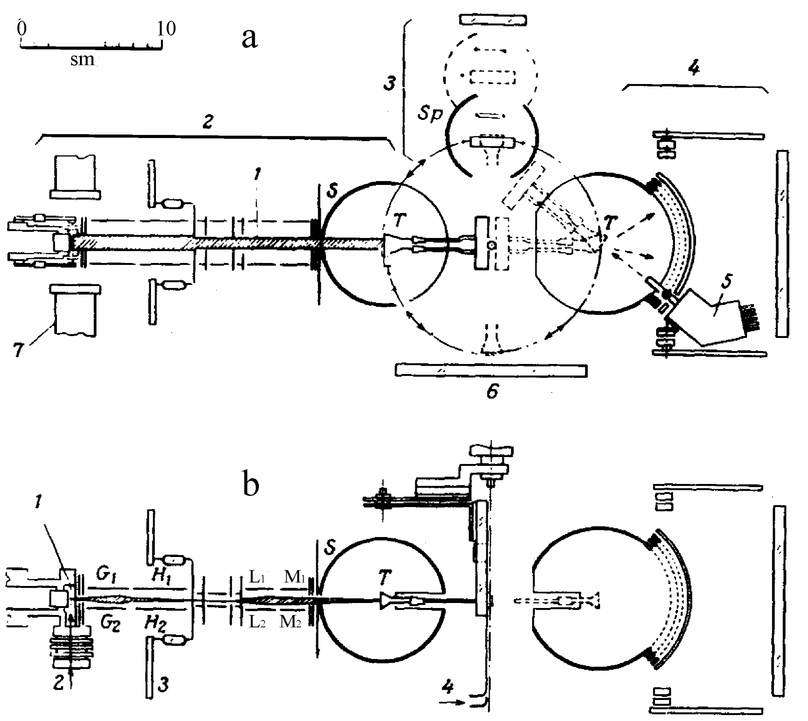

Fig. 6. 23. Scheme of the set for INS:
a – view from above: 1 – ion beam; 2 – system of ion neutralization (flange 1); 3 – system of sample control (flange 2); 4 – flange 3 for electron diffraction; 5 – electron gun; 6 – flange 4; 7 – collimating magnet;
b – front view: 1 – electron beam , 2 – gas delivery; 3 – partition; 4 – sample entrances.

surface with SED method.

At flange 7 the device is assembled which allows to accomplish ion neutralization. Ions are generated at impact ionization by an electron beam and then are focused by two systems of lenses (*G, H* and *L, M*) at the surface of target *T*. Emitted ions are collected at S; their distribution according to kinetic energy is determined by the tilt of the deceleration potential curve.

At flange 2 the system of sample movement is assembled. It enables to put the sample into the adjustable sphere Sp inside of which the target may be sputtered and bombarded by neon or argon ions.

At flange 3 the device for control over slow electrons diffraction is assembled. It enables to observe the structure of the target surface. Flange 4 is designed for visual observation.

6.3.7 Data obtained from INS

Till recently INS were mainly applied to solid samples of Cu, Ni, Si and Ge. To understand the meaning of INS data in Fig 6.24 the spectrums of INS and UVES are compared which are obtained during studies of Ni {100} surface when the sample surfaces are supposed to be pure.

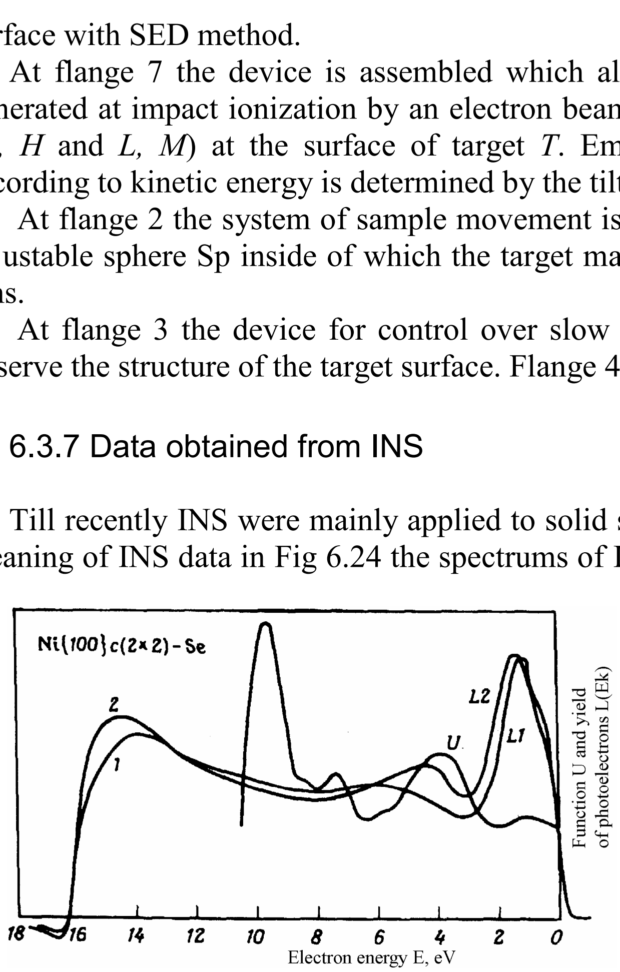

Fig. 6. 24. Comparison of INS and UVES data in case of the surface structure of Ni{100}with (2x2)–Se at normal incidence of ions (*U*), normal incidence of photons (*L*1) incidence of photons at the angle of 45° (*L*2)

The distictions between the above mentioned spectrums are clearly seeen. These distinctions are caused by the fact that the results of INS refer to d-band of surface atoms which by nature "differ" from d-bands in the volume; while UVES data correspond to volume d-states. Actually this figure shows surface sensitivity of INS method. These distinctions are most clearly seen when INS is combined with UVES, AES and SED inside one vacuum chamber. Such combination of methods allows to characterize the surface with high degree of accuracy, i.e. obtain data on crystallography, contents of chemical admixtures and structure of energy spectrum. The most direct comparison may be made in particular between the data obtained with INS and UVES.

The first results obtained with such a complicated modern plant enabled to carry out an interesting comparison of relative sensitivity of averaged angles data of INS and UVES to the electron state in the surface monolayer. For the surface of Ni{100}, covered with layer (2 x 2)–Se, there is some difference in the band energies observed in UVES at normal incidence and at incidence at angle of 45 on the one hand, and with INS data on the other hand. Let us note that measurement by INS method allows to "see" the levels which are not "seen" when UVES method is used. Taking into account the distinct difference between the processes of electron emission which lie in the basis of UVES and INS methods, one shouldn't be surprised by the differences in the results obtained by these methods. Consider the spectrums given in Fig. 6.18, b to understand how detailed the data obtained with INS might be. The data then are exposed to detailed processing and deconvolution described in the previous part; functions *U*(*E*), shown in Fig. 6.25. The levels marked with *p* correspond to *p*-orbitals of free atoms of O, S and Se. The dotted lines mark the energies of molecular orbitals of free atoms of H_2X, where X: O, S, or Se. Among six curves for adsorbed substances shown in Fig. 6.25 three spectrum types of molecular orbitals may be distinguished. Two latter spectrums which peaks are close to orbitals which belong to free molecules of H_2X are the most complicated. The mentioned peaks refer to bridge. The fact that the orbital peak is situated close to the energy of atom *p*-orbital of free H_2S and H_2Se molecules indicates presence of the relatively small negative charge.

If the structure of the surface layer changes from *c*(2x2) to *p*(2x2) as a result of removing half of adsorbed molecules, we see that the spectrums of molecular orbitals change completely and acquire the shape of curves with the single peak located below the peak of Ni d-band in accordance with local bonding symmetry. At adsorption of O at the surface of Ni{l00} the spectrums of both *c*(2x2)- and *p*(2x2)-structures consist of the single peak which is much greater shifted towards Fermi level than in case of S or Se. This result was explained taking into account the inclusion of adsorbed atoms to the upper layer of the substrate with the reconstructed surface when a relatively high charge does not significantly change work function. Indeed, by consequent studying adsorption of O at the surface of *Ni*{100} with the use of different methods it has been found that the process of chemisorption is rather complicated. However, there are no objections to the fact that local coordination structure in phases *c*(2x2) and *p*(2x2) is the same. INS spectrums are likely to be influenced by the existing oxide phase. However, in any case the presented changes in INS spectrums clearly illustrate the sensitivity of the method and its potential suitability for studying bonds of the adsorbate with the surface.

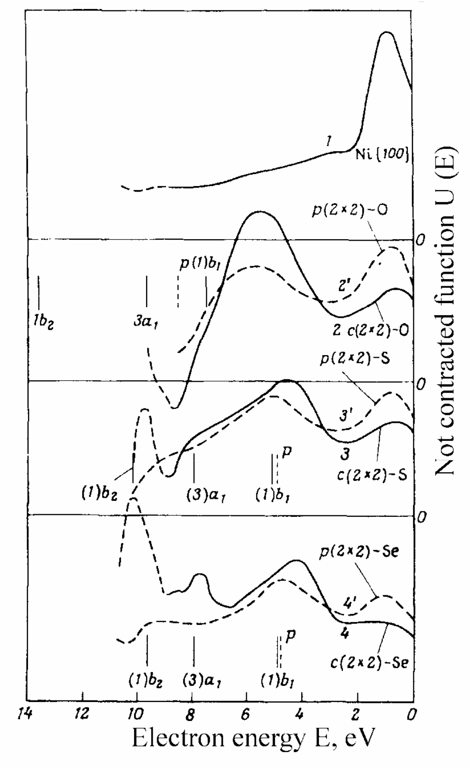

Fig. 6.25. Curves *U*(*E*) for the pure surface of Ni{100} and for the same surface covered with, O, S and Se.

8. Methods of Structural Surface Analysis

The investigation of surface crystal structure is considered to be the most developed method based on X-ray and electron beam diffraction.

X-ray diffraction is a classical and well-developed method of definition of the system of the solid *volume* crystal structure. Besides, the dimensions of the analyzed volume are defined by the length of X-ray absorption – in most experiments this length varies from 10 to 100 μm. For the investigation of *near-surface layer* there is a need for interaction pattern or geometry, which cause the diffraction on the surface or close to it. Sensitivity to surface properties usually takes place when sliding incidence angles of radiation on the surface are used or in the analysis using slow electron diffraction (SED) (or the of energy low electrons diffraction (LEED)).

Diffraction methods present a vast and independent field of investigation. There are a lot of researches and study books devoted to diffraction methods. That is why these phenomena together with focused-beam (scanning) and transmission microscopy are not observed in details in the given manual. Instead, as an example of diffraction methods let us observe slow electron diffraction and take a closer look at field methods, which are less known than the diffraction ones.

8.1 Low energy electron diffraction (LEED)

8.1.1 Diffraction parameters

For the investigation of surface crystal structure the electrons with ~100 eV are used. In all diffraction analysis methods the ordered series of atoms in crystal lattice act coherently the same way as the diffraction lattice that leads to the appearance of diffraction minima and maxima.

As it is known from the course of general physics, electron diffraction was observed by Davisson and Germer's experiments. These experiments demonstrated the validity of wave equation for the description of atomic particles, particularly Schrodinger equation. These experiments also confirmed direct of de Broglie relation between wave length of particle λ and its impulse *p:*

$$\lambda = h/p = h(2mE)^{-1/2}. \qquad (8.1)$$

Observing the interatomic distances close to 1 Å we notice that the corresponding particle energy for electrons equals 150 eV. For every type radiation a procedure of depth analysis is chosen for the each material. Diffraction is a coherent addition of radiation with the same wave length that is why the adsorption or non-coherent dispersion dependent on the prevailing element defines the possibilities of depth investigation. At X-ray diffraction the wave length comparable to the lattice constant, i.e. 1 Å, which corresponds to the energy of X-ray quanta 12.4 keV is used. X-ray adsorption is caused by photoelectron adsorption, that is why comparatively thick or volumetric samples can be used. Photoelectron effect, i.e. adsorption is a prevailing interaction for X-ray with energies ~ 10 keV. Inelastic effects caused by Compton dispersion are insignificant since photoelectron adsorption is much stronger than the Compton's scattering. X-ray diffraction occurs at the depth of 10 μm. Electron adsorption is

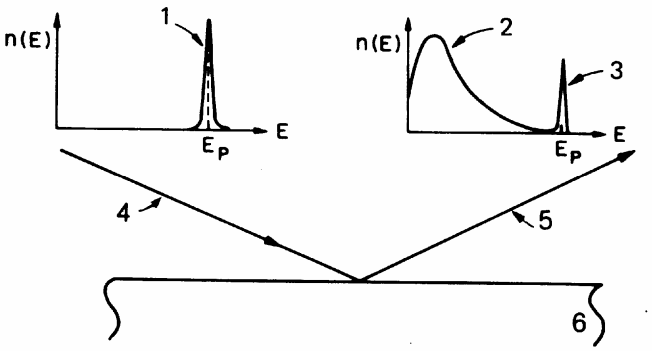

Fig. 8.1. Schematic representation of energy distribution n(E) of falling (1,4), non-elastic (2) and elastic (3, 5) scattered beams under the reflection of electrons with energy E_p from the monocrystal surface .

generally defined by the output depth (see part 5), that is why LEED is used for surface structure investigations. As a surface method LEED is not perfect because electrons may penetrate to the depth of several atomic layers.

Energy distribution of radiated electrons is shown in Fig. 8.1. This distribution appears due to non-elastic scattering (Auger-electrons, secondary electrons and plasma excitation) (part 1.2.2). These non-elastic processes, plasma losses in particular, define the output depth (part 5). For diffraction investigations the sharp peak (3, Fig. 8.1) of elastically scattered electrons is used. In the experiments this peak is observed as isolated from other particles on the energy distribution, which experienced non-elastic scattering.

8.1.2 Thermal vibrations of lattice and Debye-Waller factor

When defining the position occupied by atoms in a crystal, it is necessary to take into account their thermal vibrations near equilibrium positions that disturb the perfection of lattice. The displacement degree of atoms in thermal vibrations is root-mean-square amplitude u^2. In harmonic approach the amplitude distribution is considered to be Gaussian one:

$$P(u)=(2\pi<u^2>)^{-3/2}\exp(-u^2/2<u^2>), \qquad (8.2)$$

where $<u^2>$ – average value u^2 for this distribution. In many cases it is possible to use one-dimensional component $<u^2_x>$, for which

$$P(u_x)=(2\pi<u^2_x>)^{-1/2}\exp(-u^2_x/2<u^2_x>). \qquad (8.3)$$

For cubic systems $<.u^2_x> = <u^2_y> = <u^2_z> = <u^2>/3$. One can define two-dimensional root-mean-square amplitude of thermal vibrations $p^2 = <u^2_x> + <u^2_y>$. Debye temperature θ_D is approximately defined by the following ratio

$$\hbar\omega_D = k\theta_D\,, \qquad (8.4)$$

where ω_D – Debye cutoff according to frequency, which corresponds to phonon maximum frequency in a solid. Further,

$$<u^2>=\frac{3h^2T}{MK\theta_D^2}\left[\Phi\left(\frac{\theta_D}{T}\right)+\frac{\theta_D}{4T}\right], \qquad (8.5)$$

where $\Phi(x)=\frac{1}{x}\int\limits_0^x\frac{ydy}{\exp(y)-1}$ – Debye function (tabulated), M – atomic weight in a solid consisting of similar atoms; $<u^2>$ dependence on temperature is expressed by the ratio

$$<u^2>=\frac{439{,}2}{M\theta_D}\left[\frac{\Phi(x)}{x}+\frac{1}{4}\right](\mathring{A})^2, \qquad (8.6)$$

where $x=\theta_D/T$. This dependence is shown in Fig. 8.2. When the temperature is high, $T>>\theta_D$ value $<u^2>$ is proportional to the absolute temperature; at low temperatures $<u^2>$ tends to constant finite value corresponding to zero-point oscillations in a solid.

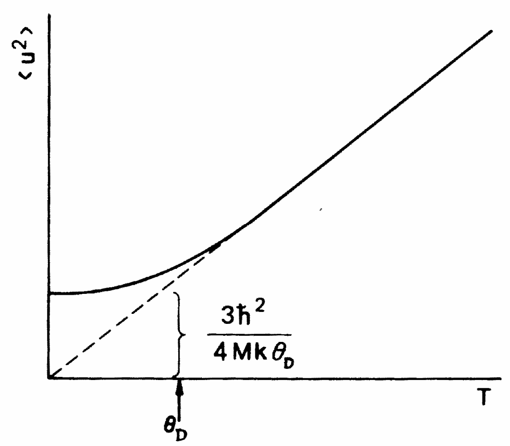

Fig. 8.2. Root-mean-square deviation $<u^2>$ as temperature function T in Debye approximation. The inclination of function asymptotic to coordinate origin is shown by the curly bracket; amplitude of oscillation at T=0 (zero-point oscillations) equals to $<u^2>=3h^2/4Mk\theta_D$.

Thermal vibrations are responsible for temperature dependence of the diffracted X-ray intensity. Diffracted spots intensity decreases as the temperature rises according to the law

$$I = I_0\exp(-2W), \tag{8.7}$$

where W – Debye-Waller factor. In case of X-ray diffraction $2\ W = (1/3) <u^2> (\Delta k)^2$, where Δk – impulse transfer at X-ray quantum scattering, i.e. $\Delta k = (4\pi/\lambda)\sin\theta$. λ – wave length of incident radiation, 2θ - scattering angle.

8.1.3 LEED Implementation

Let us examine the electron with wave length λ falling transversely to periodical atom series with interatomic distance *a* (Fig. 8.3). Waves of small amplitude will interfere with the waves of the neighboring atoms during electron scattering on one atom. In case of mutual wave acceleration new wave-fronts appear. It is necessary for waves to fold but not get absorbed. Hence, they should be in a phase, i.e. a whole number of wave lengths should be placed along the given direction between the wave front and different atoms. This condition of scattering acceleration as a result of interference is expressed in the following way

$$n\lambda = a\cdot\sin\theta, \tag{8.8}$$

where $n\lambda$ – whole number of the wave length, $a\cdot\sin\ \theta$ – interatomic distance projection along new direction of distribution, and, hence, the distance between waves scattered on the neighboring atoms. If this condition of wave acceleration under the interference is carried out for waves arising on the neighboring atoms, then it will be conducted for waves arising at any atoms series due to crystal periodicity. Depending on *a* and λ the constructive interference may take place at several values of the angle θ. As this atom range has one-dimensional symmetry, the constructing interference will arise on cones with axis located on the atom range, and the possibility of electron detection on these cones will also be final.

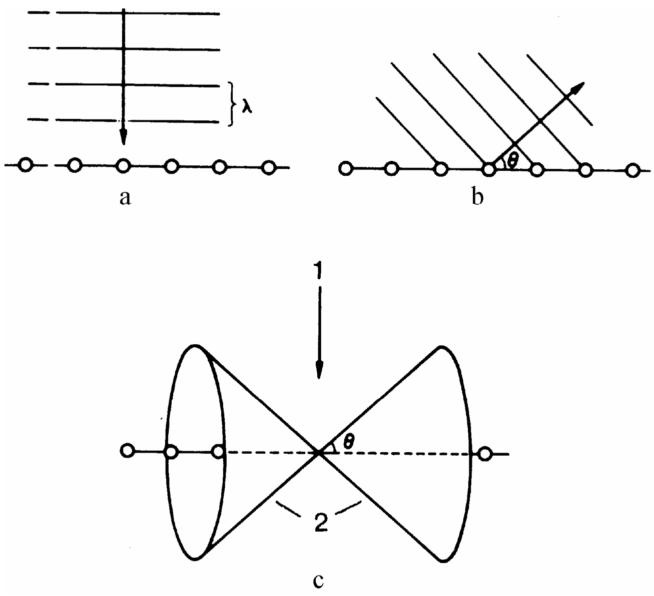

Fig. 8.3. Particle diffraction on a number of scattering centers: a – flat incident wave; b – wave-front of a scattered wave; c – cone, where the interference leads to wave acceleration; 1 – incident beam: 2 – diffracted beam.

Two-dimensional periodic position of atoms with constants of primitive lattice "a" and "b" will give two sets of diffraction conditions:

$$n_a\lambda_a = a\ \sin\theta_a \tag{8.9}$$

and

$$n_b\lambda_b = b\ \sin\theta_b. \tag{8.10}$$

A new set of cones also imposes the only possible area of constructive interference. Since these conditions should be carried out simultaneously the only area where the electron may be found is the cones intersection. As the intersection of two cones with common beginning and non-parallel axes gives straight lines, then at the diffraction of the electron on non-periodical two-dimensional atoms range it can be scattered along the lines and cores stretching from the surface. If we set up the detector across these cores set, they will be presented as dots and spots.

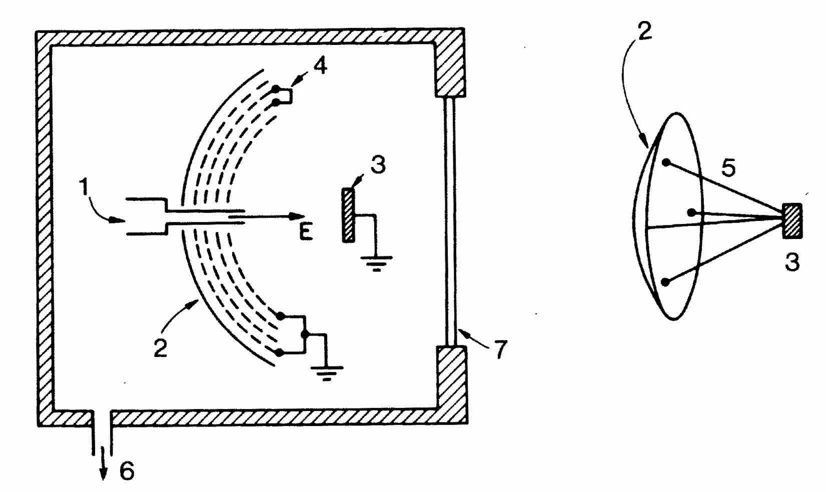

Fig. 8.4. Vacuum setting diagram to observe low energy electron diffraction: 1 – electron-beam projector; 2 – fluorescent shield; 3 – sample; 4 – retarding grids; 5 – diffracted beams; 6 – vacuum pumping socket; 7 – observation screen.

In many experiments on low energy electron diffraction (Fig. 8.4) these diffraction cores are intersected with fluorescent shield, and diffraction spots can be visually observed. Suitable definitions can be associated with these spots (n_a, n_b), where n_a and n_b – integral numbers of the wave length in *a*- and *b*- directions connected with the considered core.

Low energy electron diffraction can be used in various complex methods. The observation of low energy electron diffraction on the fluorescent screen is the simplest diagram. The devise, which is schematically shown in Fig. 8.4, contains a number of retarding grids for the reflection of non-elastically scattered electrons. Elastically reflected electrons have the energy sufficient for overcoming the deceleration system. Having passed through the grids the elastically scattered electrons accelerate to provide the luminescence of the fluorescent shield. The diagram using the low energy electron diffraction is considered to be a comparatively fast and simple definition method of crystal order on the monocrystal surface. Such experiments must be carried out under the conditions of thoroughly controlled high vacuum, because the monolayer of surface contamination may affect the image quality. Diffraction spots intensity of the radiated beams is measured by more complicated methods of the electron diffraction. Further analysis makes it possible to obtain more detailed description of the surface structure.

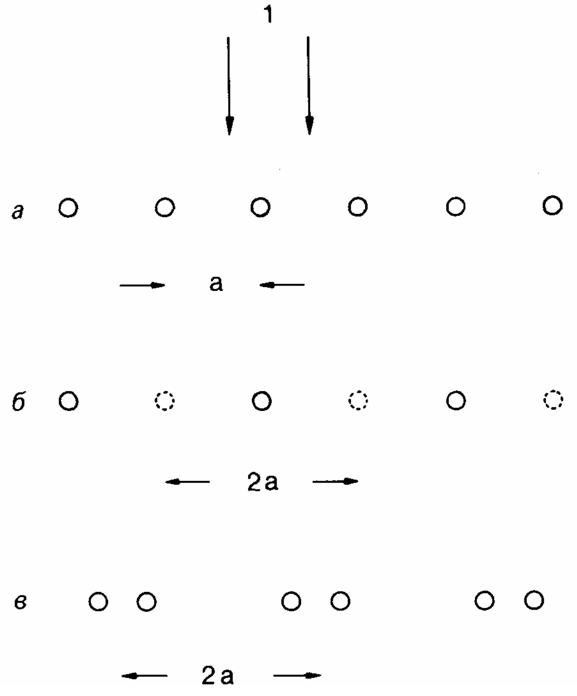

Fig. 8.5. A atomic series with periodicity: **a** – a, **b** – 2a and **c** – 2a. In events b and c there is same pattern LEED for maximums about 1/2 at various arrangements of atoms; 1 - a direction of incident beam.

It should be understood that the phenomenon of low energy electron diffraction depicts surface atoms periodicity and its general symmetry but not specific location of atoms. It can be illustrated by a simple example. Let us examine signals corresponding to zero order (θ=0°) and to the first order of diffraction n = 1 shown in Fig. 8.3. The angular difference between two diffraction orders is presented by ratio $\Delta\theta$=arcsin(λ/a).

If $\lambda/a = 1/3$, then $\Delta\theta$=19.5°. Let us replace a → 2a by reducing twice the atom density along the range. Now $\Delta\theta$=9.59°, and for n=0 and n=2 the difference is $\Delta\theta$=19.5°. As a result, there appears a group of additional spots between initial spots. Any structure leading to periodicity will give spots with order 1/2. The examples of such structures are shown in Fig. 8.5. It presents the initial structure with period *a,* structure with period 2*a*, which appears due to vacancies in every second node, and the structure with the same period 2*a*, which appears due to the doubling of the adjacent atoms doubling. Structures b and c consist of atoms, which have different locations, and the same pictures of LEED form the result.

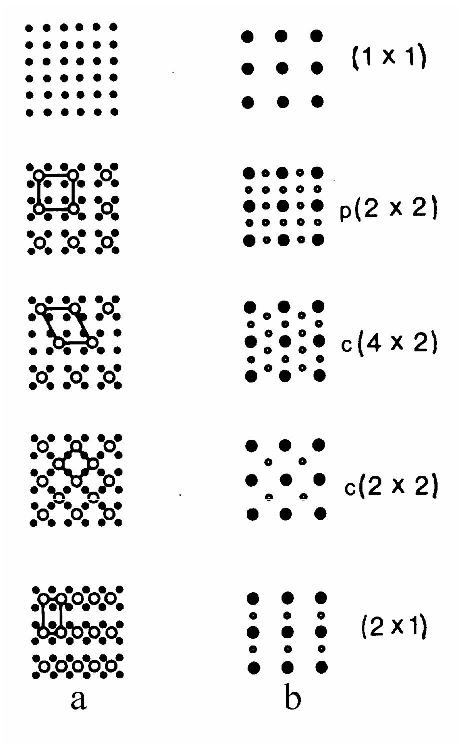

Fig. 8.6 Surface upper layer (100) of a cubic crystal (a) in real space and corresponding to LEED images in the reciprocal vector space (b).

Though the definition of atoms location using low energy electron diffraction is not well-defined, one can predict the symmetry of the diffraction image basing on atoms location in real-space. The examples of outer layers on the surface of a cubic crystal (100) are shown in Fig. 8.6. Letter *p* in Fig. 8.6, shows that the unit cell is primitive and low energy electron diffraction for *p*(2x2) has additional spots of a half-integral order. Letter "c" in Fig. 8.6 shows that there is an additional scatterer in the middle of the unit cell, which causes the appearance of spots 1/2, 1/2.

In general, surface periodicity changes result in diffraction change, which can be easily observed and interpreted in terms of new two-dimensional symmetry. Such changes are often observed, for example, during gas adsorption on a crystal surface. Gas atoms are often set in a well-ordered manner with periodicities, which are obtained by multiplying the substrate periodicity by the integral number. Standard definition for such structures (see also part 2.1.1) is *M*(*hkl*)-(*n*×*m*)-*C,* where *M* –chemical symbol of the element, whose surface is

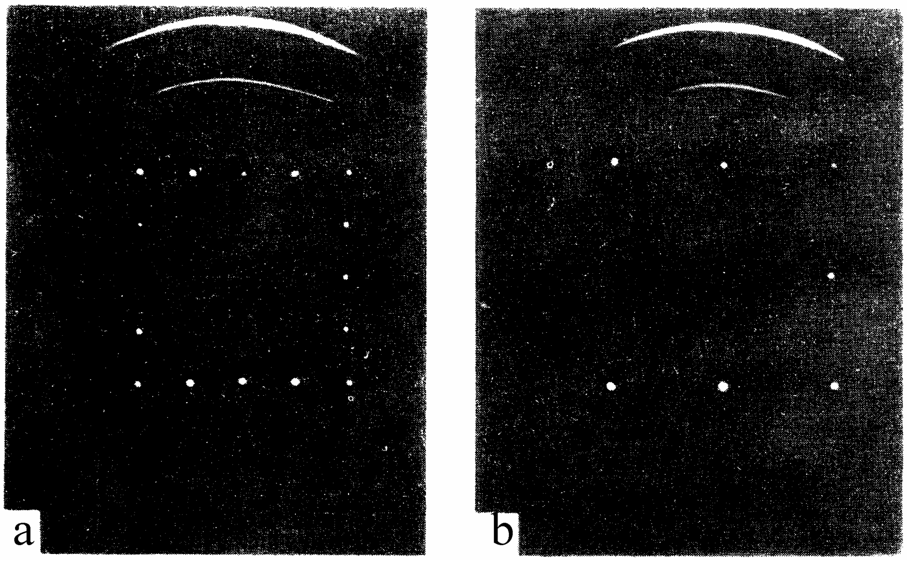

Fig. 8.7. LEED pictures on Si (100) for clean surface (*a)* and surface covered with hydrogen *(б)*. In the first case, the picture consists of two lines (2x1) rotated at 90° relatively to each other. Order maxima appear due to double periodicity on the surface. Substrate covered with hydrogen has the periodicity (1x1) and order maxima are not observed anymore.

observed; (*hkl*) is the crystal plane parallel to the surface; ($n \times m$) shows that the periodicity of a new surface structure *n* times exceeds the initial surface periodicity in *a* directions and *m* times in *b* directions. Finally, C is a chemical symbol of the adsorbed gas or of other surface contamination. The letter is often placed before ($n \times m$): for example, *p* denotes that the unit cell is primitive, or *c* denotes a centered cell. Symbol *p* is often omitted for short. If a new unit cell is turned in relation to the substrate then mutual orientation angle is indicated. The examples of such symbols are represented as Ni (111) (2×2)-0, Pt(100)-C(2×2)-C_2H_4, W(110)-C(9×5)-CO и Si(111)-(7×7). The last symbol is eliminated when the type of contamination is unknown or when it is assumed that the surface rearranged itself with new periodicity in the absence of other elements. Diffraction on a clean surface Si (l00) gives such a picture where both "normal" spots and spots of 1/2 order due to the surface rearrangement (Fig. 8.7, a) are presented. Hydrogen adsorption eliminates periodicity observed on the clean surface, and the diffraction corresponds to the inner volume structure (Fig. 8.7, б). High surface sensitivity of low energy electron diffraction is caused by large cross-section of low energies spattering on atoms. Average energy electron diffraction (AEED) and high energy electron diffraction (HEED) at reflection separate the power range boundary of used electrons up to ~50 keV, which make this methods more useful for fine films (and not for the surface). The geometry of sliding angles is used in the mentioned methods, and that leads to strict requirements to surface planarity of a sample.

8.2 Field microscopy methods

Field ion and electron microscopy is based on field ion emission phenomena (FIE) (part 1.2.1) and field electron emission (FEE) (part 1.2.2). The development of these phenomena dates back to 1936 when E.V. Muller invented the field electron microscope (FEM). This device gave a wide range of opportunities, including not only surface observation in a scale close to the scale of atomic size but also the possibility to observe rapid changes of surface atomic topography. Besides, he was the first who gave the possibility of direct determination of surface condition.

Field ion microscopy is the practical implementation of field ionization phenomena – one of the most effective methods of microscopy known nowadays. At the same time, field ion microscope (FIM) is one of the simplest technical devices used in surface investigation. The first FIM was constructed by E.V. Muller in 1951 and was similar to FEM but working the "opposite way", i.e. with opposite to FEM potential signs on the electrodes.

8.2.1 Field electron microscope (FEM)

In its simple variant FEM consists of a wire with a very sharp end (spike) placed in the middle of the spherical retort covered with the conductive luminescent shield (Fig. 8.8). After the pressure in the system equals 10^{-7}–10^{-11} *mm of mercury* the emitter is heated by conducting the electric current

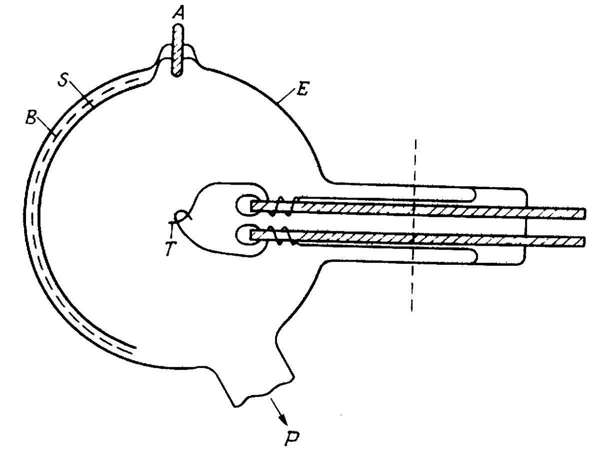

Fig. 8.8. Diagram of the simplest FEM: E – glass retort; S – luminescent shield; B – contact cover; A – vacuum intake; T – emitter (sample); P – pumping socket.

through the carrier until complete metal degasification and formation of a round spike with the smooth surface. The value of the spike radius is ~10^{-7}–10^{-6} m depending on melting temperature and degasification readiness of used metals. If potential of ~10^4 V is applied between the spike and the shield, field emission occurs as field intensity value near the spike is equal to

$$F = \frac{V}{rk}, \tag{8.11}$$

where k – constant equal to ~5, and r – spike radius; with the given values k and r $F = 10^9 – 10^{10}\ V \cdot m^{-1}$. Electrons leave the spike with low initial kinetic energy, and thus, the electrons move along trajectories parallel to the force lines F. As these lines are placed transversely to the surface of the metal spike, the trajectory of electrons is presented by bar lines showed in Fig. 8.9. Thus, the image on the luminescent shield represents the distribution or the map of electron emissions from the spike enlarged at $D/\delta = x/r$ or, to be more accurate, at cx/r, where c – compression ratio is equal to 0.6. Hence, the linear enlargements of 10^5–10^6 were obtained. Device resolution is restricted by the value ~20 Å due to the component of speed tangential of the emitted electrons (with respect to spike circle).

Usually the emitter is presented as a polycrystal wire. In the process of its preparation using wire–drawing the tendency to the orientation of separate microcrystals (texturing) is observed. In combination with the small size of the spike this leads to the formation of emitting surface by a separate monocrystal mainly along the wire axis. It can be clearly seen from the example of the emission from W, where wire axis is transverse to the plane (110). As a result, the projection map of the work function is presented by plane projection (110) located in the centre and four flatness projections {211} situated symmetrically around it. The planes of close packing of bcc lattice (e.g., {110} and {211}) are characterized by higher values of the work function in comparison with the surrounding planes, and appear in the form of dark spots on a brighter background (Fig. 8.10). With the help of standard orthographical projection on image symmetry one may define emitter's orientation and identify the planes. So, for example, symmetry axis of the forth order in a cubic crystal can be observed only in the direction <100> and symmetry axis of the third order – only in the direction <111>. Crystal models examination shows what planes of the given structure are tightly packed, and, consequently, for which of them the highest results of the work functions are expected. When the identification of two or three major distances is completed, one may compare the angular distance between them in the image with theoretical values, and define the compression ratio c.

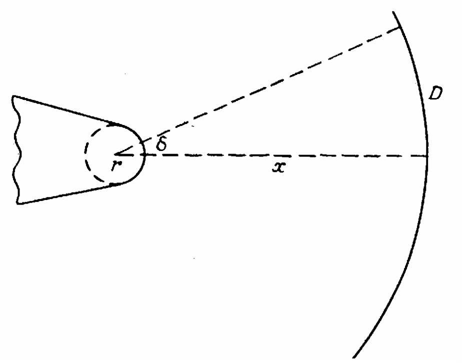

Fig. 8.9. The diagram of FEM optics: r – radius of spike curvature, x – distance from the spike to the shield. The area with linear dimension 5 increases on the shield up to D dimension.

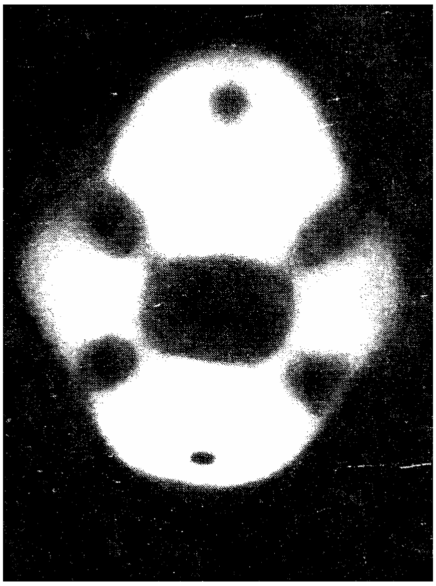

Fig. 8.10. Field emitter emission from W.

There exists a rigid requirement to emitters to accomplish the work conditions of the field electron microscope. Visual examination or photographing of the emission images is possible at current densities on the shield not less than 10^{-5} A/m^{-2}. It means that at regular distances from the spike to the shield there is a need for currents 10^{-8}–10^{-7} A. To obtain significant increase at the applied ~20 kV the spikes with radius 10^{-7}–10^{-6} m are required, that is why the minimum current densities on the spike are 10^{6}–10^{7} A/m^{2}. The length of the sharp part of the emitter rod is 10^{-3}–10^{-4} m. This length is restricted by the necessity to obtain high temperatures of the spike (in clearing), which is not possible if the rod is too long because the temperature of the spike rod is restricted by radiation cooling. Besides, if the current value is ~10 A, then to avoid the redundant voltage drop along the emitter its relative resistance must be in the range of 0.03–0.3 *Ohm·m*, which excludes the use of pure semi-conductors and dielectrics.

Maximum current density, which can be obtained with the presence of high quality conductors in a high vacuum, is in practice restricted by the resistive heating of the spike and the rod. If this current density is exceeded, it will be accompanied by evaporation; evaporated atoms meet emitted electrons and get ionized, and ions are attracted to the spike, where presence of them makes the field bigger, neutralizes the space charge and leads to great electron emission. As a result, we have a vacuum break-down and spike destruction. One can get current in the range of 10^{-4} A for refractory metals, such as W; the currents should correspond to current density in the range of 10^{9} A/m^{2} under the condition of better surrounding vacuum in the range of 10^{-7} *mm Hg.*

In addition to the above mentioned requirements it is necessary to say that to obtain minimum registered emission there is a need for fields to be equal to $(3\div6)\cdot10^{9}$ $B\cdot m^{-1}$. The calculation of mechanical stresses in circular cross-section of hemispherical field emitter proves that it should stand voltage ~10^{8} – 10^{10} $H\cdot m^{-2}$. That is why the implementation of field emission is restricted by the use of rather strong metals unless the spikes are made of perfect crystals of a visker-type. Spikes are made either of wires, if the melting temperature of a metal is > 1300 K or by epitaxial growth of the desired emitter on a substrate made of tungsten.

In fact, field electron microscopes are more complicated then it is shown in Fig. 8.8. The design of the microscope depends on types of measurements it is aimed at (for example, for surface diffusion examination, for emission measurements from epitaxially grown or scattered films, for the distribution of the emitted electrons along the energy). That is why currently there exist different designs of FEM.

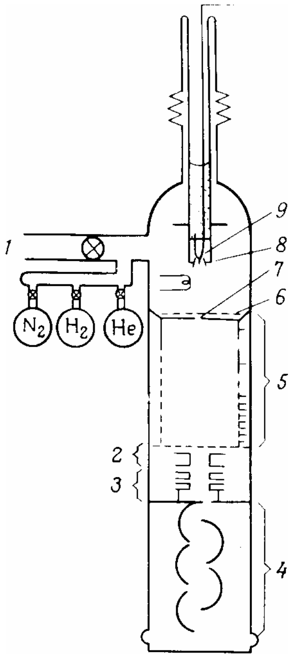

Fig. 8.11 The design of field electron microscope to investigate the process of epitaxial growth: 1 – pumping socket; 2 – tungsten field emitter; 3 – anodic ring; 4 – copper ball; 5 – choke; 6 – luminescent shield.

Considerable differences between various microscopes are not always obvious. So, for example, the construction shown in Fig. 8.11 is different from the regular field electron microscope as there is an extra source of metal evaporation, in our case copper, with the help of which epitaxial growth of copper crystals is accomplished from the gas phase on the field emitter made of tungsten. Thus, emission can be obtained in the presence of fusible metals.

8.2.2 Some spheres of FEM implementation

As it has already been mentioned FEM is used in surface diffusion investigation, for emissive measurements from epitaxially grown or sputtered films, for the distribution of the emitted electrons along the energy. One of the main applications of field electron microscope is in the work function measurement, and particularly in the measurement of the work function changes using the method of probing opening (see next part). Let's consider some results connected with aspects of the adsorption process, such as surface diffusion and thermal desorption. Although gases, which were adsorbed on the emitter from W were observed in the majority of experiments on field emission, in reality not only gas adsorbate can be examined. For example, when covering the molybdenum field emitter with silicon, the average work function decreases at simultaneous decrease in the line current of the field emission. This allows us to assume that tunneling of electrons emitted under the field influence is conducted by the resonance method. Unlimited surface diffusion takes place at small covering degree on planes (111) at 565 K. The diffusion is characterized by a sharp threshold with activation energy equal to 2.1 eV at covering degree exceeding 585 K. Fig. 8.12 shows visualization of diffusion directly on the emitter spike. It is seen, that diffusion occurs in the direction of <211> → <100>. Activation energy of surface diffusion Si in the direction of <211> → <100> was measured taking into account temperature dependence of adsorbate distribution velocities. It was found that Si adsorption on Mo is anisotropic, and if the emitter covered with silicon is annealed at 1000 K then, as a result, we get silicon-enriched surface phases with new crystallographic planes (Fig. 8.13)

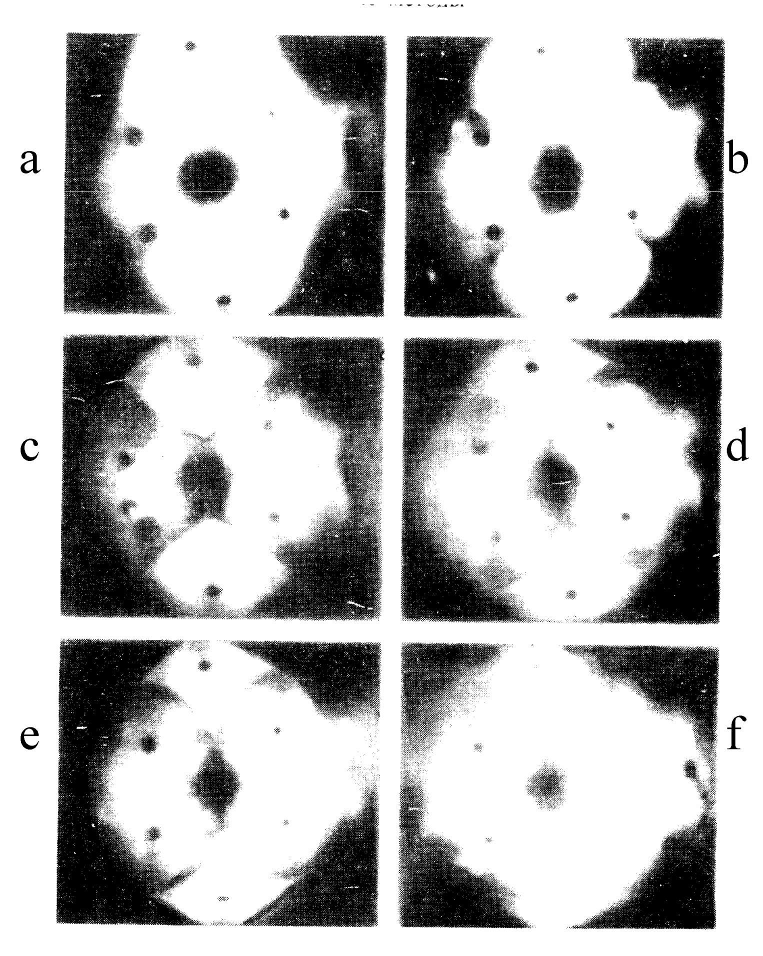

Fig. 8.12. Surface silicon diffusion on molybdenum. Si is sputtered from the left: *а* – clean spike; *б, г* – increasing Si migration at temperature ~610 K; *д* - *е* – further migration at 640 K. Dark spots on the left side of Fig. *б* and *в* – Si deposition close to the planes {211}

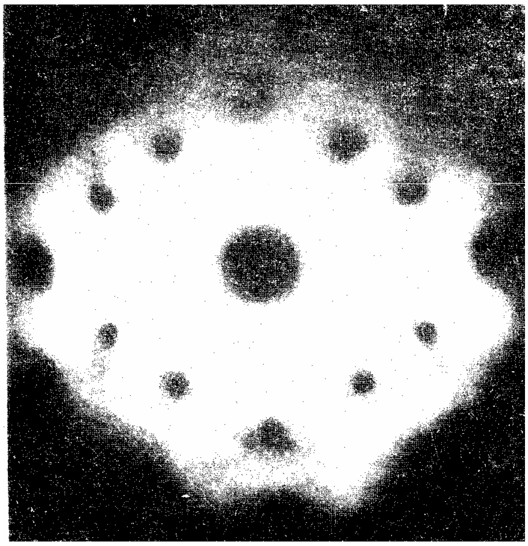

Fig. 8.13. Field emission which arises from the surface phase of molybdenum enriched with silicon.

as contrasted to the emission of the clean emitter from Mo shown in Fig. 8.12, a. As a result of measurements of the dependence of desorption velocities on temperature one may define activation energy of thermal desorption.

8.3 Field ion microscopy

Let us examine in a more detailed way some aspects of the field ionization phenomenon, field evaporation and desorption necessary to understand functions of the field ion microscope.

8.3.1 Characteristic values and processes of field ion microscopy

It was noticed in part 1.2.1 that field ionization occurs within the limits close to some specific distance from the surface. It is possible to obtain this distance, which corresponds to the probability of electrons passing the potential barrier by equating energies of both atom and ion conditions.

$$eFx_c = E_i - \phi - e^2/(4x_c) + \frac{1}{2}F^2(a_a - a_i), \tag{8.12}$$

where ϕ — metal work function, α_a, α_i – polarizability of the atom and the ion formed out of it. The third component is mirror view force potential of the electron, and the fourth one is the polarization energy differences before and after ionization. The last two components are insignificant in comparison with E_i and ϕ; that is why instead of (8.12) the following ratio is usually observed:

$$x_c = (E_i - \phi)/(eF). \tag{8.13}$$

One can get some ideas concerning x_c value when observing He atom. If E_i and ϕ are expressed in electron volts, and F – in $V\cdot\AA^{-1}$, then x_c is obtained in angstroms. For He atom ionization the ionization energy of which is 24.5 eV, for example, on the surface W with ϕ = 4.5 eV in field F= in 5 $V\cdot\AA^{-1}$ the critical distance is $x_c = 4$ $\AA$.

If the potential profile given by values, which are included into the equation (8.12) is known, then the probability of D barrier transmission can be obtained by the composition of Coulomb and applied fields. Such probability can be written in the following way:

$$D(x_c) = \exp[-6{,}83\cdot10^7 E_i^{3/2}(E_i - 7{,}6\cdot10^{-4}F^{1/2}/E_i)^{1/2}/F]. \tag{8.14}$$

The probability of atom ionization is defined by the composition of passing the barrier on frequency, at which the electron inside the atom hits the barrier. For H atom this frequency can be calculated using the Bohr model, whereas when the Bohr method and effective nuclear charge are used for other atoms it is only possible to do the assessment. Typical frequency values for *H, He* and *Ar* atoms are $4.1\cdot10^{16}$, $2.4\cdot10^{16}$ and $1.5\cdot10^{16}$ s^{-1} respectively.

The given above discussion concerned ionization probability of a separate atom, however, during the experiments this value is not measured. Direct validity check of the field ionization theory includes measurement of energetic distribution of ion formed under field action. Field ionization of gas atoms occurs at larger distances from the metal surface if compared to the critical distance x_c defined by the formula (8.13). When reaching the shield ion formed on the ionizer surface possesses energy equal to combined accelerating stress. On the other hand, the energy of the ion formed at the distance x from the surface corresponds to combined accelerating stress reduced at value $\int eF(x)dx$. That is why the measurement of ion energetic distributions that appeared as a result of field emission allows to define the location of ionization, and at the same time provides information concerning the field ionization mechanism and the formation of the field ions mirror image.

The experiments proved that half-width of energy distribution for atoms *He* on *W* at the "best image field" is about 0.8 eV. This only corresponds to a very narrow sphere of ionization with the depth of 0.18 Å or about 1/10 of *He* atom diameter. Similar results were obtained for *Ne, H* and *Ar.*

Even at the primary stage of experiments it was noticed that the measured current of field ions is 10-20 times greater than one could expect under total ionization of gas molecules that bombard the spike even at proper modification of secondary electron influence. Such effect is the result of gas inflow increase due to its attraction of gas molecules to the spike; the molecules are polarized in the inhomogeneous electric field.

The problem of obtaining necessary electrical field values ($\sim 4.0 \cdot 10^{10}$ $V \cdot m^{-1}$) without using extremely big voltage was solved basing on the fact that the field on the surface has a higher curvature radius than the one on the plane for the applied potential, so

$$F_t = V/(kr_t), \tag{8.15}$$

where V – applied potential and k – constant. This situation is similar to the one appeared in case of field emission. The only problem is the creation of surfaces with the small curvature radius – usually ~10–50 nm in case of field ion emitter. Gas molecules approaching the spike get ionized close to the surface, and formed positive ions move to the luminescent shield with the conductive substrate. Then the image on the shield reflects those field ionizer areas, whose local curvature radius is higher, such as steps or edges of atomic layers or even separate metal atoms.

If the field ionization on the spike is carried out at indoor temperature, then the tangential component of representing ions kinetic energy equal to ~0.025 eV can not disturb the functioning or distort the resolution of the field ion microscope. However, it was found that close to ionizer gas molecules reach the spike in the direction close to normal with velocity defined by dipole attraction; such velocity significantly exceeds thermal velocities in gas. Hence, those molecules are ionized which overcame double collisions, because due to diffusion radiation they stay longer in the ionization area. That is why formed ions will possess the tangential velocity components exceeding thermal velocity and reaching total value of dipole attraction velocity. On the other hand, if it was possible to slow down molecules due to their interaction with the spike being at low temperature, then the resolution could be better. The first defined resolution of the atomic grid structure was demonstrated using the mentioned method. Molecules after partial loss of their energy in the collision with the ionizing spike can be kept by a non-homogeneous field near the spike. As, for example, He atoms are not adsorbed on W at 21 K they will diffuse along the surface in jumping regime slowing the speed down approximately up to equivalent spike temperature, and then get ionized when passing through the ionization area above one of the most salient surface atoms. At low field values the ionization probability is so small that the ion drainage almost does not change gas equilibrium density near the spike. The examination within the framework of statistical mechanics shows that gas density on the spike n exceeds gas density at a spike distance n:

$$n_t / n_g = (T_g / T_t)^{1/2} \exp[\alpha F_0^2 / (2kT_g)], \tag{8.16}$$

where T_g and T_t – gas and spike temperatures. This expression is valid if gas molecules obtain the same temperature as the spike. Volume element rdr contribution into the ion current is given by the expression

$$di = 2\pi r^2 e n_t vD(r) dr, \tag{8.17}$$

where vD – ionization probability. Net current is obtained by the integration on r beyond the limits of critical distance Xc and is equal to

$$i = 2\pi n_g e \left(\frac{T_g}{T_t}\right)^{1/2} \int\limits_{r_t + x_c}^{\infty} r^2 vD(r) \exp\left(\frac{\alpha F^2 r}{2kT_g}\right) dr. \tag{8.18}$$

Ion distribution measurements according to the energy showed that the ionization area is very narrow, so $D(r)$ can be presented by the staircase function

$$D(r) = D(x_c) \qquad \textit{for } r_t + x_c \le r \le r_t + x_c + \Delta x, \tag{8.19}$$

$$D(r) = 0 \qquad \text{for } r>r_t+x_c+\Delta x. \tag{8.20}$$

At F value approximately equal to the field strength on the spike surface F_o, the equation (6.18) can be converted into the following one

$$i \approx 2\pi r_t^2 n_g e\left(\frac{T_g}{T_t}\right)^{1/2} \nu D(x_c)\exp\left(\frac{\alpha F_0^2}{2kT}\right)\Delta x\,. \tag{8.21}$$

It is seen from the given equation that current increases sharply together with field strength increase; it happens because this equation includes the composition of exponentially dependent on field D function by the exponential factor. The equation (8.21) is applicable only for the low fields. However, this area and the area of high fields, where ionization in free space is prevailing present less interest for image formation processes.

As long as kinetic energy of thermalized or repeatedly colliding atoms is less than $(l/2)\alpha_0F^2$ they remain close to the surface jumping in the inhomogeneous field surrounding the emitter. The escape of atoms into the free space can be realized in two ways. At first, the atom "jumps" at height more than x_c, and in this case it may be ionized; in small fields this process will take place in the layer close to x_c. The ion formed in this way moves faster towards the shield and is registered there. Secondly, atoms can move in jumping manner towards the emitter rod, particularly to the area where the electric intensity transversely to the surface is small. They can evaporate there.

When atoms jump they get into the area of higher potential energy where they are influenced by power $\alpha_a FdF/dr$. The atom returns to the height where its potential energy increment is equal to its initial kinetic energy. Since the field strength decreases as $F_r=F_0(r_0/r)^x$, where $1<x<2$, then the passed distance is proportional to $kTr_0/(a_0F_0^2)$, where F_0 – field strength on the surface, k – constant.

Thus, for processes taking place on the ionizing surface of an acicular shape the following is valid. When the field is turned on the speed of gas inflow towards the spike gets higher than the normal one, which is typical of molecular bombardment, because the polarizing effect of gas molecules by the field takes place. Here the cross-section of gas capture by the spike increases, the jump length becomes smaller, and the potential hole depth for captured gas equal to $(1/2)\alpha eF^2$ increases. The increase in surface density continues until the field becomes large enough to cause ionization. As it was emphasized before, ionization will occur in those places on the surface where field strength gets into its maximum. These areas have three advantages: *gas inflow is the highest as atoms accelerate towards field inhomogeneous area; diffusion losses are really low; the tunneling barrier is more transparent.*

Both jump height and the edge of the ionization area approach the surface under further field strength increase, however, jump height changes strongly (as $1/F^2$ in comparison with $1/F$ for the area edge), and as a result, the number of "jumping" ions ionized in these spots reduces. In this case some other areas with the bigger curvature radius may become more effective for ionization, and they do not draw back captured He ions. This will undoubtedly lead to the changes in the process of ionization due to the decrease in atom concentration on the surface.

When fields are very high the entering gas may undergo ionization until it collides with the surface, i.e. at some distance from x_c. The ionization process losses its dependence on the atom structure, and as a result the ion image smears.

Ionization scheme verification briefly described above together with the theory is carried out by ionization current measurement. These measurements provide necessary quantitative data to be compared with the theoretical forecast. However, due to the complexity of the considered processes, a complete agreement between the theory and the experiment has not been achieved yet.

As seen from the given part the images that are obtained using the field ion microscope are the result of radial projection of the curved spike on the screen. It is also clear that the quality of an image greatly depends on the opportunity of producing hemispherical and atomic plain surface of the spike. Such spike shape is obtained at field evaporation, which is possible if rather strong electric field is applied to the rough spike. All prominences are completely removed by self-correcting method in the form of positive ions. The increase in the local value of the field strength on the sharp edges and prominences leads to their evaporation until absolutely plain surface appears. Besides, such surface is atomically clean. The minimum value of the field strength necessary for field evaporation at the indoor temperature is 5 $V \cdot Å^{-1}$.

Since ionization probability strongly depends on field strength then the greatest currents will arise from the areas with the highest field. Field distribution near the spike is determined by atomic structure of the latter. At the first approach equipotential surfaces may be presented as spherical segments with centers on the surface atoms. Close to $x = x_c$, where the ionization takes place equipotential sphere overlapping causes structure fuzziness in comparison with the spike. Therefore, field anisotropy will be more noticeable for atoms with relatively small number of neighboring elements and less noticeable for atoms on small closely packed planes. In the first case anisotropy will appear in form of bright dots, in the second case anisotropy in the threshold field may not appear at all. Of course, even some areas of the second group will emit more effectively under the stress increase. However, ionization will become significant everywhere and the image will get smeared at high ionization fields. Hence, *we get the best resolution in those fields which slightly exceed the threshold for the most open or prominent areas of the spike surface.* Field *FI* is called “the field of the best image”, and the mentioned regime is obtained at such field.

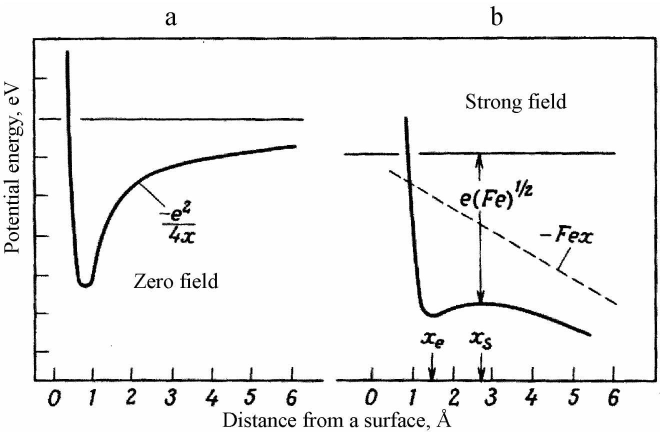

Fig. 8.14. Ion field desorption: *a* – zero field case (the location of ion ground state on the surface in relation to the vacuum level is shown); *б* – strong field case; *xs* – Schottky saddle location; x_e – balanced ion position; *F* – external field.

Atom processes were observed above. The conclusions concerning field desorption are also valid for strongly connected electronegative atoms, for which $E_i - \phi$ difference is large. The only difference is caused by greater bond force. In weak fields that connect the atom with the surface where x_c exceeds the force radius, the adsorbed atom should be thermally desorbed. Only then ionization can take place as it was described in case of He atoms. However, the ionization may occur without thermal activation at the field increase to the point of ion energy decrease to the bottom of atomic potential hole. Then, isoenergetic conversion from the atomic into the ion state under the following condition may occur

$$Fex = E_i - \phi - e^2/(4x) + \frac{1}{2}F^2(\alpha_a - \alpha_i) - V(x), \qquad (8.22)$$

where $V(x)$ — atomic potential at point x. This leads to the field growth necessary for ionization and usually increases lower values of the ionization potential. The barrier overcoming by atoms can be easily changed by applying electrical fields of different strength.

The situation is different when atom ionization potential is close to the surface work function. The attracting part of the potential energy curve in the absence of the field can be easily approximated by the power potential of a mirror image for the ion placed at the distance x_c from the surface. If to apply a large field, then maximum called the Schottky saddle will appear on the resultant curve below the vacuum level at a zero field (рис. 8.14). At further field increase the saddle may descent so that it coincides with the ion ground state. Then, even if T = 0 K field evaporation will take place equal to

$$Fe^3 = (E_d + E_i - \phi + Fex_e)^2, \qquad (8.23)$$

where E_d — ion desorption energy.

If the ground state is atomic, then the field influence should be considered as the polarized member. In this case evaporation at $T = 0$ K takes place, if the field strength satisfies the condition

$$Fe^3 = \left[E_d + E_i - \phi + \frac{1}{2}F^2(\alpha_a - \alpha_i)\right]^2 . \qquad (8.24)$$

The fact that evaporation may be induced by large fields without heating allows to get rid of thermal disorder on the sample surface. Necessary fields are evaluated by the simplest supposition that evaporation takes place as a consequence of Schottky saddle lowering (8.14) using the equation (6.23).

8.3.2. Field ion microscope (FIM)

Fig. 8.15 shows the diagram of one of the simplest FIM design.

For the given conditions of image obtaining one may determine the typical field value on the sample surface F_i , at which ions obtained as a result of field ionization give the most informative and qualitative images. This typical field known as the field of the best image depends on the character of image forming gas, especially on its ionization potential. The comparison of various image forming gases is based on it. The second important parameter is a typical field F_e necessary for field evaporation of a material surface, which depends mainly on the spike material and almost is not dependent on temperature and other conditions of the experiment [see equation (8.24)]. It is obvious that value F_i must be less then F_e to obtain stable and useful image in the field ion microscope.

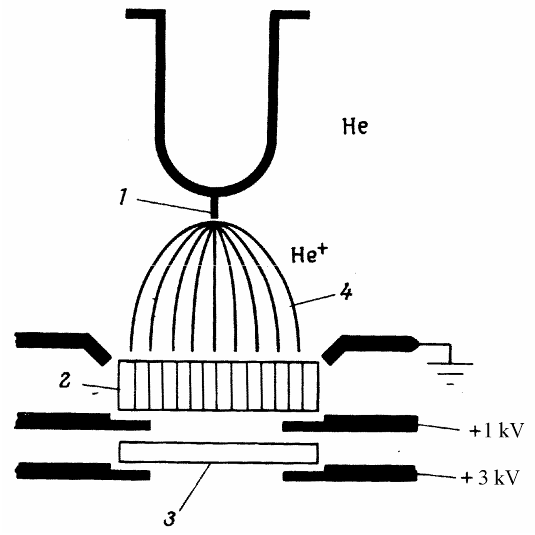

Fig. 8.15. Field ion microscope scheme with image intensifier: 1 – emitter's spike; 2 – microchannel plate; 3 – luminescent shield; 4 – field lines.

The next general requirement is that in the adsorption and steam deposition experiments the depicted surface at least in its initial state should have a well-ordered structure; in this case ion images can be easily interpreted. Generally speaking, such surface should be formed in field evaporation and remain stable in image forming conditions, especially in relation to changes caused by unavoidable adsorption and desorption. The latter usually belongs to field desorption of the adsorbed atom together with the substrate atom in a field less than F_e for clean substrate.

Due to the last circumstance inert gases are more preferable for image formation since their interaction with the sample surface is relatively weak. When the luminescent screen serves as an image detection device He is usually chosen among all inert gases. This choice is quite natural since more heavy ions are less effective and damage the luminescent layer faster. However, He has the highest field strength value, at which ionization takes place: $F_i = 4.4\ V \cdot Å^{-1}$; that is why its application is restricted by some refractory metals with larger values F_e and tightly connected adsorbates. The example of image W obtained using He is shown in Fig 8.16. The values of F_i for inert gases are placed in the following order *He>Ne>Ar>Kг>Xe*. The application of more active gases, such as *H, N* or CH_4 is usually restricted by their strong chemical interaction with material surfaces under the influence of strong fields necessary to obtain ion images. These interactions lead to *Fe* field strength decrease; the field strength is necessary for sample material evaporation. Since another condition of satisfactory image obtaining includes the fact that the sample should not change its shape or crack under the influence of high mechanical stress caused by the applied electrical field, then the possibility of surface preparation using field evaporation in hydrogen under the reduced level of mechanical stresses turns out to be an efficient consequence.

The application of *Ne* and *Ar* as image forming gases in field ion microscopy provides the possibility to obtain high-quality images of such fusible materials as *Cu, Au* and A1, the images of *Au* samples obtained using *Ar* ions usually have worse resolution then images obtained with neon.

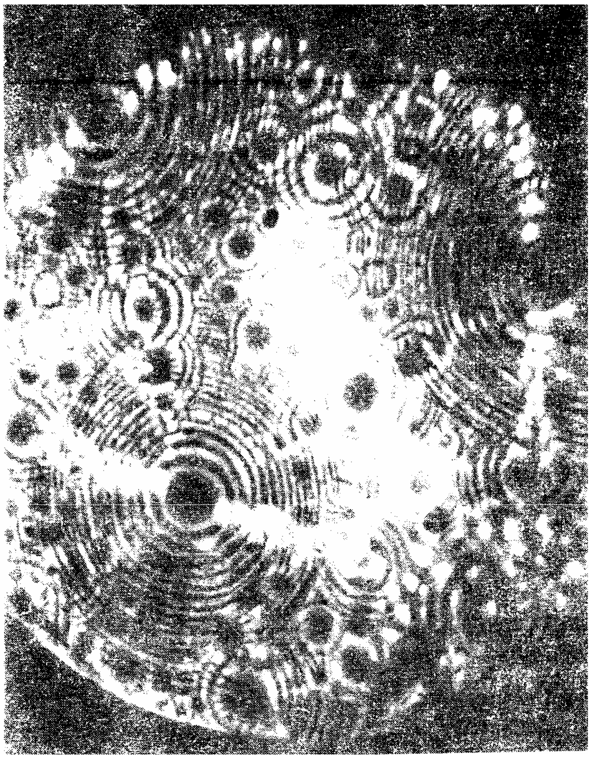

Fig. 8.16. Field ion microphotography of surface W at 78 K using He as an image forming gas.

Qualitative instructions of image forming gas choice for metals give metal melting temperatures. For example, metals with the melting temperature higher than 2000°C can be presented by *He. Ne* and *Ar* ions can be used for metals with melting temperatures in the range of 2000–1000 and 1000–600°C correspondingly. Low bound of temperature, at which the images in inert gases were obtained, comprises the temperature of 20 K for He and 55 K for *Ar*.

It is necessary to create ultrahigh vacuum for the investigation of adsorption and some problems in field ion microscope, but if He is used as image forming gas then the mentioned conditions are subdued. When we use He as image forming gas big fields are applied to the sample surface so that it becomes protected from different types of pollution. The molecules of such residual gases as CO, N_2, O_2 and so on have a very low ionization potential, and as a result they are ionized in a free space above the sample spike, and then they are repulsed. After the sample surface is cleaned by field desorption and field evaporation no other molecules can reach represented spike area form the area above it until the field on the spike is supported by the bigger one. Spike protection by high fields is effective only for He as an image forming gas; other types of image forming gases require the support of ultrahigh vacuum.

Both field ionization and ion microscope function depend on the preparation of a sample spike. The most convenient and effective method of sample spike preparation includes tapered needle shape of the thin wire end with the diameter $5 \cdot 10^{-5}$ *m* using anode electropolishing.

8.3.3 Field ion microscope with the atomic probe

During the work with the spikes one can get an atom image adsorbed on tungsten from W, however, there appears the problem of identifying the chemical nature of atoms responsible for the image. In other words, there is a possibility that the adsorbed atom causes such surface displacement of W atom that it moves forward over the surface and forms the area with a high local field (but not adsorbed). Likewise even atoms of one type forming the surface of a clean metal sample may appear in the form of spots changing within a wide range, which makes unique identification of foreign atoms impossible. This happens due to packing differences in various crystallographic directions. *This problem can be solved by the combination of the field ion microscope and the mass-spectrometer sensitive to separate particles, and this is provided by the field ion microscope with an atom probe.* It helps to identify the nature of one separate atom seen on the sample and chosen according to the observer.

Fig. 8.17 shows the scheme of the field ion microscope with an atom probe. It presents the modified field ion microscope so that the atom spot chosen for the analysis can be combined with the probing opening of the screen. This opening serves as an entrance into the time-of-flight mass spectrometer. The analysis is carried out by field desorption of a tested atom using high voltage pulse. Formed ion passes through the probing opening and drifting pipe of a mass- spectrometer towards electron multiplier detector. The desorption pulse launches horizontal deflection of an oscillograph. When the ion approaches the detector the output signal is given to the oscillograph. Thus, the ion flight time *t* to the detector located at the distance *d* is registered. As ion terminal velocity is obtained at distances of several spike radiuses from the emitter the ratio of mass to the charge can be easily calculated and defined by the expression

$$M/n = 2eV_ct^2/d^2, \qquad (8.25)$$

where n=1, 2, 3, 4 and V_c – applied evaporating voltage.

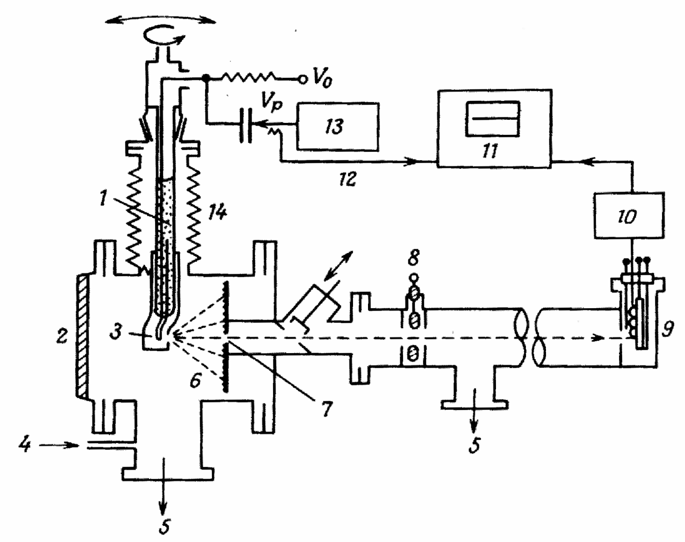

Fig. 8.17. The scheme of field ion microscope with an atom probe: 1 – cold pin; 2 – observation window; 3 – sample; 4 – image forming gas leak valve; 5 – pumping manifold; 6 – luminescent screen ; 7 – probing opening; 8 – lens element; 9 – detector; 10 – preamplifier; 11 – oscillograph; 12 – launching device; 13 – pulse generator; 14 – silphon.

So, a separate atom can be identified using mass-spectrometer, which makes this device the most sensitive microanalytical tool. An additional advantage includes the possibility to observe the processes of image formation and field evaporation. The formation and evaporation of molecular-ion compounds of spike metal with image forming gas was proved using the field ion microscope with an atom probe. Such ions as *H, He, Ne* and *Ar* are revealed; the latter two ones with a double charge and in combination with *H*. Another interesting result is the discovery of the multiple charges desorbed by the field of metal atoms. For example, it was stated that the charge state of *Mo* atoms desorbed by the field increases fourfold. An even more interesting fact included the covering of the absolutely clean spike of refractory metals with invisible and probably movable adsorbed layer of image forming gas. As a result, the accommodation of the incoming image forming gas with the kinetic energy of $(1/2)\alpha_aF^2$ to the low temperature of the spike is more efficient than it was supposed earlier due to the fact that collision happens with adsorbed gas atoms of an equal mass but not with heavier metal atoms. There is a need to examine the mechanism of the local inflow of image forming gas into the field ionization area above the prominent surface atom, because the atom of the ionizing image forming gas may be the one pulled out from an adsorbed state and not the primary atom moving in a jumping regime.

References

1. A.M. Afanasyev, P.A. Aleksandrov, R.M. Imamov. X-ray structural diagnostics in surface analysis. – M.: Mir, 1986.
2. Surface analysis by means of Auger and X-ray photoelectron spectroscopy (edited by D. Brigs and M.P. Sikh) – M.: Mir, 1987.
3. D. Woodraf, T. Delchar. Modern techniques of surface science. - M.: Mir, 1989.
4. T.A. Karlson. Photoelectron and Auger spectroscopy. – St.-Petersburg: Mechanical Engineering, 1981
5. Methods of surface analysis (edited by A. Zandernu) – M.: Mir, 1979.
6. V.I. Nefedov, V.T. Cherepin. Physical methods of solid surface analysis. – M.: Science, 1983.
7. V.M. Nefedov. X-ray photoelectron spectroscopy of chemical compounds. Reference book. – M.: Chemistry, 1984.
8. N.N. Petrov, I.A. Abroyan. Surface analysis with help of the ion beams. – St.-Petersburg: Publishing house of LSU, 1977.
9. The implementation of electron spectroscopy for surface analysis (edited by I. Ibakh) - Riga: Zinatne, 1980.
10. Spectroscopy and electron diffraction in solid surfaces analysis (edited by N.G. Rambidi) – M.: Science, 1985.
11. Sputtering by Particle Bombardment. Issue 1 and 2 (edited by R. Behrisch). – M.: Mir, 1984.
12. L. Feldman, D. Maier. Fundamentals of surface and film analysis. – M.: Mir, 1989.
13. Physical encyclopedia in 5 volumes. Moscow. Scientific publishing house "Big Russian encyclopedia ", 1998.
14. V.T. Cherepin, M.A. Vasilyev. Methods and instruments for surface analysis of materials. – Kiev: Naukovaya dumka, 1982.

CONTENTS

Tomsk Polytechnic University

Nikolay Nikolaevich Nikitenkov

THE BASICS OF ISOTOPIC, CHEMICAL AND STRUCTURAL ANALYSIS OF THE SURFACE BY MEANS OF ATOMIC PHYSICS

Textbook

The editor – Galina Vasilievna Kalitkina

Tomsk 2005